C.P. No. 287
(18,671)
A.R.C. Technical Report

C.P. No. 287
(18,671)
A.R.C. Technical Report

MINISTRY OF SUPPLY

AERONAUTICAL RESEARCH COUNCIL

CURRENT PAPERS

Fatigue Loadings in Flight Loads in the Fuselage and Nose Undercarriage of a Varsity

By

E. W. Wells

LONDON: HER MAJESTY'S STATIONERY OFFICE

1956

PRICE 3s. 6d. NET

C.P. No.287

U.D.C. No. 539.431: 629.13.012.2(42)Varsity

Technical Note No. Structures 193

May, 1956

ROYAL AIRCRAFT ESTABLISHMENT

Fatigue Loadings in Flight - Loads in the Fuselage and Nose Undercarriage of a Varsity

by

E. W. Wells

SUMMARY

Flight tests have been made on a Varsity to obtain data on the fatigue loads in the fuselage and the nose undercarriage. The data are tabulated in terms of the number of load ranges of a given magnitude occurring during various ground and flight conditions. An estimate is made of the loads in a typical operational training flight to show the relative importance of the various conditions. A relationship is established between the fuselage loads and the accelerations at the aircraft c.g. when flying in turbulence; this enables the results from the flight tests to be linked to operational data obtained on gusts.

LIST OF CONTENTS

LIST OF APPENDICES

LIST OF TABLES

LIST OF FIGURES

1 Introduction

Flight tests were made in a Varsity to obtain data on fatigue loads in various parts of the structure. The loads on the tailplane and fin have already been given;[1] this note deals with loads on the fuselage and nose undercarriage.

2 Description of Instrumentation and Flight Tests

An account of the instrumentation and strain gauge calibration is given in Appendix I. Electrical resistance strain gauges together with continuous recording equipment were used to measure the bending moment at two fuselage stations and the vertical load at the nose undercarriage. Records were taken during ground engine running, taxying, take-off, landing and when flying in turbulence. The vertical acceleration due to gusts was measured by means of an accelerometer installed at the aircraft c.g.*

3 Presentation of Results

Information on the loads measured is tabulated in terms of change of mean load (Table I) and numbers of load ranges exceeding various sizes (Tables II - IV). The method of analysis used has been described in an earlier note[1]. In analysing the landings and take-offs the change in mean load is not included in the count of load ranges. The term range has its usual definition and is twice the alternating load.

From data obtained in the flight tests an attempt is made to estimate the loads in a typical operational training flight so as to enable the relative importance, from the fatigue aspect, of the various flight conditions to be established. This typical flight consists of 4 mins ground engine running at various engine conditions, 5 mins taxying, a take-off, 33 mins flight and a landing. The number of load ranges exceeding various sizes for the various conditions are shown in Figs 2 and 3 and details of the method of estimation of the loads are given in Appendix II.

Table V gives information on the acceleration recorded at the aircraft c.g. during flight in turbulence.

Fig 4 shows the relationship between the fuselage load at the two fuselage stations and the acceleration at the aircraft c.g. that occur the same number of times when flying in turbulence.

4 Results

Fig 3 shows that the vertical loads on the nose undercarriage which cause the most fatigue damage occur during landing and taxying. The loads occurring in take-off are less severe although a few large load fluctuations occur when the undercarriage is retracted. These are due to the undercarriage hitting its stops rather violently on retraction when the impact produces shock loads which also appear at the two fuselage stations. The loads produced on the nose undercarriage during ground engine running are negligible.

As in the case of the nosewheel, the conditions producing the highest loads at the front fuselage station, as shown in Fig 2(a), are landing and taxying. The take-off loads, are again less severe and the ground engine running loads small. The loads produced by turbulence in the front fuselage are also small.

---

* The accelerometer was mounted rigidly at the centre line of the aircraft structure so that its readings will include any dynamic effects due to the flexibilities of the structure.

In the case of the rear fuselage station, Fig 2(b) shows that the landing together with the taxying and take-off conditions are the main source of fatigue loads. The loads in turbulence appear to be more significant than for the front fuselage although the number of times that the largest loads occur cannot be established with much accuracy because of the relatively few large gusts met in the flight tests. The loads occurring during ground running are again very small.

It will be seen from Figs 2(a) and 2(b) that the take-off condition is more critical for the rear than for the forward fuselage station. The larger loads on the rear fuselage station occur during the final stages of take-off when the nosewheel is clear of the ground and the aircraft is taxying at speed on its main wheels. The aircraft, which is partially airbourne at this stage, is pitching and bouncing on its main wheels and large slowly fluctuating loads are apparent both on the tailplane and rear fuselage.

5 Conclusions

Data have been obtained on loads liable to cause fatigue damage to the fuselage and nose undercarriage of a Varsity engaged on normal operational training flights. For the fuselage the most important loads occur during landing and taxying although for the rear fuselage the take-off loads are also important. Loads due to turbulence and ground engine running are small. For the nosewheel structure the most important vertical loads also occur during landing and taxying, the take-off loads are less severe and the ground engine running loads are small.

REFERENCES

No.	Author	Title etc.
1	A. Burns	Fatigue loadings in flight - loads in the tailplanes and fin of a Varsity. R.A.E. Tech. Note No. Structures 183. Dec. 1955 Current Paper No. 256.

APPENDIX I

Instrumentation and Calibration

Instrumentation

British Thermostat strain gauges were attached and waterproofed with Araldite special strain gauge cement at the stations shown in Fig 1. The signals from the gauges were fed into McMichael carrier wave amplifiers and recorded after amplification on a F & E 12 channel recorder Type IT3 - 9. The stepped signal from a Type IT.6-1 accelerometer attached to the fuselage at the c.g. position was also recorded on the F & E recorder.

When measuring changes in steady load, fixed signals were switched into the amplifier to check for amplifier drift.

Calibration

The strain gauges were calibrated directly in terms of load by placing shot bags on the centre portion of each tailplane so applying a down load on the tail resulting in a bending moment at the two fuselage stations and a decrease in vertical load on the nose undercarriage. These calibration tests were carried out before and after the flight tests. There appeared to be a slight loss of sensitivity (about 5%) during the four months between the two tests. As most of the records that were used in estimating the fuselage and nosewheel loads were obtained during the early part of the flying programme the pre-flight calibration figures were used.

Test Flying

Full details of the test flying have already been given in an earlier note[1].

APPENDIX II

Load Occurrences for Typical Flight

The numbers of occurrences of fuselage loads for the landing and take-off of the typical flight are the average values for ten landings and take-offs.

The following table gives the mean number of occurrences and the 5% confidence limits for a load range corresponding to a 0.6g acceleration range at the aircraft c.g. (0.6g corresponds approximately to a 20 ft/sec gust range at 145 knots, E.A.S. at 4000 ft and an all up weight of 33,000 lb).

Case	No. of Load Occurences	
	Mean	5% Confidence Limits
Forward Fuselage Station. Take-off	24.5	21.5 to 27.8
Forward Fuselage Station. Landing	45.9	40.9 to 50.9
Rear Fuselage Station. Take-off	18.74	16.44 to 21.04
Rear Fuselage Station. Landing	35.7	29.8 to 41.6

The fuselage and nose undercarriage loads due to ground engine running were obtained on the assumption that the following ground running took place during each flight.

Engines	R.P.M.	Time
Both	2400	5 secs
Both	1200	185 secs
Port only	2400	10 secs
Port only	2000	15 secs
Stbd. orly	2400	10 secs
Stbd. only	2400	15 secs

Half minute records were taken at the various engine conditions and the results were proportioned to conform to the times shown above. The fuselage loads due to the single engine cases at 2400 R.P.M. were not measured in the tests but for the purpose of ground running loads in the typical flight an estimation was made of them from the loads at the other engine conditions. The tests showed however that both the fuselage and nose undercarriage loads at all ground running conditions are very small and in some cases are negligible as shown in Tables II - IV.

For estimation of the loads in turbulence the aircraft was assumed to spend 10 minutes at 130 knots at 1,000 ft. (an average for the climb

and descent) and 23 minutes at 145 knots at 2,000 ft.* It was estimated from operational data obtained on a number of aircraft that the average number of miles travelled to meet a 10 ft/sec gust (up or down) was 3.2 at 1,000 ft and 7.4 at 2,000 ft. Hence the Varsity in its typical flight would meet 16.3 up and down gusts of 10 ft/sec or, rounding up, 8.2 fluctuations of 20 ft/sec.** As the relative frequency of the different sized gusts in the flight tests was compatible with that obtained operationally the flight test results were merely proportioned to give 8.2 occurrences at 20 ft/sec. The corresponding fuselage loads were then determined from Fig 4 after first converting the c.g. accelerations into vertical gust velocities.

The taxying loads for the representative flight were obtained by proportioning five taxying records of varying length to five minute periods and then taking the average.

---

* Based on average figures for Varsities engaged in training flights at Swinderby R.A.F. Station.

** It is assumed here that the number of fluctuations is equal to half the sum of negative and positive gusts. A check from the flight tests showed that this method of estimating fluctuations gives a slight over estimate.

APPENDIX III

Nosewheel Out-of-Balance Loads

From a study of the records of landing and take-off it was noticed that a small out-of-balance of the nosewheel produced a steady oscillation in the trace of vertical load at the nose undercarriage. Attempts were made, by changing the nosewheel tyres, to eliminate this out-of-balance, but it was not found possible to remove it entirely. All records of the nose undercarriage vertical loads were analysed with this out-of-balance effect included but Figs 5 and 6 show results for two take-offs and landings where this oscillation has been smoothed out. It can be seen that out-of-balance of the nosewheel produces a noticeable increase in the number of occurrences of the smaller loads but has little effect on the larger loads.

TABLE I

Ground to Air Loads

A.U.W. 34,600 lbs
C.G. Position 30.45 ft Aft of Datum

Aircraft Condition			Change in B.M. or Load at Position of Strain Gauge		
			Fwd Fuselage Stn. B.M. (Tons Ins.)	Rear Fuselage Stn. B.M. (Tons Ins.)	Nose Undercarriage Vertical Load(Tons)
Ground To Air	0 kts. To 90 kts.	Engines Idling To Just Airborne, $\frac{1}{3}$ Flap u/c down	195	156	1.89
Ground To Air	0 kts. To 145 kts.	Engines Idling To 2000 ft, Flaps Up u/c up	221	180	

TABLE II

Bending Moment Cycles at Forward Fuselage Station

Bending Moment Range Tons Ins.	Number of Times Bending Moment is Exceeded																																						
	Landing										Take-off										Ground Engine Running ½ Min Records						Turbulence Knots				Taxying					Circuit					
																					Stbd Only R.P.M.		Port Only R.P.M.		Both R.P.M.		170	130	145	145	Record Length Secs									
	1	2	3	4	5	6	7	8	9	10	1	2	3	4	5	6	7	9	13	14	2400	2000	2400	2000	2400	1200	180	113	180	120	60	45	60	75	55	1	2	3			
26.2	92	82	65		89	72	71	84	66	86	119	72	87	88	51	86	73	93	67	76	44.4*	30	44.4*	28.7	74	Negligible	99	7.4	70	21.1	66	36	98	59	51	105	6.8	9.2			
39.3	69	63	59	51	71	60	52	57	48	59	63	40	44	47	34	55	45	43	38	41	20.4*	12.2	20.4*	14.7	45		19.5	2.0	15	4.5	38	22.7	61	32	25.2	41	2.8	5.2			
52.4	57	49	47	40	56	48	39	45	36	43	33	20.7	22.1	24	16.7	28	27	24.6	27.5	23	8.7*	4.7	8.7*	6.6	25.8		3.7		4.2	1.4	25.6	15.5	36	12.1	19.2	14.9	1.4	2.8			
65.5	49	38	36	32	44	39	32	39	28.1	36	20.5	10.9	11.0	15.7	8.0	14	14.5	16.9	18.5	13.6	3.3*	1.7	3.3*	2.6	14.5				2.9	0.4	19.6	6.0	20.9	5.0	5.0	3.4	1.0	0.8			
78.6	39	31	28.2	26	31	27	24.6	34	20.2	32	15.1	7.5	8.0	12.3	4.8	8.7	7.9	12.2	11.4	7.7	1.0*		1.0*		6.5				1.9		13.2	4.2	14.2	3.5	3.4	1.7	0.4			
91.7	33	16.7	22.9	20.5	19.4	21	18.6	31	14.8	24.8	10.6	5.0	6.9	7.5	3.0	6.5	4.4	7.0	9.0	4.8					2.4				1.0		9.0	3.0	11.5	2.4	3.0	1.0					
104.8	27	7.7	19.4	17.5	13.8	17.5	14.9	27.5	11.2	19.4	7.2	4.0	2.3	3.3	1.4	4.0	1.7	5.3	6.3	2.0					0.4						5.7	2.4	9.3	2.0	3.0	0.4					
117.9	22	5.0	16.7	15.3	10.2	13.7	12.3	23.9	8.9	15.1	4.7	3.4	1.1	1.4	1.0	1.8	1.0	4.0	2.6	2.0											4.5	2.0	6.8	2.0	2.4						
131	19	4.4	15.0	11.7	7.9	9.5	9.2	22.0	5.0	11.9	2.7	2.4	1.0	0.4	1.0	1.0	1.0	2.8	0.3	2.0											3.0	1.4	5.5	0.7	0.8						
144.1	18	3.4	14.4	8.5	6.4	6.9	8.0	19.3	4.5	7.2	1.4	2.0	1.0		1.0	1.0	1.0	2.0		0.8											2.4	1.0	4.4								
157.2	16	3.0	13.7	7.5	5.5	6.0	7.5	13.8	3.0	3.5	0.4	1.4			1.0	0.4	0.4	1.4													2.0	0.4	3.4								
170.3	11.9	2.0	9.0	6.5	4.4	4.8	5.2	11.0	1.0	1.0		1.0			1.0			1.0													2.0		2.4								
183.4	9.1	1.4	7.5	5.4	3.0	4.0	3.4	9.9	0.4	0.4		0.4			0.4			1.0													2.0		1.4								
196.5	8.5	1.0	6.1	5.0	3.0	4.0	1.8	7.9										1.0													2.0		1.0								
209.6	7.3	1.0	5.0	3.6	3.0	1.8	1.0	6.5										0.4													2.0		1.0								
222.7	7.1	1.0	4.4	2.4	3.0	0.4	1.0	6.0																							0.7		1.0								
235.8	6.2	0.4	3.7	2.0	2.4		1.0	6.0																									0.4								
248.9	4.9		3.7	2.0	2.0		1.0	6.0																																	
262	4.7		3.7	2.0	2.0		0.4	4.7																																	
275.1	3.7		3.7	1.4	2.0			2.7																																	
288.2	3.5		3.7	1.0	1.4			2.0																																	
301.3	3.2		3.1	0.4	1.0			1.0																																	
314.4	2.4		2.5		1.0			1.0																																	
327.5	2.4		1.2		1.0			1.0																																	
340.6	2.4		1.2		0.4			1.0																																	
353.7	2.4		1.2					1.0																																	
366.8	1.2		1.2					1.0																																	
379.9	1.2		1.2					0.4																																	
393.0	0.5		1.2																																						
406.1			0.5																																						

* Estimated figures

TABLE III

Bending Moment Cycles at Rear Fuselage Station

Bending Moment Range Tons ins.	Number of Times Bending Moment Range Is Exceeded																																						
	Landing										Take-off										Ground Engine Running ⅓ Min Records						Turbulence				Taxying					Circuit		
																					Stb'd Only R.P.M.		Port Only R.P.M.		Both R.P.M.			Knots			Record Length Secs							
	1	5	6	7	8	9	10	11	12	13	1	3	4	7	9	12	13	14	15	16	2400	2000	2400	2000	2400	1200	170 180	130 Record 113	145 Secs. 180	145 " 120	60	45	60	75	55	1	2	3
30	82	84	78	60	79	82	99	62	65	91	124	70	100	83	93	82	91	70	79	71	26*	15.2	26*	19.7	62	Negligible	132	23.2	80	41	72	44	125	80.5	70	130	51	112
45	68	70	67	48	64	63	79	46	55	75	68	52	56	50	52	54	54	48	43	41	8.4*	4.0	8.4*	7.2	34		45	7.3	34	10	39	26.7	88	39.2	36	65	20	56
60	56	60	53	37	51	51	62	36	43	56	38	28.5	33	38	31	35	38	35	28.8	24.4	0.9*		0.9*	1.2	14.7		17.2	3.0	14.5	3.7	21.8	9.0	57	16.8	16.2	33	9.6	26
75	46	51	42	27	40	40	51	26.7	34	43	24	19	24.5	23.7	21	21.2	29.5	21.1	20.3	18.9					1.4		6.8	1.4	5.5	2.0	12.6	6.7	35	6.0	7.5	18.7	5.3	14
90	37	40	33.5	19.7	32	31.1	41	18.9	29	36	14.9	16	16.4	15.0	12.5	15.2	23.5	13.9	14.8	16.4					0.4		2.3	1.0	3.0	0.8	7.3	5.0	18.7	2.2	4.4	12.1	2.7	6.6
105	29.3	29	29	12.2	27.5	25.2	30	14	23	31	10.3	11.4	9.9	10.0	8.3	12.4	18.1	10.7	12.9	12.0							1.0	1.0	1.7		4.0	2.2	10.7	0.4	2.7	8.8	2.0	3.0
120	23.5	20.5	25	8.0	21	18.9	22.2	8.7	17.8	25.4	7.9	7.8	6.9	7.5	7.0	9.7	12.4	6.4	7.5	8.9							1.0	0.4	1.0		2.8	1.0	6.5		1.4	5.9	2.0	2.4
135	18.7	15.4	19.5	5.4	14.7	13.7	17.1	6.5	13	19.7	4.3	4.2	6.0	5.0	5.9	7.4	10	6.2	3.0	7.5							0.4		1.0		2.0	1.0	3.9		0.4	4.4	2.0	2.0
150	12.7	11.5	19.5	3.0	12.5	9.5	12	4.0	9.9	16.5	1.4	2.4	5.4	2.7	5.0	5.9	8.9	4.4	1.0	5.0									1.0		1.4	1.0	3.0			3.0	2.0	2.0
165	8.7	8.9	11.7	2.0	10.9	6.9	9.5	2.8	7.8	15.2	1.0	2.0	4.4	2.0	2.0	5.0	7.5	3.4	1.0	2.7									1.0		1.0	0.4	1.7			3.0	2.0	1.4
180	6.4	6.8	7.5	1.5	9.5	4.0	7.8	2.0	4.0	9.8	1.0	2.0	2.8	1.6	1.4	4.5	6.4	2.0	0.4	2.0											0.4		1.0			1.7	2.0	
195	4.7	4.9	5.8	1.0	7.7	2.8	5.9	2.0	2.0	7.9	0.4	1.4	2.0	1.0	1.0	3.0	4.8	1.4		2.0													0.4			1.0	1.4	
210	2.6	4.0	2.8	1.0	5.9	2.0	5.0	2.0	2.0	6.4		1.0	2.0	1.0	1.0	2.4	4.0	1.0		2.0																1.0	1.0	
225	1.2	2.8	2.0	0.4	5.0	2.0	3.7	0.4	1.4	4.2		1.0	1.4	1.0	1.0	2.0	2.8	1.0		1.4																1.0	1.0	
240	1.2	2.0	1.4		4.5	2.0	1.0			2.0			1.0	1.0	1.0	1.4	1.4	1.0		1.0																	0.4	
255	1.2	1.4			4.0	1.4				1.4			0.4	1.0		1.0	1.0			1.0																		
270	1.2				4.0					1.0							1.0																					
285	0.5				4.0												1.0																					
300					2.7												1.0																					
315					1.4												1.0																					
330																	0.4																					

* Estimated figures

TABLE IV

Vertical Load Cycles at Nose Undercarriage

Vertical Load Range Tons	Number of Times Vertical Load Range is Exceeded																															
	Landing										Take-off										Ground Engine Running ½ Minute Records						Taxying				
																					Stb'd Only		Port Only		Both		Record Length Secs				
	1	2	3	4	5	6	7	8	9	10	1	2	3	4	5	6	7	9	13	14	2400	2000	2400	2000	2400	1200	60	45	60	75	55
0.308	52	67	44	53	161	104	61	143	152	116	120	81	63	68	44	57	28	94	179	39	9	Negligible	5.3	5.8	2.2	Negligible	41	24.4	79	25.3	23.2
0.462	47	54	36	39	95	73	47	78	70	88	73	72	32	30	31	43	10.2	58	62	14.4	0.4		1.4	1.4	0.4		28.4	14.0	45	7.7	8.9
0.616	39	38	28	26	48	49	34	46	34	55	46	38	10.3	11.6	9	27.2	5.0	33	21	7.5			1.0				20.7	5.2	24	3.0	5.9
0.770	33	27	22.2	20	29.5	37	28	35	21.5	36	19	11.9	4.0	5.0	2.7	14.8	2.7	13	9.9	4.9							15.5	2.4	14.1	1.0	4.4
0.924	27.7	20	19.4	16.3	19	31.5	22	29.5	16.8	25.4	6.2	4.2	3.0	2.0	2.0	3.6	2.0	5.7	6.9	3.0							8.9	2.0	7.5	1.0	3.5
1.078	22.2	14	17.4	13.4	12.5	28	17.4	25.5	12.7	17.8	3.4	2.4	2.4	2.0	2.0	1.0	2.0	3.4	4.7	2.2							5.4	2.0	5.5	1.0	2.4
1.232	17.5	9.7	14.1	11.5	7.5	20	13.7	22.4	7.7	13.3	3.0	2.0	2.0	2.0	2.0	1.0	2.0	2.4	4.0	1.5							3.0	2.0	5.0	0.4	0.7
1.386	14.1	6.8	9.4	8.5	4.2	12.5	10.9	20	5.5	10.9	3.0	2.0	2.0	1.4	2.0	1.0	2.0	2.0	4.0	1.5							2.0	2.0	3.8		
1.540	12.4	4.8	6.9	7.0	2.4	8.9	8.2	17.3	5.0	8.2	2.4	2.0	1.4	1.0	1.4	1.0	2.0	2.0	3.4	1.5							1.0	1.0	2.4		
1.694	11.3	4.0	6.2	7.0	2.0	6.2	5.9	13.8	3.7	5.0	1.4	2.0	1.0	1.0	1.0	1.0	2.0	2.0	3.0	0.9							1.0		1.4		
1.848	10.1	4.0	5.6	5.9	2.0	4.5	5.0	10.7	2.4	3.4	1.0	2.0	1.0	1.0	1.0	1.0	1.4	2.0	2.4	0.5							1.0		1.0		
2.000	8.8	3.4	5.0	5.0	2.0	2.4	3.7	9.5	1.4	3.0	1.0	1.4	1.0	0.4	1.0	1.0	1.0	2.0	1.4	0.5							1.0		0.4		
2.156	7.7	2.0	5.0	4.4	2.0	2.0	3.0	9.0	1.0	2.4	1.0	0.4	1.0		1.0	0.4	1.0	1.0	1.0	0.5							1.0				
2.312	6.8	2.0	4.2	4.0	2.0	2.0	3.0	7.9	1.0	2.0	1.0		1.0		1.0		0.4	1.0	1.0	0.5											
2.464	3.6	1.4	3.0	2.7	2.0	1.4	3.0	7.0	1.0	2.0	1.0				1.0			1.0	0.4	0.5											
2.618	2.6	1.0	1.5	1.4	2.0	0.4	2.4	5.5	1.0	2.0	0.4				1.0			1.0													
2.772	2.0	1.0	1.5	1.0	2.0		2.0	4.4	1.0	1.0					0.4			1.0													
2.926	1.4	1.0	1.5	1.0	2.0		2.0	2.7	1.0	0.4																					
3.080	0.7	1.0	0.75	0.4	2.0		1.4	2.0	0.4																						
3.234		1.0			1.4		1.0	2.0																							
3.388		0.4					1.0	2.0																							
3.542							1.0	2.0																							
3.696							0.4	1.4																							
3.850								0.4																							

TABLE V

Accelerations Measured at Aircraft C.G. During Turbulence Flying

Acceleration Range g	No. of Occurrences of Acceleration Range		
	I.A.S. Knots		
	170	145	130
	Record Time.		Seconds
	180	300	113
0.2	65.0	69.5	23.0
0.3	39.0	42.8	9.1
0.4	23.7	23.2	3.6
0.5	11.7	11.4	
0.6	5.2	5.8	
0.7	2.7	2.2	
0.8	2.0		
0.9	1.4		
1.0	0		

WT.2078.C.P.287 - K3 - Printed in Great Britain

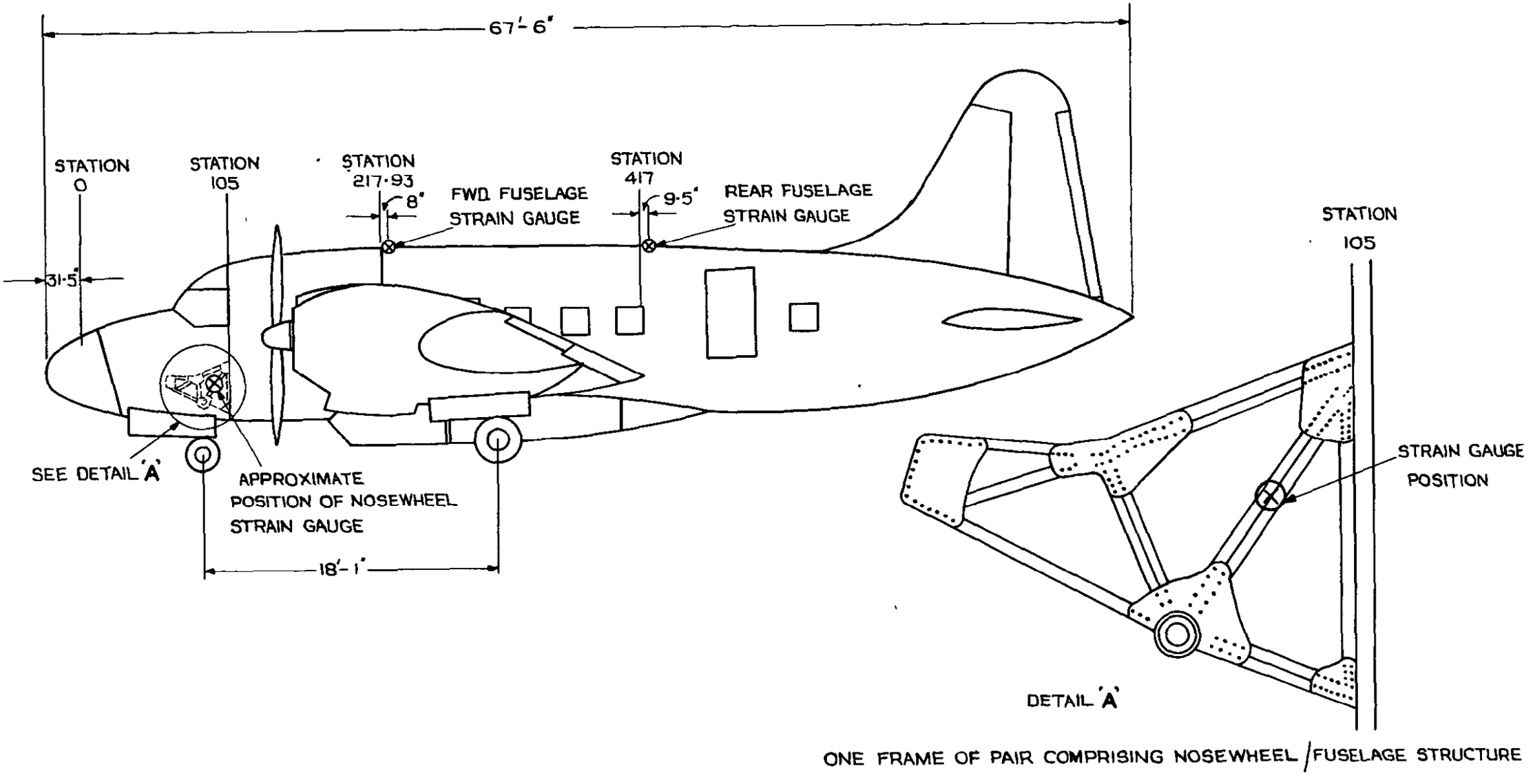

FIG. 1. POSITIONS OF STRAIN GAUGES ON FUSELAGE AND NOSE UNDERCARRIAGE.

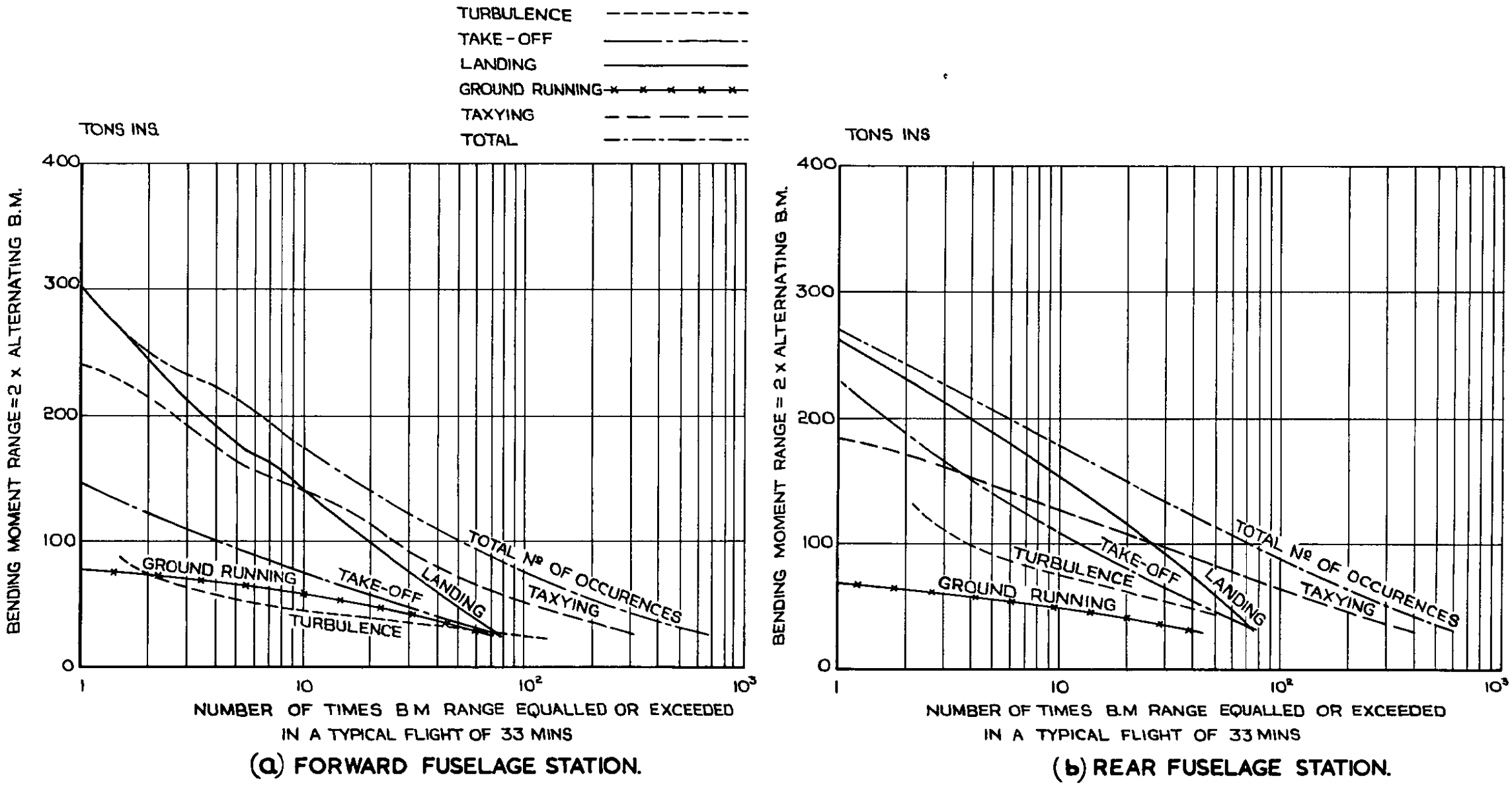

FIG. 2. (a & b) FUSELAGE LOADS IN A TYPICAL FLIGHT.

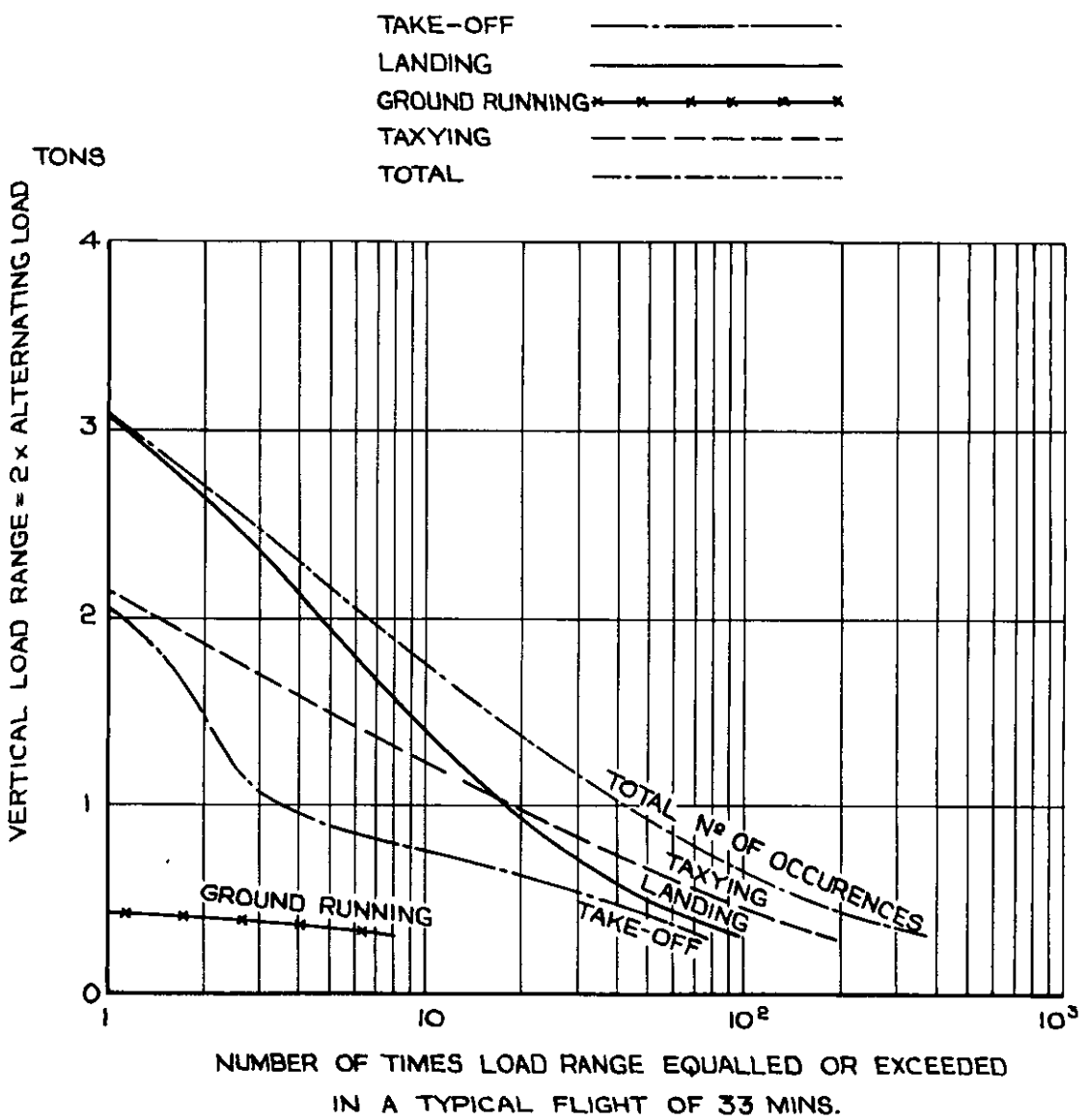

FIG. 3. VERTICAL LOADS ON NOSE UNDERCARRIAGE IN A TYPICAL FLIGHT.

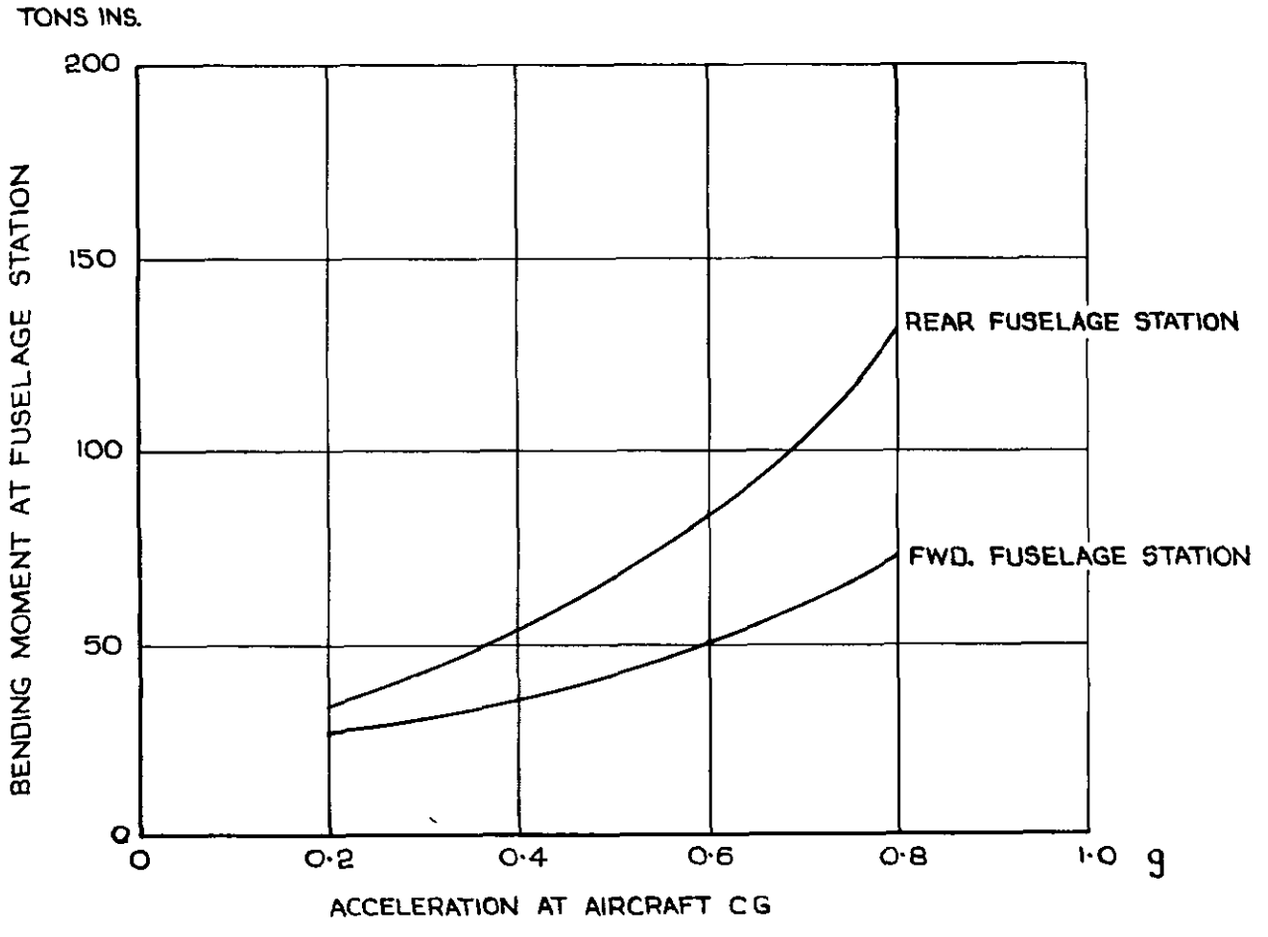

FIG. 4. RELATIONSHIP BETWEEN BM. RANGES AT FUSELAGE STATIONS AND ACCELERATION AT AIRCRAFT C.G. EXCEEDED THE SAME NUMBER OF TIMES IN TURBULENCE.

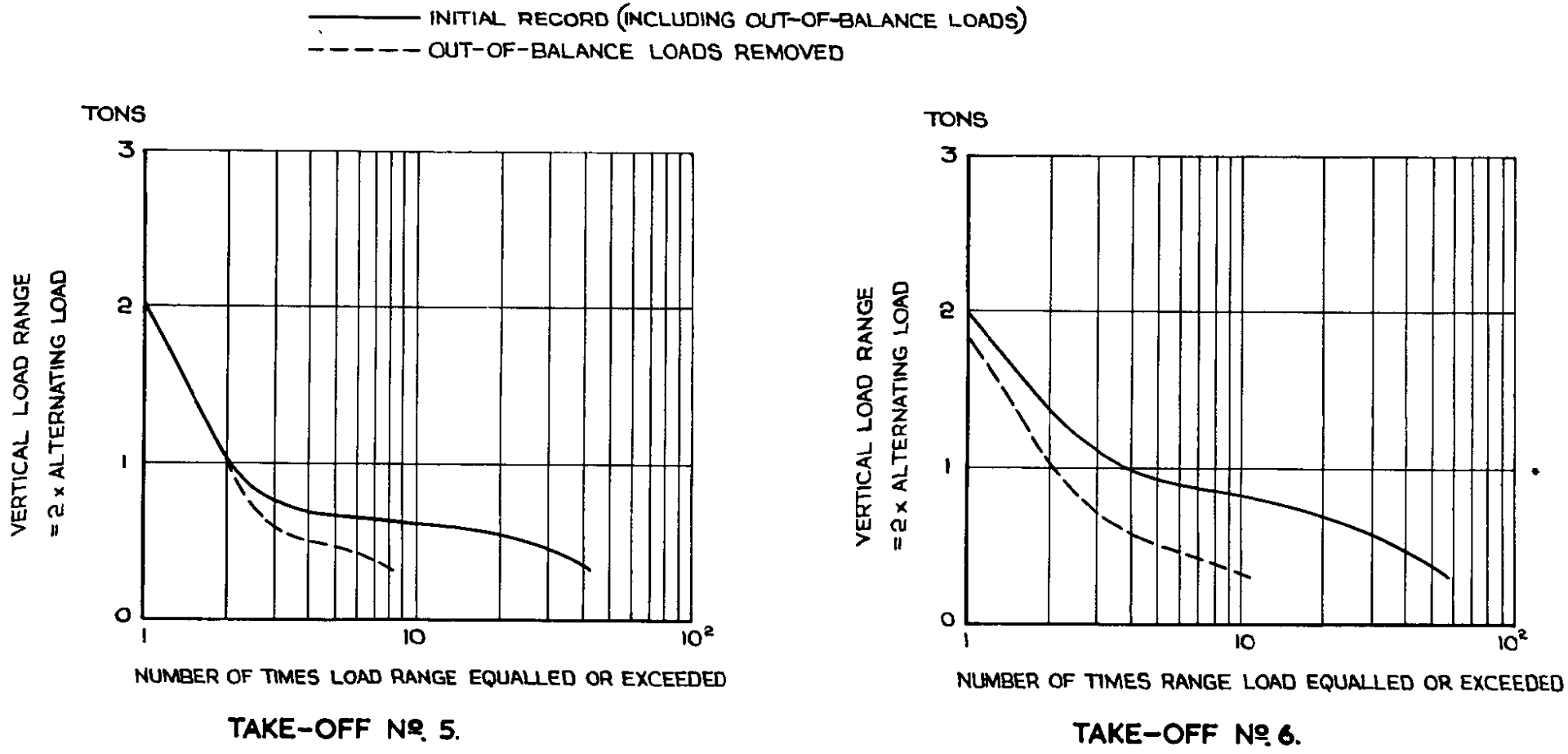

FIG. 5. EFFECT OF WHEEL OUT-OF-BALANCE ON VERTICAL NOSE UNDERCARRIAGE LOADS MEASURED DURING TAKE-OFF.

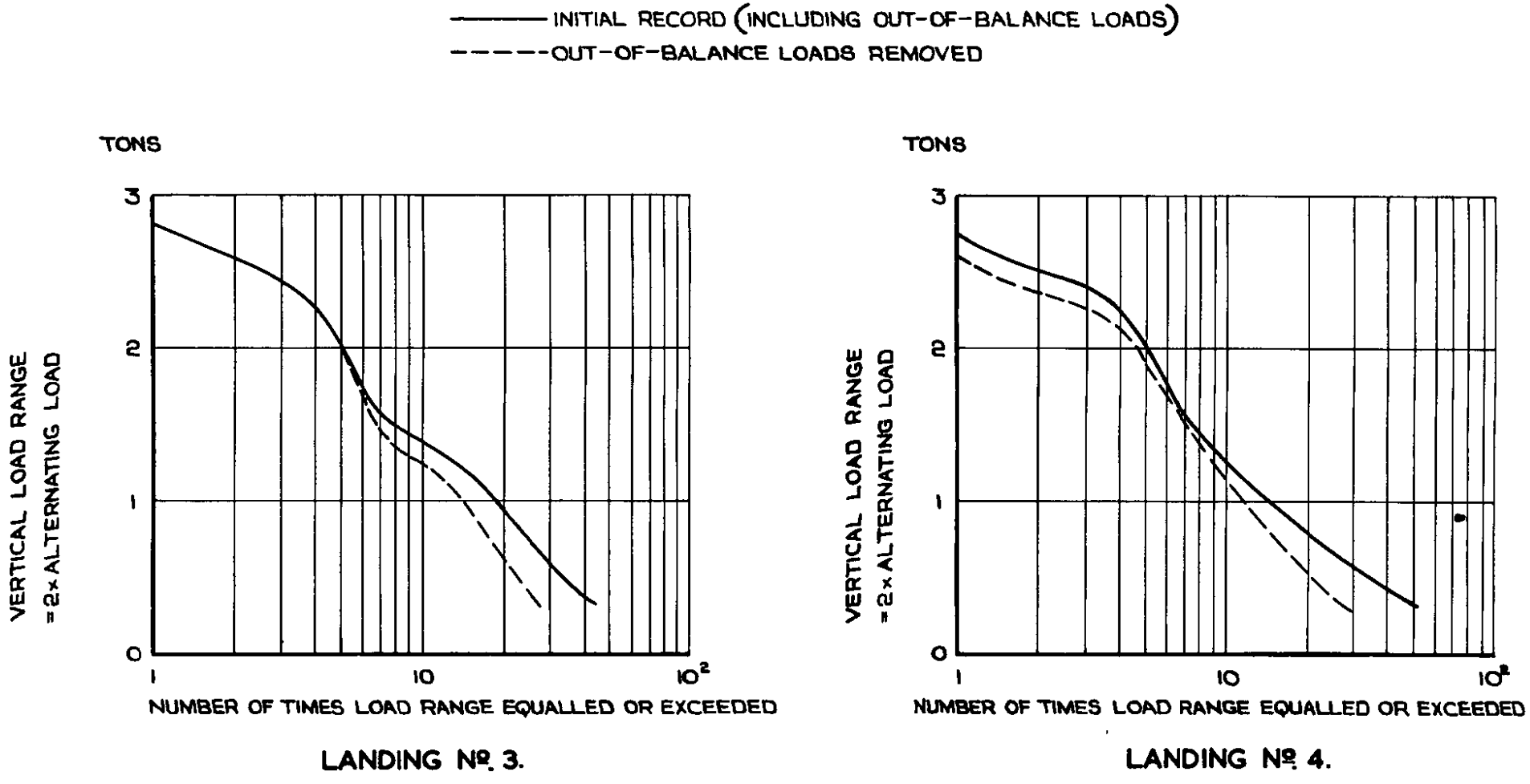

FIG. 6. EFFECT OF WHEEL OUT-OF-BALANCE ON VERTICAL NOSE UNDERCARRIAGE LOADS MEASURED DURING LANDING.

C.P. No. 287
(18,671)
A.R.C. Technical Report

Published by
HER MAJESTY'S STATIONERY OFFICE

To be purchased from
York House, Kingsway, London W C 2
423 Oxford Street, London W 1
P O Box 569, London S.E 1
13A Castle Street, Edinburgh 2
109 St Mary Street, Cardiff
39 King Street, Manchester 2
Tower Lane, Bristol 1
2 Edmund Street, Birmingham 3
80 Chichester Street, Belfast
or through any bookseller

PRINTED IN GREAT BRITAIN

S.O. Code No. 23-9009-87

C.P. No. 287

C.P. No. 301
(18,124)
A.R.C. Technical Report

C.P. No. 301
(18,124)
A.R.C. Technical Report

MINISTRY OF SUPPLY

AERONAUTICAL RESEARCH COUNCIL

CURRENT PAPERS

Fin-and-Rudder Loads in a Yawing Manoeuvre: Effect of Direct and Power Assisted Rudder Movement

By

D. R. Puttock, D.C.Ae.

LONDON: HER MAJESTY'S STATIONERY OFFICE

1956

SEVEN SHILLINGS NET

C.P. No. 301

U.D.C. No. 629.13.014.4 : 533.69.048.1

Technical Note No. Structures 169

July, 1955

ROYAL AIRCRAFT ESTABLISHMENT

Fin-and-rudder loads in a yawing manoeuvre: effect of direct and power assisted rudder movement

by

D. R. Puttock, D.C.Ae.

SUMMARY

The severity of a yawing manoeuvre specified[1] for design purposes is investigated. It is found that the manoeuvre does not always represent the most critical case, higher fin-and-rudder loadings being obtainable when the specified frequency of rudder movement is changed. The inclusion of a power unit in the circuit may however impose restrictions on the rudder movement, leading to a reduction in the severity of the loading.

The analytical treatment includes the derivation of exact expressions for the angle of sideslip, fin-and-rudder load and rudder hinge moment induced by a sinusoidal rudder movement of arbitrary frequency. These expressions are analysed to determine how the maxima of each of the quantities are affected by variations in the frequency of the rudder movement. Computational charts are included to simplify the determination of these effects in particular instances.

The problems are illustrated with reference to a numerical example.

LIST OF CONTENTS

LIST OF APPENDICES

LIST OF TABLES

LIST OF ILLUSTRATIONS

1 Introduction

One of the present design requirements[1,2] stipulates that all aircraft shall have sufficient strength to permit the execution of two yawing manoeuvres. In one of these manoeuvres the rudder is to be moved sinusoidally through 1 or $1\frac{1}{2}$ cycles at a frequency equal to the damped natural yawing frequency of the aircraft, with an amplitude corresponding to a specified pedal force.

It will be noted that with the manoeuvre defined in this manner, the maximum rate of rudder movement needed for its execution is also implicitly determined. However, if the rudder circuit contains a power unit, the maximum rate of rudder movement is, in general, limited, and may well be less than that required for the above manoeuvre. The question then arises whether the associated design requirement, which normally determines the design loads for the fin-and-rudder, is not too severe in these cases.

The present note is primarily concerned with any limitations that a power unit may impose on the fin-and-rudder design conditions. Additionally, however, it also contains the results of a detailed study of the effects of the frequency of manual or power assisted sinusoidal rudder movement on the fin-and-rudder loading conditions. This study, which was a necessary preliminary to the main objective, has yielded some significant information on the manoeuvre executed without power assistance, and therefore, the results are presented and discussed.

The investigation is treated throughout from the airworthiness standpoint, so that the chief interest lies in the maximum loading conditions for a given effort during manoeuvres which the pilot is <u>able</u> to perform. No consideration is given to the determination of the most <u>likely</u> yawing manoeuvre, i.e. the one occurring most frequently.

2 Details of the investigation

For the preliminary study, exact analytical solutions, based on the equations of motion of the aircraft as used in response theory, were derived for the angle of sideslip, fin-and-rudder load and rudder hinge moment produced by a sinusoidal rudder movement of unit amplitude and arbitrary frequency (see Appendix I para.A.3). These solutions were analysed to determine how the quantities were affected by variations in the frequency of movement, attention being concentrated on their local maxima. The range of frequencies considered was from 0.5 to 1.5 times the damped natural yawing frequency of the aircraft. It was found that, for conventional aircraft, this range was sufficient to cover all the critical loading conditions.

In the presentation of this part of the investigation, the effects of frequency of rudder movement on the local maxima of the angle of sideslip are illustrated graphically. Unfortunately no such general approach is possible for the associated effects on the fin-and-rudder load and rudder hinge moment because of the increased number of significant parameters affecting these two quantities. However, with the use of approximate formulae, it has been possible to minimize the labour required to determine these effects in particular instances. A further simplification results from the use of a number of computational charts (see Appendix III). The effects of frequency are illustrated with the aid of a typical example, the data for which are given in Table I.

With a knowledge of the foregoing results the effects of the inclusion of a power unit into the rudder circuit have been assessed. Here too, a completely general presentation has been precluded by the number of

significant parameters involved, but the trends are illustrated by an extension of the above example (see Table I and para.3.4).

3 Discussion:

3.1 General note

The following paragraphs cover the most important aspects of the problem. A more detailed discussion of these aspects is presented in Appendix II. The suffix m is used throughout to denote local maxima of the various quantities.

3.2 Effect of frequency of rudder movement on the response in yaw

3.21 Introduction

The design yawing manoeuvre is specified in terms of a pedal force, which, in the absence of a power unit, is a function of the rudder angle and the response of the aircraft in yaw, itself a function of the rudder angle. Again, if a power unit is present, and limitations are imposed on the fin-and-rudder design conditions, it is probable that, the limitations will, in the first instance, relate to the amplitude and frequency of the specified rudder movement. It is therefore clear that, as a first step the response of the aircraft in yaw to unit sinusoidal rudder movement of different frequencies should be derived.

In this note the frequency of the rudder movement is, by definition, proportional to the parameter f, which is the ratio of the frequency of rudder movement to the damped natural yawing frequency of the aircraft (see Appendix I eqns. 3 and 4). Thus, when the response of the aircraft is expressed in terms of the amplitude of rudder movement, a change in f indicates a proportional change in both the frequency, and maximum (initial) rate of that movement. When the response is expressed in terms of pedal force, however, a change in f still indicates a proportional change in the frequency of the rudder movement, but the maximum rate depends upon the amplitude of the movement, which in turn depends on the hinge moment characteristics of the rudder. The case f = 1 corresponds to movement of the rudder at a frequency equal to the damped natural frequency of the aircraft (designated the damped resonant frequency) i.e. the frequency specified for the design manoeuvre.

3.22 Response per unit amplitude of rudder movement (See also Appendix II para B.1.2)

The response of an aircraft in angle of sideslip, β, to sinusoidal rudder movement is dependent (see Appendix I equation 5) on the frequency of the rudder movement, proportional to f, and on the ratio $\frac{R}{J}$, which is a measure of the aerodynamic characteristics of the aircraft. The influence of f on the response of a particular aircraft (i.e. at a particular value of $\frac{R}{J}$) is illustrated in Fig.(1), whilst its influence, and that of $\frac{R}{J}$, on the magnitude of the three local maxima which occur during a manoeuvre of $1\frac{1}{2}$ cycles of rudder movement, and which are of primary interest in the present note, is illustrated in Figs.(2), (3), (4) and (8). Fig.(8) relates to a specific example, the data for which are contained in Table I. Since the equation describing the lateral motion of the aircraft in the present problem, see Appendix I equation 2 and 4, is identical in form to that of a simple mass-spring-damping system subjected to a sinusoidal disturbance, it is therefore to be expected, and in fact confirmed by the figures, that the peak values of the local maxima occur with a frequency closer to the damped resonant frequency (f = 1) as the manoeuvre proceeds, and also that, at low frequencies of rudder movement, the first or second local maximum (in time) may be the absolute maximum in the manoeuvre.

The associated response in fin-and-rudder load, P, (see Appendix I equation 9 and Fig.(10)) is similar to that in β except for the insignificant maximum which occurs at the beginning of the manoeuvre, and, by comparing Fig.(8) and (11) it will be seen that the general effects of f on the significant P_m are similar to those on the β_m. Any qualitative differences between Figs.(8) and (11) are primarily dependent on the magnitude of the ratio $\frac{a_1}{a_2}$, but for conventional aircraft the differences will be small.

The response in rudder hinge moment, C_h (see Appendix I equation 17) is also illustrated in Fig.(10) and the variations of its local maxima with f are shown in Fig.(12). Here it should be noted that the values of f associated with the peak values of the C_{h_m} are much higher than in either of the cases covered above, cf. Figs.(8), (11) and (12). The dotted line in Fig.(12) represents the special case $b_1 = 0$ and divergence from it at any value of f is entirely due to $b_1\beta$ i.e. the effect of the response in sideslip on the hinge moments of the aircraft. In this connection the sign and magnitude of the ratio $\frac{b_1}{b_2}$ is of importance (see Appendix II para.B.1.2.3); with the value used in the derivation of Fig.(12) the response of the aircraft relieves the hinge moment due to rudder angle alone at low values of f.

The general equations for P and C_h are complex and somewhat unwieldy for use in detailed calculation of the local maxima, and in Appendix I para.A4 and A5 respectively approximate but more rapid methods are devised. The associated computational charts, are given in Appendix III. The accuracy of the approximate methods may be gauged from Fig.(10).

3.23 Response per unit maximum hinge moment or pedal force
(See also Appendix II para. B.1.3)

So far, the discussion has been confined to the effects of f on the β_m and P_m per unit rudder movement. The results presented in support of this discussion may now be re-examined to determine the effects of f on the β_m and P_m per unit maximum rudder hinge moment. These effects are illustrated in Figs.(19) and (20). The important difference to be noted between these Figs and Figs.(8) and (11) is that the peak values of the β_m and P_m no longer occur in the neighbourhood of f = 1. Consequently the damped resonant condition, which forms a basis for the determination of the design loading condition[1], does not necessarily represent the most critical loading condition. In the present example, see Table I, a load on the fin-and-rudder some 15% greater than the design load is obtained by moving the rudder sinusoidally with a frequency equal to 0.84 of the damped resonant frequency. This is due to the relieving effect of the aircraft response in yaw on the rudder hinge moments at low frequencies, and the ratio $\frac{b_1}{b_2}$ has, therefore, a significant effect on the absolute maximum loading condition. Other significant parameters are $\frac{R}{J}$ and $\frac{a_1}{a_2}$, but they affect the picture to a minor extent only.

3.3 Effect of a power unit on the rudder movement
(See also Appendix II para B.1.2)

To determine what limitations a power unit may impose on the fin-and-rudder design conditions, it is first necessary to consider what limitations, if any, the power unit will place on the rudder movement when an attempt is made to execute the specified manoeuvre. The precise limitations are difficult to assess, but for a qualitative investigation refined assumptions are probably not necessary, and in this note the rudder movement is assumed to be as illustrated in Fig.(22a), i.e. the frequency remains the same, but the amplitude is reduced. It is further assumed that the pedal force is proportional to rudder angle. However, to complete the picture it is desirable to consider also the effect of change in the frequency of the assumed movement, see Fig.(22b), on the response of the aircraft and to determine the critical conditions with the power unit present. The results of the preceding paragraphs are of use in this respect. The general effect of frequency changes on the amplitude of rudder movement, under the foregoing assumption, is illustrated in Fig.(23).

3.4 Effect of a power unit on the response of an aircraft
(See also Appendix II para.B.3)

To illustrate these effects the example of Table I has been extended to cover the case with a power unit in the rudder circuit. The characteristics of the power unit are assumed to be such that its maximum rate is reached when f = 0.7.

Thus below this frequency the power unit does not restrict the amplitude of movement, but above it the amplitude is reduced according to the relevant curve in Fig.(23).

The curves of the β_m and P_m per unit pedal force for a range of frequencies are given in Figs.(24) and (25) respectively. The full curves relate to the original example, i.e. without power unit, whilst the dotted and chain dotted curves relate to the example with power unit present, applying the assumed rudder displacement of para.3.3 and another, less realistic, and unconservative, approximation (see Appendix II para.B2) respectively. In practice it is to be expected that the actual curve would lie between the dotted and chain dotted curves.

The sets of curves indicate that, if a power unit restricts the movement of the rudder such that the design conditions cannot be met, the critical β_m and P_m obtained are lower than those associated with the specified design conditions. Further these critical conditions do not necessarily occur at the damped resonant frequency of the aircraft.

4 Conclusions:

(1) If the design manoeuvre is defined in terms of the amplitude of the rudder movement, the absolute maxima of the angle of sideslip and fin-and-rudder load occur, as would be expected, when the frequency of the rudder movement is very close to the damped natural yawing frequency of the aircraft, i.e. close to the damped resonant conditions.

(2) The absolute maximum hinge moment for usual values of b_1 and b_2 i.e. $\frac{b_1}{b_2}$ positive and b_2 negative, occurs at a much higher frequency than the damped resonant frequency, depending on the value of $\frac{b_1}{b_2}$. At low frequencies the response of the aircraft has a relieving effect on the

hinge moments, through b_1, which allows the application of greater rudder amplitudes for a given pedal force than would be predicted from a knowledge of the hinge moment due to rudder angle alone.

(3) If the design manoeuvre is defined in terms of a maximum hinge moment or pedal force, the absolute maxima of the angle of sideslip and fin-and-rudder load occur at frequencies much below the damped resonant frequency, the precise values depending on $\frac{R}{J}$, $\frac{a_1}{a_2}$ and $\frac{b_1}{b_2}$.

(4) It follows from (3) that the present design requirement, which calls for movement of the rudder at the damped resonant frequency up to a specified pedal force, does not always form the critical case. In some cases greater angles of sideslip and fin-and-rudder loads may be obtained by a slight reduction in the frequency of rudder movement.

(5) If a power unit limits the rudder movement such that the design conditions cannot be realised the ensuing fin-and-rudder loads are in general lower than those of the present design requirement.

NOTATION

A,B,C	coefficients in equation 9
$a_1 = -\frac{\partial C_{Yf}}{\partial \beta}$	(including effects of local sidewash at the tail)
$a_2 = \frac{\partial C_{Yf}}{\partial \zeta}$	
b	wing span
$b_1 = -\frac{\partial C_h}{\partial \beta}$	(including effects of local sidewash at the tail)
$b_2 = \frac{\partial C_h}{\partial \zeta}$	
C_h	rudder hinge moment coefficient
C_{Yf}	lateral force coefficient of the fin and rudder
f	ratio $\frac{\text{frequency of the sinusoidal rudder movement}}{\text{natural frequency of the damped yawing oscillations of the aircraft}}$
g	gravity constant
H	rudder hinge moment
H_e	amplification factor in equation 5
i_c	coefficient of inertia about the z axis
J	non-dimensional damped natural circular frequency of the aircraft in yaw

ℓ	fin-and-rudder arm
ℓ_R	distance of C.P. of fin-and-rudder load due to rudder deflection to C.G. of aircraft
$\overline{M}_r$	response factor, see equations 21 and 27
n_v	static stability derivative
n_r	damping derivative in yaw
P	fin-and-rudder load
Q_r $Q_{\pi/2}$	response factors, see Figs.2, 3, 4 and 13
R	non-dimensional damping factor of the lateral oscillation
$\hat{r}$	non-dimensional angular velocity in yaw
S	wing area
S"	fin-and-rudder area
t	time in seconds
$\hat{t} = \frac{W}{g\rho SV}$	unit of aerodynamic time in seconds
V	velocity of C.G. of the aircraft
$\overline{V}_R = \frac{S''\ell_R}{Sb}$	fin-and-rudder volume coefficient
W	weight of the aircraft
$\overline{X}$, $\overline{Y}$	response factors, see equation 15
x_r	variable in approximate equation, see equations 12, 18 and 23
$\overline{x}_r$	value of variable for which the approximate equations give maximum values
$\overline{y}_v = -y_v$	lateral force derivative due to β
$\overline{y}_\zeta = \frac{1}{2}\frac{S''}{S} a_2$	lateral force derivative due to ζ
β	sideslip angle
δ_n	non-dimensional rudder effectiveness
ε_r, $\varepsilon_{r-1,r}$	phase angles, see Figs.5, 6, 7, 15 and 16
ζ	rudder angle
μ_2, μ_3	non-dimensional mass of the aircraft - alternative expressions

$\nu_n = -\frac{1}{i_c} \cdot n_r$ non-dimensional damping parameter in yaw

ρ air density

τ non-dimensional aerodynamic time

φ_r frequency factor, see equation 24

$\omega_n = \frac{1}{i_c} \cdot \mu_2 \cdot n_v$ non-dimensional static stability parameter

Suffices

e maximum rudder angle

m local maxima

r pertaining to the r^{th} maximum of the response quantities r = 1,2 and 3

REFERENCES

No.	Author	Title, etc.
1		Design Requirements for Aeroplanes. (A.P.970, Vol.I and II).
2	T. Czaykowski	Dynamic Fin-and-Rudder Loads in Yawing Manoeuvres. R.A.E. Report Structures 76. June 1950.
3	J.P. Den Hartog	Mechanical Vibrations. McGraw-Hill Book Co., Inc. 1947.
4	D.R. Puttock	Effect of Rolling on the Fin-and Rudder Loads in Yawing Manoeuvres. Current Paper No.153. January, 1953.
5	S. Neumark	A Simplified Theory of the Lateral Oscillations of an Aircraft with Rudder Free Including the Effect of Friction on the Control System. R & M 2259, May 1945.

Attached: Appendices I, II and III
Table I
Figs.1 - 27
Drg. Nos. SME 77654/R - 77670/R inclus.
Detachable Abstract Cards

APPENDIX I

Analysis

A.1 Equations of motion

The non-dimensional equations of lateral motion of an aircraft may be written in the form, with the notation of ref.5.

$$\frac{d\beta}{d\tau} + \bar{y}_v\beta + \hat{r} = 0 \qquad (1a)$$

$$-\omega_n\beta + \frac{d\hat{r}}{d\tau} + \nu_n\hat{r} = -\delta_n\zeta \qquad (1b)$$

The underlying assumptions are that:

1. the forward speed is constant throughout the manoeuvre,
2. the fin-and-rudder force derivative due to rudder displacement ($\bar{y}_\zeta$) is negligible in equation (1a),
3. the vertical principal axis of inertia of the aircraft coincides with the z axis,
4. all rolling motion is neglected.

Equation (1a) and (1b) may be expressed in the form

$$\left.\begin{aligned} &\frac{d^2\beta}{d\tau^2} + (\bar{y}_v + \nu_n)\frac{d\beta}{d\tau} + (\omega_n + \nu_n\bar{y}_v)\beta = \delta_n\zeta \\ \text{or}\quad &\frac{d^2\beta}{d\tau^2} + 2R\frac{d\beta}{d\tau} + (R^2 + J^2)\beta = \delta_n\zeta \end{aligned}\right\} \qquad (2)$$

where

$$\left.\begin{aligned} R &= \tfrac{1}{2}(\bar{y}_v + \nu_n) = \text{non-dimensional damping factor of the oscillatory motion.} \\ J &= \sqrt{\omega_n - \tfrac{1}{4}(\nu_n - \bar{y}_v)^2} = \text{non-dimensional damped natural circular frequency factor of the oscillatory motion.} \end{aligned}\right\} \qquad (3)$$

It has been shown[4] that, with the present trends in aircraft design, the assumption of zero rolling motion is tending to become invalid. However, it is also shown that the main effect of neglect of the rolling is to modify the numerical values of the parameters R and J, and that the effect of rolling may be taken into account by using the exact values of R and J in all the response formulae obtained from the simplified approach. Fundamentally, it is necessary to add a further equation, an equation of rolling moments, to equations (1a) and (1b), and solve the resulting quartic to obtain the exact values of R and J. In practice, however, a method of factorization introduced by Neumark[5] may be used for this purpose. In the analysis of

particular cases where neglect of rolling if likely to incur appreciable error, it is suggested that equation 3 should not be used to calculate the values of R and J. Instead the formulae presented in Ref.4 should be used.

A.2 Definition of the manoeuvre:-

Consider a general fish-tail manoeuvre induced by the rudder, in which the rudder is moved to and fro in a sinusoidal motion at a frequency proportional to the natural frequency of the damped yawing oscillations of the aircraft then

$$\zeta = \zeta_e \sin Jf\tau \tag{4}$$

where the non-dimensional frequency of the rudder motion is Jf and

$$f = \frac{\text{frequency of rudder movement}}{\text{damped natural frequency of yawing oscillations of the aircraft}} .$$

A.3 Solution for the Angle of Sideslip

The solution of equation 2 for β , including equation 4, is

$$\beta = \delta_n \zeta_e H_e \left\{ fe^{-\frac{R}{J}J\tau} \left[2\frac{R}{J} \cos J\tau + \left(\frac{R^2}{J^2} - 1 + f^2\right) \sin J\tau \right] - 2\frac{R}{J} f \cos Jf\tau + \left(\frac{R^2}{J^2} + 1 - f^2\right) \sin Jf\tau \right\} \tag{5}$$

then

$$\frac{d\beta}{d\tau} = \delta_n \zeta_e H_e J \left\{ fe^{-\frac{R}{J}J\tau} \left[-\frac{R}{J}\left(\frac{R^2}{J^2} + 1 + f^2\right) \sin J\tau - \left(\frac{R^2}{J^2} + 1 - f^2\right) \cos J\tau \right] + 2\frac{R}{J} f^2 \sin Jf\tau + f\left(\frac{R^2}{J^2} + 1 - f^2\right) \cos Jf\tau \right\} \tag{6}$$

and

$$\frac{d^2\beta}{d\tau^2} = \delta_n \zeta_e H_e J^2 \left\{ fe^{-\frac{R}{J}J\tau} \left[-2\frac{R}{J} f^2 \cos J\tau + \left\{ \left(\frac{R^2}{J^2} + 1\right)^2 + f^2\left(\frac{R^2}{J^2} - 1\right) \right\} \sin J\tau \right] + 2\frac{R}{J} f^3 \cos Jf\tau - f^2\left(\frac{R^2}{J^2} + 1 - f^2\right) \sin Jf\tau \right\} \tag{7}$$

$$H_e = \frac{1}{J^2\left[\frac{R^2}{J^2} + (1+f)^2\right]\left[\frac{R^2}{J^2} + (1-f)^2\right]} .$$

These equations are valid for the ranges of f above and below resonance conditions (f = 1), but much of the following analysis only applies to the range f < 1.

Czaykowski[2] has considered a particular case of the fish-tail manoeuvre in which f = 1. For this particular case he was able to simplify the equation for the angle of sideslip and present graphically all the local maxima required for design purposes. In the general case, however, many of the simplifications are not valid and it is necessary to resort to numerical solution of the equation for β to obtain the required information for design. This involves the solution of the transcendental equation,

$$e^{-\frac{R}{J}J\tau} = \frac{2\frac{R}{J}f\sin Jf\tau + \left(\frac{R^2}{J^2} + 1 - f^2\right)\cos Jf\tau}{\frac{R}{J}\left(\frac{R^2}{J^2} + 1 + f^2\right)\sin J\tau + \left(\frac{R^2}{J^2} + 1 - f^2\right)\cos J\tau} \qquad (8)$$

which is the condition for the local maxima of β for any set of the parameters $\frac{R}{J}$ and f. In the present note the effect of f on the magnitude and times of occurrence of the first three local maxima of β have been calculated for a wide range of $\frac{R}{J}$ and the results are presented in Figs. 2, 3, 4, 5, 6 and 7. For convenience, the times of occurrence of the maxima are expressed in terms of a phase angle ε_r; the difference in positions of the corresponding maxima of β and ζ. Since $\zeta = \zeta_e \sin Jf\tau$, this is equivalent to measuring the angular position of each maximum of β from a datum $Jf\tau = \frac{\pi}{2}(2r - 1)$, where r (= 1, 2 and 3) signifies the particular maximum under consideration. The magnitudes of the maxima are given in terms of $Q_r = (-1)^{r+1} \cdot \frac{J^2}{\delta_n} \cdot \left(\frac{\beta_m}{\zeta_e}\right)_r$. Defined in this way Q_r is always positive. The range of f covered, 0.5 < f < 1.0 is considered to be the most important range likely to be met in practice.

A.4 Fin-and-Rudder Load:

A.4.1 General formulae

The aerodynamic load on the fin-and-rudder during a lateral manoeuvre may be written (cf. Ref. 2)

$$\frac{P}{A} = -B\beta - C\frac{d\beta}{d\tau} + a_2\zeta \qquad (9)$$

where $A = \frac{1}{2}\rho V^2 S''$ $\qquad C = \frac{1}{\mu_3}a_1$

$$B = \left(1 + \frac{\bar{y}_v}{\mu_3}\right)a_1 \qquad \mu_3 = \frac{W}{g\rho S\ell}.$$

The condition for the maximum fin-and-rudder load is

$$- B \frac{d\beta}{d\tau} - C \frac{d^2\beta}{d\tau^2} + a_2 \frac{d\zeta}{d\tau} = 0. \qquad (10)$$

Using equations 4, 6 and 7 this condition may be rewritten as

$$e^{-\frac{R}{J}J\tau} = \frac{\left\{ f\left[\frac{2BR}{J} - CJ\left(\frac{R^2}{J^2}+1\right)\right] + CJ\, f^3 \right\} \sin Jf\tau + \left\{ f^2\left(\frac{CJ2R}{J} - B\right) + B\left(\frac{R^2}{J^2}+1\right) - \frac{a_2}{\delta_\eta H_e} \right\} \cos Jf\tau}{\left\{ f^2\left[B \cdot \frac{R}{J} - CJ\left(\frac{R^2}{J^2}+1\right)\right] + \left(\frac{R^2}{J^2}+1\right)\left[B \cdot \frac{R}{J} - CJ\left(\frac{R^2}{J^2}+1\right)\right]\right\} \sin J\tau + \left\{ f^2\left(\frac{2R}{J} CJ - B\right) + B\left(\frac{R^2}{J^2}+1\right)\right\} \cos J\tau} \qquad (11)$$

It is obvious that this equation is too complex to be of any practical value. The complexity is due to the nature of the equations for β and $\frac{d\beta}{d\tau}$, and, as implied in the previous paragraph, it is not possible to introduce general simplifications into the equations for β and $\frac{d\beta}{d\tau}$. However, it is possible to replace them locally by simpler functions for use in equations 9 and 10. In this way the labour can be kept to a minimum without any great loss in accuracy.

A.4.2 Approximate formulae for the fin-and-rudder load

Calculations have indicated that, in the general case, the component of the fin-and-rudder load which is dependent on $\frac{d\beta}{d\tau}$ has a marked influence on the precise positions of the maxima of the total load, although the magnitudes of these maxima are not appreciably affected. It is usually necessary to know both the total fin-and-rudder load and the load due to the rudder alone, and, since the load due to the rudder displacement alone is directly proportional to the position of the rudder at the P_m, it appears that the position of the P_m should be determined as accurately as possible. It is felt, therefore, that the term proportional to $\frac{d\beta}{d\tau}$, which may be neglected in the particular case $f = 1$ (cf. Ref.2), should be retained in the general case.

An analysis of the time histories of β and P in the general manoeuvre - see Fig.10 for example - suggests that, with the usual ranges of parameters, the various maxima of P occur later in the manoeuvre than the corresponding maxima of β (i.e. if the first small maximum of P is ignored). However, the phase angle between them is usually small. The new functions for β and $\frac{d\beta}{d\tau}$ need only be accurate, therefore, in the regions of the corresponding maxima of β and P. The response in β is oscillatory in character and a suitable function to describe the motion locally is found to be a circular function in which the coefficients and phase angles are chosen to give the local maxima exactly both in position and magnitude. The frequency of the new function may be assumed to be the same as that of the rudder movement. For convenience a separate datum is considered for each maximum. For the r^{th} maximum the local function for β is, using the notation of Fig.9

$$\frac{J^2}{\delta_n \zeta_e} \cdot (\beta)_r = (-1)^{r+1} Q_r \cos\left(Jf\tau - (2r-1)\frac{\pi}{2} - \varepsilon_r\right)$$

$$= (-1)^{r+1} Q_r \cos(x_r - \varepsilon_r) \qquad (12)$$

where $x_r = Jf\tau - (2r - 1)\frac{\pi}{2}$ and the particular datum is at $Jf\tau = (2r-1)\frac{\pi}{2}$. The first derivative of β may be obtained from equation 12 by differentiation.

The rudder movement about the new datum may be described as

$$\frac{J^2}{\delta_n \zeta_e}(\zeta)_r = (-1)^{r+1}\frac{J^2}{\delta_n}\cos x_r. \tag{13}$$

In these equations r(= 1, 2 and 3) indicates the particular local maximum under consideration. The angle ε_r is the phase angle between corresponding maxima of β and ζ and is considered positive when the β_m occurs after the corresponding ζ_m. Substituting these new functions in the general expression for P, equation 9, we have

$$\frac{J^2}{AB\delta_n}\left(\frac{P}{\zeta_e}\right)_r = (-1)^{r+1} Q_r\left[\frac{CJ}{B} f \sin(x_r - \varepsilon_r) - \cos(x_r - \varepsilon_r)\right] + \frac{a_2 J^2}{B\delta_n}\cos x_r$$

$$\text{or } \frac{1}{A}\left(\frac{P}{\zeta_e}\right)_r = (-1)^{r+1}\left[\bar{X}_r \sin(x_r - \varepsilon_r) + \bar{Y}_r \cos(x_r - \varepsilon_r) + a_2 \cos x_r\right] \tag{14}$$

$$\text{where} \quad \bar{X}_r = C \cdot \frac{\delta_n}{J} \cdot Q_r \cdot f$$

$$\bar{Y}_r = -B \cdot \frac{\delta_n}{J^2} \cdot Q_r \cdot \tag{15}$$

The equation for the position of the P_m is then

$$\bar{x}_r = Jf\bar{\tau}_r - \frac{\pi}{2}(2r - 1)$$

$$= \tan^{-1}\frac{\bar{X}_r \cos\varepsilon_r + \bar{Y}_r \sin\varepsilon_r}{a_2 + \bar{Y}_r \cos\varepsilon_r - \bar{X}_r \sin\varepsilon_r}. \tag{16}$$

Thus, for a given value of f, the only response quantities required for the calculation of the magnitude and position of a particular maximum of P are Q_r and ε_r. The values of these quantities, for a wide range of $\frac{R}{J}$ and f have been calculated from equations (5) and (8), and are given in Figs.2, 3, 4, 5, 6 and 7. The ringed points in Fig.10 indicate the accuracy of the new approach. The computational charts presented in Appendix III may be used for rapid estimation of the P_m.

A.5 Hinge Moment

The rudder hinge moment coefficient at any point in a lateral manoeuvre is

$$C_h = -b_1\beta + b_2\zeta. \tag{17}$$

The condition for the C_{h_m} is rather unwieldy, and the investigation of a particular case would be tedious. However, using the same technique as has been used in the previous section, approximate formulae may be derived to reduce the labour in such instances without any great loss in accuracy. All the maxima except the first may be obtained from a general formula.

1st Maximum:-

With typical values of b_1 and b_2, the first maximum of C_h occurs close to $Jf\tau = \frac{\pi}{2}$. In this region the response in β varies approximately as $(1 - \cos Jf\tau)$. If the new function for β is chosen such that it is exact at $Jf\tau = 0$ and $\frac{\pi}{2}$, we have, assuming the frequency of the motion to be the same as the frequency of the rudder displacement

$$\frac{J^2}{\delta_n}\left(\frac{\beta}{\zeta_e}\right) = Q_{\pi/2} \cdot (1 - \cos x_r) \tag{18}$$

where $x_r = Jf\tau$ and $r = 1$.

Equation (17) becomes

$$\left(\frac{C_h}{\zeta_e}\right)_1 = -\frac{\delta_n}{J^2} \cdot b_1 \cdot Q_{\pi/2} \cdot (1 - \cos x_1) + b_2 \sin x_1 \tag{19}$$

$$= \bar{M}_1 (1 - \cos x_1) + b_2 \sin x_1 \tag{20}$$

where $\bar{M}_1 = -\frac{\delta_n \cdot b_1}{J^2} \cdot Q_{\pi/2}$. (21)

The position of the maximum is at

$$\bar{x}_1 = \tan^{-1}\left(-\frac{b_2}{\bar{M}_1}\right). \tag{22}$$

Further Maxima:-

The dominant term in the equation for C_h, equation (17), is $b_2\zeta$. Thus for normal values of b_1 and b_2, the maxima in C_h will occur close to the corresponding maxima in ζ and the phase angle between corresponding maxima of β and C_h may be large. The function previously used to replace β locally (A.4.2) is only accurate in the region of each β_m. A more general function is therefore needed if accurate values of the remaining C_{h_m} are to be obtained.

A suitable general function is a sine function which gives exactly, the positions of $\beta = 0$ and the following β_m (in the region of the C_{h_m} in question) and also the magnitude of the β_m. The frequency of the new function is then automatically defined.

The function is (see also Fig.9)

$$\frac{J^2}{\delta_n}\left(\frac{\beta}{\zeta_e}\right)_r = (-1)^{r+1} Q_r \sin \varphi_r (x_r - \varepsilon_{r-1,r}) \tag{23}$$

where the local datum is at $Jf\tau = \pi(r-1)$ and $r = 2, 3$ etc.

$(\varepsilon_{r-1,r})$ is the phase angle between the positions of the corresponding $\beta = 0$ and $\zeta = 0$, considered positive when $\beta = 0$ occurs after $\zeta = 0$ and

$$\varphi_r = \frac{\text{local frequency of the response in } \beta}{\text{frequency of applied rudder movement}}$$

$$\simeq \frac{\pi/2}{\pi/2 + \varepsilon_r - \varepsilon_{r-1,r}} \tag{24}$$

Also

$$\frac{J^2}{\delta_n}\left(\frac{\zeta}{\zeta_e}\right)_r = (-1)^{r+1} \frac{J^2}{\delta_n} \cdot \sin x_r. \tag{25}$$

Hence equation (17) becomes

$$\left(\frac{C_h}{\zeta_e}\right)_r = (-1)^{r+1}\left(- Q_r \cdot \frac{\delta_n}{J^2} \cdot b_1 \cdot \sin \varphi_r(x_r - \varepsilon_{r-1,r}) + b_2 \sin x_r\right)$$

$$= (-1)^{r+1} (\bar{M}_r \sin \varphi_r (x_r - \varepsilon_{r-1,r}) + b_2 \sin x_r) \tag{26}$$

where
$$\bar{M}_r = - Q_r \cdot \frac{\delta_n}{J^2} \cdot b_1 . \tag{27}$$

The positions of the maxima are given by the following equation

$$\frac{\cos \bar{x}_r}{\cos \varphi_r(\bar{x}_r - \varepsilon_{r-1,r})} = - \frac{\bar{M}_r \varphi_r}{b_2} . \tag{28}$$

Within the ranges of $\frac{R}{J}$ and f considered in this note the range of φ_r is $0.8 < \varphi_r < 1.2$. For such cases

$$\cos \varphi_r(\bar{x}_r - \varepsilon_{r-1,r}) \simeq \cos(\bar{x}_r - \varepsilon_{r-1,r}) \tag{29}$$

and equation (28) may be simplified to

$$\frac{\cos \bar{x}_r}{\cos(\bar{x}_r - \varepsilon_{r-1,r})} = -\frac{\bar{M}_r \varphi_r}{b_2} . \qquad (30)$$

The solution to an equation of this type is given in Fig.27 for a considerable range of parameters.

Thus for rapid estimation of the C_{h_m}, the only additional response quantities, over and above those used in the estimation of the P_m, are $Q_{\pi/2}$ and $\varepsilon_{r-1,r}$. These may be found from equation (5). The values have been derived in the present note for a wide range of $\frac{R}{J}$ and f; the results are given in Figs.13, 15 and 16.

Fig.10 gives the exact response in β, P and C_h to a fish-tail manoeuvre for the aircraft considered in Table I. The ringed points are the maxima of P and C_h as calculated by the above formulae. It is seen that the approximate values are accurate to within 5%.

APPENDIX II

Detailed Discussion

The primary object of the present investigation has been to examine the effects of direct and power assisted rudder movement in relation to the design requirement[1]. This has necessitated a very detailed analysis of the general effects of rudder movement on the ensuing loading conditions. The chief points of interest are reported in para.3 of the main text, but the detailed discussion covering these points and further points of perhaps secondary interest from the airworthiness aspect are given in this Appendix. The Appendix is self contained and has the same general layout as para.3.

B.1 Effect of Frequency of Rudder Movement on the Response in Yaw

B.1.1 Introduction

To simplify the discussion, consideration is first given to the manner in which the various response quantities are affected by variations in the frequency of a sinusoidal rudder movement of constant amplitude (para.1.2). Then the quantities are considered in terms of a maximum pedal force for the same frequency range (para.1.3).

The rudder movement is defined as $\zeta = \zeta_e \sin Jf\tau$ where J is the non-dimensional, damped, natural circular frequency of the aircraft in yaw, and ζ_e is the amplitude of the movement. The non-dimensional circular frequency of the rudder movement is Jf, and f is, therefore, the ratio between the rudder frequency and the damped, natural yawing frequency of the aircraft. The case f = 1 corresponds to movement of the rudder at the damped resonant frequency of the aircraft in yaw. The non-dimensional rate of movement of the rudder is $\frac{d\zeta}{d\tau} = Jf\zeta_e \cos Jf\tau$ and the maximum (initial) rate is $Jf\zeta_e$. Thus when the response is expressed in terms of the amplitude of rudder movement, a variation in f indicates a proportional variation in both the frequency and maximum rate of movement of the rudder. However, if the response is expressed in terms of the maximum pedal force, a variation in f still indicates a proportional change in the frequency of the displacement, but the maximum rate of displacement depends on ζ_e, which, in turn, depends on the hinge moment characteristics of the rudder and, as will be seen later, on f itself although not proportional to it.

B.1.2 Response per unit amplitude of rudder movement

B.1.2.1 Angle of sideslip

The curves in Fig.1 give the response of an aircraft in angle of sideslip to sinusoidal movement of the rudder at four different frequencies. All the curves are presented with $Jf\tau = \left(\frac{Jf}{\hat{t}}\right) . t$, which is proportional to non-dimensional time, as a common base. In this way the disturbing movement, $\zeta = \zeta_e \sin Jf\tau$, appears as a single curve irrespective of the frequency. Plotted against $J\tau$, the curves of response would be considerably closer together with a resultant loss in clarity. It is seen that, while the general character of the curves is the same, both the positions and magnitudes of the local maxima are affected by variations in f. It is also apparent that the manner in which each of these maxima is affected depends on the particular local maximum in question.

For given values of δ_n, the rudder effectiveness, and J, the angle of sideslip is a function of $\frac{R}{J}$, f and time, (Appendix I equation (5)) and it is simple, although laborious, to determine the magnitudes and positions of its local maxima for different combinations of $\frac{R}{J}$ and f. The results of such an investigation are presented in Figs.2 to 4 and 5 to 7 respectively, and cover the three local maxima that occur in the duration of a manoeuvre of $1\frac{1}{2}$ cycles of rudder movement.

Examination of Figs.2 - 4, indicates that the magnitude of the individual maxima Q_1, Q_2 and Q_3 are all affected in a similar manner by the parameters $\frac{R}{J}$ and f, i.e. the maxima decrease if $\frac{R}{J}$ is increased, and increase to a peak and then decrease if f is increased. The effects become more pronounced as the manoeuvre develops, and the percentage change in Q_3 following a change in $\frac{R}{J}$ or f, or both, is much larger than the corresponding percentage change in Q_1. Also, as the manoeuvre develops, for a given value of $\frac{R}{J}$, the values of f associated with the peak values of Q_r tend towards the damped resonance value. Resonance conditions might be expected to give the peak value of Q_r, but there are two reasons why this is not so in any problem of the present type. Firstly, steady values are not reached in the specified duration of the manoeuvre, and secondly, the motion of the aircraft is damped. If the motion of a system is damped, the maximum response occurs at a frequency somewhat below resonance conditions, (cf. Ref.3) even if asymptotic conditions are reached. Further if the motion is overdamped, the maximum response drops away as the frequency is increased from zero, (cf. Ref.3 page 66), and no peak is apparent. In the case under consideration, where the damping is moderate, the peak values of Q_3 occur in the region of f = 0.9 to 0.95.

The positions of the maxima, see Figs.5 - 7, are all affected in a similar way by changes in $\frac{R}{J}$ and f, but not to the same extent. For a given value of $\frac{R}{J}$, the phase angles ε_1, ε_2 and ε_3 increase as f is increased. Thus, as the frequency of the displacement of the rudder is increased, the response in β tends to lag more and more behind the rudder displacement, cf. Fig.1. However, as the manoeuvre develops, the angles ε_r gradually decrease and approach a steady value. This value depends on $\frac{R}{J}$ and f, and may be obtained from a consideration of the asymptotic conditions (i.e. at $Jf\tau = \infty$). The positions of the maxima are not affected greatly by changes in $\frac{R}{J}$ except possibly at the lower end of the frequency range considered in this note.

The effects of $\frac{R}{J}$ and f on Q_r become more noticeable as the manoeuvre develops; this is best illustrated if the values of Q_r, for a given value of $\frac{R}{J}$, are plotted on the same frequency base, as in Fig.8, where the data of the example in Table I are used. It is seen that, at the lower end of the frequency range, Q_1 is the critical maximum for the manoeuvre. If the frequency is increased a point is reached at which Q_1 and Q_2 become equal. For a certain region beyond this frequency, Q_2 is the critical maximum and finally, as the damped resonance conditions are approached, Q_3 becomes the critical one. If the disturbing frequency is increased beyond f = 1, Q_2 and Q_1 in that order,

again become critical. The values of f, below the resonance conditions, at which Q_1 and Q_2 and Q_2 and Q_3 become equal are given in Fig.14, for a range of values of $\frac{R}{J}$. The values of f are little affected by $\frac{R}{J}$, except when this parameter is small.

The general equation for β, equation 5, contains trigonometrical functions of two distinct frequencies; one is the frequency of the disturbing motion, the other, the transient frequency, is the damped natural yawing frequency of the aircraft. With the range of f considered in this note, the two frequencies are of the same order. Where the initial effect of the transient response on the overall response is considerable, a condition approximating to the characteristic "beating" phenomenon is to be expected, i.e. motion with periodically varying amplitude. The transient response component is usually well damped, so that a true beating condition cannot develop. The remarks made above indicate that the amplitude of the response in β does vary in some complex way, and it appears that a form of beating is present in the sideslipping motion induced by sinusoidal rudder movement of frequencies close to the damped resonant yawing frequency of the aircraft.

B.1.2.2 Fin-and-rudder load

A time history of the fin-and-rudder load induced by sinusoidal rudder movement of a specific frequency is given in Fig.10 for the example of Table I. It is seen that the form of the response in P is similar to that in β, except at the beginning of the manoeuvre. The additional maximum that occurs in the initial stages of the manoeuvre is usually very small, and, for design purposes, may be disregarded. An examination of the general equation for P, equation (9), and the ranges of the parameters involved, indicates that the contribution to the total load of the component proportional to β is paramount. Thus, the fin-and-rudder load is affected by changes in $\frac{R}{J}$ and f in a similar way as the angle of sideslip, (cf. Figs.8 and 11) and, in the general case, it is necessary to have a knowledge of the three local maxima of P before the critical condition is stated.

Since P is greatly dependent on β, the corresponding maxima of these two quantities (disregarding the first, very small, maximum of P) occur at roughly the same times in the manoeuvre. With the usual values of the pertinent parameters, each maximum in β is closely followed by a maximum in P. The proximity of each pair of maxima depends on the value of f, i.e. on the frequency of the rudder displacement. For the particular case of $f = 1$, (see Ref.2), these maxima occur at $Jf\tau \simeq \pi$, 2π and 3π, i.e. when the rudder is central. In this special case, the contributions to the total loads of the components proportional to ζ and $\frac{d\beta}{d\tau}$ are negligible. However, for values of f other than unity, the maxima in β, and hence the maxima in P, do not occur in the region of $Jf\tau = \pi$ etc., but when the rudder is in a deflected position (cf. Fig.10). Thus, in the general case, each P_m contains a component due to the angular position of the rudder, and also, since the P_m occur after the corresponding β_m, a small component due to $\frac{d\beta}{d\tau}$ (see equation (9)).

Detailed calculations have indicated that the component of P due to $\frac{d\beta}{d\tau}$ has a marked influence on the precise positions of the P_m, although the magnitudes are not appreciably affected. Since the designer often needs to have a knowledge of the separate components of the P_m, as well as the values the P_m themselves, an accurate knowledge of the position of the P_m is also

desirable. The rudder angles associated with the P_m are usually small, although they vary appreciably with f, and the components of P_m due to the position of the rudder, which are proportional to $\zeta_e \sin Jf\tau$ are much affected by inaccuracies in the estimation of the rudder angles for the P_m. Thus it appears that the component of P due to $\frac{d\beta}{d\tau}$ should be retained in any computations involving the P_m and their components.

The general equation for P is complex, and rather unwieldy for use in detailed calculations of the maxima in P. This complexity arises from the presence of the components containing β and $\frac{d\beta}{d\tau}$. In Appendix I para.A.4.2, a method is developed to reduce the computational work involved in such a task. In this method, the exact equations for β and $\frac{d\beta}{d\tau}$ are replaced by simpler, approximate equations, which give good agreement with the exact equations in the neighbourhood of each β_m. A convenient expression for β_m is $Q_r \cos(Jf\tau-\varepsilon_r)$. The approximate equation for $\frac{d\beta}{d\tau}$ follows by differentiation. The two parameters Q_r and ε_r are precisely those used in para.B.1.2.1 to describe the β_m in magnitude and position. The accuracy of the new approach may be gauged from Fig.10. The "ringed" points are obtained from the computational chart. The curve shows exact values.

To illustrate the effect of f on the various maxima of P, all other factors considered constant, the example in Table I has been analysed. The results are obtained from the simplified formulae, and are presented in Fig.11. The curves confirm that the maxima in β and P are affected in a very similar manner by changes in f. The values of f for the peak values of the P_m are a little higher than those for the peak values of the β_m. These differences depend on the ratio $\frac{a_1}{a_2}$. If it is high the shape of the curves for the β_m and P_m are almost identical.

B.1.2.3 Rudder hinge moment

An example of the response in C_h to a sinusoidal rudder movement is given in Fig.10. Again the character of the response is similar to that in β. However, with the usual values of b_1 and b_2, the term $b_2\zeta$ in the equation for C_h, equation (17), is the dominant one, and the response in C_h follows the disturbance more closely than is the case with the response in β and P. Although the term $b_2\zeta$ is the dominant term, the effect of f on the response is considerable. This is mainly due to the changes in phase which occur between β and ζ when f is varied. This is especially marked when $\frac{b_1}{b_2}$ is positive and b_2 is negative, for, in such cases, the components of C_h, $b_1\beta$ and $b_2\zeta$, tend to oppose each other throughout the manoeuvre, and slight changes in phase between the two components cause considerable changes in the overall C_h response.

The effect of f on the various maxima of C_h for the example in Table I, is illustrated in Fig.12. The curves have the same general characteristics as the corresponding ones for the β_m and P_m. However, the values of f for

the peak values of the C_{h_m} are higher than in either of the other cases. The dotted line represents the maxima of C_h for the special case $b_1 = 0$ and divergence from this line, at any value of f, is entirely the effect of $b_1\beta$ i.e. the effect of the response of the aircraft in β. Below $f = 0.9$ in this particular example, the response of the aircraft reduces the hinge moment below the value obtained from the rudder alone. This tendency is likely to be present if $\frac{b_1}{b_2}$ is positive and b_2 is negative. The ratio $\frac{b_1}{b_2}$ has a controlling influence on the value of f at which the effect of the response of the aircraft changes sign. The significance of this feature will be discussed more fully in para.B.1.3.

The curves in Fig.12 indicate that it is necessary to calculate the values of all three C_{h_m} before stating the absolute maximum for the manoeuvre. However, the character of the equation for C_h, equation (17), is basically the same as that for P, and it is consequently unsuitable for use in detailed calculations because of the labour involved. In Appendix I para.A.5 further approximate equations for β are introduced to simplify the equation for C_h. For the 1st maximum of C_h, β is expressed as a function $Q_{\pi/2}(1-\cos Jf\tau)$ where $Q_{\pi/2}$ is a response factor involving the value of β at $Jf\tau = \frac{\pi}{2}$ (see Fig.13), and for the 2nd and 3rd maxima, β is expressed as a function of $Q_r \sin \varphi_r (Jf\tau - \varepsilon_{r-1,r})$. In both cases, the approximate equation for C_h may be tabulated for calculation of the maxima. The relevant charts are given in Appendix III. The accuracy of the approach may be gauged from Fig.10. The squared points are obtained from the approximate equations; the curve shows the exact values.

B.1.3 Response per unit maximum pedal force

So far the discussion has been confined to consideration of the effect of f on the response in β, P and C_h induced by unit amplitude sinusoidal rudder movement. The present design requirement specifies an amplitude of movement corresponding to a given pedal force being the maximum force applied in the manoeuvre. To compare the fin-and-rudder load for the design case $f = 1$, and the load induced by sinusoidal movement of the rudder at other frequencies, the effects of f on such quantities as the β_m and P_m per unit maximum C_h are required. Because of the large number of parameters involved, the effects are best illustrated by an example. In the previous paragraphs, the effects of f on $\frac{\beta_m}{\zeta_e}$, $\frac{P_m}{\zeta_e}$ and $\frac{Ch_m}{\zeta_e}$ have been given for the the example in Table I - see Figs.8, 11 and 12. At any value of f, the uppermost curve in each figure gives the absolute maximum value of each quantity produced in the full manoeuvre of $1\frac{1}{2}$ cycles of rudder displacement. If only one cycle of rudder displacement is to be considered, the curve for the third maximum $r = 3$, may be neglected in each case. If the reciprocal of the values on the upper boundary in Fig.12 are calculated, the resultant curve gives the value of ζ_e at each value of f, which must be applied to obtain unit C_{h_m} at some point in the manoeuvre. The curve is given in Fig.17. Any combination of ζ_e and f below this curve does not produce unit C_{h_m} at any time during the manoeuvre considered. Conversely, if a combination

above the curve is selected, unit C_{h_m} will be exceeded. It is seen that, as f is increased, the amplitude of rudder movement to produce unit maximum C_h decreases considerably. This effect is likely to occur in all cases where $\frac{b_1}{b_2}$ is positive and b_2 is negative. The rapidity with which ζ_e decreases as f is increased depends on the magnitude of $\frac{b_1}{b_2}$. The curve is discontinuous since it is based on the upper boundary in Fig.12. The points of discontinuity correspond to values of f at which the absolute maximum of C_h for the manoeuvre changes from one local maximum to the next (see para.B.1.2.3). The dotted line represents the special case $b_1 = 0$. The relieving effect of the aircraft response is clearly demonstrated.

If the combination of f and ζ_e at each frequency, to produce unit maximum C_h is known, the corresponding maximum (initial) rates of displacement of the rudder may be calculated since the maximum rate is proportional to $f\zeta$. The curve for the present example is given in Fig.18. The area below the curve corresponds to conditions which do not produce unit maximum C_h in the specified duration of the manoeuvre. The maximum rate increased to a peak and then drops as f is increased. In general, the position and magnitude of the peak depends on $\frac{b_1}{b_2}$.

The curves of the β_m and P_m per unit maximum C_h are plotted in Figs.19 and 20. They are similar in character to those for the β_m and P_m per unit ζ_e, but there is one important difference, namely that the peak values of the β_m and P_m per unit maximum C_h do not occur at or close to f = 1. Consequently, the damped resonance condition (i.e. the present design case) does not necessarily represent the critical loading case. In the present example, the greatest β_m, at f = 0.765, is 30% greater than the largest β_m at f = 1. Similarly the greatest value of P_m, at f = 0.84, is nearly 15% greater than the largest P_m at f = 1. A similar state exists if the duration of the manoeuvre is restricted to one cycle of rudder displacement.

Thus although the pilot may tend to displace the rudder at the damped natural yawing frequency of the aircraft if he executes a manoeuvre approximating to the fish-tail manoeuvre, he will be able, with conventional rudder controls and control characteristics, to apply a greater rudder amplitude for a given maximum pedal force than in the damped resonance condition by reducing the frequency of the displacement slightly (because of the relieving effect of the response of the aircraft on the hinge moments at low frequencies). Such an action will give rise to greater angles of sideslip and fin-and-rudder loads than those associated with the resonance case. The maximum rate of movement will be slightly higher than that associated with resonance conditions but, with direct control, it should be attainable without undue effort.

These remarks only apply strictly to the chosen example. The important parameters are a_1, a_2, b_1, b_2 and $^R/_J$, and provided these do not change much the overall picture will be similar.

B.2 Effect of a power unit on the rudder movement and pedal forces

In certain circumstances, the addition of a hydraulic power unit to the rudder circuit may impose restrictions on the movement of the rudder. In particular, there may be a restriction on the maximum rate at which the rudder can be moved. If the rudder pedals are moved sinusoidally at a low frequency, with low amplitude, the power unit is normally able to produce a corresponding movement at the rudder. However, if the frequency of the pedal movement is increased without altering the amplitude an initial rate of movement equal to the maximum rate of the power unit is eventually reached, cf. Fig.21.. Beyond this point, the pilot is not completely free to apply the movement he desires but is influenced by the characteristics of the power unit. The present design requirement specifies the frequency of the rudder movement, and also a pedal force (the maximum force applied in the manoeuvre). Implicit in this requirement is a maximum rate of rudder movement. If this rate cannot be realised through the power unit, the specified manoeuvre cannot be performed and the design requirement may then be too severe.

To examine this point, an assumption must be made with regard to the actual rudder movement obtained by the pilot when he attempts to perform the required manoeuvre. If the rudder is operated directly, the pilot is likely to move it at the damped natural yawing frequency of the aircraft. The addition of a power unit will probably not alter this tendency, although there is likely to be a small phase lag between the pedal and rudder movement. The phase lag is of no consequence however, in the present investigation since the aircraft response induced by the movement of the rudder is of primary interest. The effect of the power unit in restricting the rate of movement is probably to reduce the amplitude of the rudder displacement. Just how much the amplitude will be reduced is difficult to assess. A first approximation might be that the pilot moves the rudder sinusoidally at the specified frequency, with an initial rate equal to the maximum rate of the power unit. However, if he attempts to apply the specified movement of the rudder, corresponding to a pedal force of 100 lb, the amplitude may be greater than given by this approximation. In the absence of any flight or laboratory data to justify a more realistic approach it is assumed that the rudder is moved at a frequency equal to the damped natural yawing frequency of the aircraft, with an amplitude equal to the arithmetic mean of the specified amplitude and the amplitude given by the first approximation suggested above (see Fig.22a). Thus, the maximum initial rate of movement is higher than the maximum rate of the power unit. However, such an assumption is not unreasonable because it is usually possible, through the follow-up mechanism of the power unit, to boost up slightly the maximum rate a few percent. Also the movement of the rudder at a rate at, or close to the maximum rate of the power unit makes the execution of an exact sinusoidal movement difficult, and the initial movement is likely to be approximately linear rather than sinusoidal. Nevertheless the resultant rudder movement is assumed to be of sinusoidal form in order that use may be made of many of the graphs and charts already presented and discussed. Thus the conclusions reached are mainly qualitative, although they indicate the trends to be expected.

The specified amplitude of the rudder movement is that which can be obtained with a pedal force of 100 lb. The assumption with regard to the actual amplitude of movement of the rudder when a power unit is in the circuit, implies that the applied pedal force is less than this amount, provided that the relationship between pedal movement and pedal force is a linear one. However, if the pilot chooses to move the rudder at a lower frequency than the damped resonant frequency, he is able, without increasing the maximum rate of movement to obtain a bigger amplitude and consequently a bigger pedal force, i.e. a force closer to the specified 100 lb. This

reduction in frequency, which involves a corresponding increase in amplitude, may give rise to a greater fin-and-rudder load than could be obtained with the assumed movement - in much the same manner as in the case of the manoeuvre induced by direct operation of the rudder (para.8.1). If the maximum rate of the power unit is very much lower than the rate implicit in the specified manoeuvre, the power unit affects the pedal movement over a considerable range of frequencies. In this range, the effect of the power unit will be assumed to be as before, namely that and the amplitude is equal to the arithmetic mean of the specified amplitude and the amplitude corresponding to movement at the optimum rate of the power unit and the frequency in question (see Fig.22b). Thus the assumed rate of movement varies with the frequency of movement.

B.3 Effect of a power unit on the response of an aircraft

B.3.1 Example chosen

To illustrate the effects of a power unit, on the various response quantities, the previous example of Table I is extended to cover the case with a power unit in circuit. The characteristics of the unit are assumed to be such that its maximum rate is 0.7 of the maximum rate required to perform the specified fish-tail manoeuvre, i.e. the maximum attainable frequency of movement of the rudder, with the amplitude corresponding to a pedal force of 100 lb, is 0.7 of the damped natural yawing frequency of the aircraft, or simply, f = 0.7. At low frequencies, below f = 0.7, the pilot can apply the amplitude of movement corresponding to 100 lb pedal force, and the maximum initial rate of movement depends on the frequency he chooses to use. Above f = 0.7, with the influence of the power unit, the resultant amplitude of movement depends on the frequency as shown in Fig.23.

It is felt that the chosen characteristics of the power unit represent almost an extreme practical case, since it is not expected that the optimum rate of the unit will be much less than 0.7 of that required for the execution of the fish-tail manoeuvre. If it is, it will probably mean that the aircraft cannot be manoeuvred in the most efficient manner.

B.3.2 Angle of sideslip

Consider now Fig.24. The full line represents the case in which, for the range of frequencies considered, the power unit has no effect on the control motion i.e. the present design conditions, at f = 1, can be met. The β_m are expressed in terms of pedal force, and are obtained directly from Fig.8. In making this step it is assumed that the pedal force is proportional to pedal displacement. The dotted curve represents the case in which the power unit is added to the circuit. The amplitude of the rudder movement above f = 0.7 is reduced according to the relevant curve in Fig.23. The chain dotted curve has been produced by assuming that the rudder movement above f = 0.7 is sinusoidal but that the maximum rate is limited to the maximum rate of the power unit, i.e. the first approximation mentioned in para.B.2. In this case the amplitude of the movement decreases as the frequency is increased such that the maximum rate remains constant.

The curves indicate that, if the power unit restricts the movement of the rudder such that the design conditions cannot be reached, the maximum angle of sideslip obtainable is lower than that associated with the present design conditions. Also, this maximum may occur at a frequency considerably lower than the damped resonant frequency of the system.

B.3.3 Fin-and-rudder load

A similar set of curves has been produced for the fin-and-rudder load at various frequencies, Fig.25. The curves are very similar to those for the

angle of sideslip. If the assumed effect of the power unit on the pedal displacement is accepted rough quantitative conclusions may be drawn. In the example chosen, it is seen that the maximum load is approximately 18% lower than the specified design load. The maximum occurs when the rudder is moved at a frequency approximately equal to the damped resonant frequency. However, it is likely that in other examples, the critical frequency may differ from the damped resonant frequency.

B.3.4 Rudder hinge moment

The rudder hinge moment, which may be needed for the determination of the strength of components on the rudder side of the power unit, has also been calculated (see Fig.26). The effects of a power unit are similar to those found in the other two response quantities.

APPENDIX III

Computational Charts

The following charts may be used to calculate the local maxima of the fin-and-rudder load and rudder hinge moment produced by unit amplitude of sinusoidal rudder movement of a chosen frequency (αf), and the local maxima of the angle of sideslip and fin-and-rudder load per unit maximum C_h for the same frequency of movement. The corresponding maximum angle of sideslip per unit rudder movement may be obtained from Figs. 2, 3 and 4. If the duration of the manoeuvre is $1\frac{1}{2}$ cycles of rudder movement, three local maxima of each quantity are produced, corresponding to r = 1, 2 and 3 (for 1 cycle of movement the number of maxima is only two, r = 1 and 2), and for the chosen value of f, all three local maxima should be computed before stating the absolute maximum of the quantity for the chosen manoeuvre. The charts are based on the approximate formulae derived in Appendix I, namely

$$\frac{1}{\Lambda}\left(\frac{P_m}{\zeta_e}\right)_r = (-1)^{r+1}\left\{\bar{X}_r \sin(\bar{x}_r - \varepsilon_r) + \bar{Y}_r \cos(\bar{x}_r - \varepsilon_r) + a_2 \cos \bar{x}_r\right\}$$

$$r = 1, 2 \text{ and } 3$$

$$\left(\frac{C_{h_m}}{\zeta_e}\right)_r = \bar{M}_r(1 - \cos \bar{x}_r) + b_2 \sin \bar{x}_r$$

$$r = 1$$

$$\left(\frac{C_{h_m}}{\zeta_e}\right)_r = (-1)^{r+1}\left\{\bar{M}_r \sin \varphi_r (\bar{x}_r - \varepsilon_{r-1,r}) + b_2 \sin \bar{x}_r\right\}$$

$$r = 2 \text{ and } 3.$$

The charts may also be used to calculate the local and absolute maxima of the above quantities over a range of rudder movement frequencies thereby permitting the determination of the frequencies which produce the greatest angle of sideslip and fin-and-rudder load per unit rudder movement and maximum C_h, and the magnitudes of these quantities. In general, the critical frequency will lie in the range $0.5 < f < 1.0$.

The numerical values included in the charts illustrate the orders of magnitude of the quantities in the various columns etc.

Data required.

(see also List of Symbols):

a_1	ℓ_R	(ft)
a_2	n_v	

b	(ft)	n_r	
b_1		S	(ft^2)
b_2		S''	(ft^2)
f	a range	V	(ft/sec T.A.S.)
g	(ft/sec^2)	$\overline{V}$	
i_c		W	(lb)
ℓ	(ft)	y_v	

Basic formulae:

$$\mu_2 = \frac{W}{g\rho Sb} \qquad \delta_n = \frac{\mu_2 \overline{V}_R a_2}{i_c} \qquad A = \tfrac{1}{2}\rho V^2 S''$$

$$\mu_3 = \frac{W}{g\rho S\ell} \qquad R = \tfrac{1}{2}(\overline{y}_v + \nu_n) \qquad B = \left(1 + \frac{\overline{y}_v}{\mu_3}\right) a_1$$

$$\omega_n = \frac{\mu_2 n_v}{i_c} \qquad J = \sqrt{\omega_n - \tfrac{1}{4}(\nu_n - \overline{y}_v)^2} \qquad C = \frac{1}{\mu_3} a_1$$

$$\nu_n = -\frac{n_r}{i_c}$$

$$\overline{y}_v = -y_v$$

CHART I

Maximum Fin-and-Rudder Load Per Unit Amplitude of Simusoidal Rudder Displacement

	a_2	$\frac{C \cdot \delta_n}{J}$	$-\frac{B \cdot \delta_n}{J^2}$	f	r	Q_r	ε_r (degrees)	$Q_r \cdot f$	$\frac{C \cdot \delta_n}{J} \cdot Q_r \cdot f$	$-\frac{B \cdot \delta_n}{J^2} \cdot Q_r$	sin ε_r	cos ε_r	$\bar{X}_r \cos \varepsilon_r + \bar{Y}_r \sin \varepsilon_r$	$a_2 + \bar{Y}_r \cos \varepsilon_r - \bar{X}_r \sin \varepsilon_r$	tan $\bar{x}_r'$	$\bar{x}_r'$ (degrees)	$(\bar{x}_r' - \varepsilon_r)$ (degrees)	sin$(\bar{x}_r' - \varepsilon_r)$	cos$(\bar{x}_r' - \varepsilon_r)$	cos $\bar{x}_r'$	$\bar{X}_r \sin(\bar{x}_r' - \varepsilon_r) + \bar{Y}_r \cos(\bar{x}_r' - \varepsilon_r) + a_2 \cos \bar{x}_r'$	$(-1)^{r+1}.0$	$\frac{1}{A}\left(\frac{P_m}{\zeta_e}\right)_r$	$\left(\frac{P_m}{\zeta_e}\right)_r$
						Figs 2,3,4	Figs 5,6,7	4 × 6	2 × 8	3 × 6	sin 7	cos 7	9×12+10×11	1 + 10 × 12 − 9 × 11	$\frac{13}{14}$	$\tan^{-1}$ 15	16 − 7	sin 17	cos 17	cos 16	9×18+10×19 +1×20	$(-1)^{5+1}.0$	21 × 22	A × 23
1	2	3	4	5	6	7	8	9	10	11	12	13	14	15	16	17	18	19	20	21	22	23	24
2	0.576	−4.00	0.6	1	1.23	66	0.984	0.566	−4.92	0.914	0.407	−4.26	−0.518	8.264	83.1	17.1	0.294	0.956	0.120	−4.30	1	−4.30	
"	"	"	"	2	1.75	53	1.400	0.806	−7.0	0.799	0.602	−5.11	−2.86	1.789	60.8	7.8	0.136	0.991	0.488	−5.85	−1	5.85	
"	"	"	"	3	1.88	45	1.503	0.867	−7.52	0.707	0.707	−4.70	−3.93	1.196	50.1	5.1	0.089	0.996	0.641	−6.13	1	−6.13	
"	"	"	0.8	1	"	"	"	"	"	"	"	"	"	"	"	"	"	"	"	"	"	"	
"	"	"	"	2	"	"	"	"	"	"	"	"	"	"	"	"	"	"	"	"	"	"	
"	"	"	"	3	"	"	"	"	"	"	"	"	"	"	"	"	"	"	"	"	"	"	
"	"	"	0.7	1	"	"	"	"	"	"	"	"	"	"	"	"	"	"	"	"	"	"	
"	"	"	"	2	"	"	"	"	"	"	"	"	"	"	"	"	"	"	"	"	"	"	
"	"	"	"	3	"	"	"	"	"	"	"	"	"	"	"	"	"	"	"	"	"	"	

CHART IIa

Maximum Rudder Hinge Moment per Unit Amplitude of Sinusoidal Rudder Displacement (First Local Maximum)

b_1	b_2	$-\frac{\delta_n \cdot b_1}{J^2}$	f	r	$Q\pi/2$	$\bar{M}_1 = \frac{-\delta_n \cdot b_1}{J^2} \cdot Q\pi/2$	$\tan \bar{x}_1 = \frac{-b_2}{\bar{M}_1}$	$\bar{x}_1$ (degrees)	$\sin \bar{x}_1$	$\cos \bar{x}_1$	$1 - \cos \bar{x}_1$	$C_{h_1}/\zeta_e = \bar{M}_1(1 - \cos \bar{x}_1) + b_2 \sin \bar{x}_1$
					fig 13	3 x 6	-2/7	$\tan^{-1}$ 8	sin 9	cos 9	+(1 - 11)	7 x 12 + 2 x 10
1	2	3	4	5	6	7	8	9	10	11	12	13
-0.1	-0.3	0.127	0.6	1								
=	=	=	0.7	1								
=	=	=	0.8	1	0.59	0.075		76	0.970	0.242	0.758	-0.235

CHART IIb

Further Local Maxima of the Rudder Hinge Moment

b_1		1	-0.1			0.8 "	2 3	1.75 1.88	53 45	53 48	0.222 0.239	1.0 1.034	- 0.740 0.824	50 36.5	-3 -11.5	-3 -11.9	-0.052 -0.206	0.766 0.595	-0.241 -0.228	-1 1	0.241 -0.228
b_2		2	-0.3																		
$-\frac{\delta_n \cdot b_1}{j^2}$		3	0.127																		
f		4	0.6 "			0.7 "															
r		5		2 3	2 3																
Q_r	figs 2,3,4	14																			
ε_r (degrees)	figs 5,6,7	15																			
$\varepsilon_{r-1,r}$ (degrees)	figs 15,16	16																			
$\overline{M}_r = \frac{-\delta_n \cdot b_1}{j^2} \cdot Q_r$	3 × 14	17																			
$\varphi_r = \frac{90}{90 + \varepsilon_r - \varepsilon_{r-1,r}}$	$\frac{90}{90 + 15 - 16}$	18																			
$-\frac{\overline{M}_r \varphi_r}{b_2}$	$-\frac{17 \times 19}{2}$	19																			
$\overline{x}_r$ (degrees)	fig.27	20																			
$\overline{x}_r - \varepsilon_{r-1,r}$ (degrees)	20 - 16	21																			
$\varphi_r(\overline{x}_r - \varepsilon_{r-1,r})$ (degrees)	18 × 21	22																			
$\sin \varphi_r(\overline{x}_r - \varepsilon_{r-1,r})$	sin 22	23																			
$\sin \overline{x}_r$	sin 20	24																			
$\overline{M}_r \sin \varphi_r(\overline{x}_r - \varepsilon_{r-1,r})$ $+ b_2 \sin \overline{x}_r$	17 × 23 + 2 × 24	25																			
$(-1)^{r+1} 1.0$	$(-1)^{5+1} 1.0$	26																			
$\left(\frac{C_{h_m}}{\zeta_e}\right)_r$	25 × 26	27																			

CHART III

Maxima of the Angle of Sideslip and the Fin-and-Rudder Load per Unit Maximum Rudder Hinge Moment

$\frac{\delta_n}{J^2}$	f	r	Q_r	$(-1)^{r+1}$	$(-1)^{r+1} \cdot \frac{\delta_n}{J^2} \cdot Q_r = \left(\frac{\beta_m}{\zeta_e}\right)_r$	$\frac{1}{A}\left(\frac{P_m}{\zeta_e}\right)_r$	$\left(\frac{C_{h_m}}{\zeta_e}\right)_r$	$\text{Maximum}\left(\frac{C_{h_m}}{\zeta_e}\right)$	$\left(\frac{\beta_m}{\text{Maximum } C_{h_m}}\right)_r$	$\frac{1}{A}\left(\frac{P_m}{\text{Maximum } C_{h_m}}\right)_r$
			figs 2,3,4	$(-1)^{3+1.0}$	1 x 4 x 5	Chart I	Chart II	Absolute maximum of 8 at each f considered positive	7/9	8/9
1	2	3	4	5	6	7	8	9	10	11
1.27	0.7									
=	=									
=	0.8	1	1.23	1	1.562	-4.30	-0.235		6.481	-17.83
=	=	2	1.75	-1	-2.223	5.85	0.241	0.241	-9.224	24.27
=	=	3	1.88	1	2.388	-6.13	-0.228		9.909	-25.44

TABLE I

Data for example

R	$= 0.664$	B	$= 2.527$
J	$= 3.775$	C	$= 0.115$
$\frac{R}{J}$	$= 0.175$	$\frac{a_1}{a_2}$	$= 1.39$
δ_n	$= 17.64$	a_2	$= 1.8$
$\frac{\delta_n}{J^2}$	$= 1.257$	b_1	$= -0.1$
		b_2	$= -0.3$
		$\frac{b_1}{b_2}$	$= 0.33$

WT.2078.CP.301.K3 - Printed in Great Britain

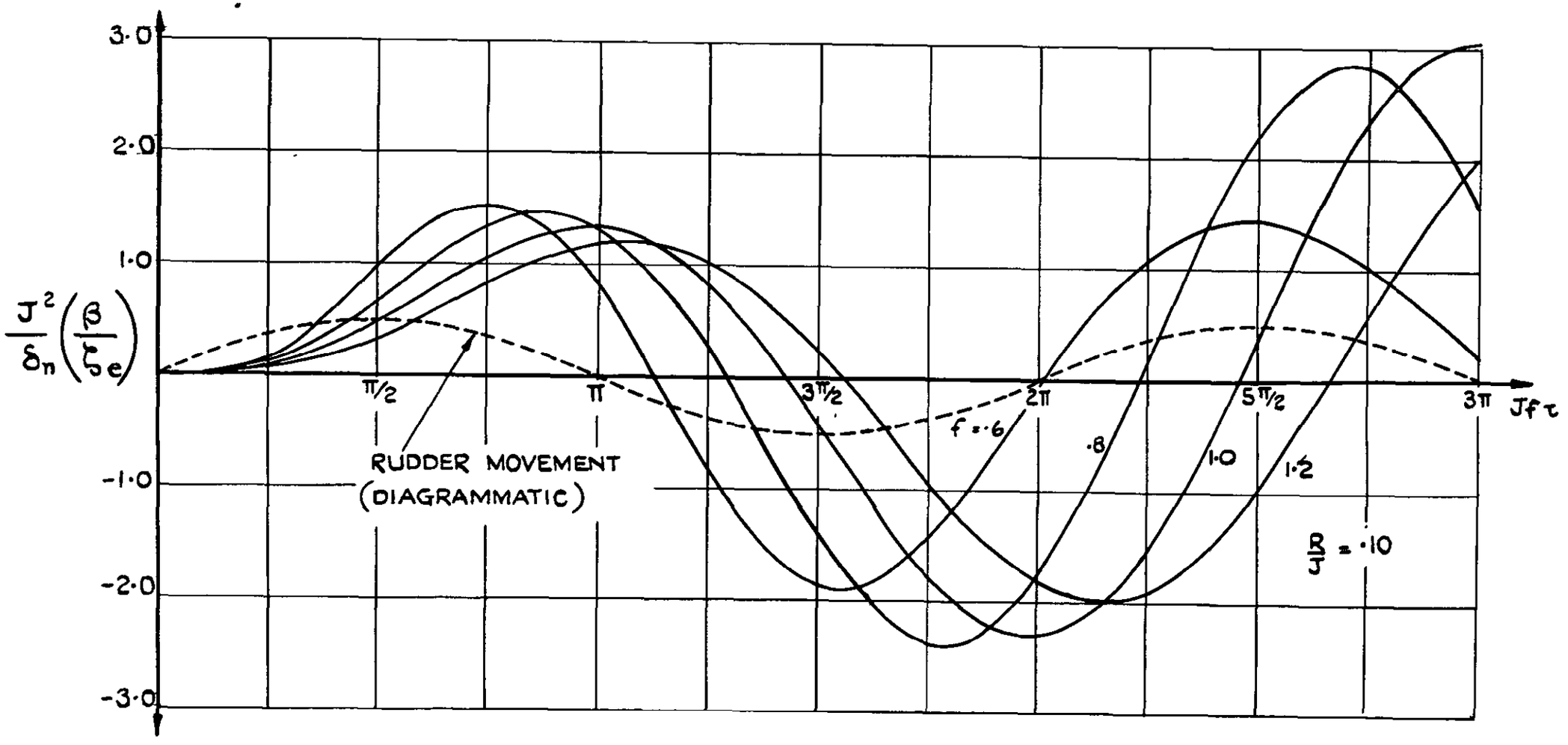

FIG. 1. EFFECT OF VARIATIONS IN THE FREQUENCY OF THE SINUSOIDAL RUDDER MOVEMENT ON THE RESPONSE IN ANGLE OF SIDESLIP.

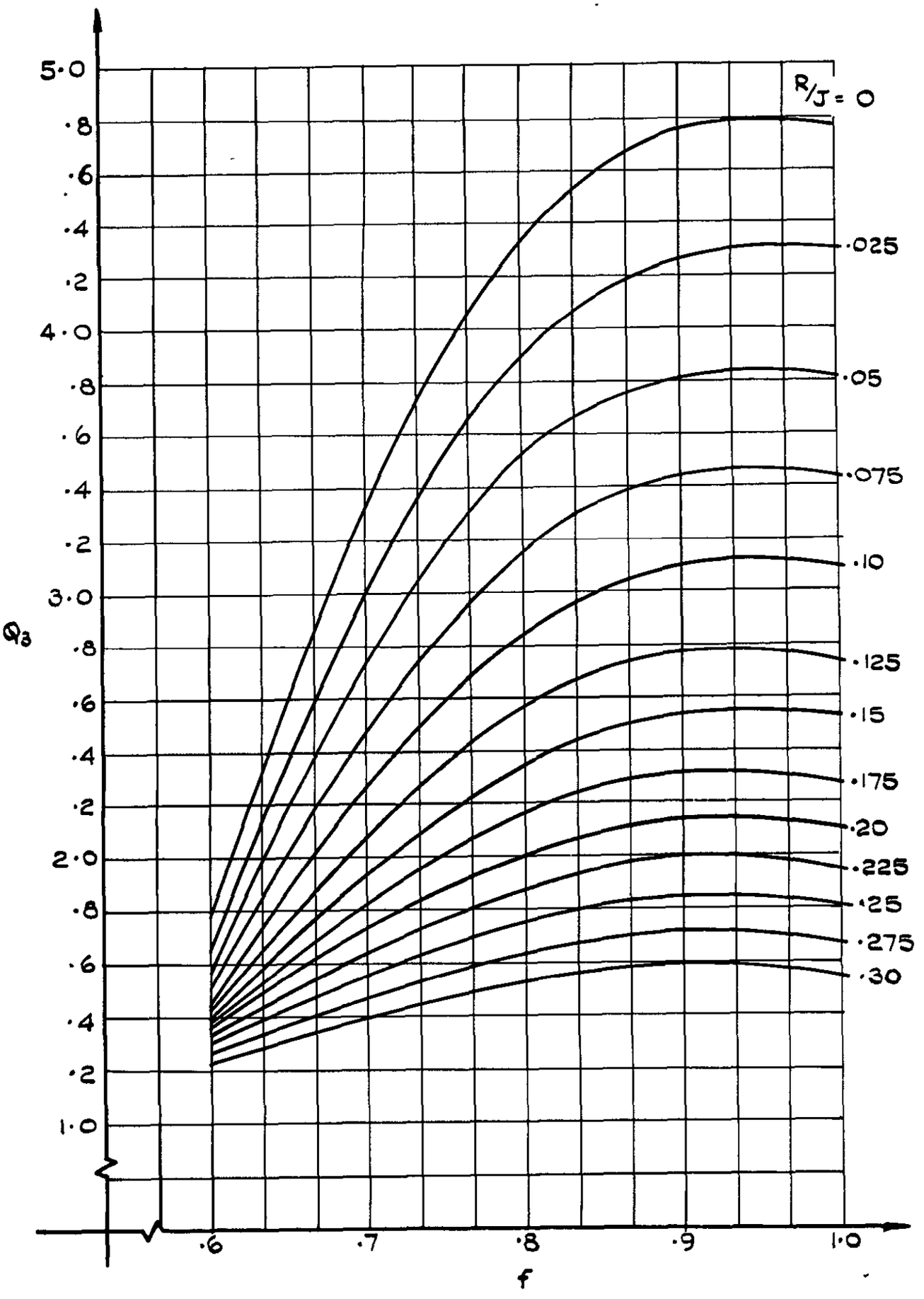

FIG. 2. RESPONSE FACTOR = $Q_r = (-1)^{r+1} \frac{J^2}{\delta n} \left(\frac{\beta m}{\zeta_e}\right)_r$:- r = 3

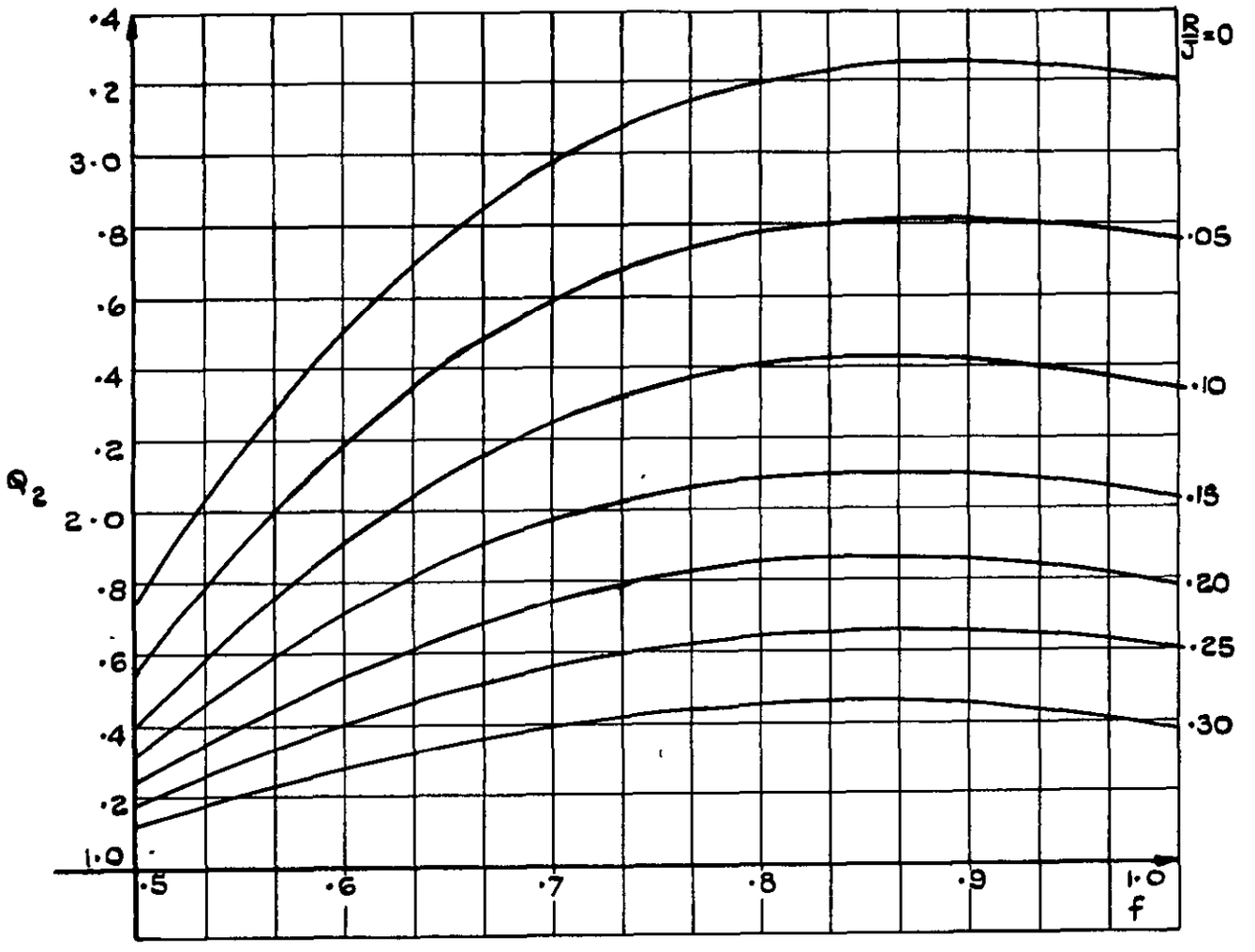

FIG. 3. RESPONSE FACTOR

$$Q_r = (-1)^{r+1} \frac{J^2}{\delta n} \left(\frac{\beta_m}{\zeta_e}\right)_r \quad :- \; r = 2$$

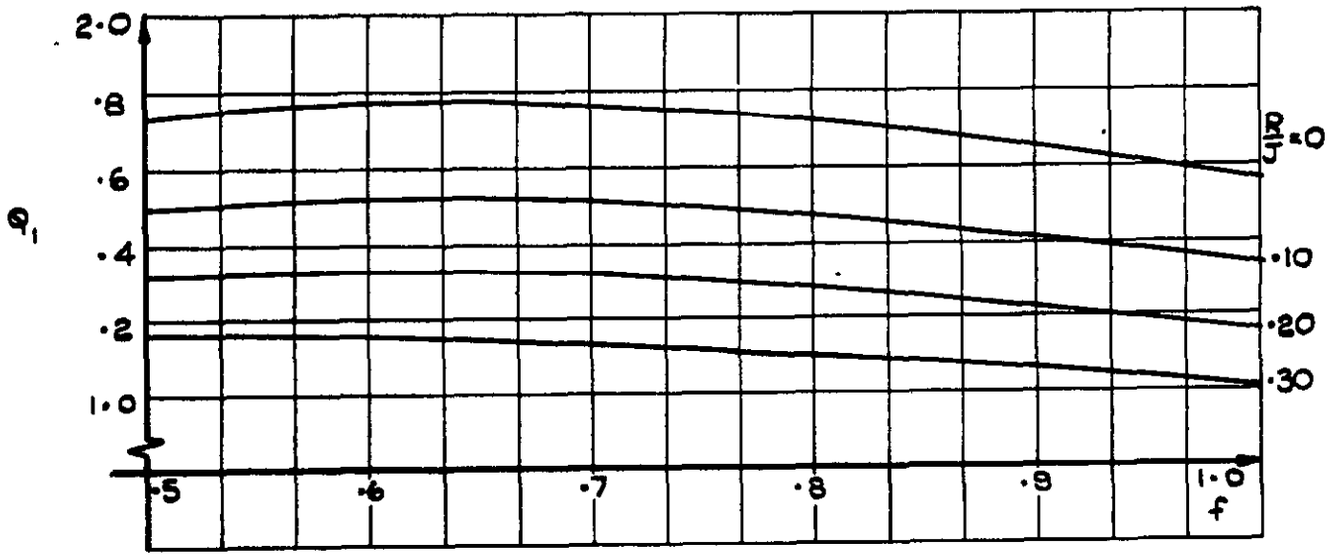

FIG. 4. RESPONSE FACTOR

$$Q_r = (-1)^{r+1} \frac{J^2}{\delta n} \left(\frac{\beta_m}{\zeta_e}\right)_r \quad :- \; r = 1$$

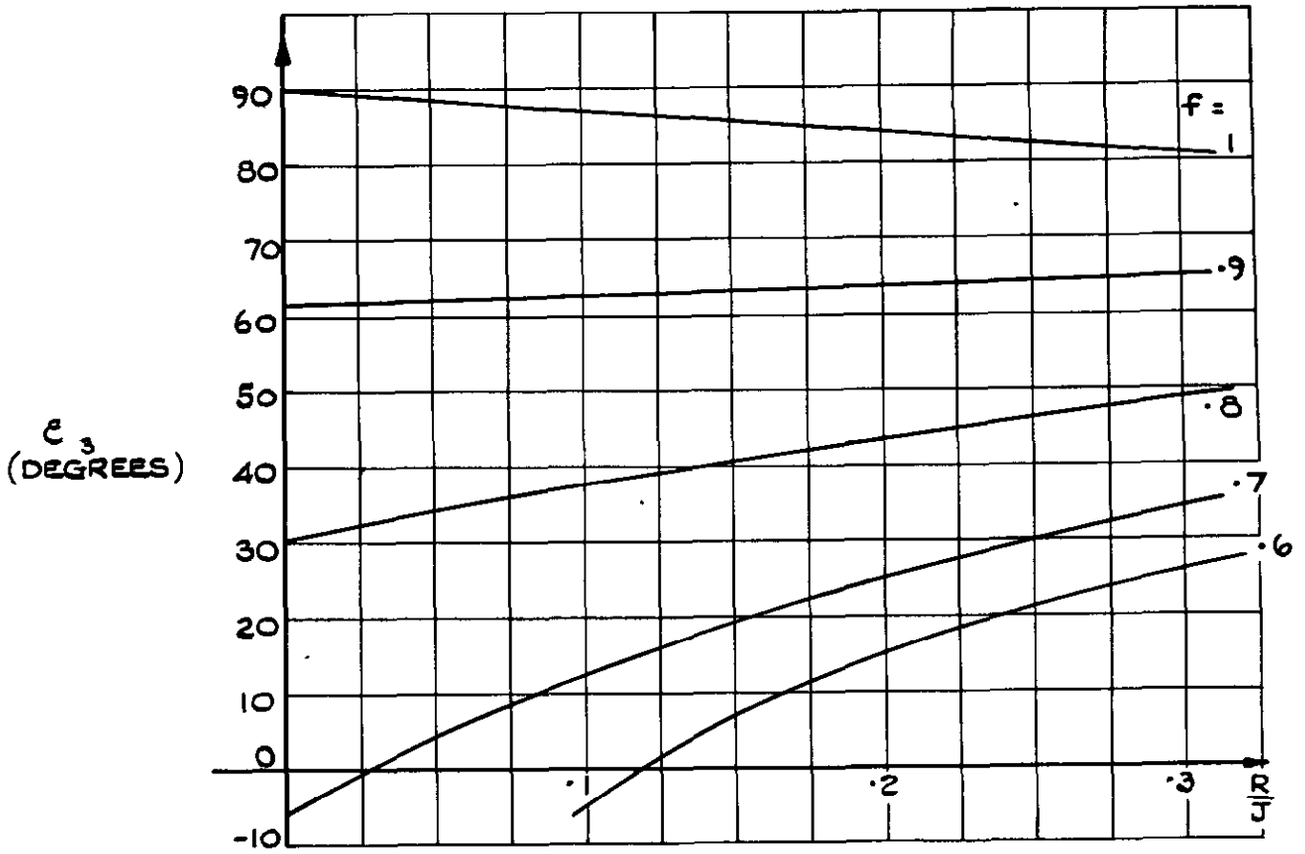

FIG. 5 PHASE ANGLE ε_r, $r = 3$

(APP. I § A3)

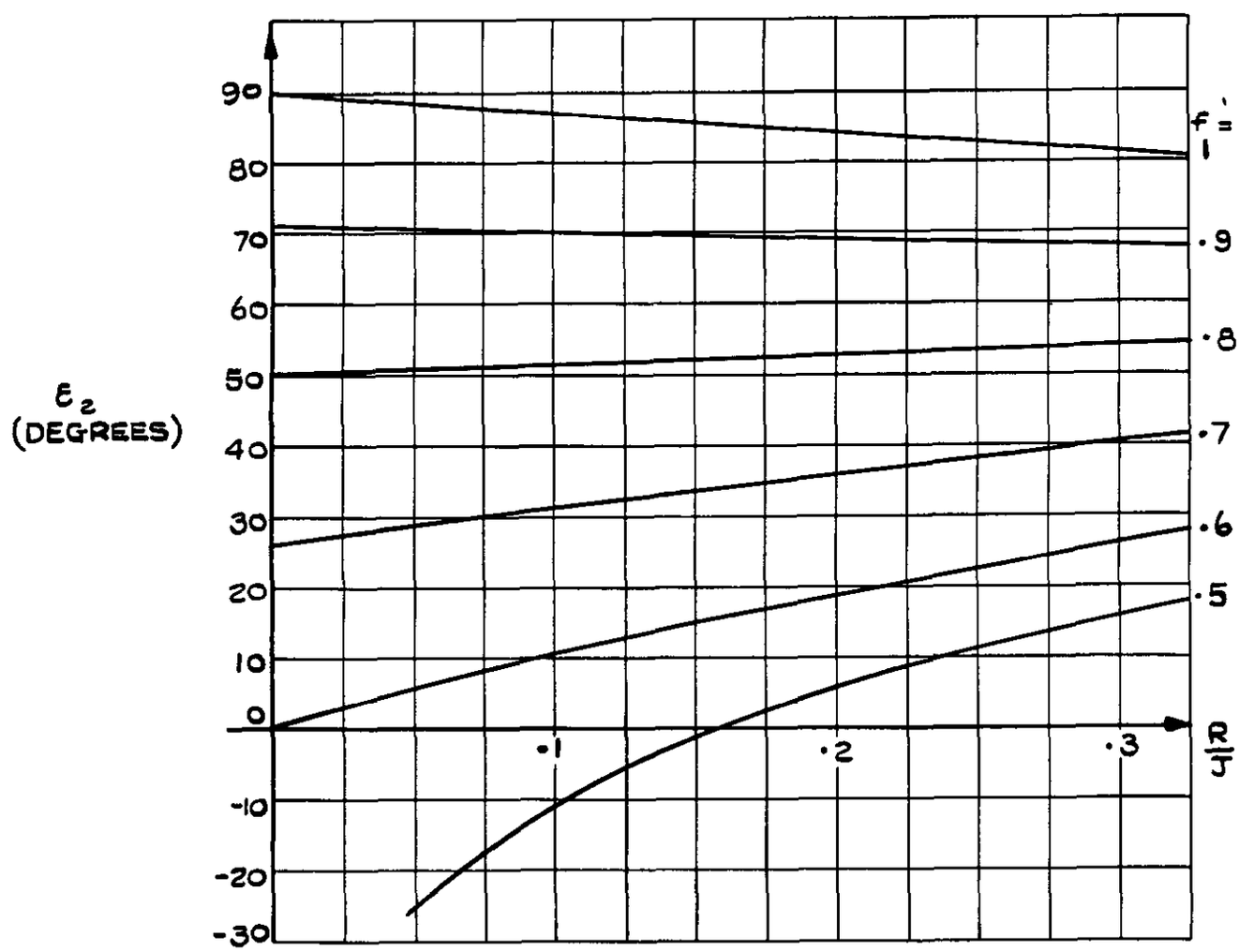

FIG. 6 PHASE ANGLE ε_r, $r = 2$

(APP. I § A3)

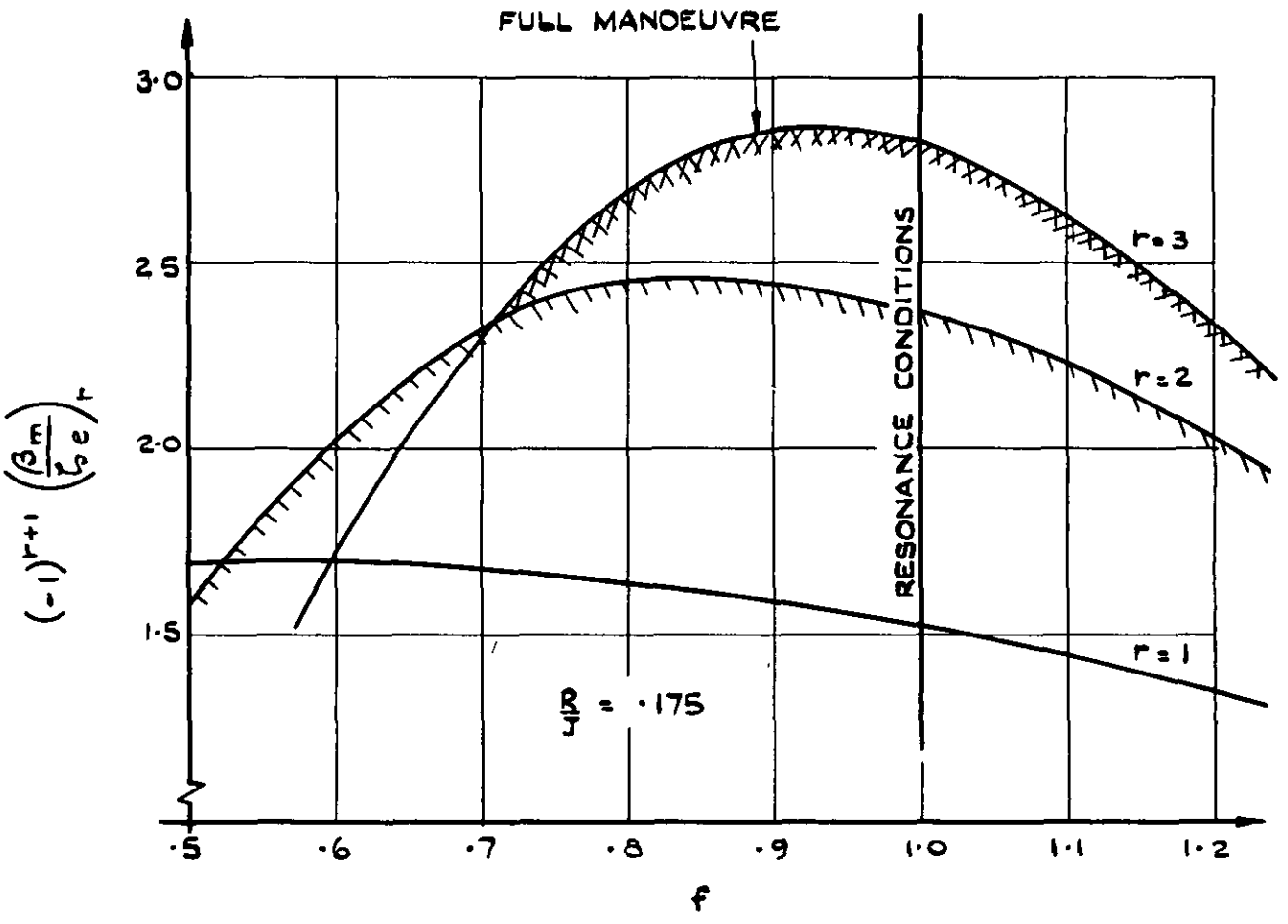

FIG. 8. AN EXAMPLE OF THE EFFECT OF f ON THE βm PER UNIT AMPLITUDE OF RUDDER MOVEMENT. DATA — TABLE I.

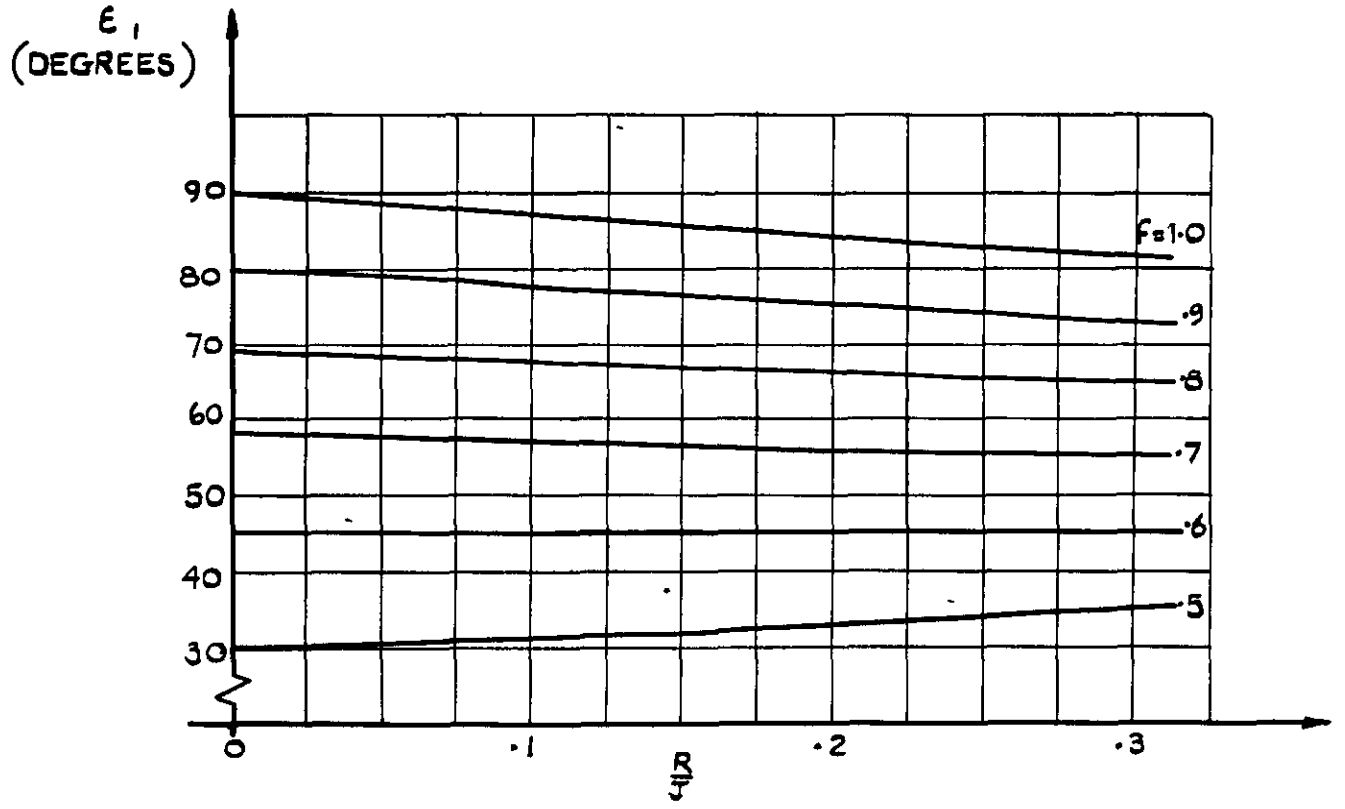

FIG. 7. PHASE ANGLE ε_r, r = 1
(APP. I. § A 3)

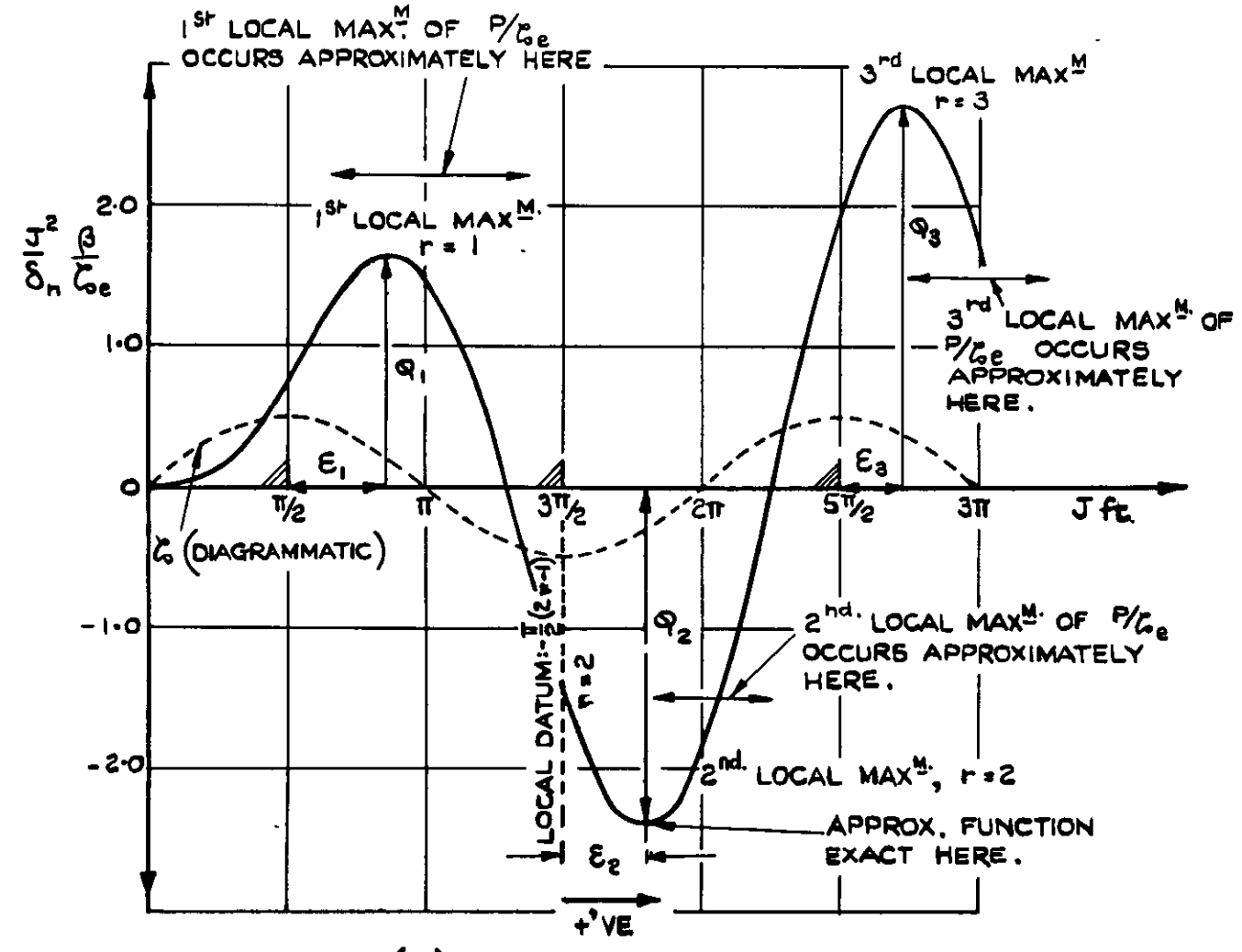

(a) FIN-AND-RUDDER LOADS.

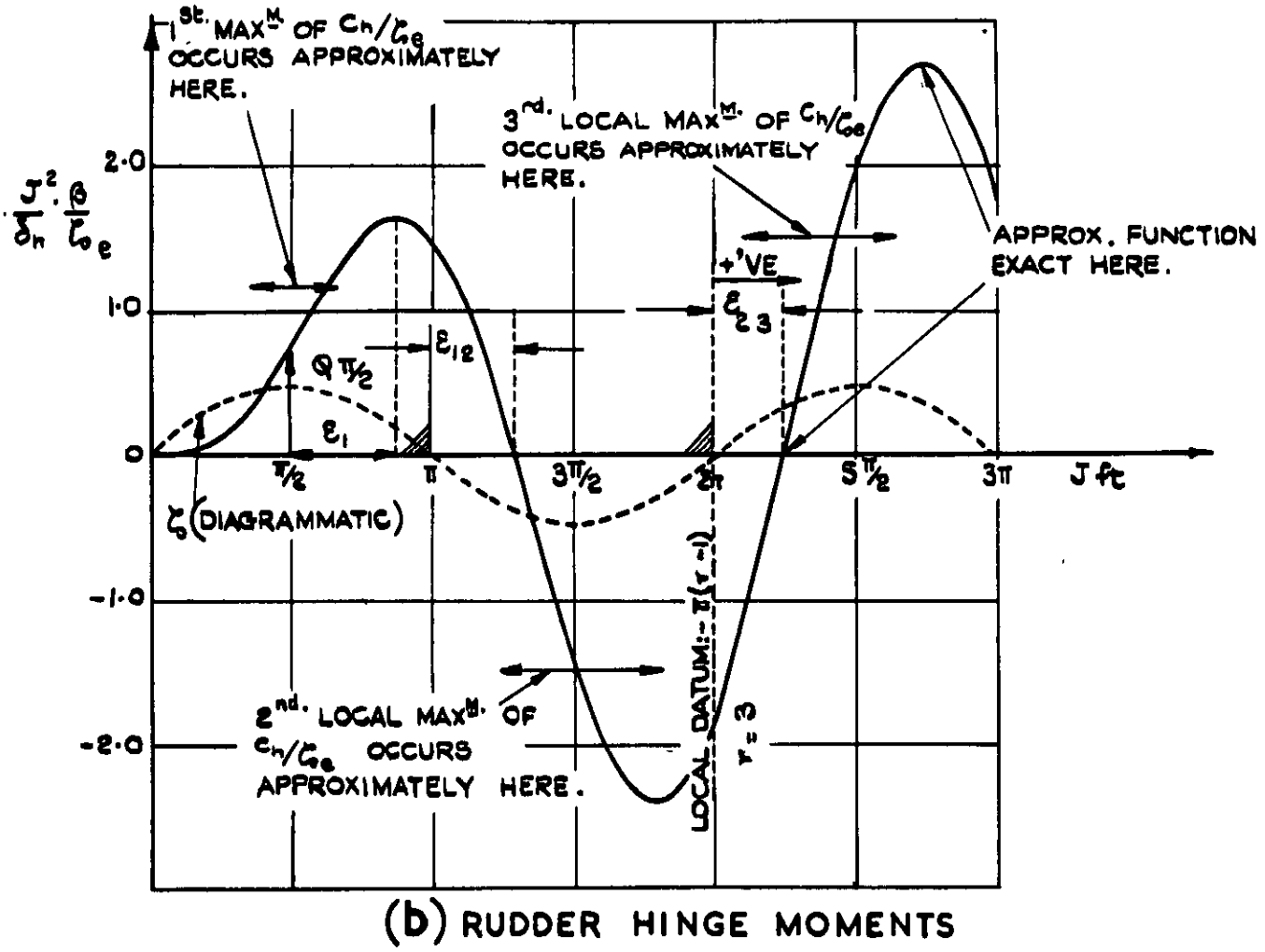

(b) RUDDER HINGE MOMENTS

FIG. 9(a & b) NOTATION AND SIGN CONVENTION USED IN THE DERIVATION OF THE APPROX. FORMULAE IN APPENDIX I.

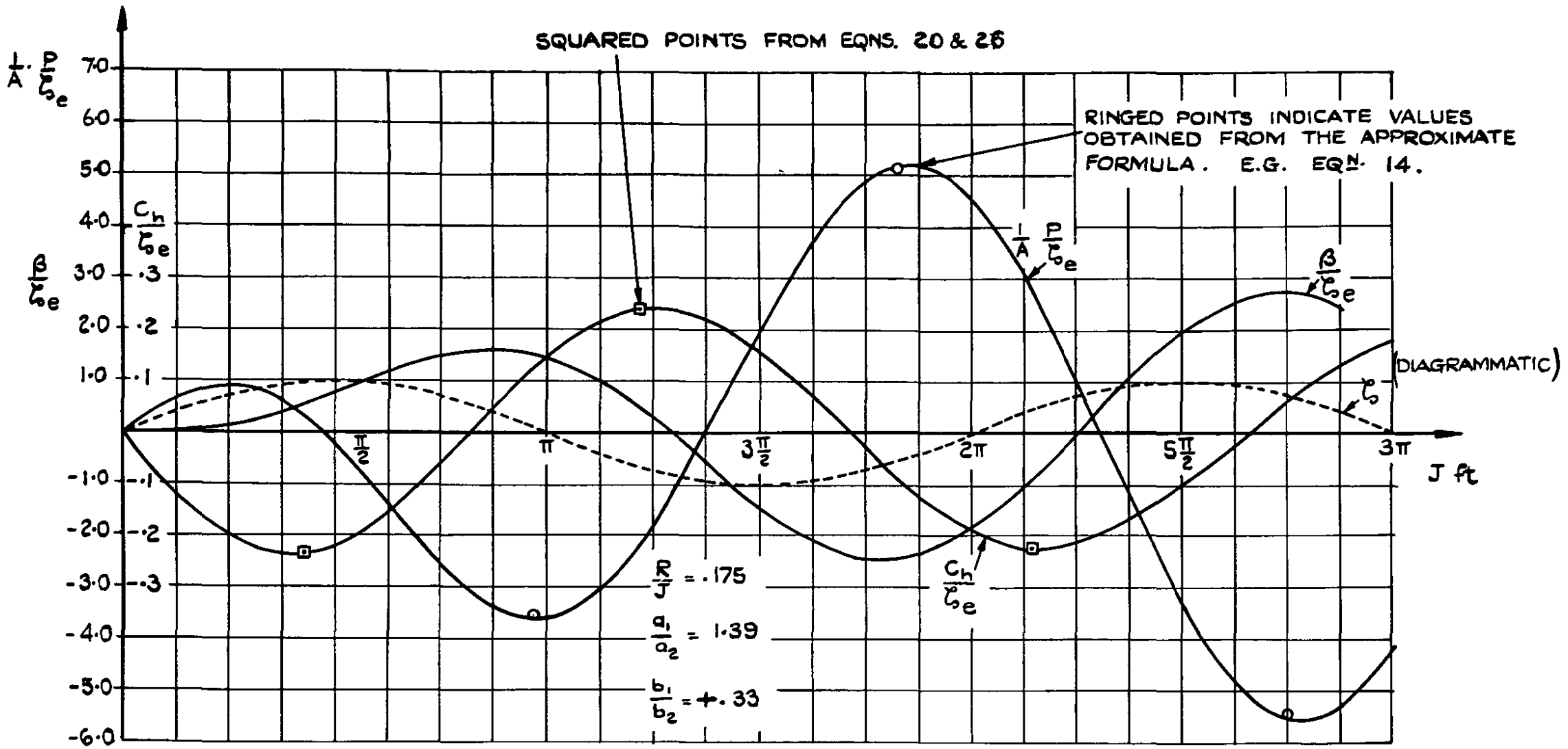

FIG. 10. TIME HISTORIES OF THE ANGLE OF SIDESLIP, FIN-AND-RUDDER LOAD & RUDDER HINGE MOMENT DUE TO SINUSOIDAL MOVEMENT OF THE RUDDER AT A PARTICULAR FREQUENCY :- f = 0.80 DATA IN TABLE I.

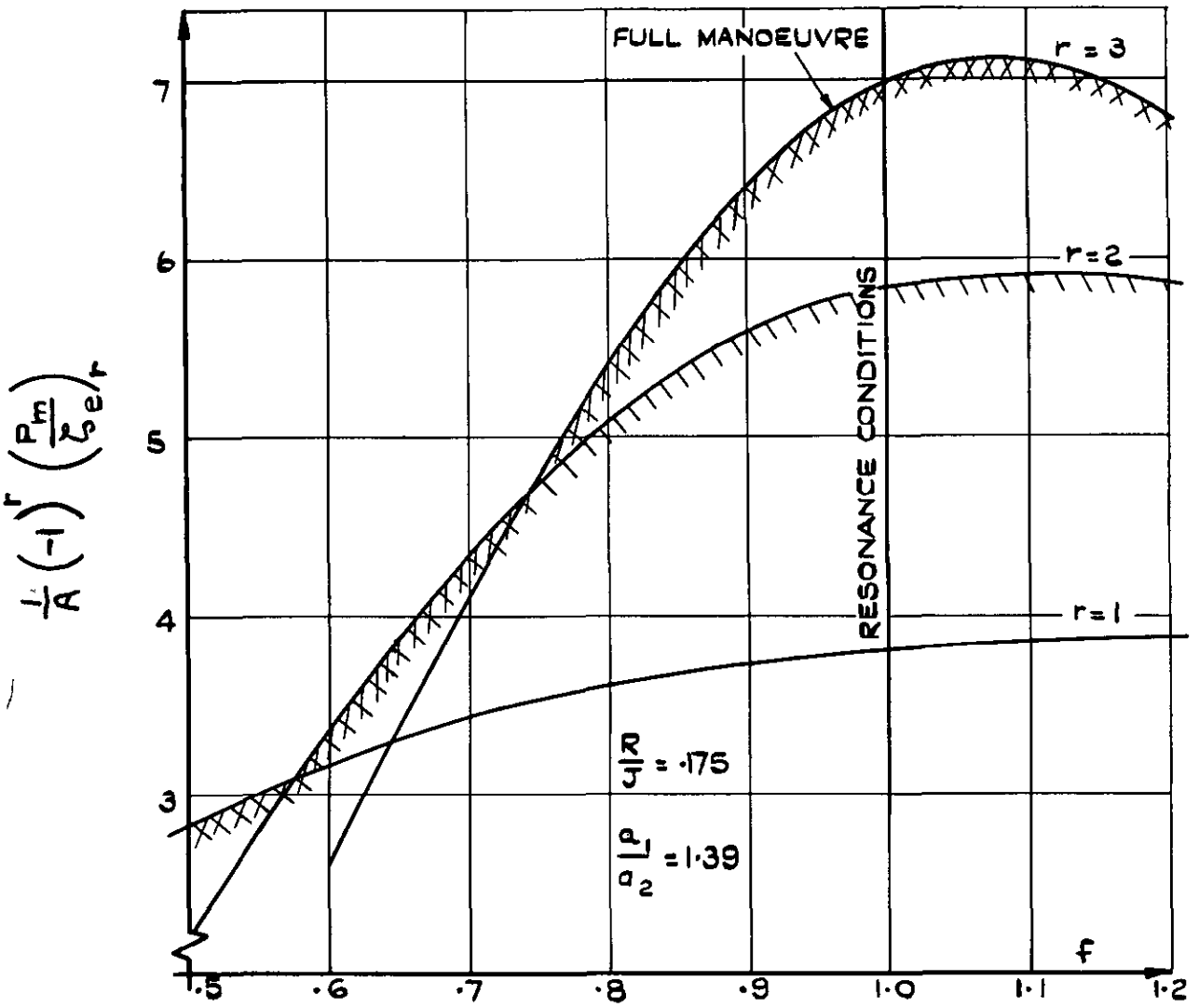

FIG. 11. AN EXAMPLE OF THE EFFECT OF f ON THE Pm PER UNIT AMPLITUDE OF RUDDER MOVEMENT. DATA - TABLE I.

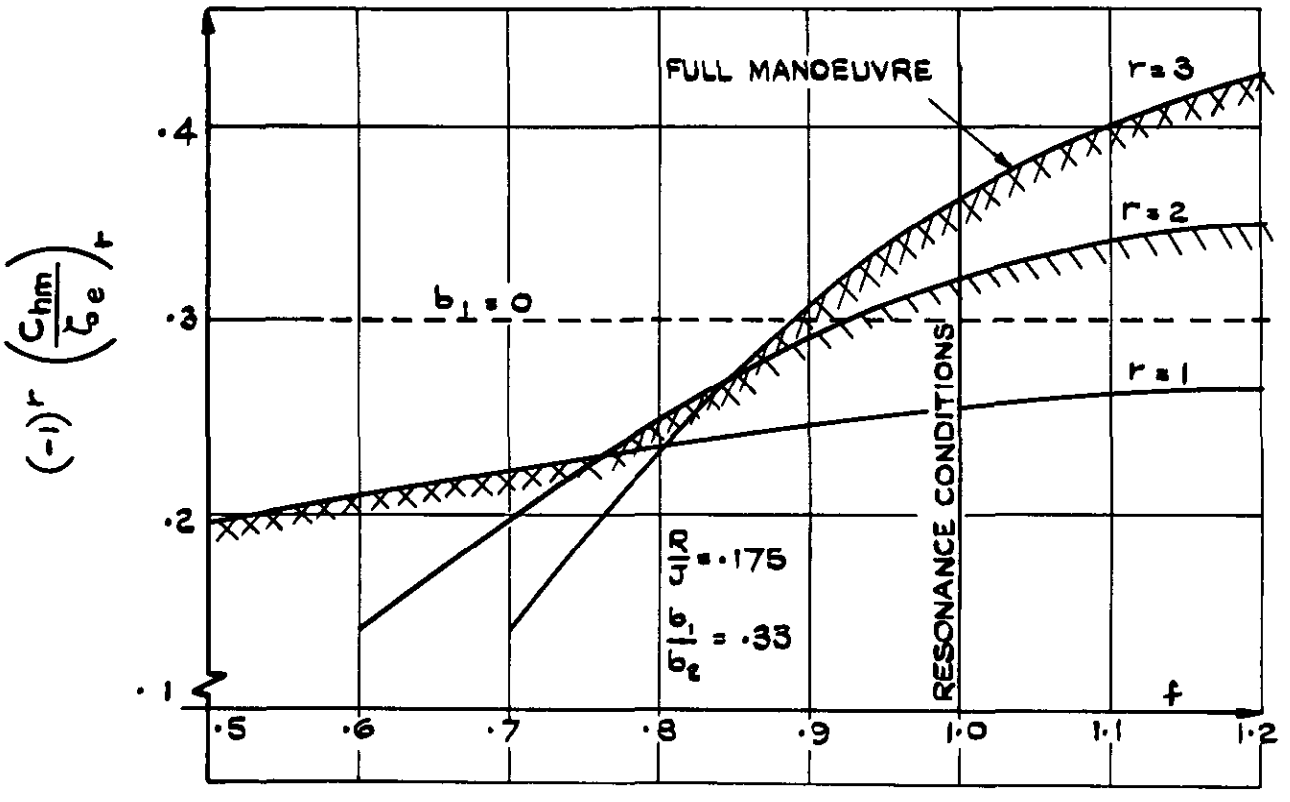

FIG. 12. AN EXAMPLE OF THE EFFECT OF f ON THE CHm PER UNIT AMPLITUDE OF RUDDER MOVEMENT. DATA - TABLE I.

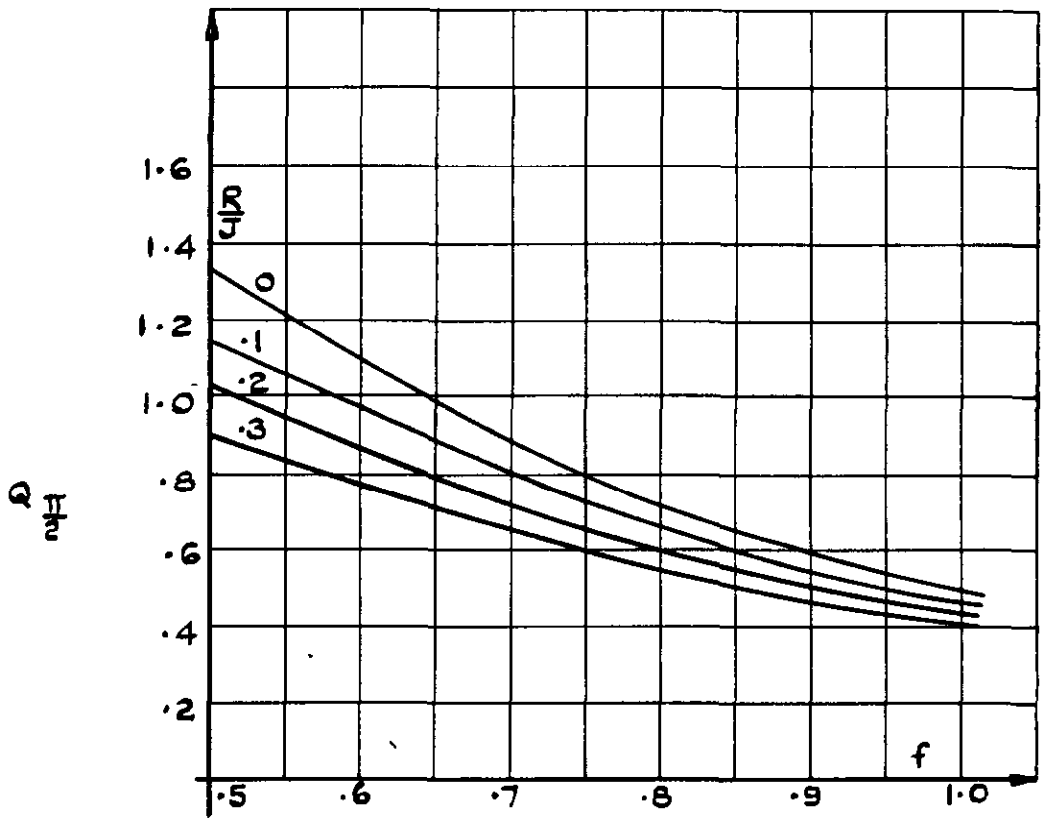

FIG. 13. RESPONSE FACTOR

$$Q_{\frac{\pi}{2}} = \frac{J^2}{\delta n}\left(\frac{\beta}{\zeta_e}\right) \quad J f \tau = \frac{\pi}{2}$$

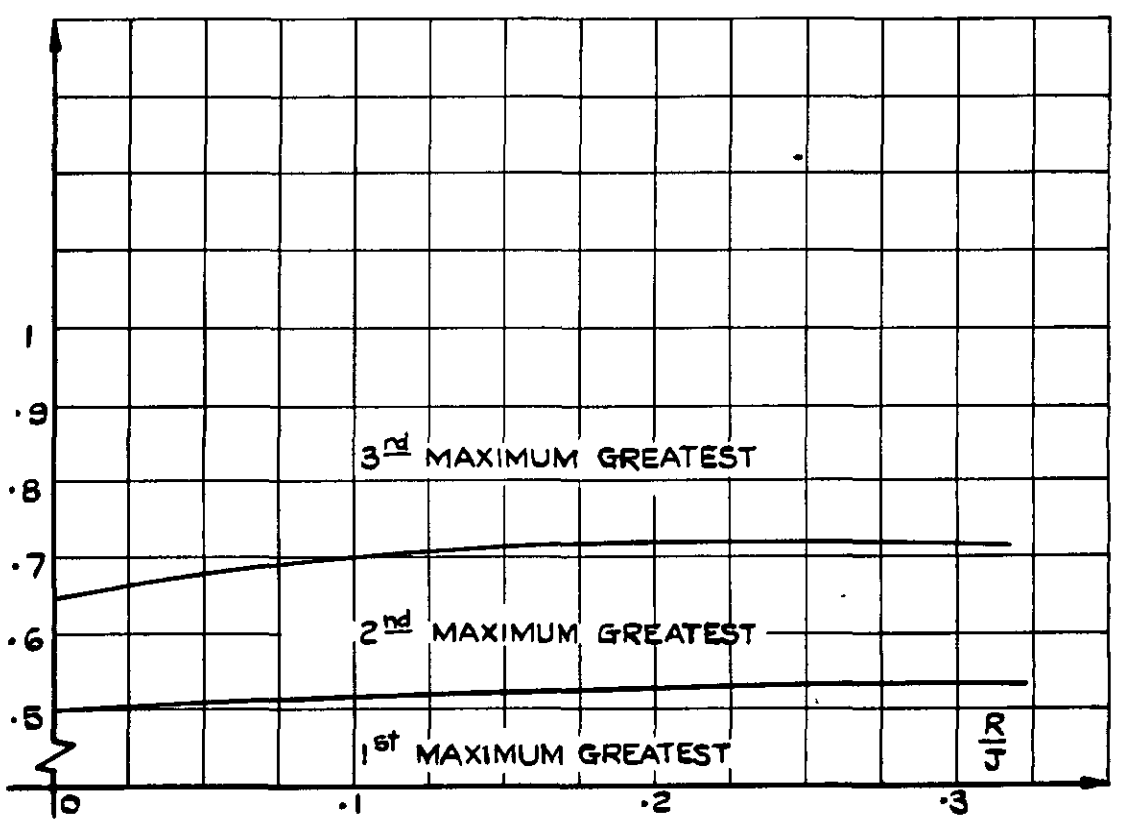

FIG. 14. VALUES OF f FOR WHICH 1st & 2nd & 2nd & 3rd LOCAL MAXIMA OF THE RESPONSE IN β ARE NUMERICALLY EQUAL.

$\varepsilon_{1,2}$.

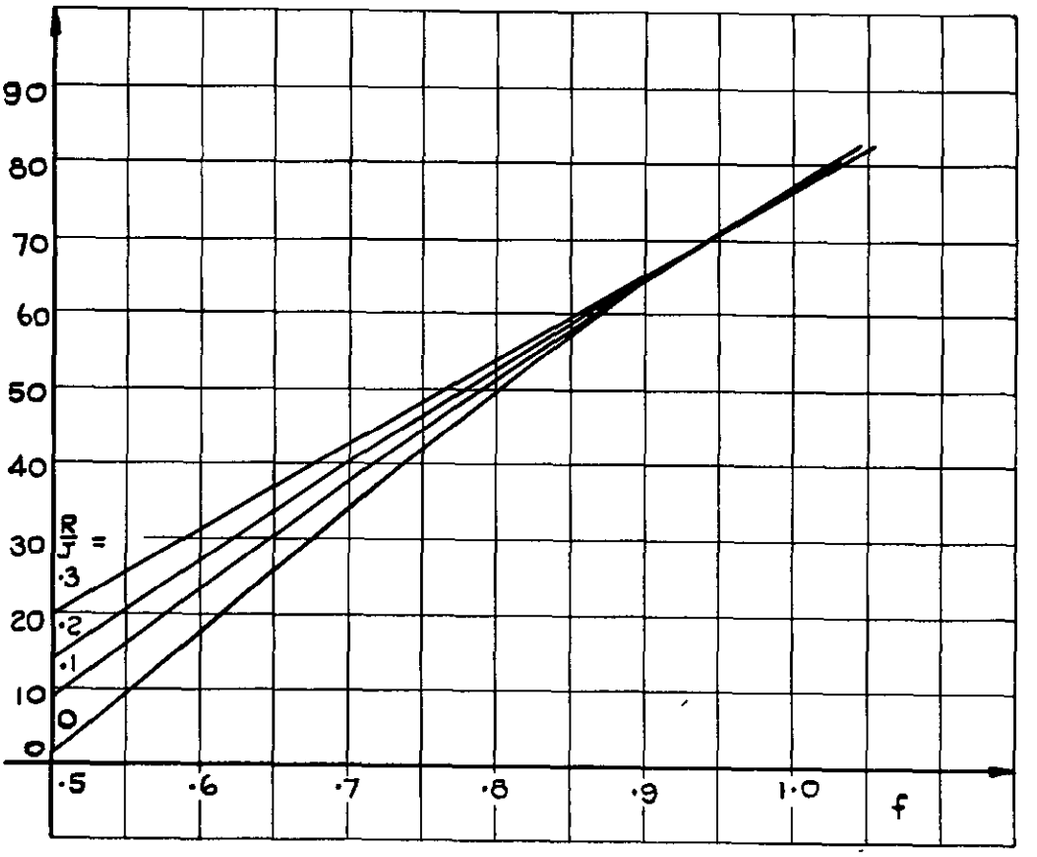

FIG. 15. PHASE ANGLE $\varepsilon_{r-1,\,r,\,r=2}$
(APP. § A5)

$\varepsilon_{2,3}$

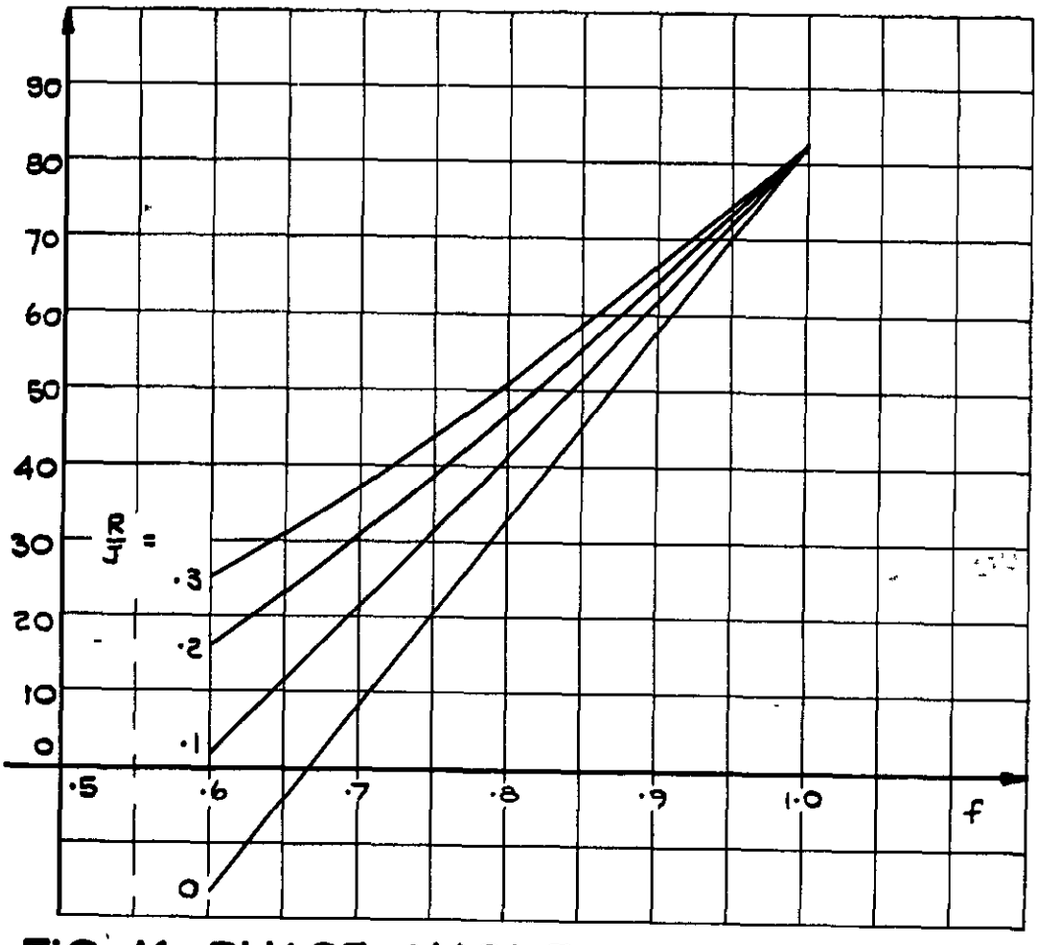

FIG. 16. PHASE ANGLE $\varepsilon_{r-1,\,r,\,r=3}$
(APP. § A5)

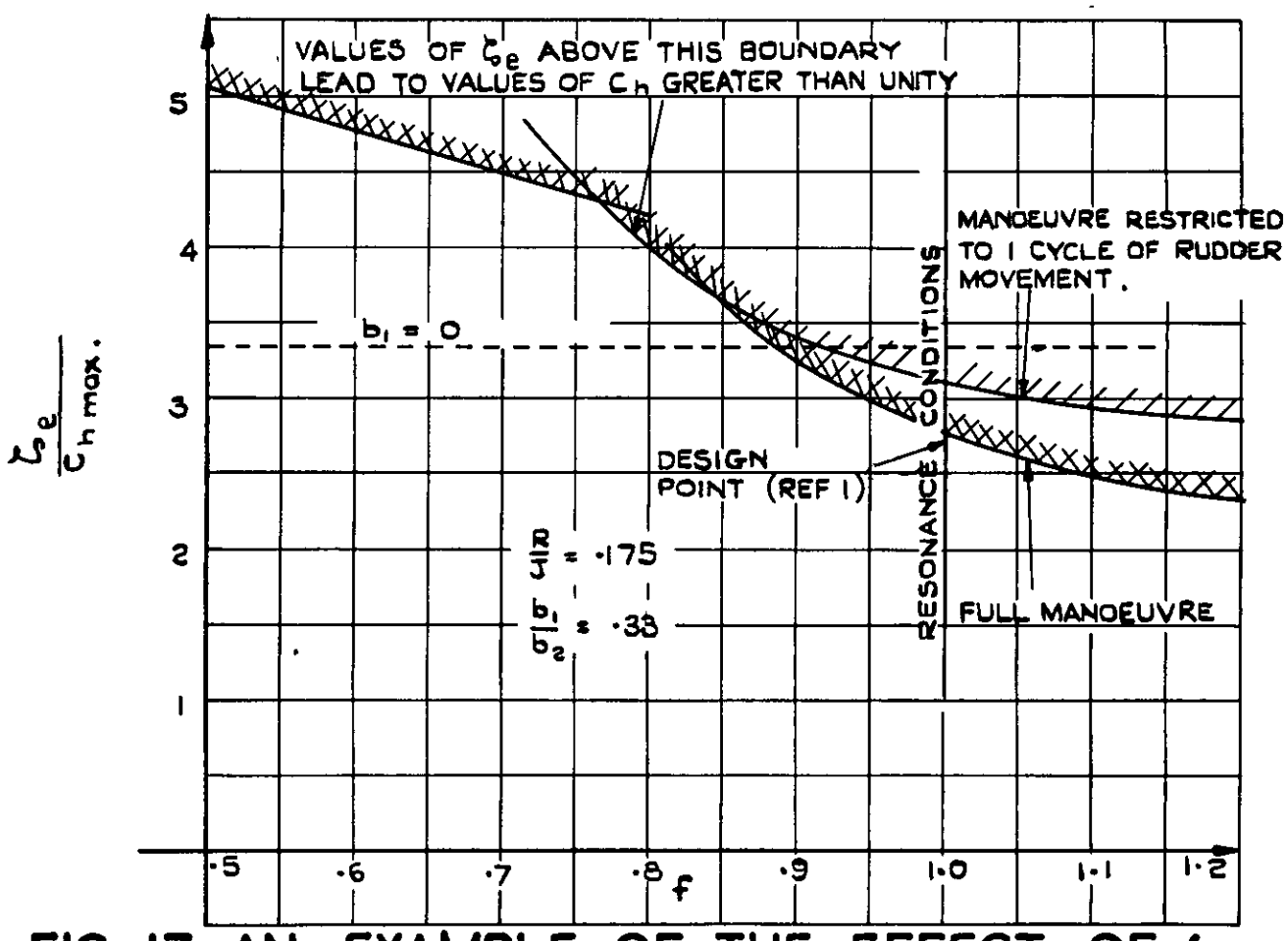

FIG. 17. AN EXAMPLE OF THE EFFECT OF f ON THE VALUE OF ζ_e REQUIRED TO REACH UNIT MAXIMUM C_h IN THE MANOEUVRE. DATA :— TABLE I.

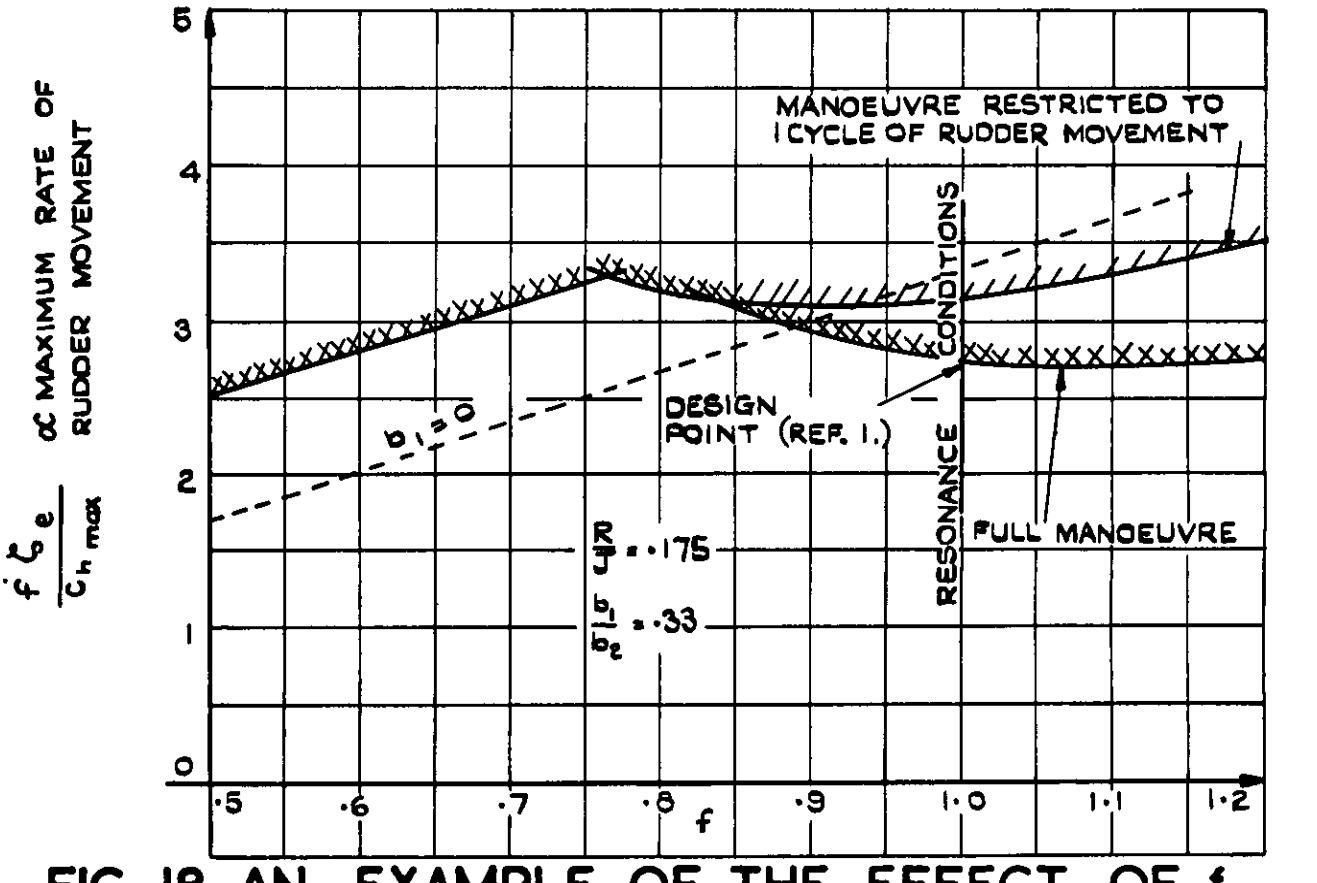

FIG. 18. AN EXAMPLE OF THE EFFECT OF f ON THE MAXIMUM (INITIAL) RATE OF RUDDER MOVEMENT ASSOCIATED WITH UNIT MAXIMUM C_h. DATA :— TABLE I.

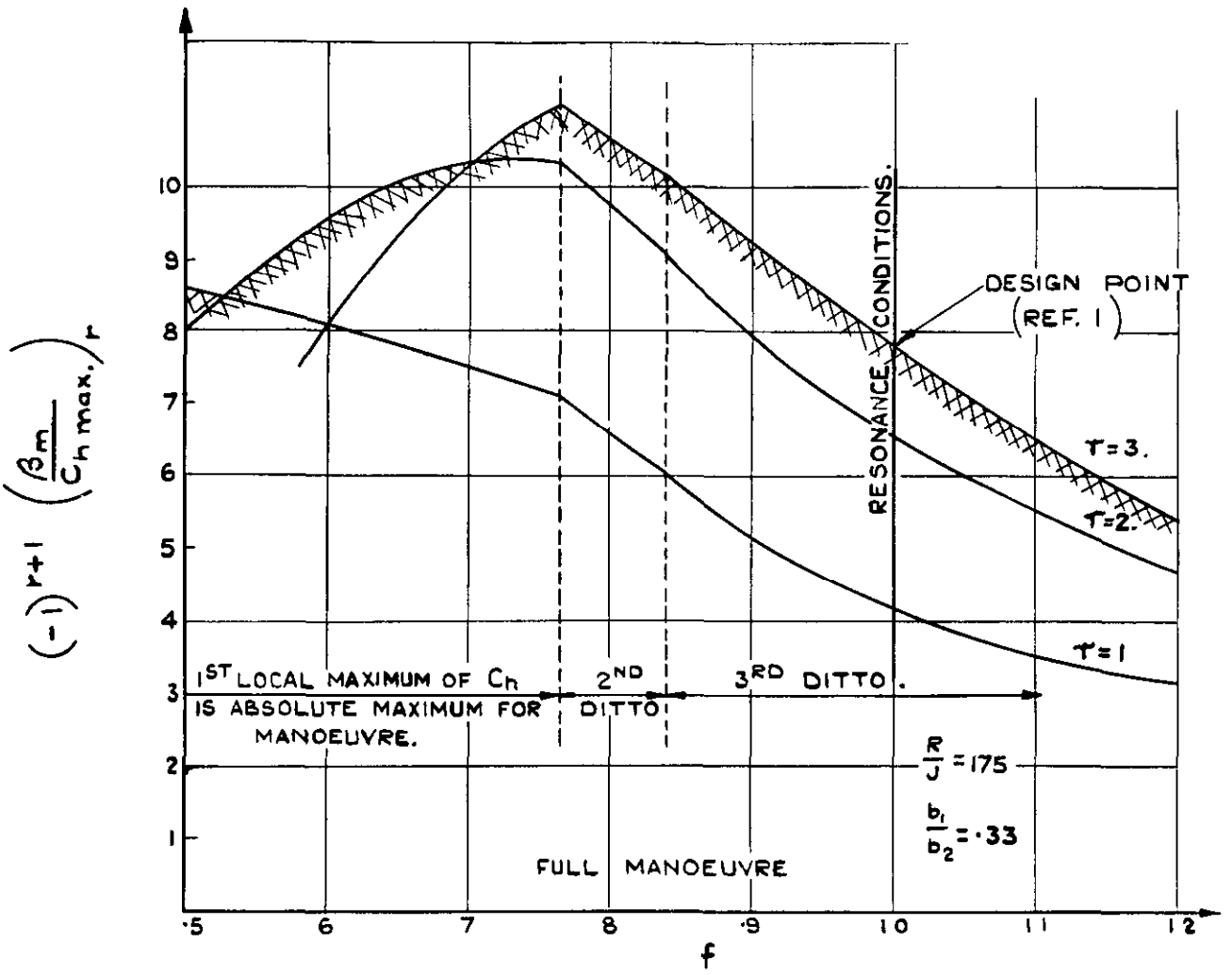

FIG. 19 AN EXAMPLE OF THE EFFECT OF f ON THE β_m PER UNIT MAXIMUM C_h, DATA IN TABLE I.

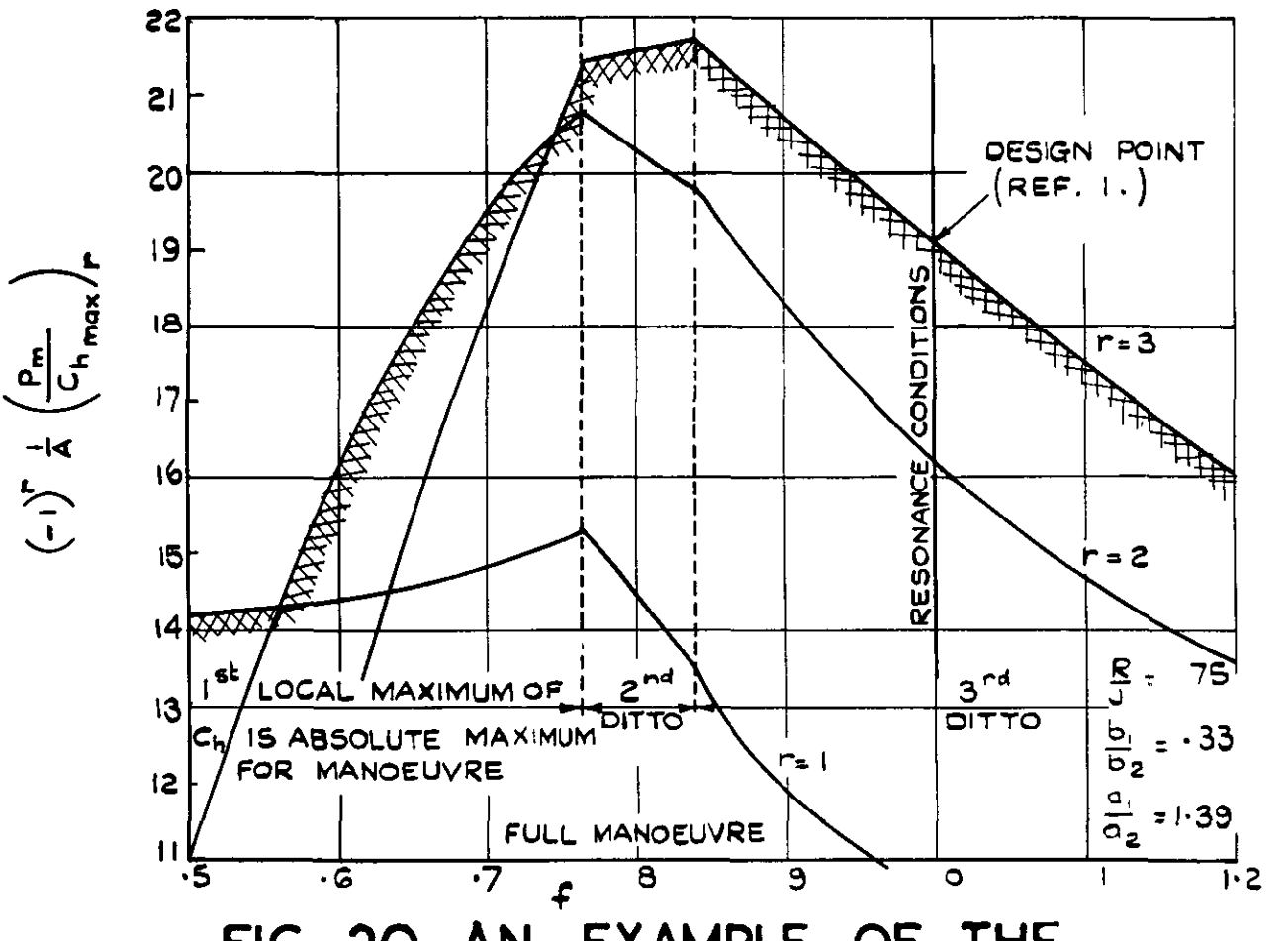

FIG. 20 AN EXAMPLE OF THE EFFECT OF f ON THE P_m PER UNIT MAXIMUM C_h, DATA IN TABLE I.

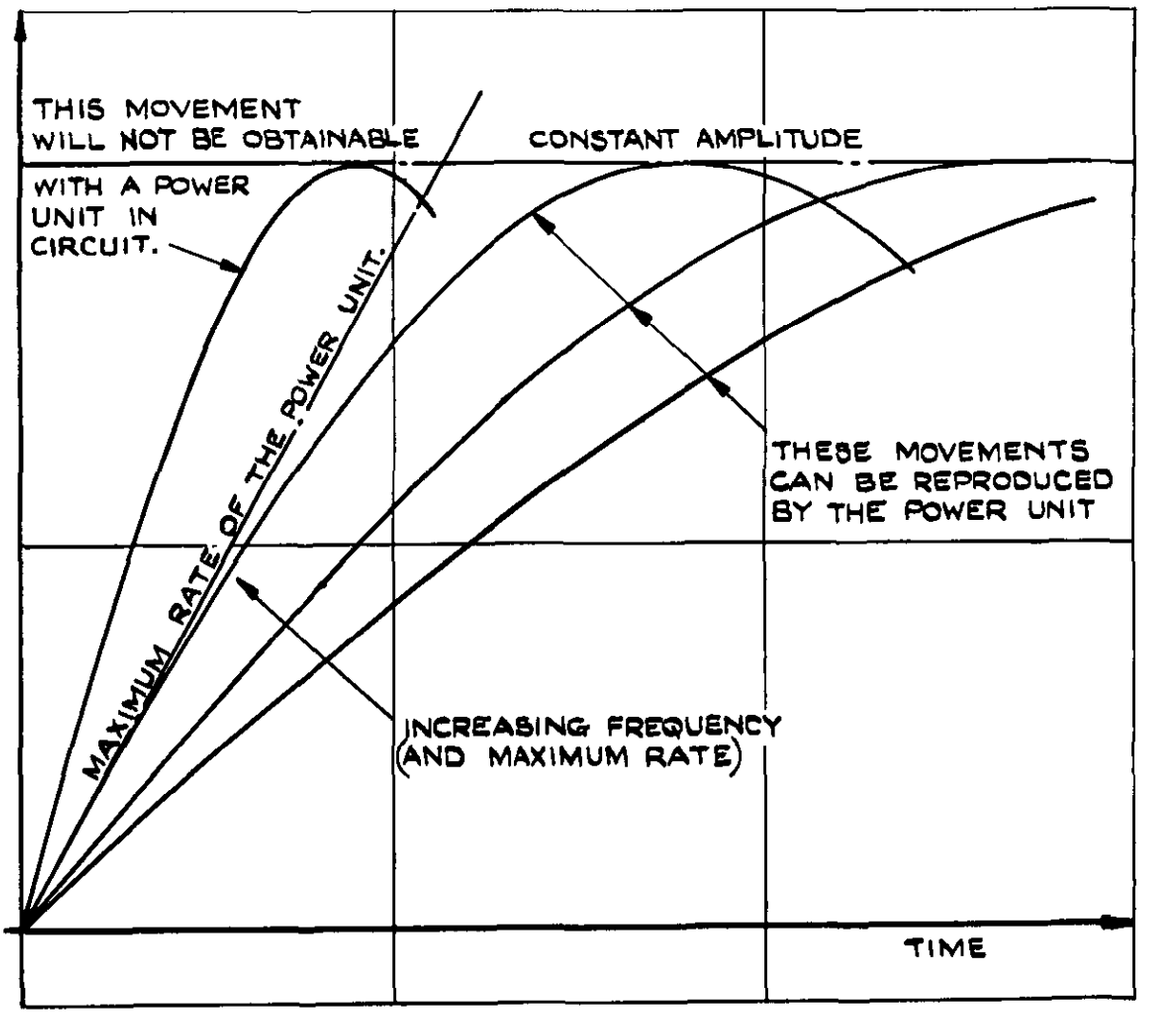

FIG. 21. EFFECT OF FREQUENCY ON THE MAXIMUM RATE OF MOVEMENT.

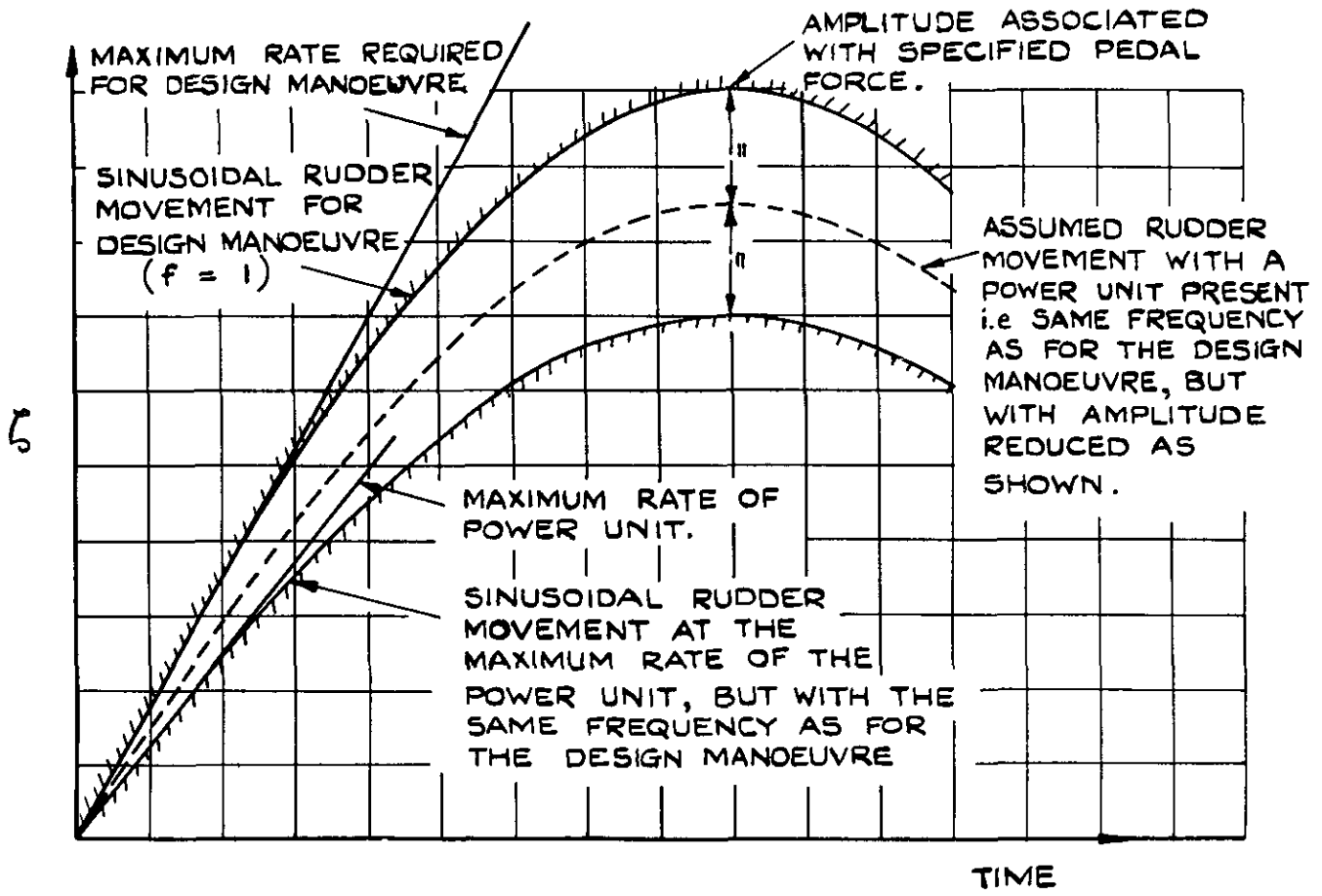

(a)

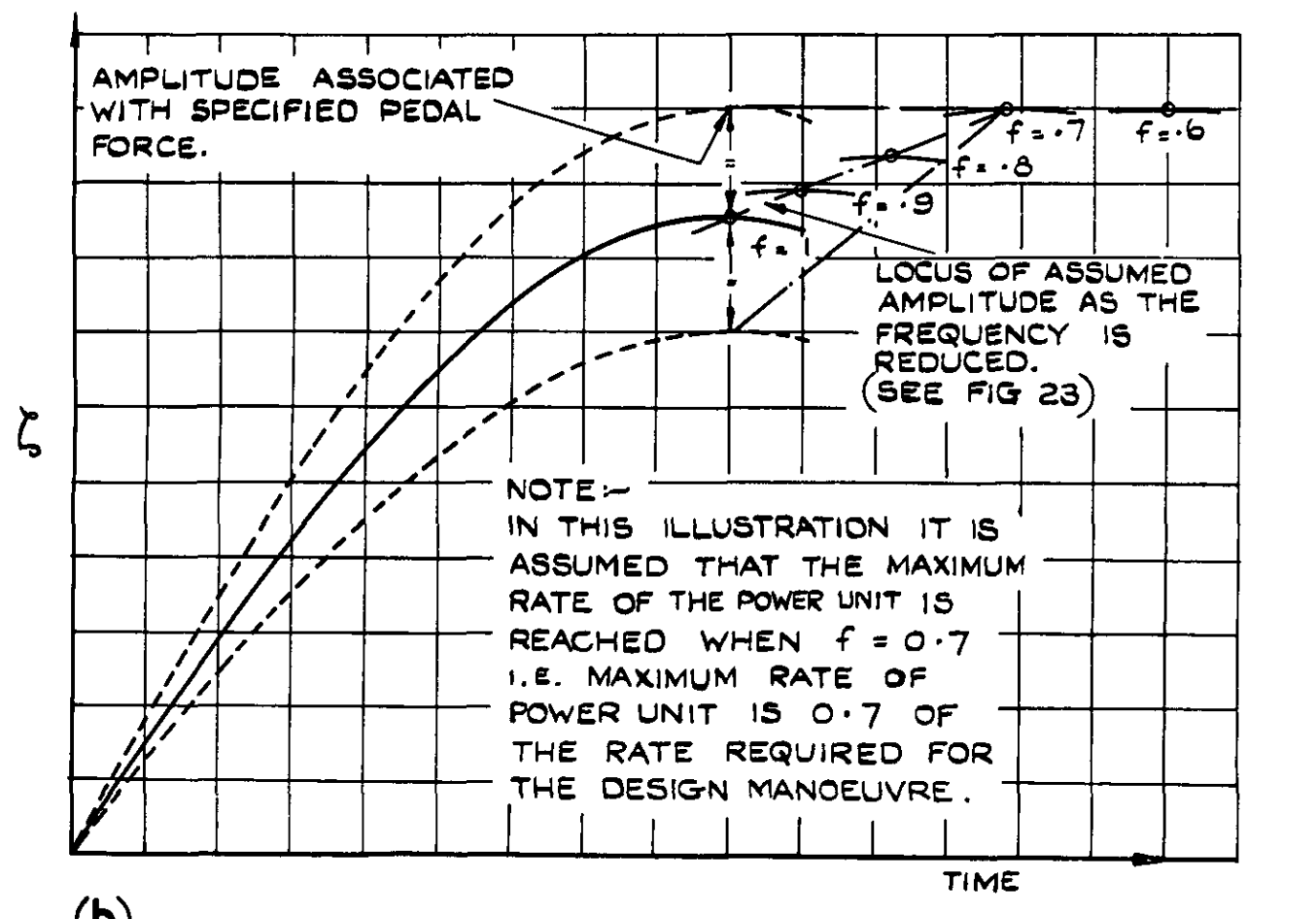

(b)

FIG. 22 (a & b) ASSUMED EFFECT OF A POWER UNIT ON THE RUDDER MOVEMENT WHEN AN ATTEMPT IS MADE TO EXECUTE THE DESIGN MANOEUVRE f = 1. AND ON THE MOVEMENT AT LOWER FREQUENCIES.

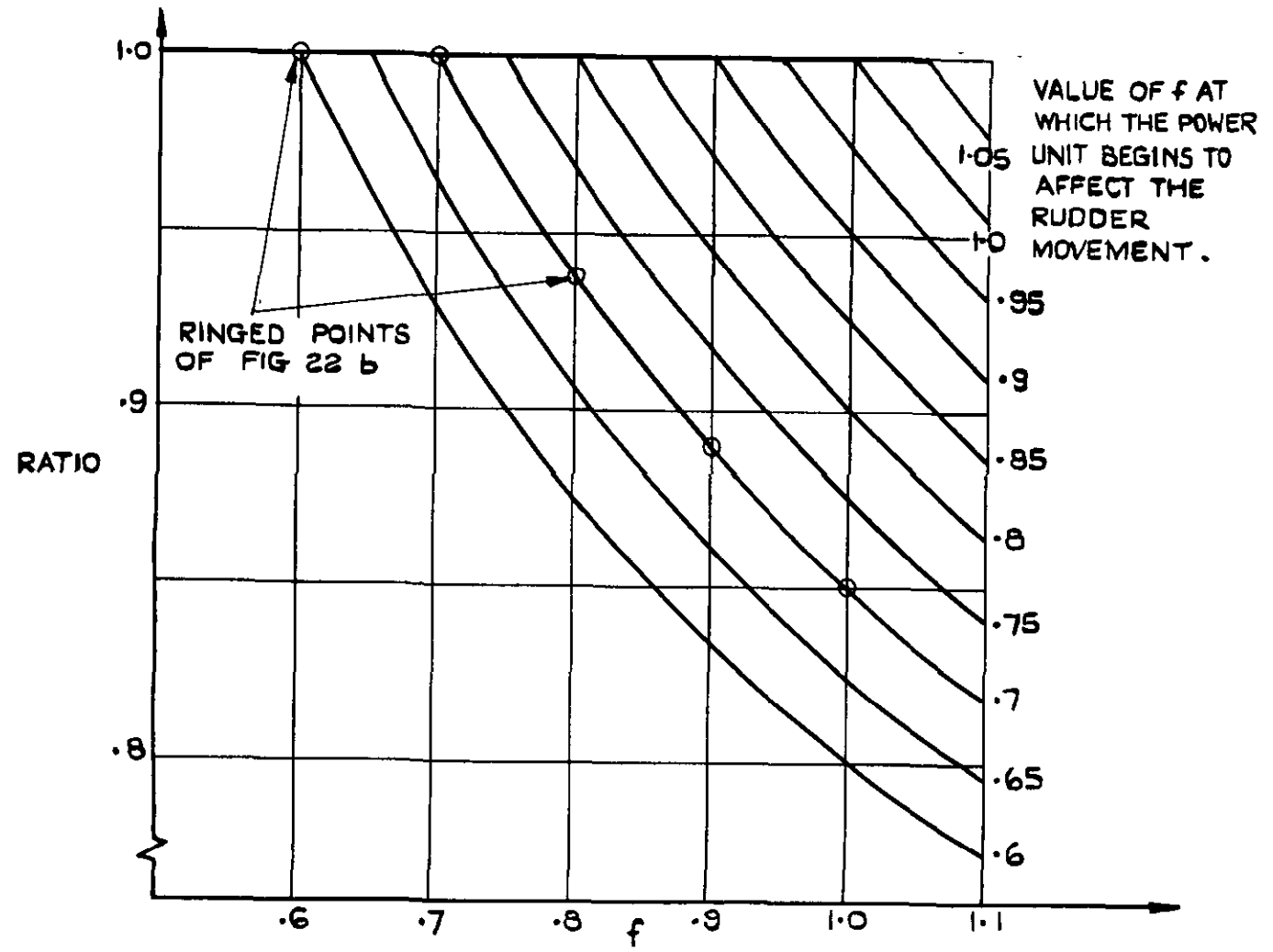

FIG. 23. RATIO $\frac{\text{AMPLITUDE OF ASSUMED RUDDER MOVEMENT — POWER UNIT PRESENT}}{\text{AMPLITUDE OF RUDDER MOVEMENT — POWER UNIT ABSENT}}$

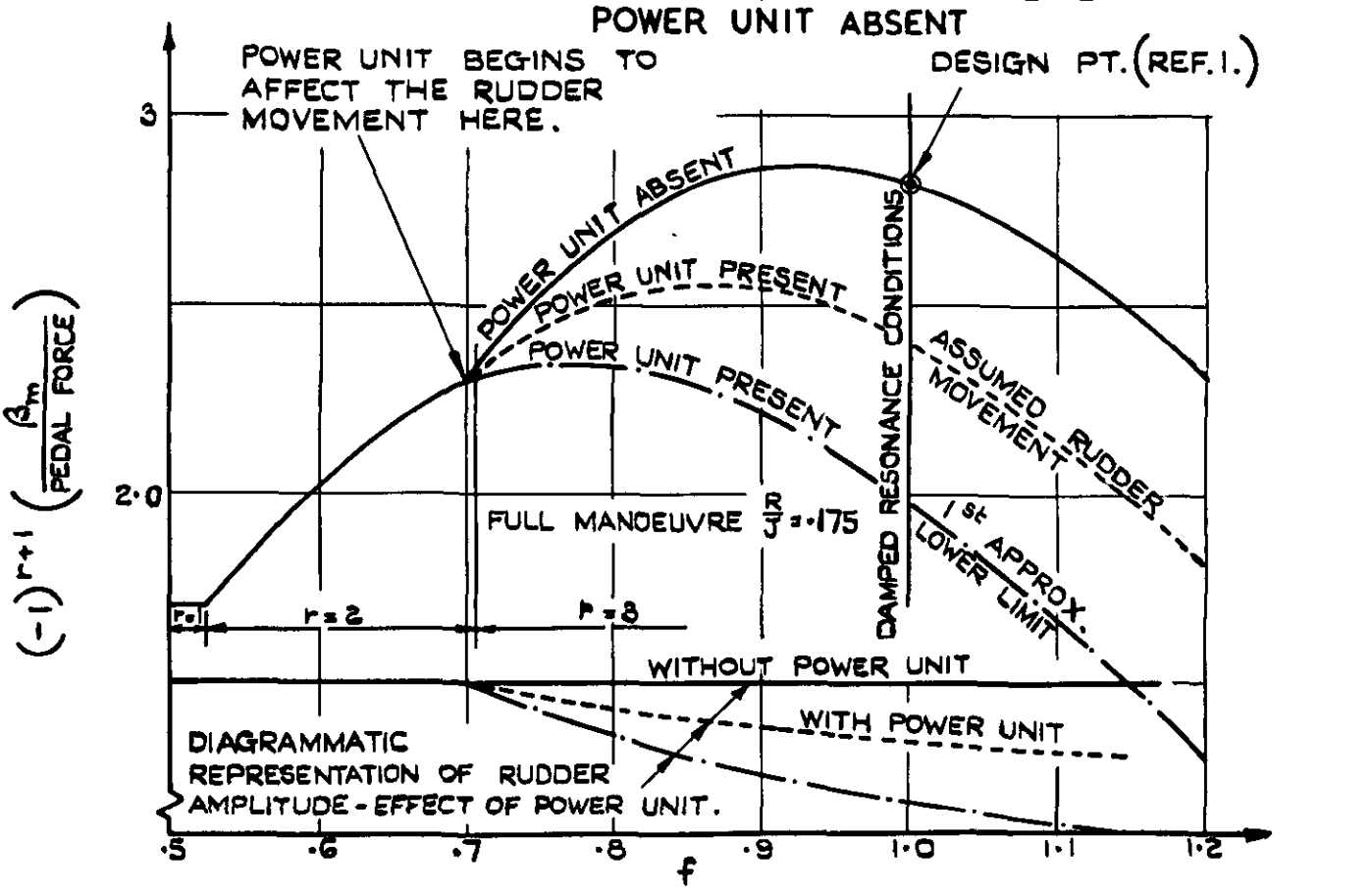

FIG. 24. EXAMPLE SHOWING EFFECT OF POWER UNIT ON THE β_m AT VARIOUS VALUES OF f. EXAMPLE DATA IN TABLE I.

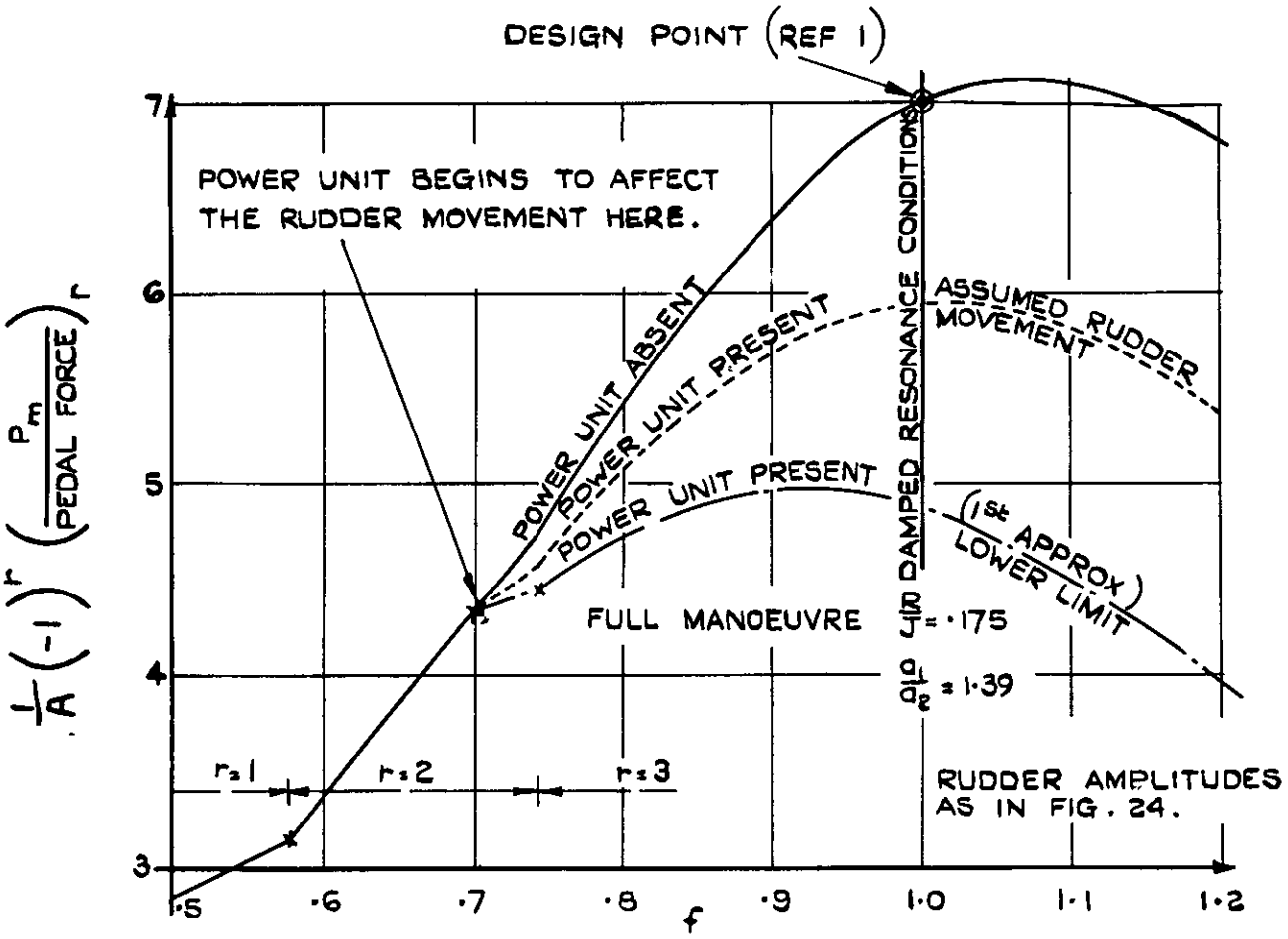

FIG. 25. EXAMPLE SHOWING EFFECT OF POWER UNIT ON THE P_m AT VARIOUS VALUES OF f. EXAMPLE DATA IN TABLE I.

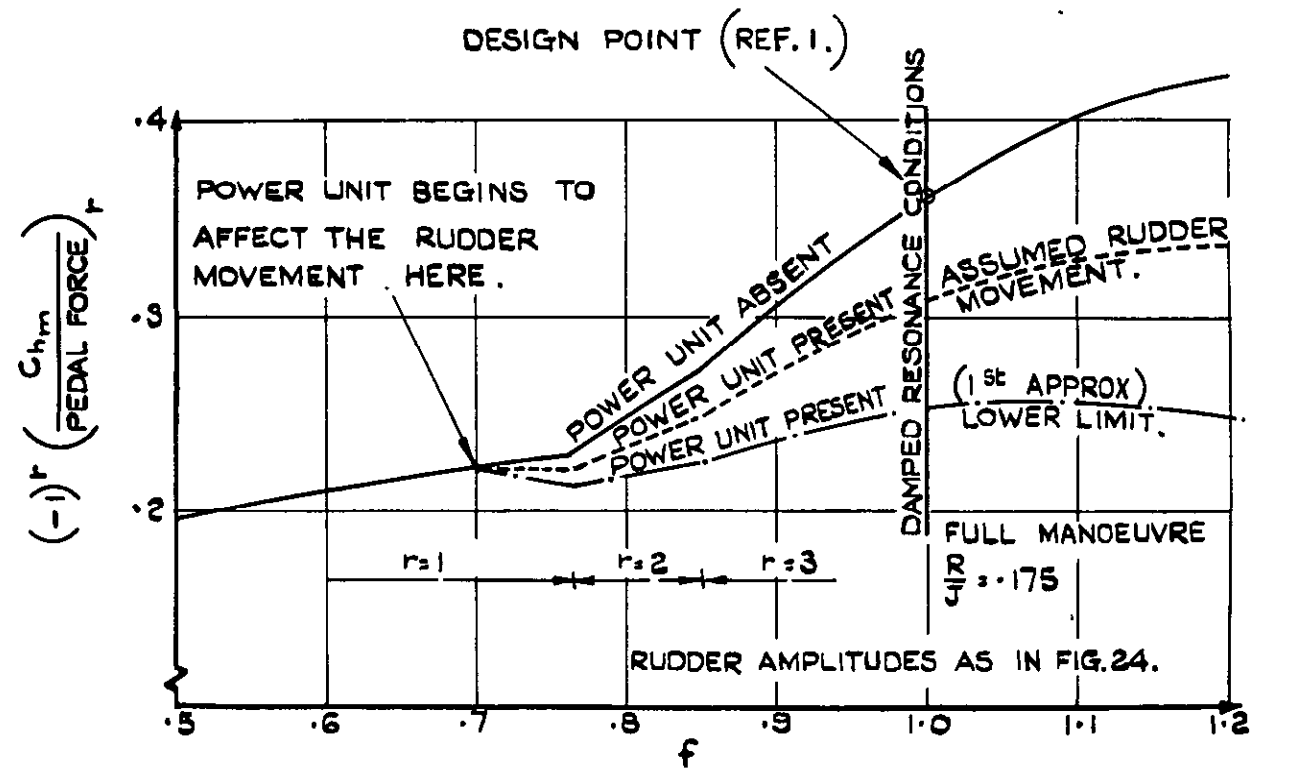

FIG. 26 EXAMPLE SHOWING EFFECT OF POWER UNIT ON THE C_{hm} AT VARIOUS VALUES OF f EXAMPLE DATA IN TABLE I.

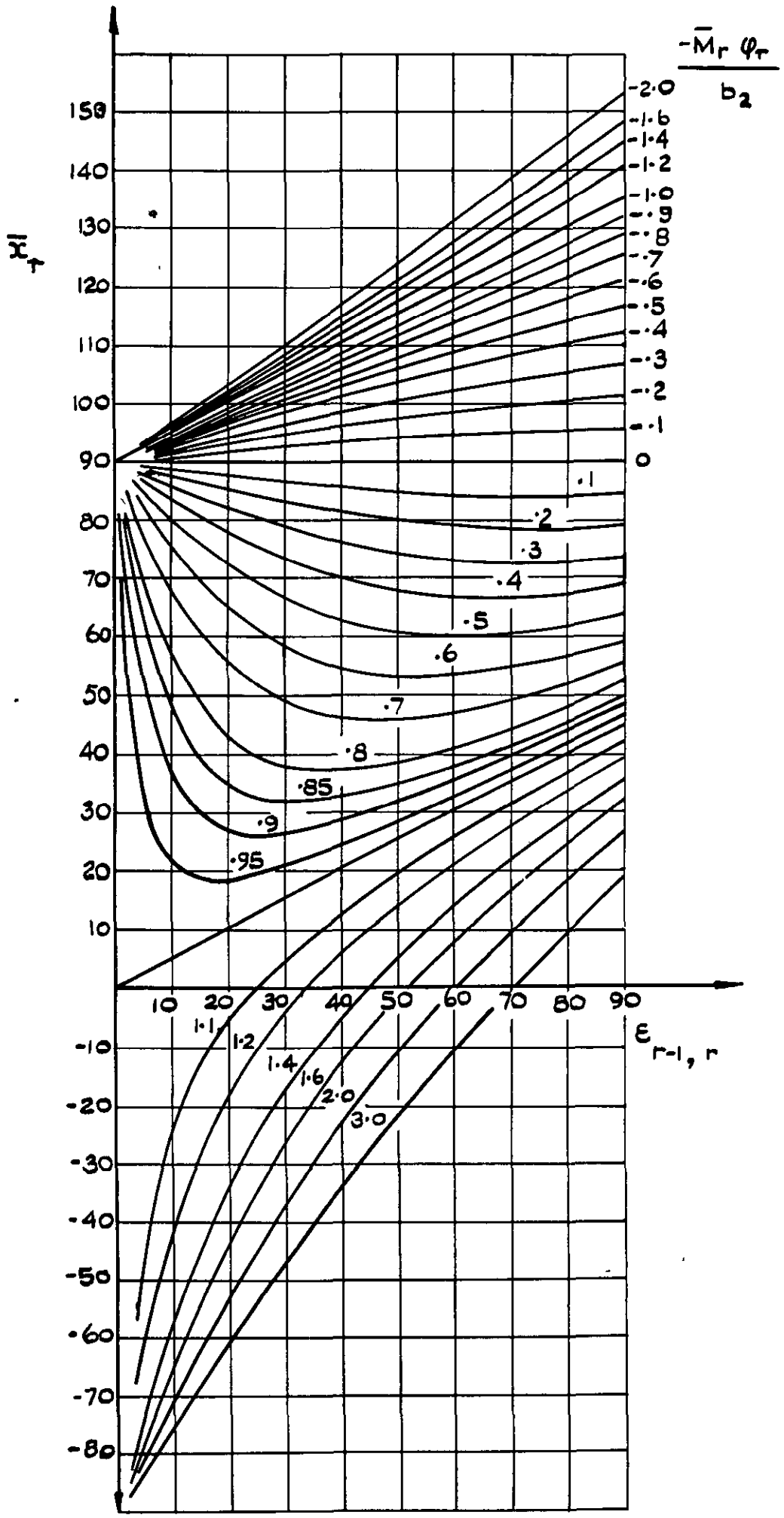

FIG. 27. SOLUTION OF THE EQUATION

$$\frac{\cos \bar{x}_r}{\cos\left(\bar{x}_r - \varepsilon_{r-1,r}\right)} = -\frac{\bar{M}_r \varphi_r}{b_2}$$

C.P. No. 301
(18,124)
A.R.C. Technical Report

Published by
HER MAJESTY'S STATIONERY OFFICE

To be purchased from
York House, Kingsway, London W C 2
423 Oxford Street, London W 1
P O Box 569, London S E 1
13A Castle Street, Edinburgh 2
109 St Mary Street, Cardiff
39 King Street, Manchester 2
Tower Lane, Bristol 1
2 Edmund Street, Birmingham 3
80 Chichester Street, Belfast
or through any bookseller

PRINTED IN GREAT BRITAIN

S.O. Code No. 23-9010-01

C.P. No. 301

C.P. No. 304
(17,990)
A.R C. Technical Report

C.P. No. 304
(17,990)
A.R.C. Technical Report

MINISTRY OF SUPPLY

AERONAUTICAL RESEARCH COUNCIL

CURRENT PAPERS

Three-Dimensional Wind-Tunnel Tests of a 30° Jet Flap Model

By

J. Williams, M.Sc., Ph.D., and

A. J. Alexander, B.Sc.,

of the Aerodynamics Division, N.P.L.

LONDON · HER MAJESTY'S STATIONERY OFFICE

1957

EIGHT SHILLINGS NET

Three-Dimensional Wind-Tunnel Tests of a 30° Jet Flap Model

- By -
J. Williams, M.Sc., Ph.D.
and
A. J. Alexander, B.Sc.
of the Aerodynamics Division, N.P.L.

9th November, 1955

SUMMARY

As a first investigation of finite aspect ratio effects in relation to the jet flap scheme, pressure plotting experiments were made on a small-scale model, with a 12½% thick wing section already tested under two-dimensional conditions at the N.G.T.E. The spanwise distribution of 'pressure lift' loading induced by T.E. blowing was evaluated by chordwise integration of the surface static pressures, and followed closely that which would be expected for a conventional wing at incidence (without T.E. blowing). The total lift, drag and pitching moments were derived for values of jet momentum coefficient C_J up to 2 at wing incidences between -5° and 20°, and up to 5 at zero incidence, by summing the corresponding integrated pressure forces and jet reaction components.

CONTENTS

1./

Published with permission of the Director, National Physical Laboratory

1. Introduction

The jet flap scheme developed at the N.G.T.E.[1] is essentially a means of producing an asymmetry of flow about a wing in order to increase lift at constant wing incidence, without recourse to mechanical devices such as large T.E. flaps. Air is ejected with high velocity at an angle θ to the chord-line, through a narrow spanwise slot at the wing T.E. In the so-called 'shrouded jet flap', a small hinged T.E. flap is included merely to turn the jet through the required angle by Coanda effect, instead of inclining the direction of the blowing slot to the chord line. The jet-flap scheme may be contrasted with blowing over normal size T.E. flaps, where the asymmetry of the flow is basically engendered by the flap deflection, and the blowing prevents flow separation over the flap nose, thus ensuring that the flap attains its theoretical efficiency* (see Fig.1 of Ref.3). Even in this case, if the blowing momentum is increased beyond that required to prevent flow separation, the lift is also further increased (supercirculation) by the effective extension of the flap chord (or downward displacement of the dividing streamline extending from the T.E. of the flap[4]).

Extensive two-dimensional wind-tunnel tests on 12½% thick elliptic sections have been made at the N.G.T.E.[2] for various jet deflection angles θ up to and including 90°. At the request of the A.R.C. Performance Sub-Committee, tests on a three-dimensional jet flap model were carried out at the N.P.L. to obtain quickly some idea of the magnitude of finite aspect ratio effects†. A small pressure-plotting model of rectangular planform, with a 12½% thick elliptic section and a jet angle of 31.3°, was provided by N.G.T.E. and was mounted with a plate at one end to give an effective aspect ratio slightly less than 3.0 (see § 2). The lift, drag and pitching moment forces were calculated from measurements of the surface static pressures and the jet reaction. For completeness, tests were also made on the same wing with a second end-plate added, in an attempt to approach two-dimensional flow conditions (see § 2).

2. Experimental Set-up

The model was made of metal, with a chord c of 8 inches and with a span s of 12 inches excluding the ellipsoidal tip fairing which added a further 0.25 inches. A turntable, attached at the model root, rotated about the mid-chord axis in a fixed end-plate as illustrated in Fig.1a; the end-plate extended about 0.8 chord upstream of the wing L.E., two chords downstream of the T.E. (jet exit), one chord vertically above the zero-incidence chord-line and two chords below. Fig.2a, which was derived from the theoretical results of Ref.4, gives the effective aspect ratio of the wing as 2.75 for the appropriate ratio of wing span to end-plate height. The set-up of the supplementary experiments, with the ellipsoidal tip removed and a second end-plate added, did not represent strictly two-dimensional conditions. With the present end-plate size, which was limited by

structural/

---

*The quantity requirements to achieve a moderate lift by blowing over a normal size T.E. flap are considerably less than those needed with the simple jet flap at the same angle.

†Provisional conclusions were communicated to the A.R.C. Performance Sub-Committee in February, 1954, immediately the tests were completed, and advance copies of some of the graphs contained herein have already been given very limited circulation.

structural and accessibility considerations, the loading was sensibly constant across the span but according to Fig.2a, the effective aspect ratio was only 6.8.

For the measurement of surface static pressures, 26 tappings were provided at each of the four spanwise stations 0.2s, 0.5s, 0.8s and 0.95s from the wing root, closely spaced near the L.E. and T.E. of the model. Some static pressure tappings were also included in the end-plate at the wing root but these were only useful for general guidance. Unfortunately, it was not possible to incorporate static tubes in the blowing slot walls. The upper lip of the blowing slot was located at the T.E. of the elliptic section with the lower lip just on the undersurface to give a mean slot width w of 0.025 in., i.e., w/c = 0.003; the spanwise variation was less than 0.0025 in. N.G.T.E. measurements showed that at zero wind-speed the jet issued at an angle 31.3° to the chord-line, with no observable variation spanwise or change with jet efflux over the practical range. The internal structure of the model is shown in Fig.1b.

The model was located centrally in the N.P.L. Low Turbulence Wind-Tunnel (regular 16-sided cross-section, 7 ft height), so that the tunnel interference effects were small. The general arrangement of the model and the external ducting to the Broom-Wade compressor unit is depicted in Fig.1a. A simple pitot comb traverse gear was employed to explore briefly the development of the jet wake (see Fig.1c). The jet could be straddled at any spanwise location and at distances downstream up to three chords behind the T.E; the axis of the comb could be aligned along the local mean direction of the jet flow. Detailed explorations were not possible, however, owing to shortage of tunnel time and lack of a sufficiently closely spaced pitot comb.

The calibration curve given in Fig.2b, of jet reaction J against the jet total pressure measured in the blowing duct, was used to derive the values of the non-dimensional jet reaction coefficient C_J ($\equiv J/\frac{1}{2}\rho_o U_o^2 S$). The curve was determined at the N.G.T.E. from balance measurements of thrust with the model at zero incidence and with zero wind-tunnel speed, a correction being applied to allow for the static pressure distribution arising from the flow induced about the model by the jet efflux.

3. Range of Tests and Reduction of Observations

Most of the wind tunnel tests were carried out at a windspeed of 100 ft/sec ($R = 0.1 \times 10^6$), when the available air supply permitted C_J - values up to 0.5 to be used. Higher values of C_J were obtained by reducing the windspeed to 50 ft/sec ($C_J < 2.1$) and to 30 ft/sec ($C_J < 4.8$). Observations were first made with the three-dimensional model at zero incidence and C_J - values up to 4.8. Transition wires were located on the front upper and lower surfaces of the model, at 0.2c behind the L.E., as far forward as possible without causing interference at the closely spaced static holes in the wing nose. Similar experiments were then made at incidences ranging between -5° and 20° for C_J values up to 2.1, both with and without transition wires. Unless otherwise stated the results discussed in the text and plotted in the graphs refer to those obtained with transition wires.

The lift coefficient C_L on the wing may be regarded as comprising the vertical component $C_J \sin(\theta + \alpha)$ of the jet reaction at the nozzle and the vertical 'pressure force' C_{Lp} arising from the airflow over the aerofoil surface. Thus we write

$$\left.\begin{aligned} C_L &= C_J \sin(\theta + \alpha) + C_{Lp} \\ C_D &= -C_J \cos(\theta + \alpha) + C_{Dp} \\ C_M &= -\tfrac{2}{c} C_J + C_{Mp} \end{aligned}\right\} \quad \ldots\ldots(1)$$

where/

where n is the perpendicular distance from the point about which moments are taken onto the extended centre-line of the jet nozzle. For moments about mid-chord, as quoted for the present tests, $n/c \simeq \frac{1}{2} \sin\theta$. The sectional pressure-force coefficients were obtained from the measured static pressures by chordwise integration. The overall force coefficients were then derived by integration across the span, and for convenience were based on the area S of the rectangular plan-form excluding the small ellipsoidal tip[x]. Some simplifying assumptions had to be made for the chordwise integration of the static pressures close to the T.E. since there were no static pressure holes inside the slot throat. Although the resulting error in the lift coefficients is insignificant, this may not be so for the pitching moment and drag coefficients under all conditions.

The quasi two-dimensional experiments, made with the ellipsoidal tip removed and a second end-plate added, covered roughly the same ranges of C_J and incidence as those tested on the three-dimensional model. It was first checked that the set-up gave sensibly constant loading across the span, i.e., nominally two-dimensional flow, for a few representative conditions. Then for the remainder of the tests, the static pressures were recorded only at the mid-span section and the pressure force coefficients evaluated therefrom.

4. Three-Dimensional Model Results

4.1 Lift

The spanwise distribution of 'pressure lift' loading induced by T.E. blowing, with the wing at zero incidence, seems little different from that given by simple lifting-line theory (see Fig.3a) or that due to wing incidence without blow (Fig.3b).

The total lift C_L at zero wing incidence is plotted against $C_J^{\frac{1}{2}}$ in Fig.4a, both with and without transition wires and for various windspeeds. At C_J-values below unity, the experimental results lie reasonably close to the straight line $C_L = 1.4\, C_J^{\frac{1}{2}}$, and at higher C_J-values are slightly above this. The relative magnitudes of the jet reaction and pressure force contributions to the total lift are also indicated. Curves of C_L against $C_J^{\frac{1}{2}}$ for other incidences are plotted in Fig. 4b for the case with transition wires; the slope $dC_L/dC_J^{\frac{1}{2}}$ at a prescribed C_J is seen to increase with incidence. The C_L-values obtained without transition wires are in most instances not more than 0.1 different from those with.

Lift-incidence curves for a range of C_J-values with transition wires are shown in Fig.5. As C_J is increased from zero there is no significant loss in stalling incidence; at C_J-values above unity there is even some increase in stalling incidence which, though possibly peculiar to the low Reynolds number and particular wing configuration of the tests, is at least encouraging. The value of $dC_L/d\alpha$ for small incidences rises steadily as C_J increases, from 0.055/deg without blow to about 0.1/deg at $C_J = 2$. The increase is roughly proportional to $C_J^{\frac{1}{2}}$, and is made up of contributions from both the jet reaction and pressure force components. With α measured in degrees,

$$dC_L/d\alpha = 0.0175\, C_J \cos(\theta + \alpha) + dC_{Lp}/d\alpha \qquad \ldots\ldots(2)$$

$$\simeq 0.015\, C_J + dC_{Lp}/d\alpha \text{ for small } \alpha \qquad \ldots\ldots(3)$$

The removal of the transition wires had little effect on $dC_L/d\alpha$, except for the results without blowing, when the value became extraordinarily high. This seemed to be associated with the presence of a thin laminar boundary layer right back to the T.E. at the low test Reynolds number combined with the unusual slotted T.E. shape.

4.2/

---

[x] The tip increased the wing area by only about $1\frac{1}{2}\%$.

4.2 Pitching Moment

Fig.6 gives curves of total pitching moment C_M about the half-chord axis plotted against the corresponding total lift C_L, for a range of values of α and C_J, from the tests with transition wires.

Probably not more than broad conclusions should be drawn from the results, in view of the few static pressure holes in the vicinity of the slot. It is seen that the mean slope $(dC_M/dC_L)_{C_J}$ of the curves for constant C_J (α varied) is about 0.25 at low but non-zero values of C_J, so that the aerodynamic centre is located close to the quarter-chord position. As C_J increases, the value of $(dC_M/dC_L)_{C_J}$ decreases so that the aerodynamic centre tends to move further aft, say by about 0.04c as C_J is raised from 0.2 to unity. The C_M - C_J curves for zero C_J are, however, somewhat unusual in that the slopes both with and without transition wires differed appreciably from 0.25, being respectively greater and less. This peculiar behaviour in the absence of blowing was again accredited to the unconventional T.E. shape and low Reynolds number of the tests.

As C_J increases with α constant, the nose-down pitching moment becomes steadily larger*, because the induced suction forces on the wing upper surface are much higher near the T.E. than the L.E. (see later discussion on pressure distributions). The chordwise location of the centre of total lift is plotted against C_L in Fig.7, and in general moves rearward appreciably as C_J is increased at constant incidence or as the incidence is decreased at constant C_J.

4.3 Drag

The total drag coefficient C_D on the wing, as defined by equation(1) of §3, is plotted against C_J in Fig.8a, for a range of wing incidences both with and without transition wires. Again the drag results do not warrant more than a qualitative examination.

It will be recalled that the drag is made up of the chordwise components of the direct jet reaction and the pressure forces on the aerofoil surface; the relative magnitudes of the two contributions are indicated in Fig.8a for the zero incidence case. Thus, without blowing, C_D includes the conventional form drag of the wing sections and the induced drag arising from downwash effects, but excludes the skin-friction drag. With blowing, we might therefore regard C_D as comprising a chordwise component $-C_J \cos(\theta + \alpha)$ from the direct jet reaction, a form drag together with any recovery of thrust which manifests itself in the pressure distribution, and an induced drag resulting from downwash effects over the wing. For ideal conditions, i.e., potential flow in the mainstream flow and no mixing, it can be shown that the direct jet reaction and thrust recovery terms taken together contribute the amount $-C_J$ corresponding to the gross thrust. In our measurements the so-called form drag, induced drag and thrust recovery terms are of necessity lumped together as pressure drag. Fig.8a shows that the rate of decrease in C_D with C_J is appreciably less than the amount $C_J \cos(\theta + \alpha)$ associated with the direct jet reaction. Thus, because of the low aspect ratios and small jet angle, the combined form and induced drag contributions to the pressure drag completely outweigh and mask any negative contribution arising from thrust recovery.

For comparisons with the pressure drag associated with more conventional methods of producing pressure lift on a wing, namely by incidence and camber, the value of C_{Dp} for the present jet flap wing

has/

---

*On a complete aircraft with tail this could at least be partially trimmed out by the increased downwash over the tail.

has been plotted against C_{Lp}^2. Fig.8b, for the wing at zero incidence shows that for C_J-values below 0.5 the points lie close to the straight line

$$C_{Dp} = 0.013 + 0.14\ C_{Lp}^2$$

while for C_J-values up to 2 the value of C_{Dp} does not exceed $0.013 + 0.16\ C_{Lp}^2$. Fig.8c, giving results for other incidences, shows that up to 11° the trend is also much the same. The combined form and induced drags of a conventional wing of aspect ratio 2.75 producing corresponding pressure lifts at the same Reynolds number would not in fact be greatly different from the above (see § 6).

4.4 General Flow Characteristics and Pressure Distributions

Tuft and china clay observations were made to visualise the flow about the model. For C_J-values up to 2.1, with the wing at zero incidence, no separation was evident on the upper surface due to the adverse pressure gradients at the front[7]. As the wing incidence was increased a small bubble of separated flow appeared, at the inboard sections first, being formed by separation of the laminar boundary layer close to the L.E. with subsequent reattachment as a turbulent boundary layer ahead of the transition wire. Without blowing, the bubble did not expand appreciably chordwise until the incidence exceeded 10°, after which the position of reattachment moved steadily rearwards, again at the inboard sections first. The behaviour with blowing operative was similar, but the wing incidence at which the bubble began to expand decreased somewhat as C_J was increased.

Some representative pressure distributions with the wing at zero incidence and transition wires on are shown in Figs.9a and 9b for the chordwise sections at $y/s = 0.20$ and $y/s = 0.95$, and selected C_J-values up to 2.1. It is seen that they are similar in shape to the pressure distributions on the main part of a wing when a T.E. flap is deflected. In order to obtain some idea of the variation in pressure distribution with incidence as well as C_J, the values of the peak suctions occurring near the L.E. and T.E. of the two chordwise sections have been plotted against incidence for C_J-values ranging up to 2.1 (see Fig.10). As the incidence increases at constant C_J the peak suction on the nose grows more rapidly at the inboard than the outboard section, so flow separation may be expected earlier inboard which agrees with the deduction from flow visualisation experiments. Furthermore, although the peak suction near the T.E. of the outboard section grows with increasing incidence, that at the T.E. of the inboard section varies little at first and eventually diminishes. As C_J increases at constant incidence, the T.E. peak suctions grow much more rapidly than those near the L.E., partly because the latter are much reduced by downwash effects.

Some total head traverses of the jet were carried out at various distances downstream of the T.E. and at a few spanwise locations, but unfortunately the tests had to be severely limited. Fig.11a shows the mean line of the jet (locus of maximum total head) and also the distribution of the total head in the wake downstream of the mid-span station (6 in. from the root), for the wing at zero incidence with $C_J = 0.5$. It is seen that the width of the wake increases rapidly near the slot exit, being about 1 in. at a quarter-chord behind the T.E., by which time the inclination of the mean-line to the chord has fallen to about 15°. Fig.11b compares a few measurements of the mean-line of the jet downstream of the mid-span station with those further outboard. Spanwise variations are clearly evident further outboard than 10 in. from the root, i.e., beyond about 85% span.

5./

[7] In the absence of transition wires, laminar flow seemed to persist right back to the T.E.

5. Quasi Two-Dimensional Model Results

The pressure force coefficients were derived from static pressure measurements at the mid-span section only, since the lift loading was sensibly constant across the span‡. The curves of total lift, pitching moment and drag for the quasi two-dimensional model (effective aspect ratio = 6.8) are generally similar in character to those already discussed for the three-dimensional model.

At C_J-values below unity, the results for the total lift C_L at zero incidence both with and without transition wires, lie reasonably close to the straight line $C_L = 1.7\ C_J^{\frac{1}{2}}$ and at higher C_J-values are slightly above this (see Fig.12a). Curves of C_L against $C_J^{\frac{1}{2}}$ for other incidences derived from tests with transition wires are plotted in Fig.12b. Lift-incidence curves for a range of C_J-values are also shown in Fig.13, the value of $dC_L/d\alpha$ at small incidences rising steadily from about 0.075/deg without blow to 0.15/deg at $C_J = 2$.

The total pitching moment C_M about the half-chord axis is plotted against C_L for a range of C_J in Fig.14. At low C_J the aerodynamic centre is located close to the quarter-chord position and moves rearward about 0.06c as C_J increases from 0.2 to unity. The chordwise location of the centre of total lift also moves rearward in general as C_J increases with α constant, or as α decreases at constant C_J (see Fig.15).

The total drag coefficient C_D is plotted against C_J in Fig.16a for a range of incidences. It is immediately evident that the rate of decrease of C_D with C_J at zero incidence is less than $C_J \cos\theta$, so that the increase in pressure drag due to the so-called form and induced drag components again outweighs any decrease from the thrust recovery term. The values of the pressure drag, with the wing at zero incidence and with front transition wires, satisfy fairly well the relation

$$C_{Dp} = 0.015 + 0.068\ C_{Lp}^2$$

for C_J values up to 2 (see Fig.16b). This relation also holds with the wing at higher incidences, up to at least 6.5° (see Fig.16c), and is not far different from that for the combined induced and form drags of a conventional wing of aspect ratio 6.8 giving the same pressure lift (see § 6).

Some representative pressure distributions for the mid-span section with the wing at zero incidence and transition wires on are given in Fig.17 for a range of C_J-values. As the incidence increases at constant C_J, the peak suction near the T.E. varies little at first but eventually diminishes (see Fig.18); the value at moderate incidences is little different from that measured for the inboard sections of the three-dimensional model (c.f. Fig.10). The peak suction at the nose of course increases with incidence, until a certain maximum value ($-C_p \simeq 5$) is reached. For any prescribed incidence below that corresponding to this maximum value, the peak suction in general exceeds that measured on the three-dimensional model. The maximum is reached at a lower incidence, as would be expected because of the smaller downwash effects, but its value is not vastly different.

The mean line of the jet and the distribution of total head in the wake downstream of the T.E. are plotted in Fig.19 for the wing at zero incidence with C_J-values of 0.18 and 0.5.

6./

---

‡This was also checked for us theoretically by Miss Weber of the R.A.E., Farnborough.

6. General Conclusions on Finite Aspect Ratio Effects

The investigation described in the present report was a preliminary and first attempt to explore the effects of finite aspect ratio on the jet flap scheme. The experiments were not intended to provide comprehensive data for detailed project studies nor to establish fundamental postulates for a three-dimensional jet flap theory, but simply to give some idea of the magnitude of finite aspect ratio effects, particularly in relation to lift. Nevertheless, in summarising the results obtained for wing aspect ratios in the vicinity of 2.75 and 6.8, it is at least worth considering them in the light of simple aspect ratio correction factors for conventional wings without T.E. blowing*.

6.1 Summary of Experimental Results

(a) Total Lift (Figs.4 and 12) - For zero incidence, and $C_J < 1$, the results for the aspect ratio 2.75 and 6.8 wings lie close to the values

$$C_L = 1.4\ C_J^{\frac{1}{2}} \text{ and } C_L = 1.7\ C_J^{\frac{1}{2}} \text{ respectively,}$$

and are about 0.6 and 0.7 respectively of the corresponding N.G.T.E. two-dimensional values[2]. The appropriate values of the aspect ratio correction factor $[1 + (a_o/\pi Ae)]^{-1}$ for lift on conventional wings are 0.58 and 0.77 respectively, assuming elliptic loading ($e = 1$) and a sectional lift curve slope a_o equal to the flat-plate value of 2π.

(b) Pressure Drag (Figs.8 and 16) - For zero incidence and $C_J < 1$, the results for the aspect ratio 2.75 and 6.8 wings satisfy approximately the relations

$$C_{Dp} = 0.013 + 0.14\ C_{Lp}^2 \text{ and } C_{Dp} = 0.015 + 0.068\ C_{Lp}^2$$

respectively. The corresponding induced (pressure) drag $C_{Lp}^2/\pi Ae$ for conventional wings producing the lift C_{Lp} takes the values $0.116\ C_{Lp}^2$ and $0.047\ C_{Lp}^2$ respectively, assuming elliptical loading ($e = 1$). The remaining contribution ($\doteq 0.015 + 0.02\ C_{Lp}^2$) could reasonably be accounted for as sectional form drag in both cases. The approximate agreement between the measured pressure drags and the corresponding conventional drag estimates (induced and form) may well be fortuitous, but at least it seems that the pressure drag on the jet flap wing is not likely to be much larger than that of a conventional wing producing the same pressure lift.

(c) Lift-Incidence Curves (Figs.5 and 13) - For both aspect ratios the measured slopes $dC_L/d\alpha$ at constant C_J and small incidences are about doubled as C_J is raised from near zero to 2.0, and the increase is roughly proportional to $C_J^{\frac{1}{2}}$. There is also no significant loss in stalling incidence ($dC_L/d\alpha = 0$) as C_J is raised.

(d) Pitching Moments (Figs.6, 7, 14 and 15) - For small C_J-values, the aerodynamic centre is located near the quarter-chord position, and the centre of total lift at zero incidence lies close to half-chord. Both move steadily rearward as C_J increases at constant incidence.

6.2 Fundamental Considerations

The foregoing correlation of the pressure drag C_{Dp} in terms of C_{Lp}^2 would at first sight imply that

(a)/

---

*i.e., with the lift produced by incidence or camber.

(a) the downwash due to trailing vorticity affects only the pressure force contribution to the lift vector.

(b) the downwash is generated only by the pressure lift.

The general consensus of opinion held at present supports the first postulate that the pressure lift only is affected, since there seems little reason for the downwash to have other than small effects on the jet reaction. However, in preference to the second, it is generally considered[1] that the downwash results from the reaction of the total lift on the mainstream. On this basis, the effective downwash angle at the wing is by conventional arguments $\phi = C_L/\pi Ae$ and the corresponding induced drag contribution to the pressure drag is $C_{Lp}\, C_L/\pi Ae$, where e represents an efficiency factor which would be unity for a wing at incidence without blowing and with elliptic loading. The measured C_{Dp} values are plotted against $C_{Lp}\, C_L$ in Figs.8d and 16d respectively for the aspect ratio 2.75 and 6.8 wings at zero incidence. It is seen that, as C_J increases, the efficiency factor e satisfying a relation of the type

$$C_{Dp} = \text{const.} + (C_L\, C_{Lp}/\pi Ae)$$

also increases/. This would imply an effective increase in aspect ratio with increasing C_J possibly due to the interaction between the jet and the mainstream[1]. Thus, in general, e may well be dependent on C_J, θ and A as well as on planform.+

As far as aspect ratio corrections for lift are concerned it can likewise be argued that the jet produces effectively a change in the sectional no-lift angle, that the pressure lift only is affected by downwash, but that the latter should again be based on the total lift. Simple formulae are then readily obtainable for the pressure lift and the slope of the pressure lift-incidence curve in terms of the corresponding two-dimensional values for the same C_J, but these again involve the product Ae, i.e., the effective aspect ratio.

6.3 Further Work Proposed

Although some attempts have been made to analyse the present experimental data in terms of the above and other arguments, the experiments were not sufficiently comprehensive to permit a careful resolution of fundamental considerations on aspect ratio effects. For this reason, further experiments are proposed on a larger scale model with variable aspect ratio and jet angle. It is intended to determine the forces by balance as well as pressure-plotting measurements, and to make a detailed study of the nature of the three-dimensional flow.

References/

/Note that the value of e derived in this case is lowered by the form drag contribution.

+It can also be argued that the total lift should be used throughout to derive the induced drag, giving a formula of the type $C_{Dp} = \text{const} + (C_L^2/\pi Ae)$. Detailed theoretical studies are being carried out at the R.A.E., Farnborough, to clarify these points.

References

No.	Author(s)	Title, etc.
1	I. M. Davidson	The jet flap. R.Ae.Soc. Lecture, October, 1955.
2	N. A. Dimmock	An experimental introduction to the jet flap. N.G.T.E. Rep.R.175. July, 1955. A.R.C. 18,186.
3	J. Williams	An analysis of aerodynamic data on blowing over T.E. flaps for increasing lift. A.R.C. C.P.209, September, 1954.
4	W. Mangler and J. Rotta	Theory of the three-dimensional aerofoil. Part I - Theory of the supporting line. AVA Monograph F_1. M.O.S. R. & T.1023. A.R.C. 11,553 November, 1947.

Acknowledgements

The writers are much indebted to N.G.T.E. for constructing the model and providing the pumping equipment, in particular to Mr. N. A. Dimmock. The lengthy computations and graphical integrations associated with the reduction of the observations were carried out by Miss E. M. Love, Miss L. N. Esson and Miss A. K. Kernaghan, and the wake traverse gear was designed by Mr. N. Marcus, all of the Aerodynamics Division, N.P.L.

List of Symbols

a_o slope of two-dimensional total lift-incidence curve

A wing aspect ratio

c wing chord

C_{lp}, C_{Dp}, C_{Mp} Pressure lift, drag and pitching moment coefficients (about $\frac{1}{2}$-chord); derived by integration of pressure forces on aerofoil

C_L, C_D, C_M Total lift, drag and pitching moment coefficients (about $\frac{1}{2}$-chord); derived by adding direct jet reaction components to pressure forces on aerofoil. See eqn.(1), § 3)

C_J/

C_J jet coefficient = $J/\frac{1}{2}\rho_o U_o^2 S$

C_p static pressure coefficient = $(p - p_o)/\frac{1}{2}\rho_o U_o^2$

e wing efficiency factor. See §6.

h end-plate height

J total jet reaction

p static pressure

p_o, ρ_o, U_o mainstream static pressure, density, and velocity

R mainstream Reynolds number based on wing chord

s span of wing (excluding small ellipsoidal tip)

S area of wing (excluding small ellipsoidal tip)

w width of blowing slot

x chordwise distance

y spanwise distance from root

α wing incidence

θ jet deflection angle relative to wing chord-line

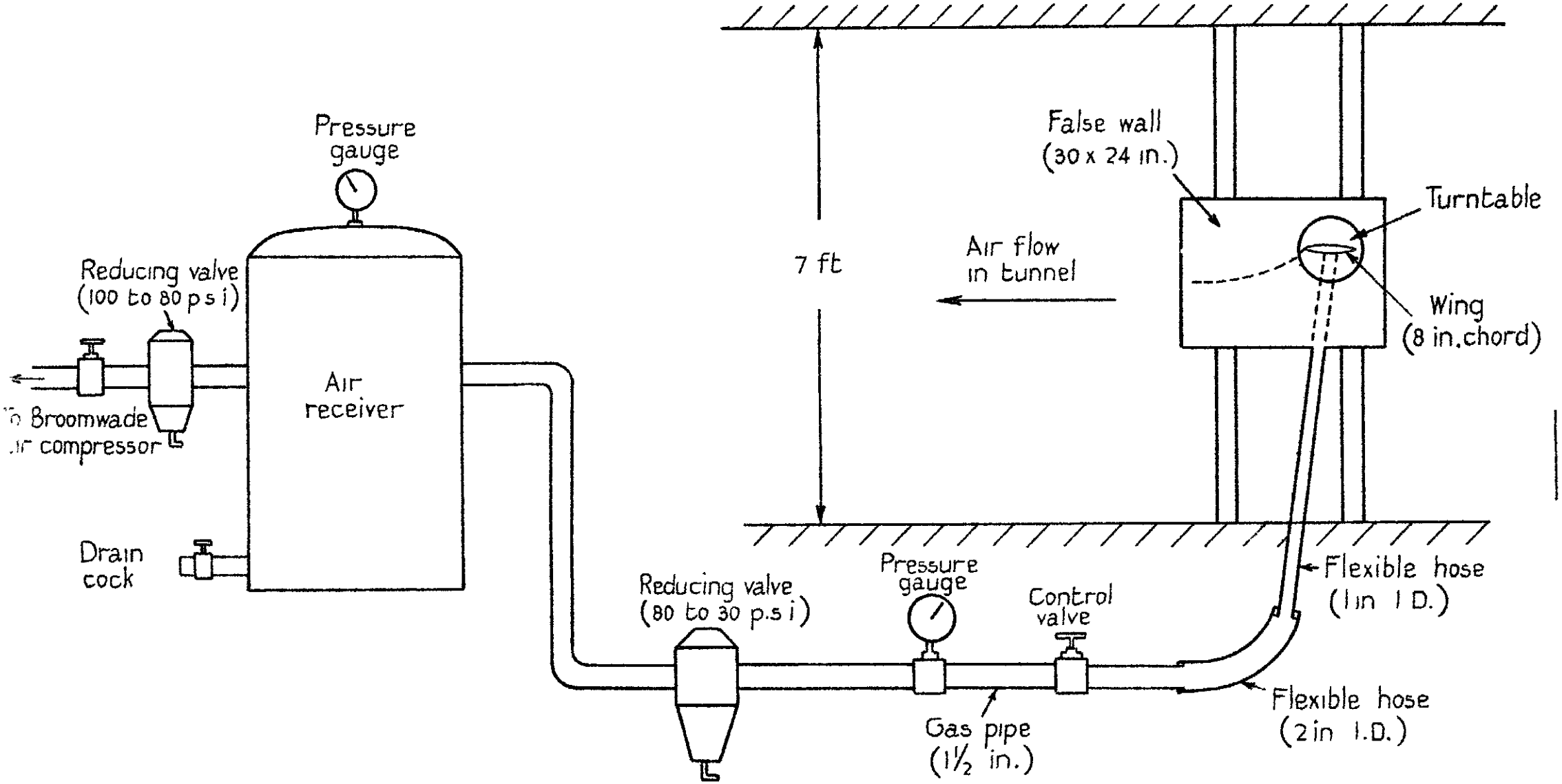

FIG. 1a.

Arrangement of jet flap model and external ducting

FIG. 1b.

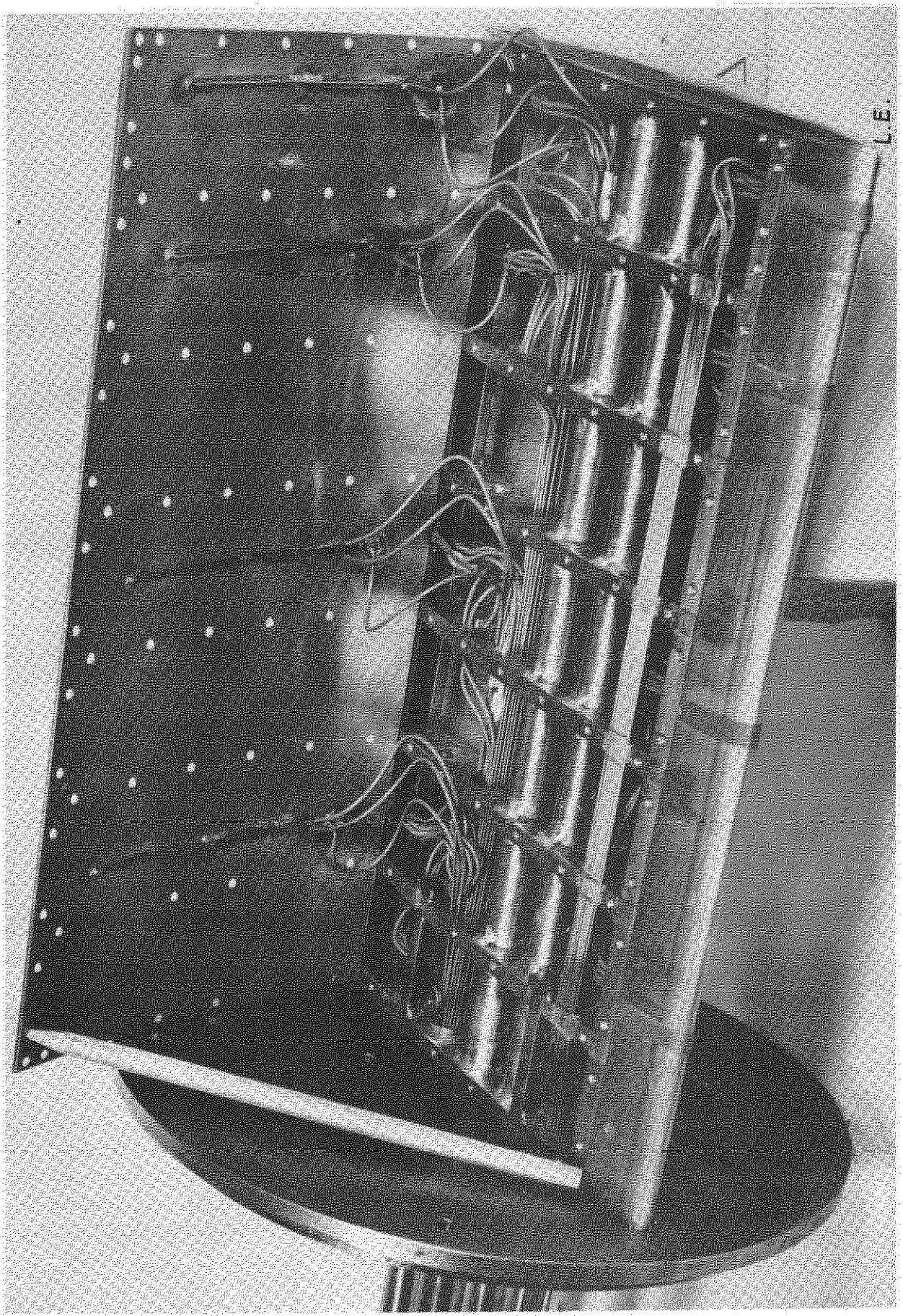

Internal structure of three-dimensional jet flap model.

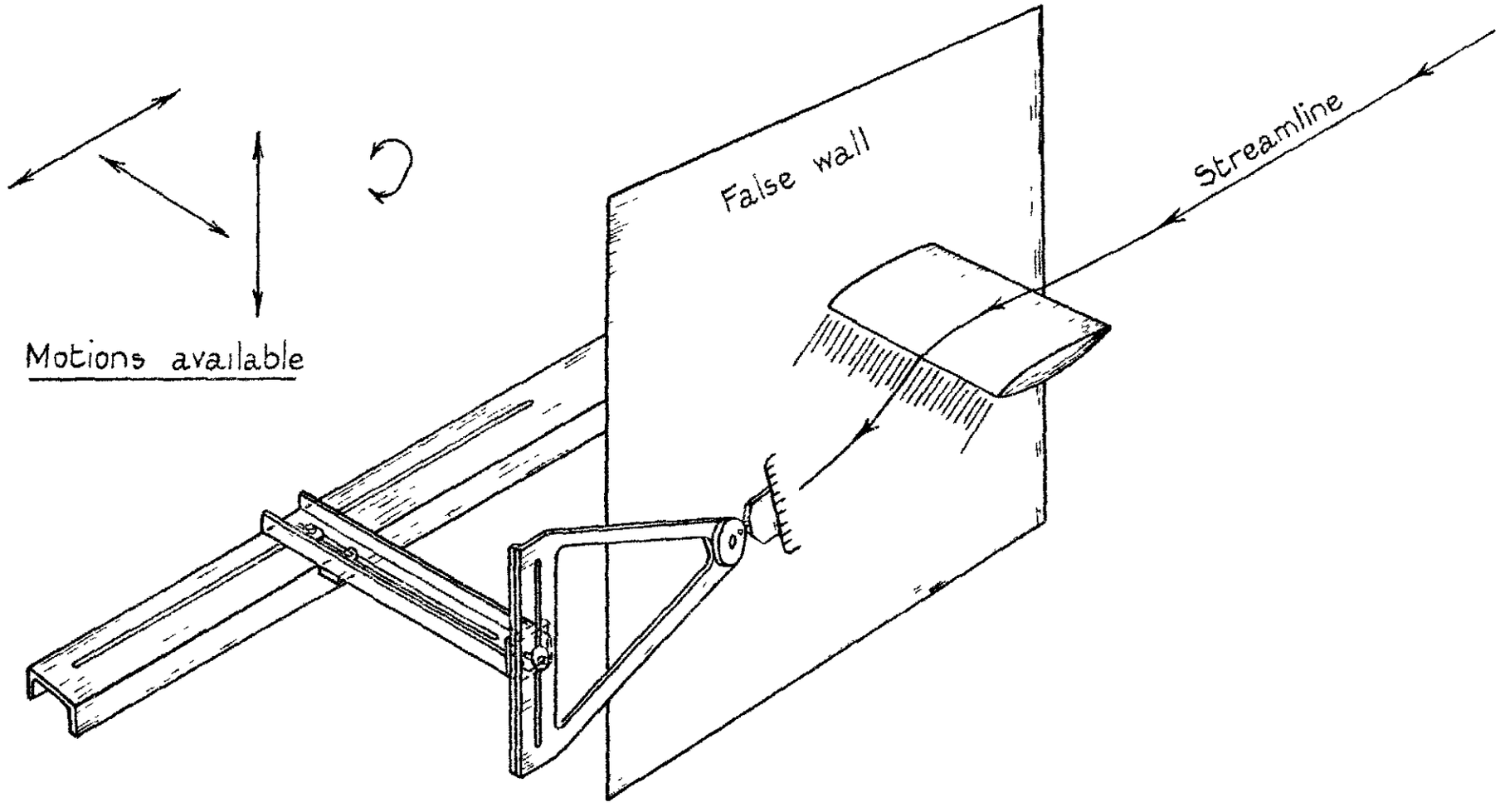

Scale : ≏ 1/10

Pitot comb wake traverse gear.

FIG. 1c

FIG. 2a.

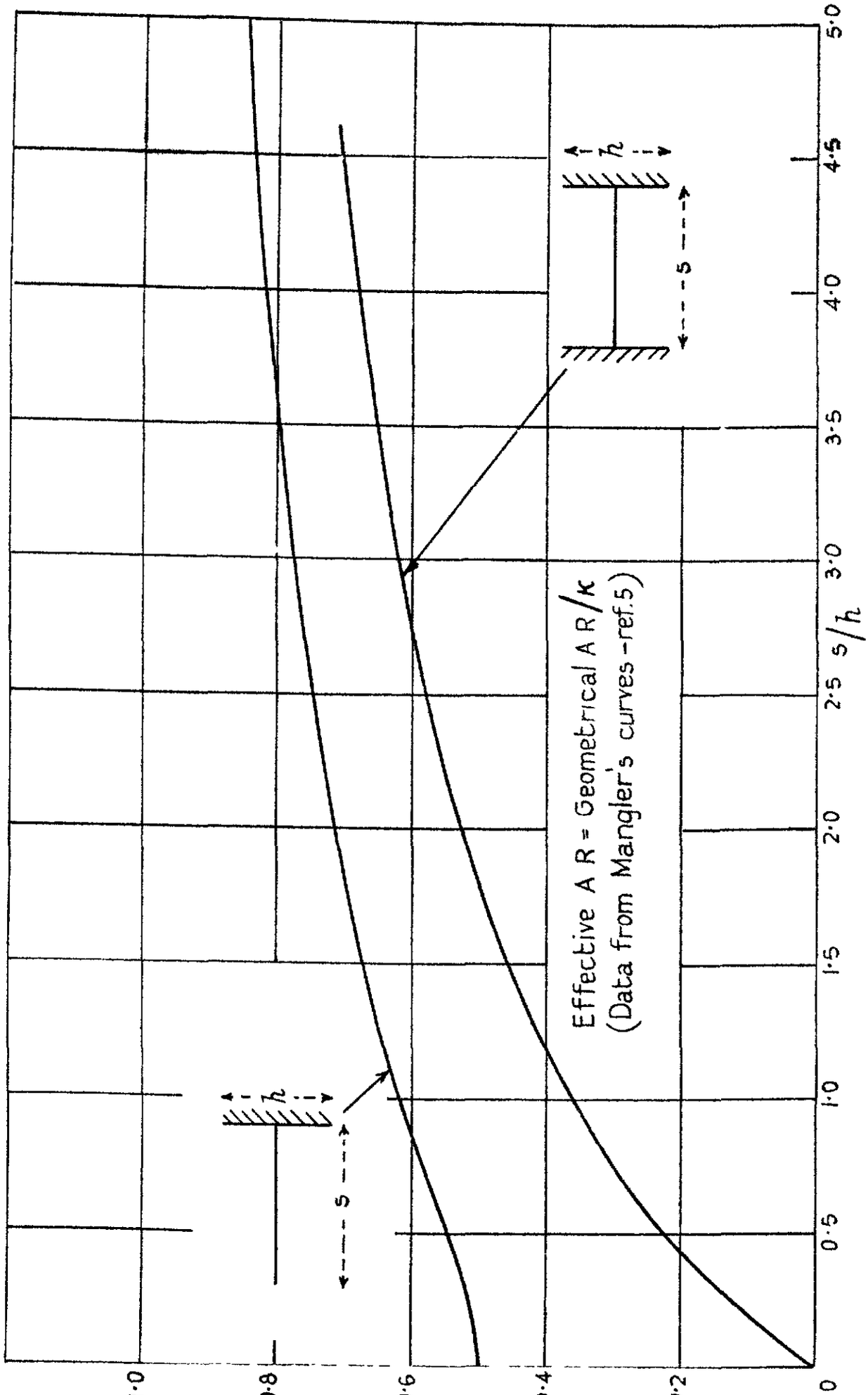

Variation of aspect ratio factor κ with ratio of wing span to end-plate height

Fig 2b.

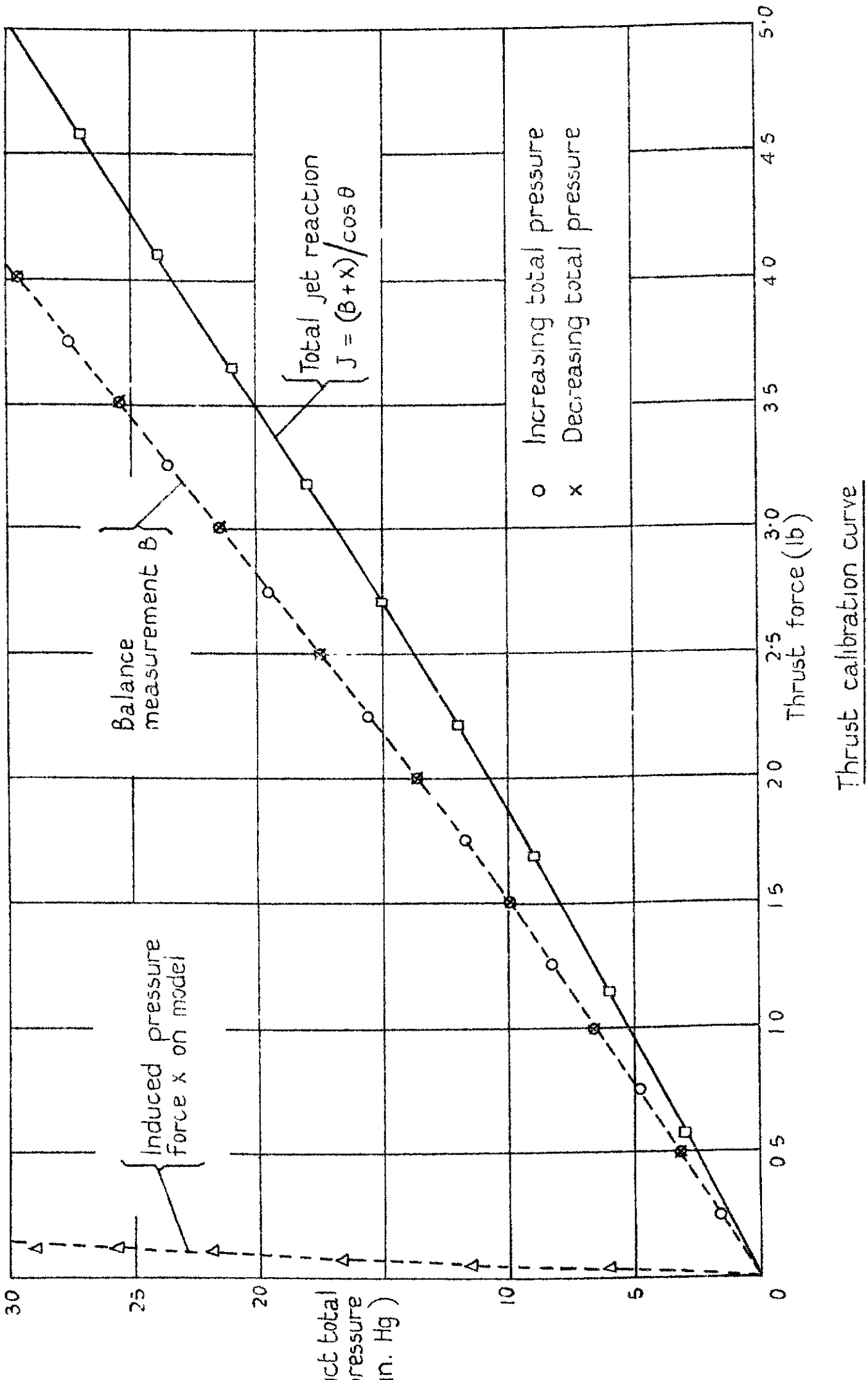

Thrust calibration curve

Fig 3a

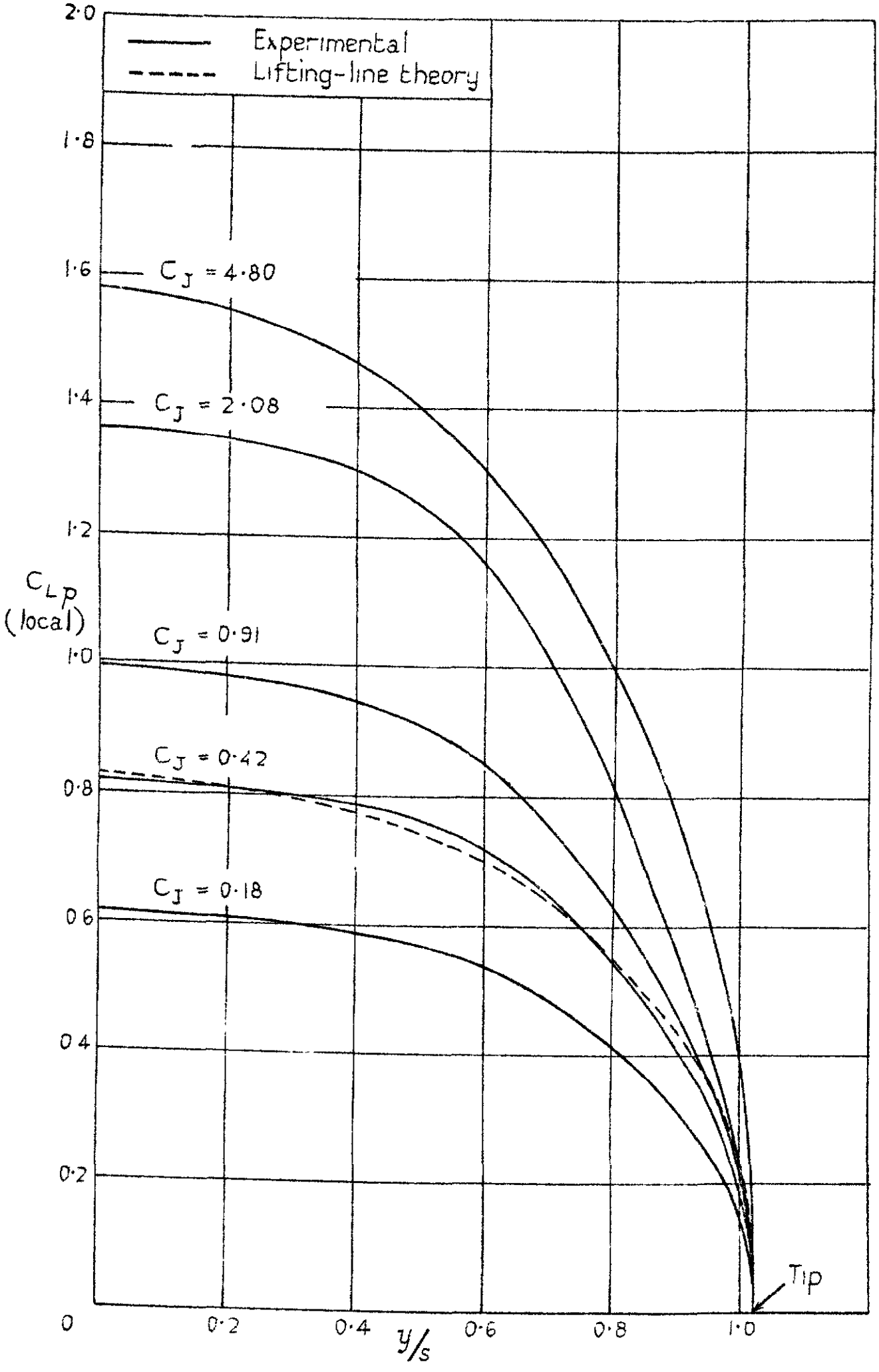

Spanwise distribution of pressure lift at zero incidence – Variation with C_J

Fig 3b.

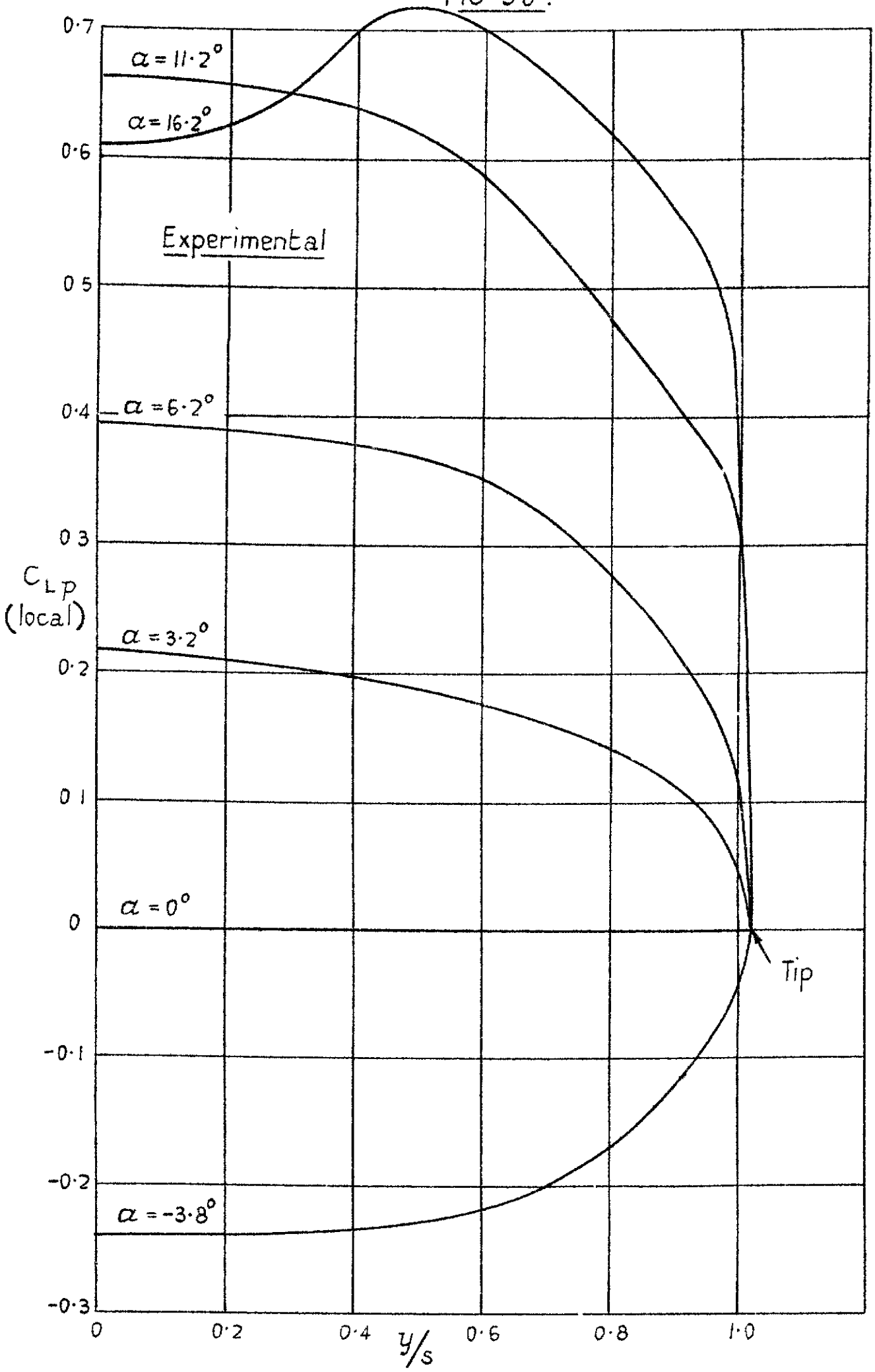

Spanwise distribution of lift without blowing.
Variation with incidence

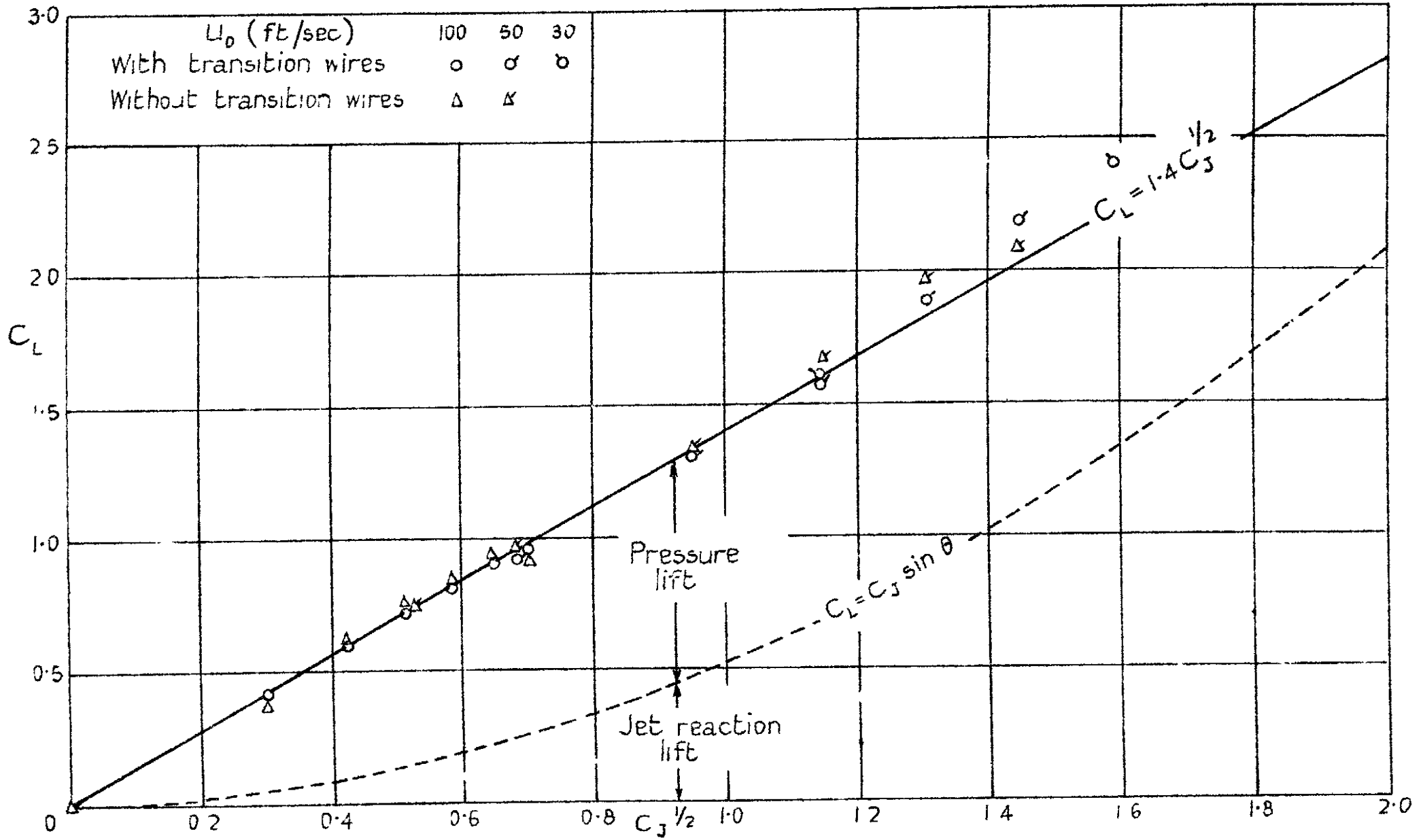

Variation of total lift C_L with $C_J^{1/2}$ at zero incidence

FIG 4a

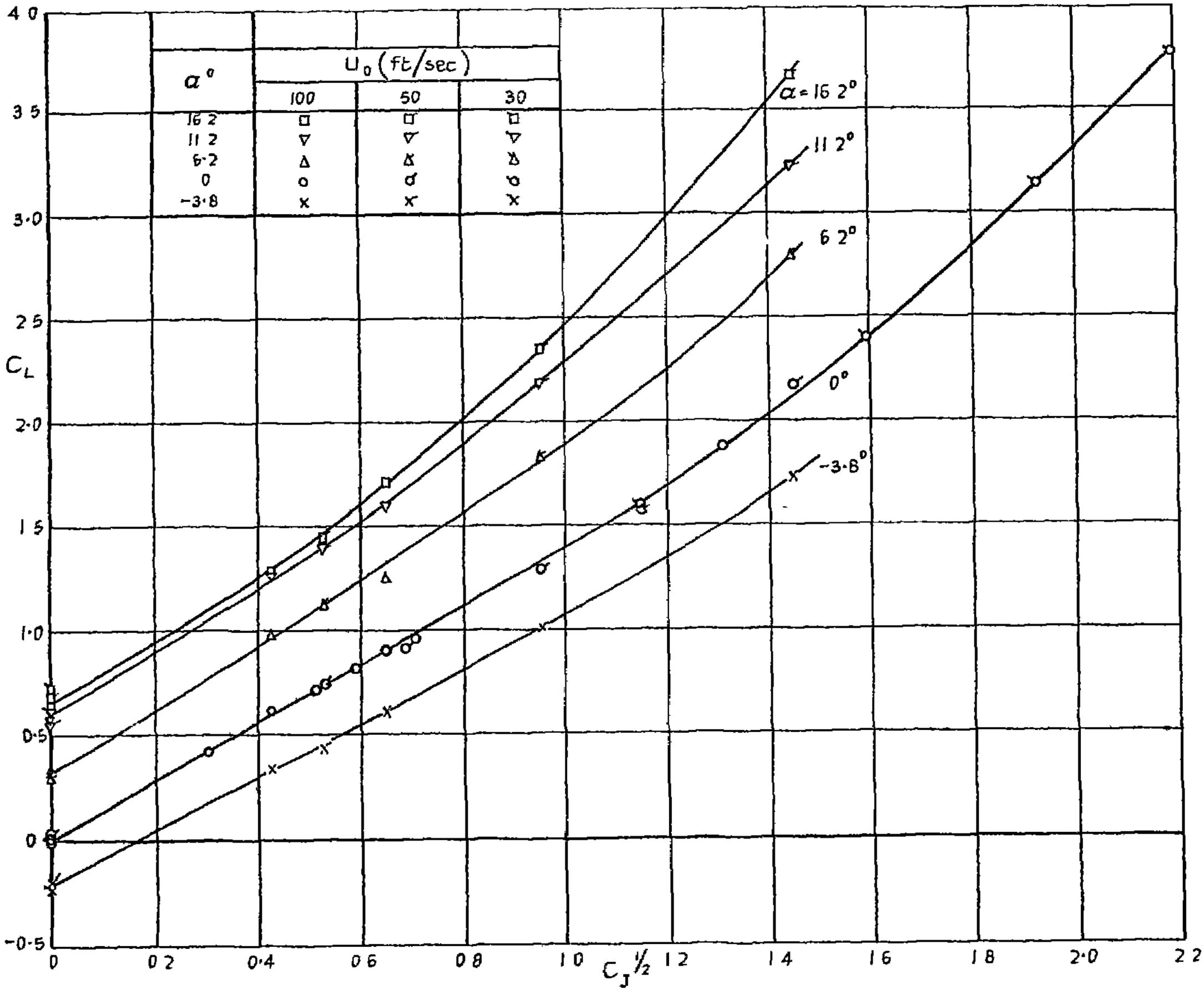

Variation of total lift with $C_J^{1/2}$ at constant incidence

FIG 5.

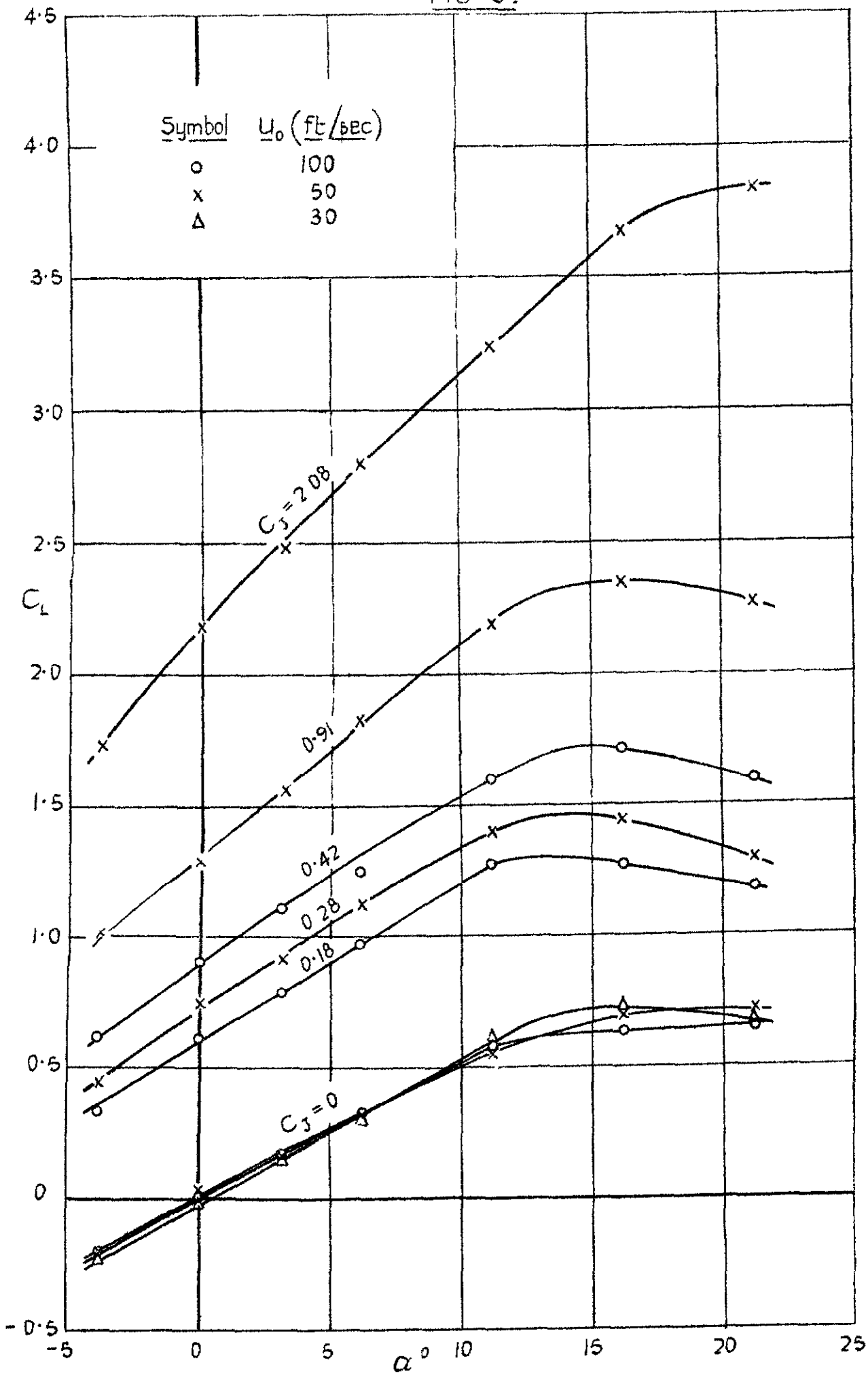

Variation of total lift with incidence at constant C_J

FIG. 6.

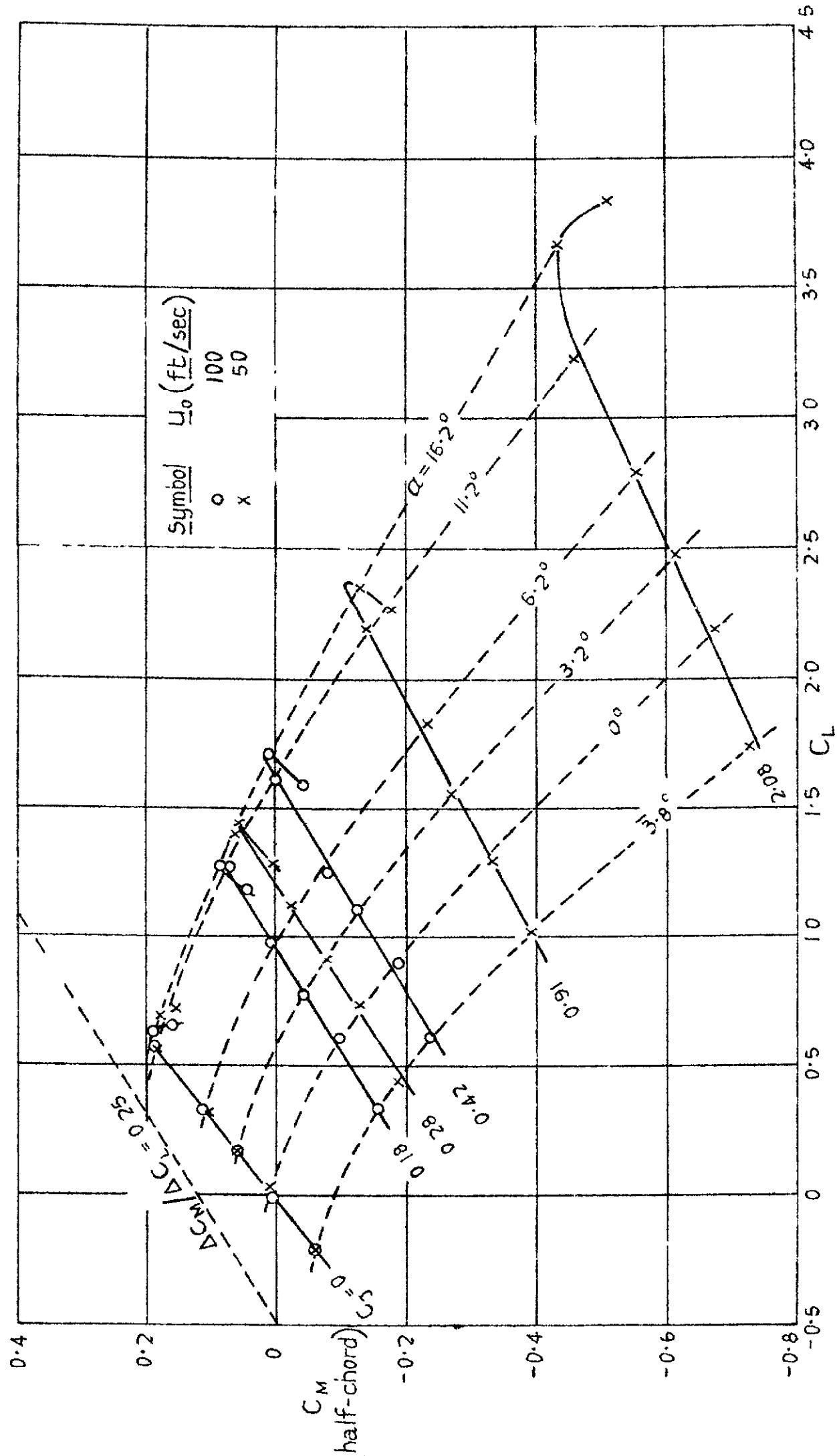

Variation of total pitching moment with total lift.

FIG. 7.

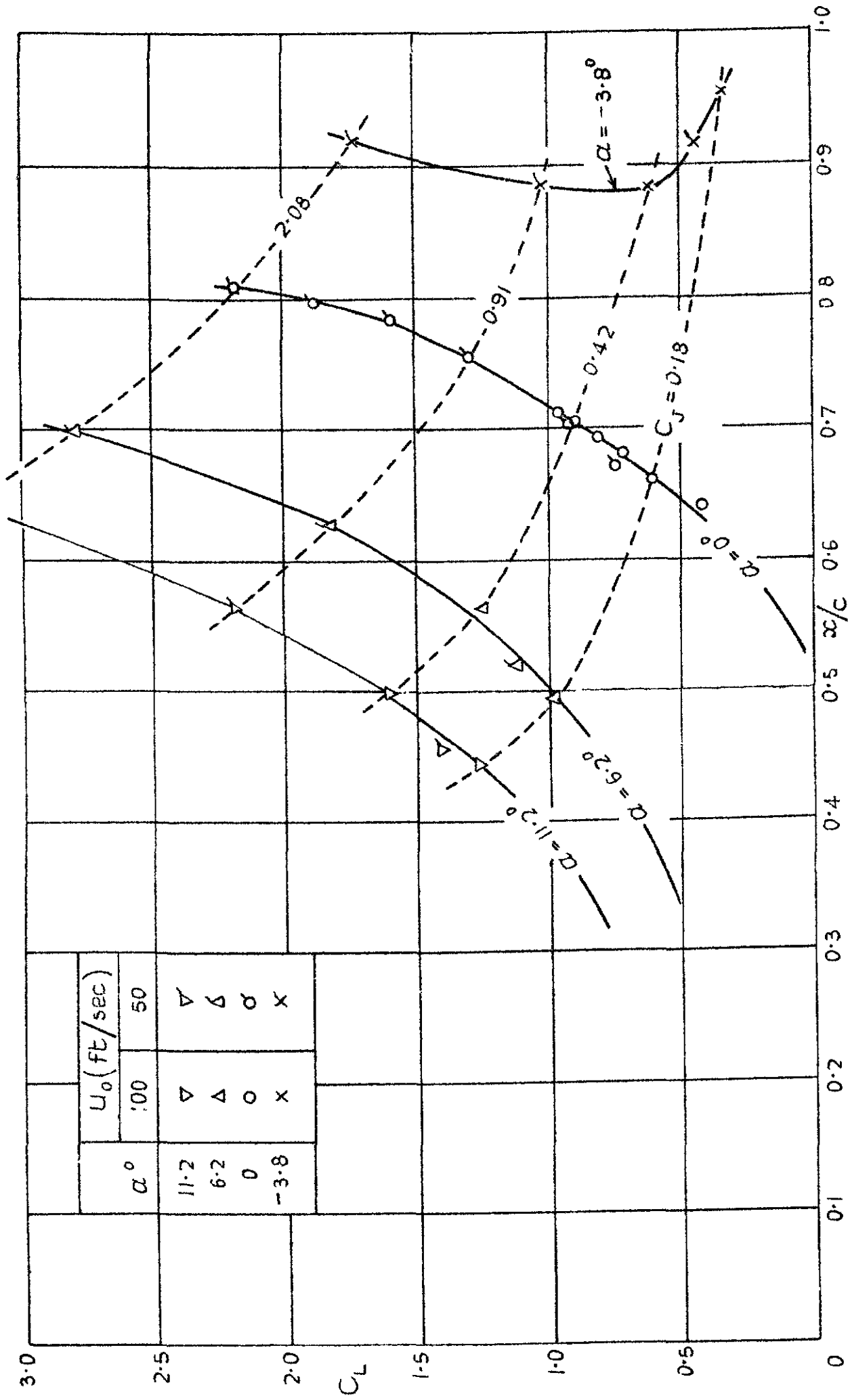

Variation in position of centre of total lift.

FIG. 8a.

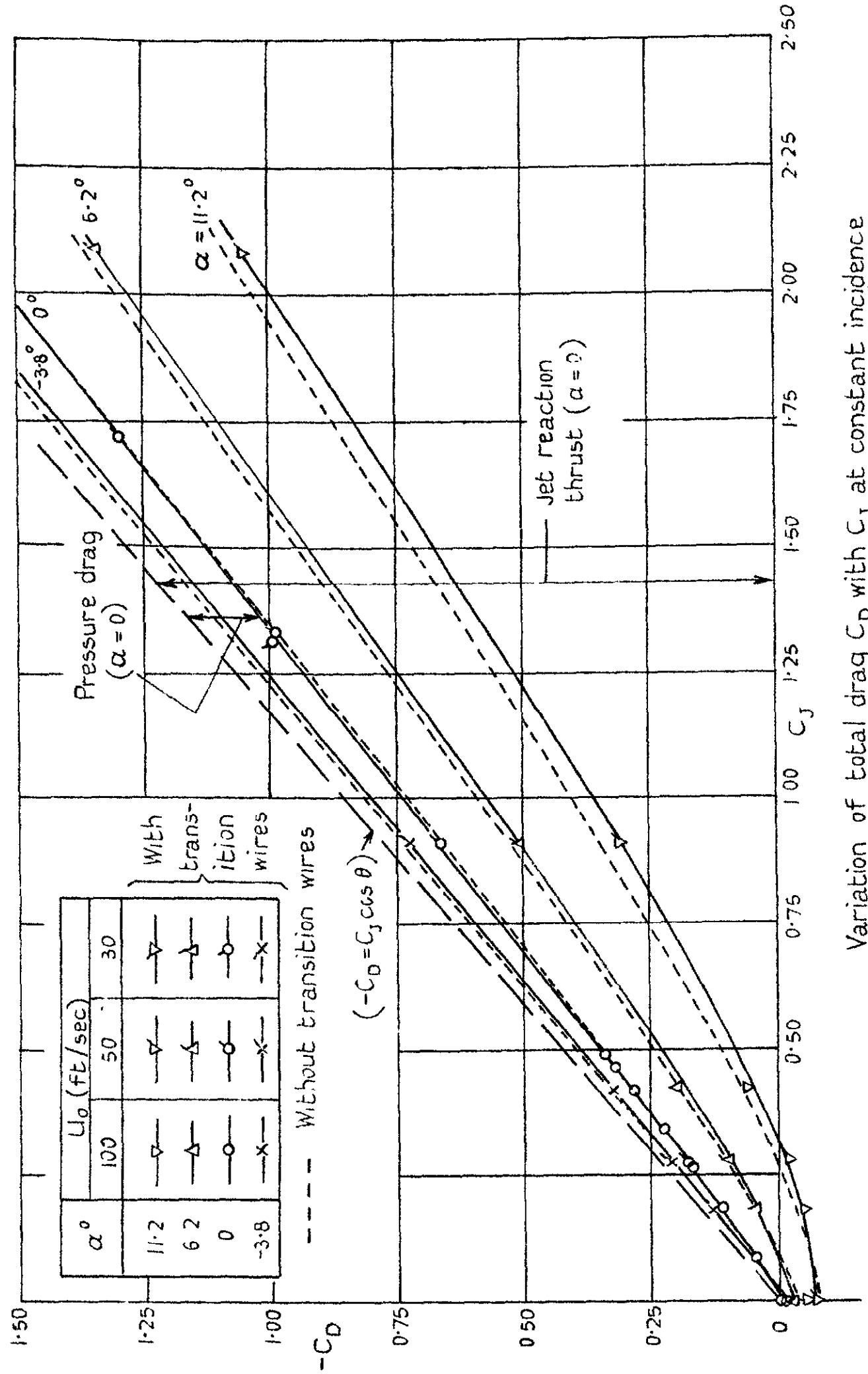

Variation of total drag C_D with C_J at constant incidence

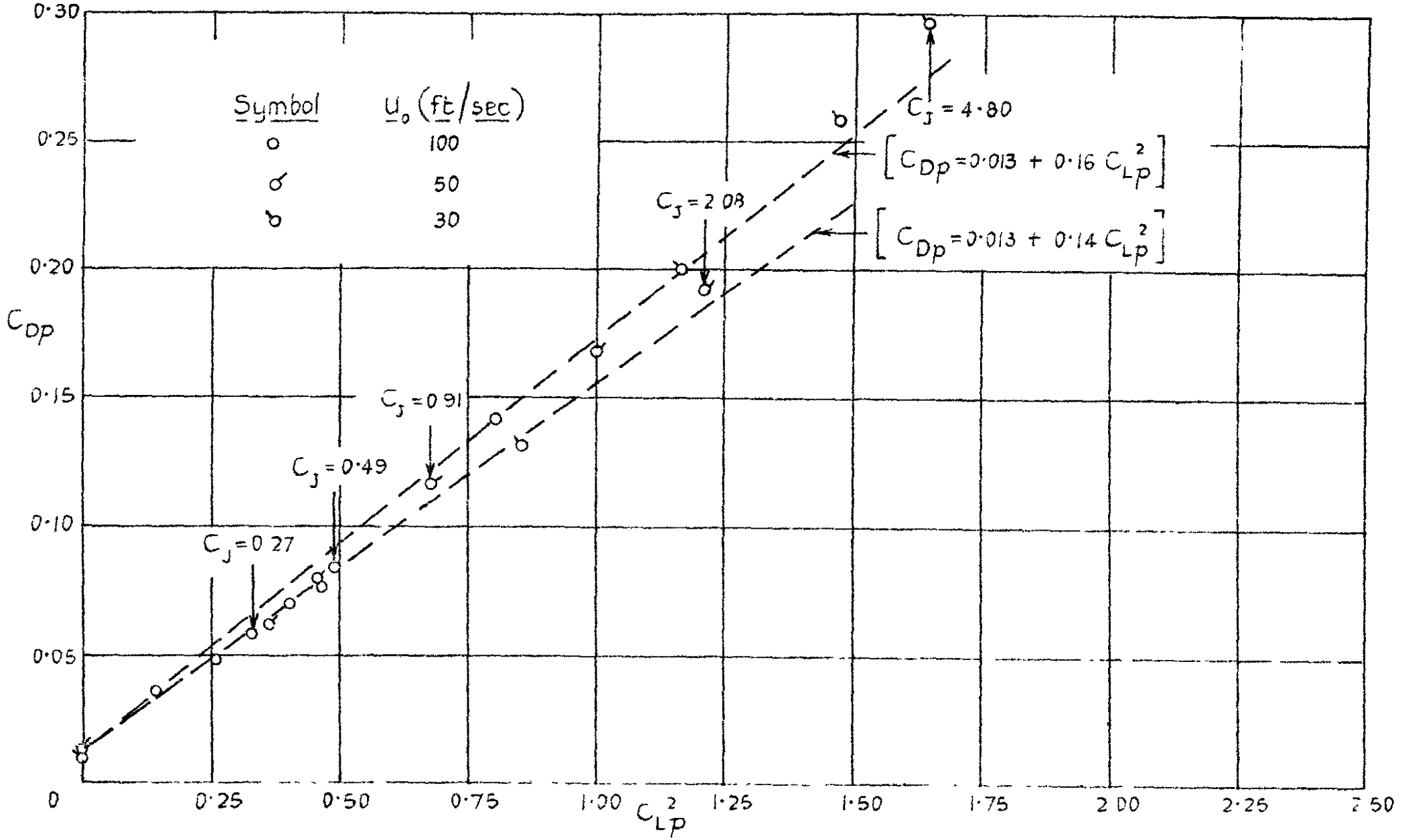

Fig. 8b.

Variation of pressure drag C_{Dp} with C_{Lp}^2 at zero incidence.

FIG. 8c.

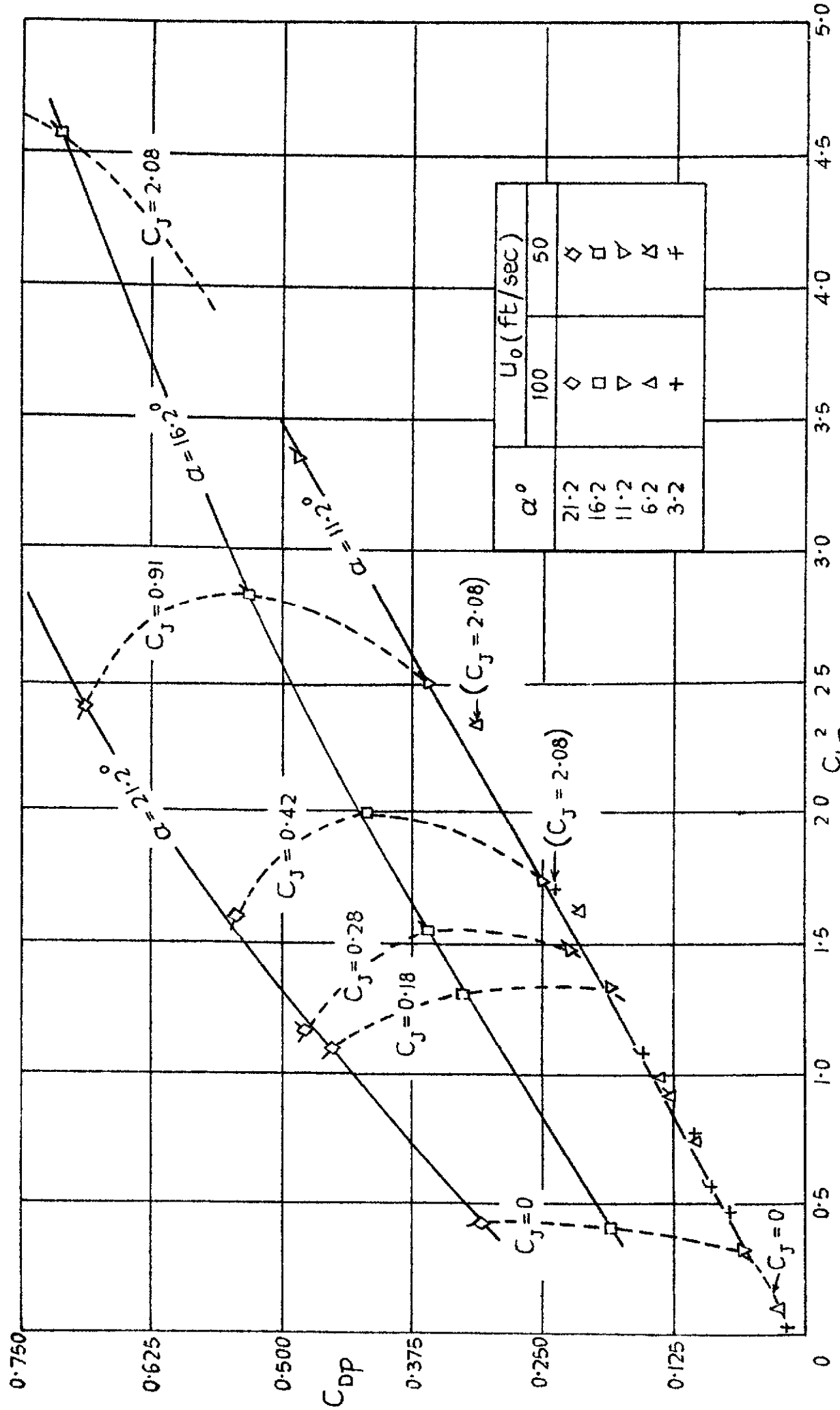

Variation of pressure drag C_{Dp} with C_{Lp}^2.

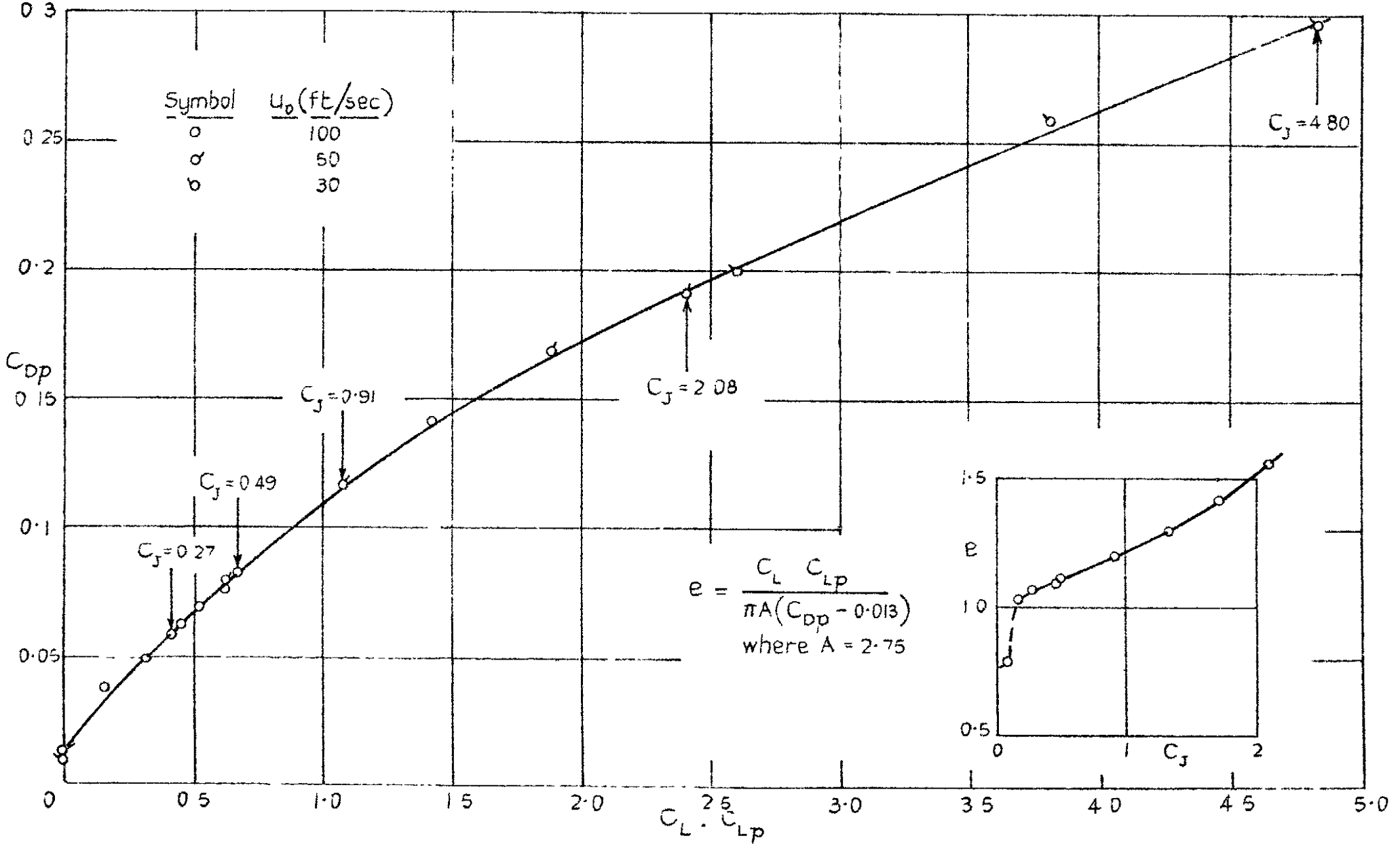

Fig 68

Variation of pressure drag C_{Dp} with $C_L \cdot C_{Lp}$ at zero incidence

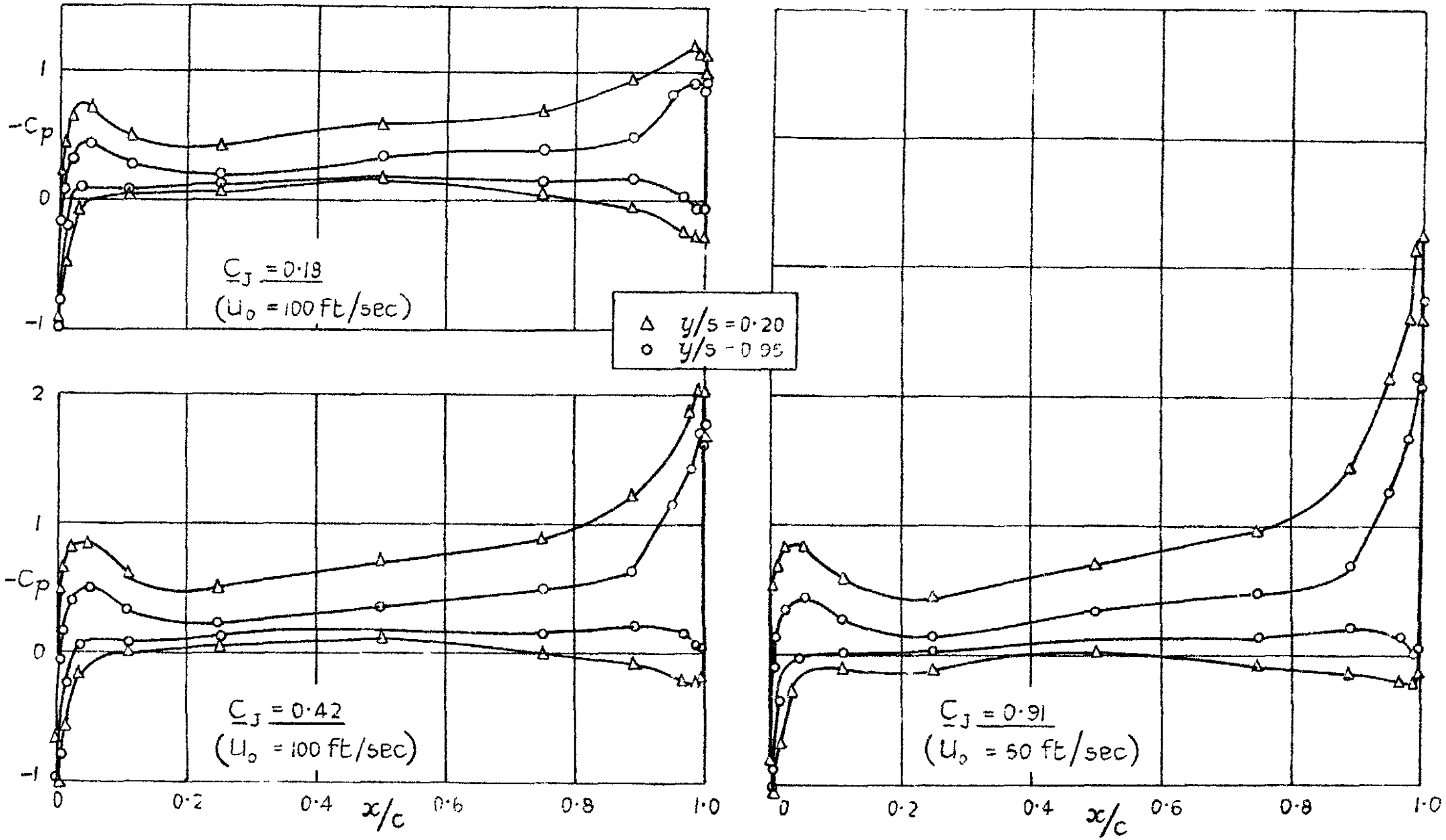

Chordwise pressure distributions at zero incidence Variation with C_J

Fig 9.2

Fig 9b

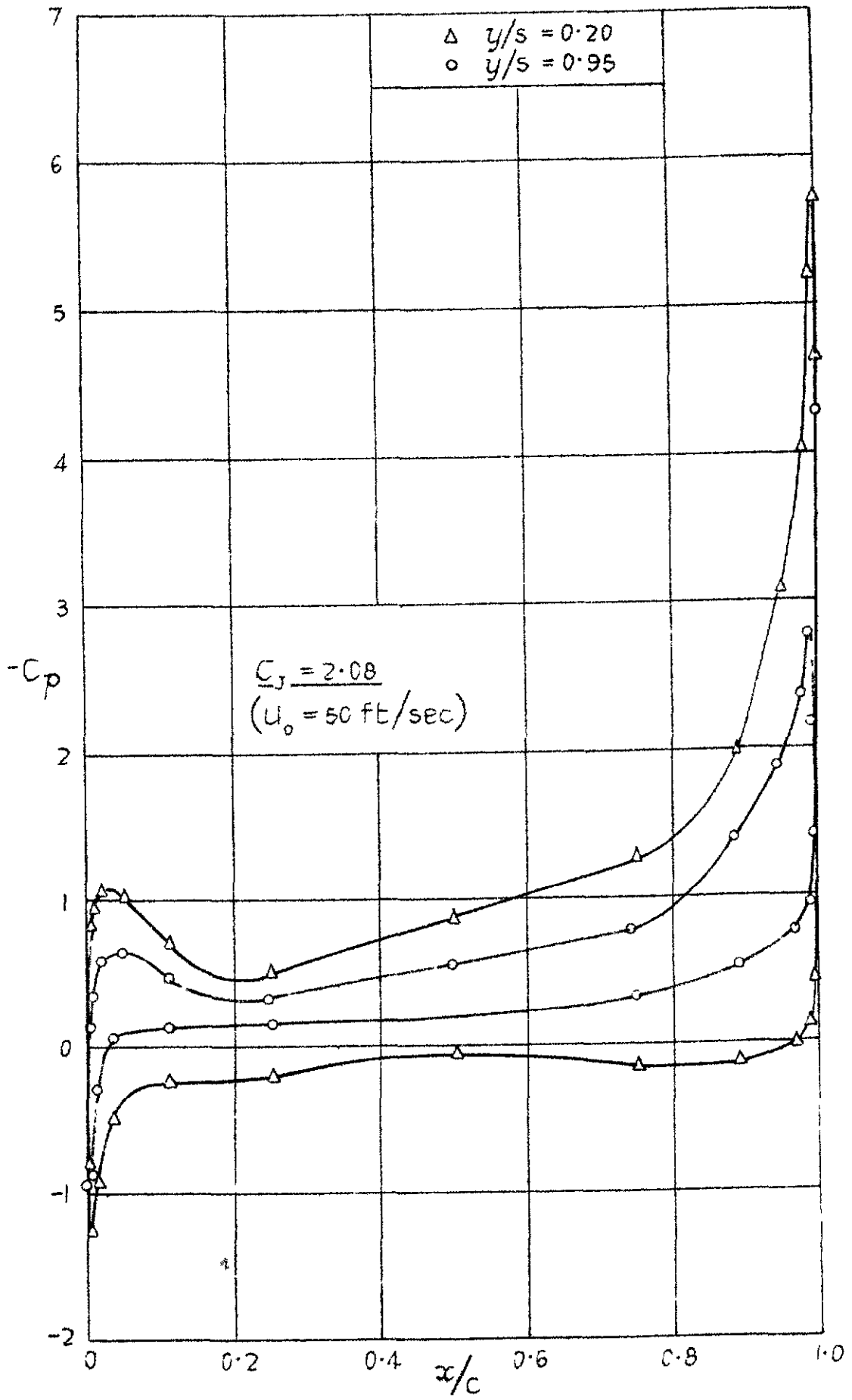

Chordwise pressure distributions at zero incidence
Variation with C_J.

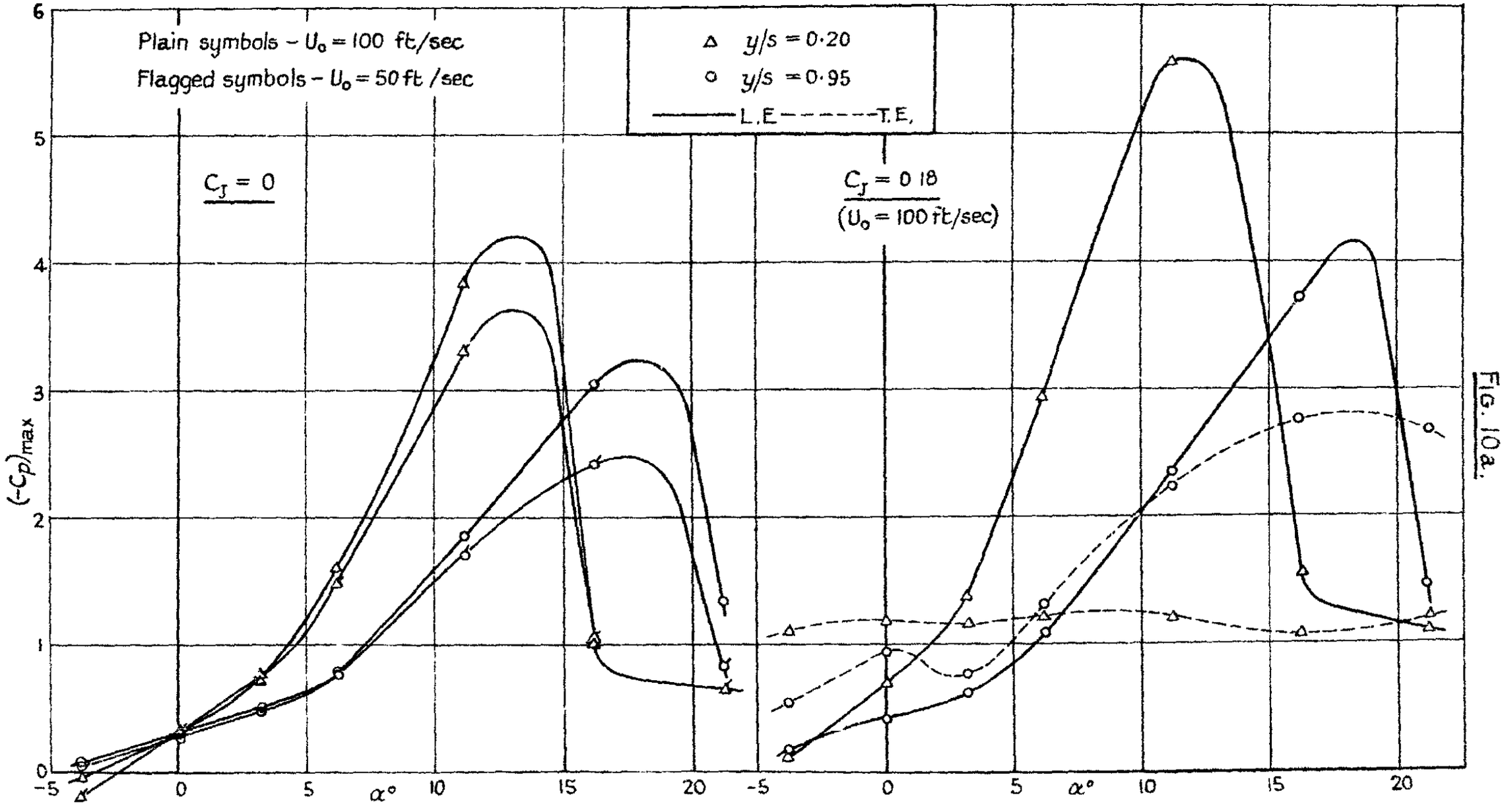

FIG. 10a.

Variation of peak suctions near L.E and T.E.

FIG. 10 c

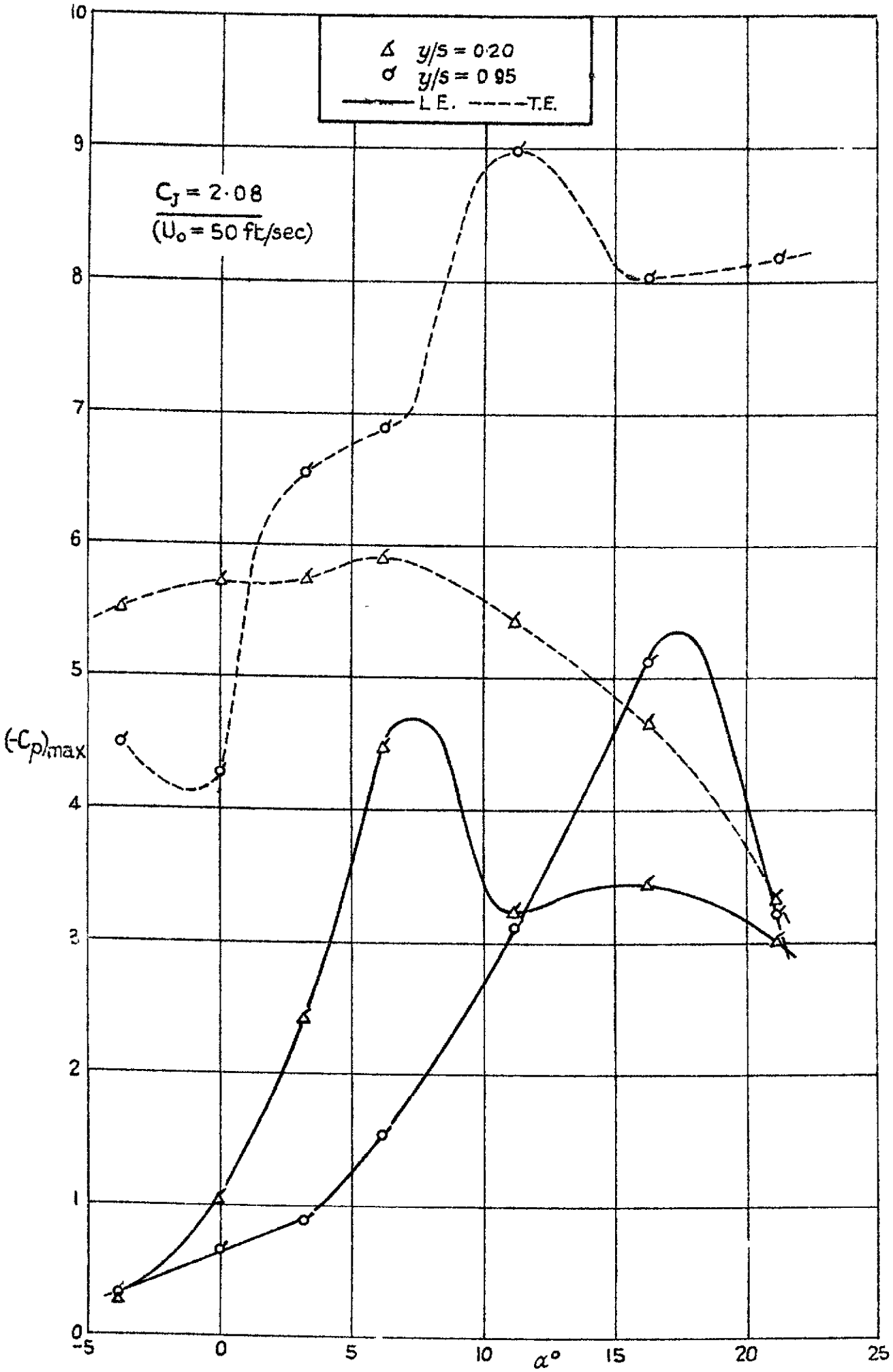

Variation of peak suctions near L.E and T.E

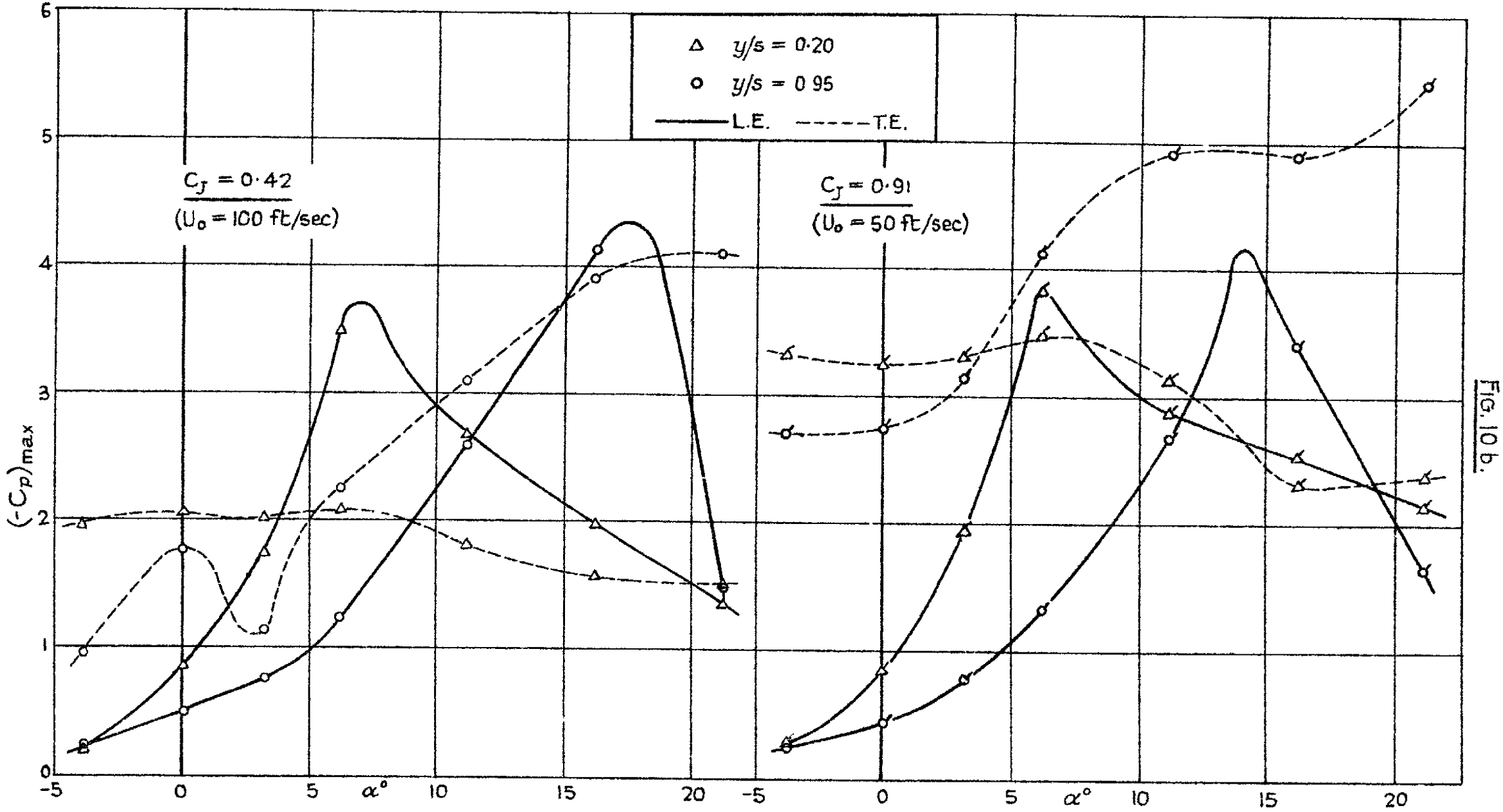

Fig. 10 b.

Variation of peak suctions near L.E. and T.E

FIG. 10 c

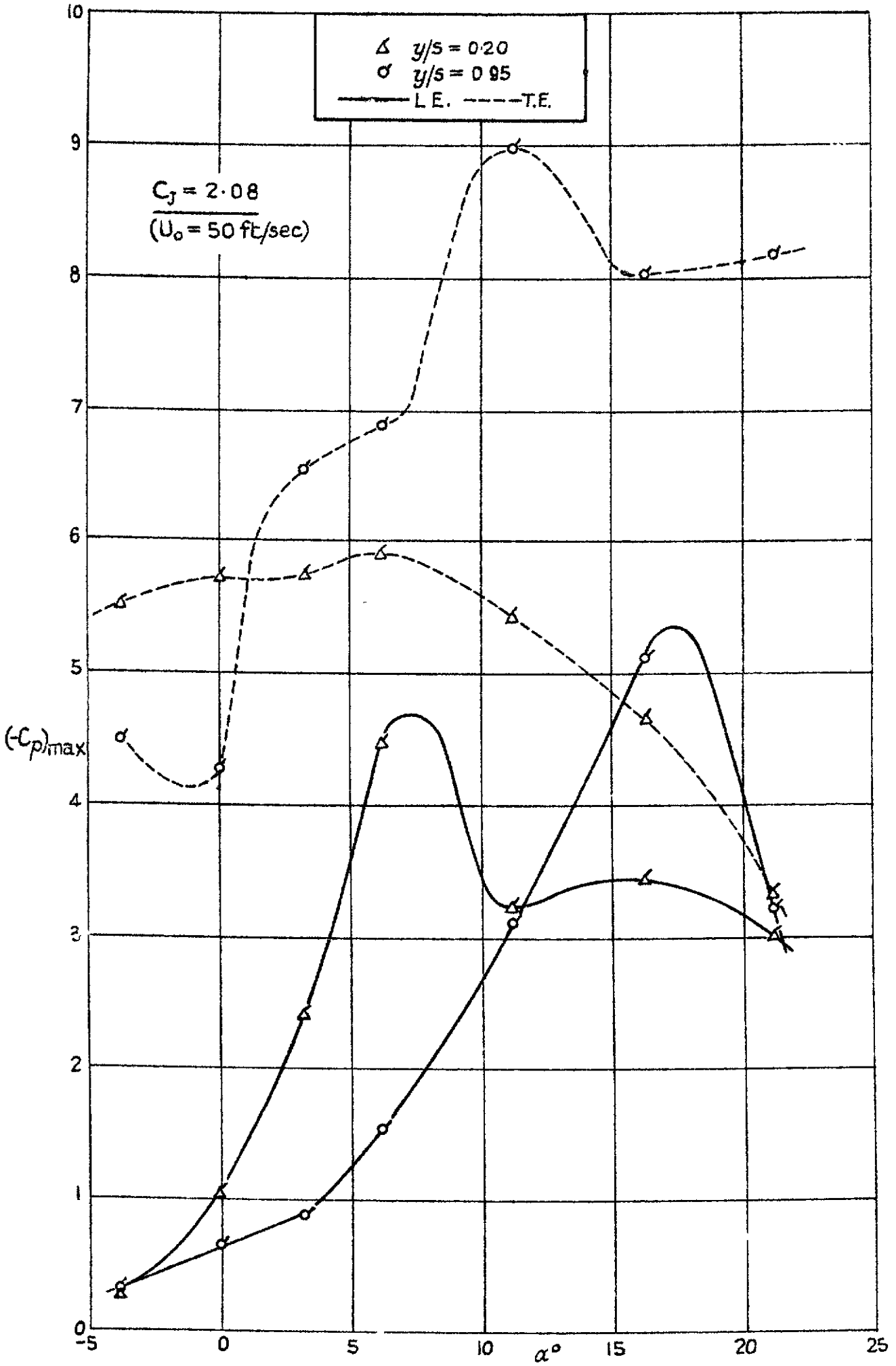

Variation of peak suctions near L.E. and T.E

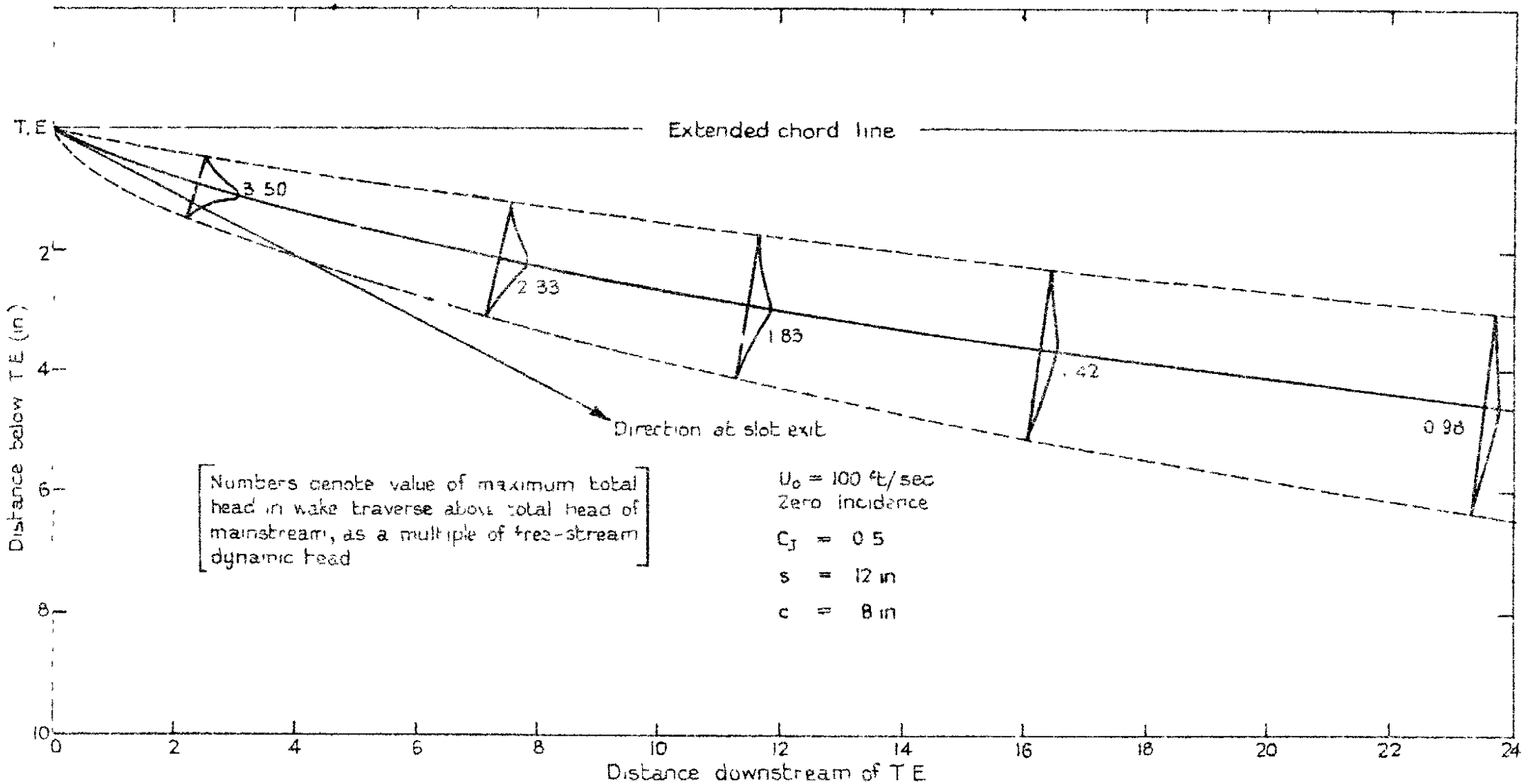

Fig 11a

Mean line and total head profiles of jet at mid-span position

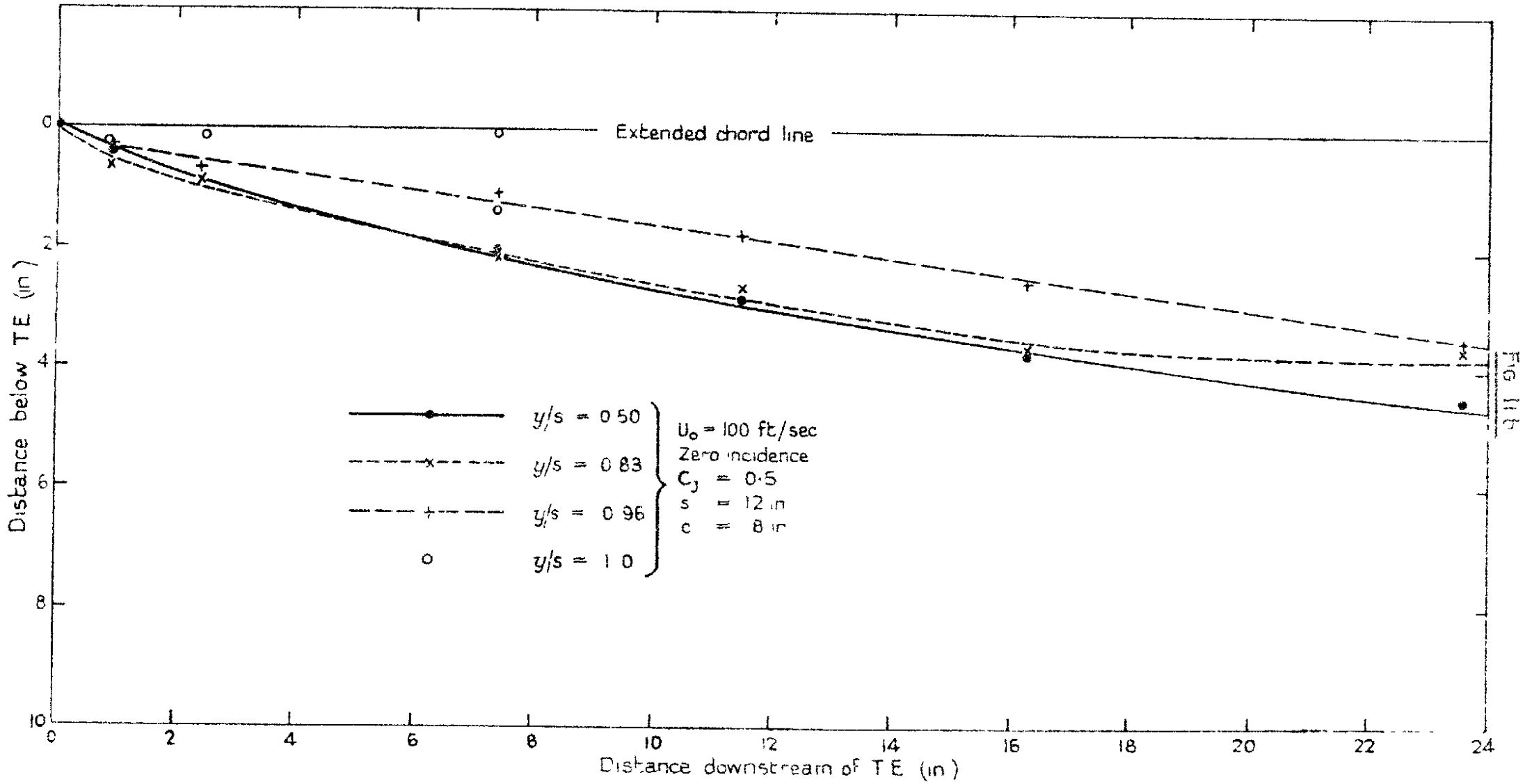

Fig 11b

Spanwise variation of mean line of jet

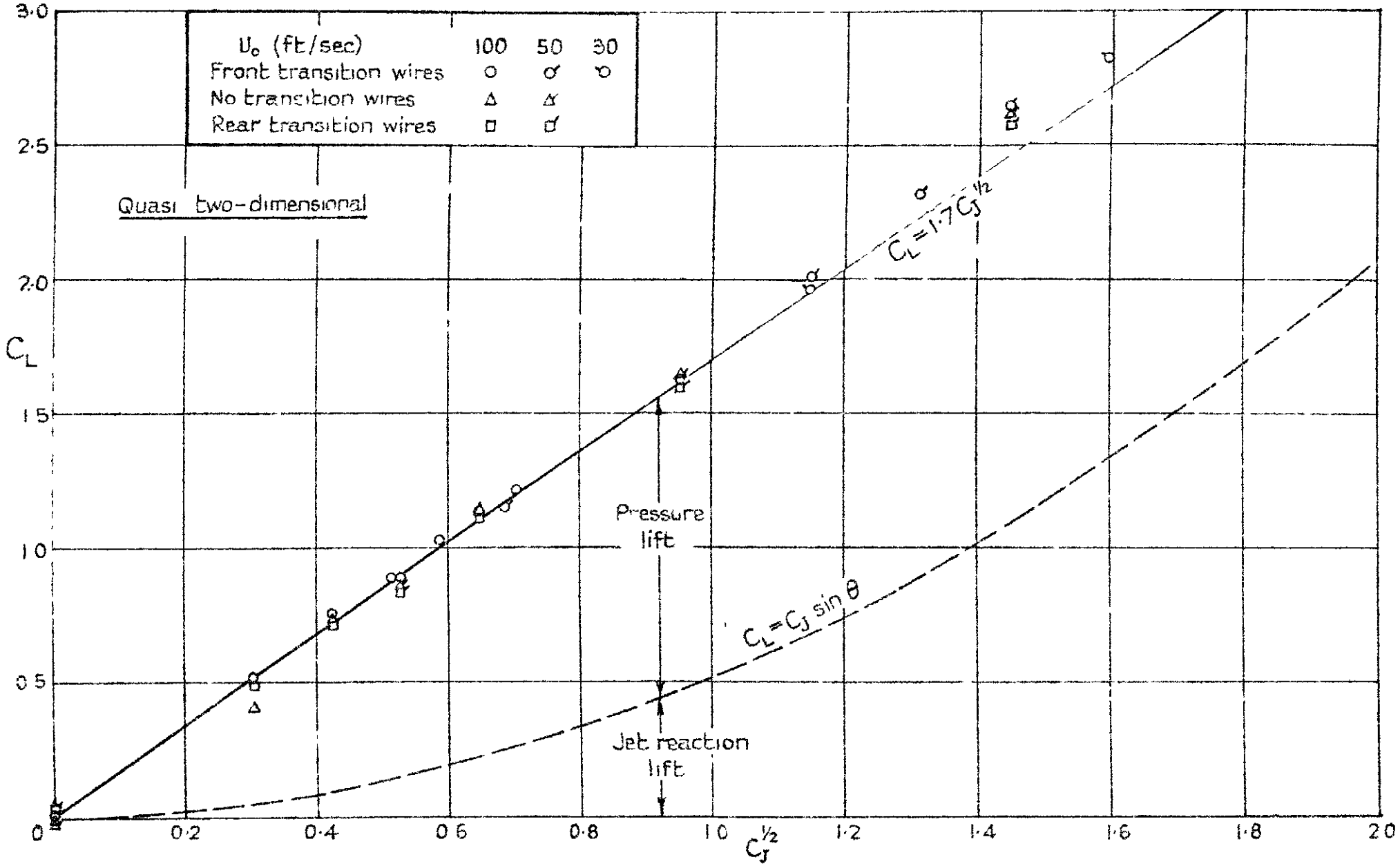

Variation of total lift C_L with $C_J^{1/2}$ at zero incidence

FIG. 12a

Quasi two-dimensional

$\alpha°$	U_0 ft/sec	
	100	50
11 5	▽	▽
6 5	△	△
0	○	○
−3 5	×	×

$\alpha = 11\,5°$

6 5°

0°

−3 5°

C_L

4 5
4 0
3 5
3 0
2 5
2 0
1 5
1 0
0 5
0
−0 5

0 0·2 0·4 0·6 0·8 1·0 1·2 1·4 1·6 1·8 2·0

$C_J^{1/2}$

Variation of total lift C_L with $C_J^{1/2}$ at constant incidence

Fig 13.

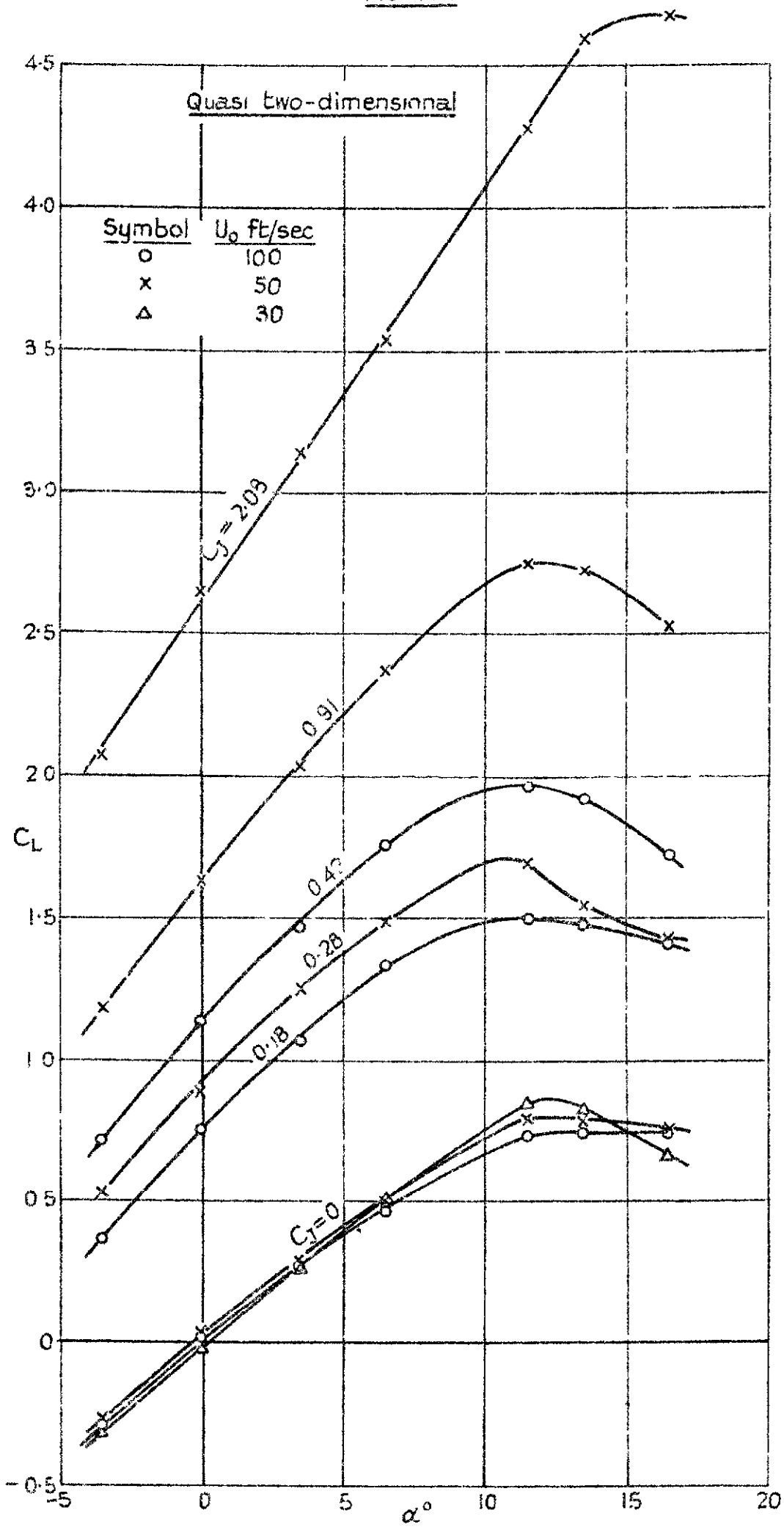

Variation of total lift with incidence at constant C_J

(Ref. 4A/6/18)

FIG. 14.

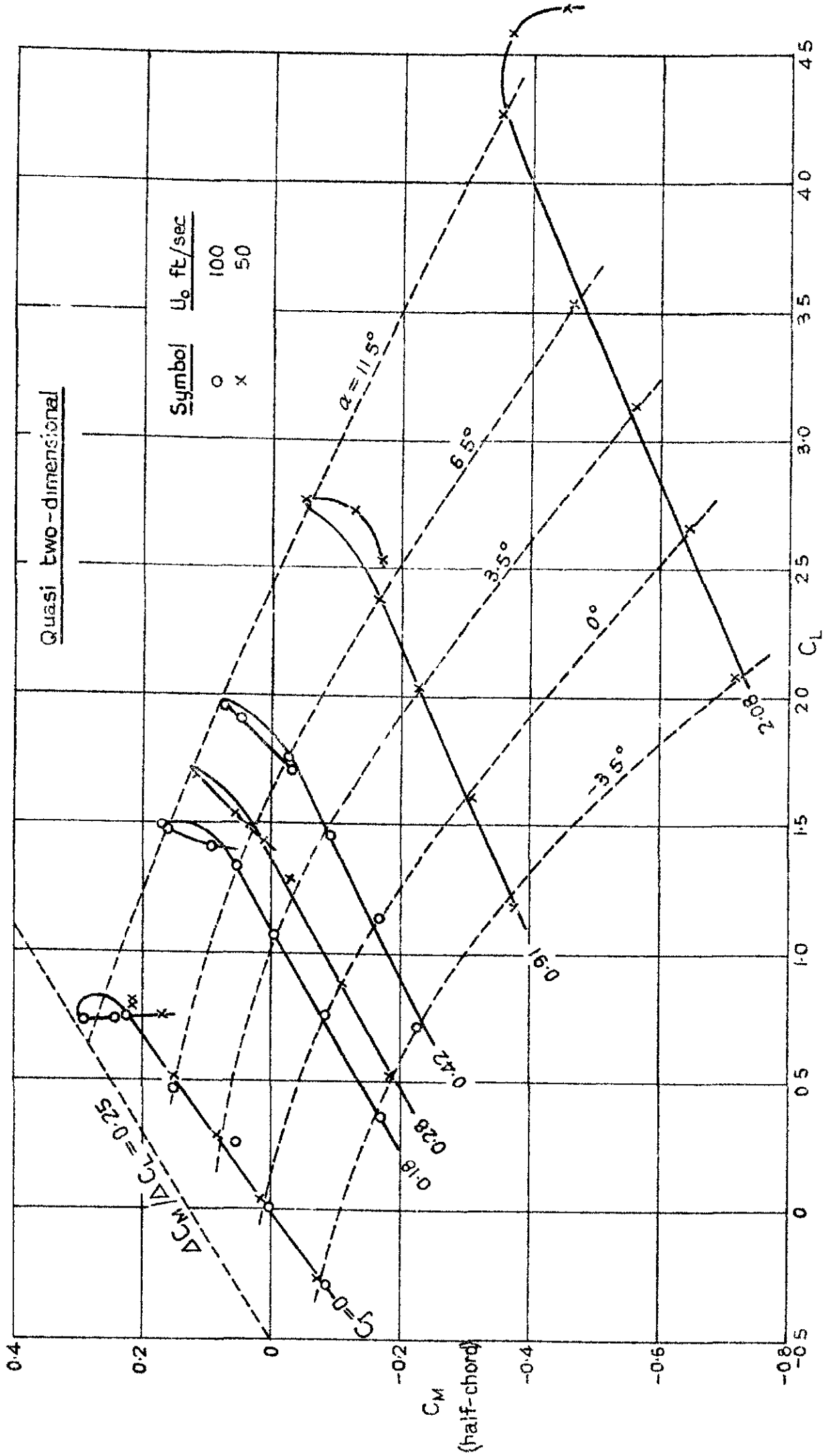

Variation of total pitching moment with total lift

FIG 15

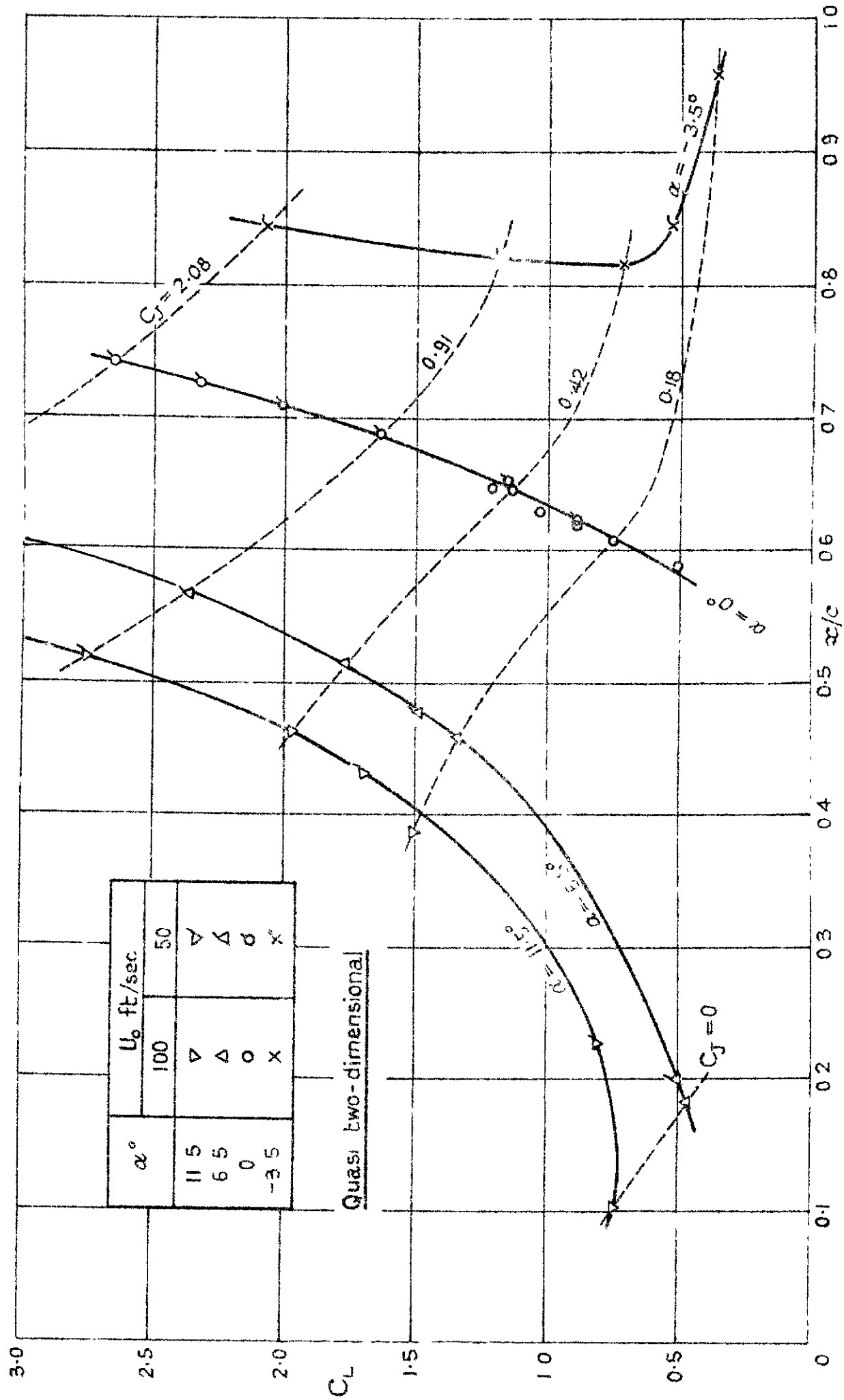

Variation in position of centre of total lift.

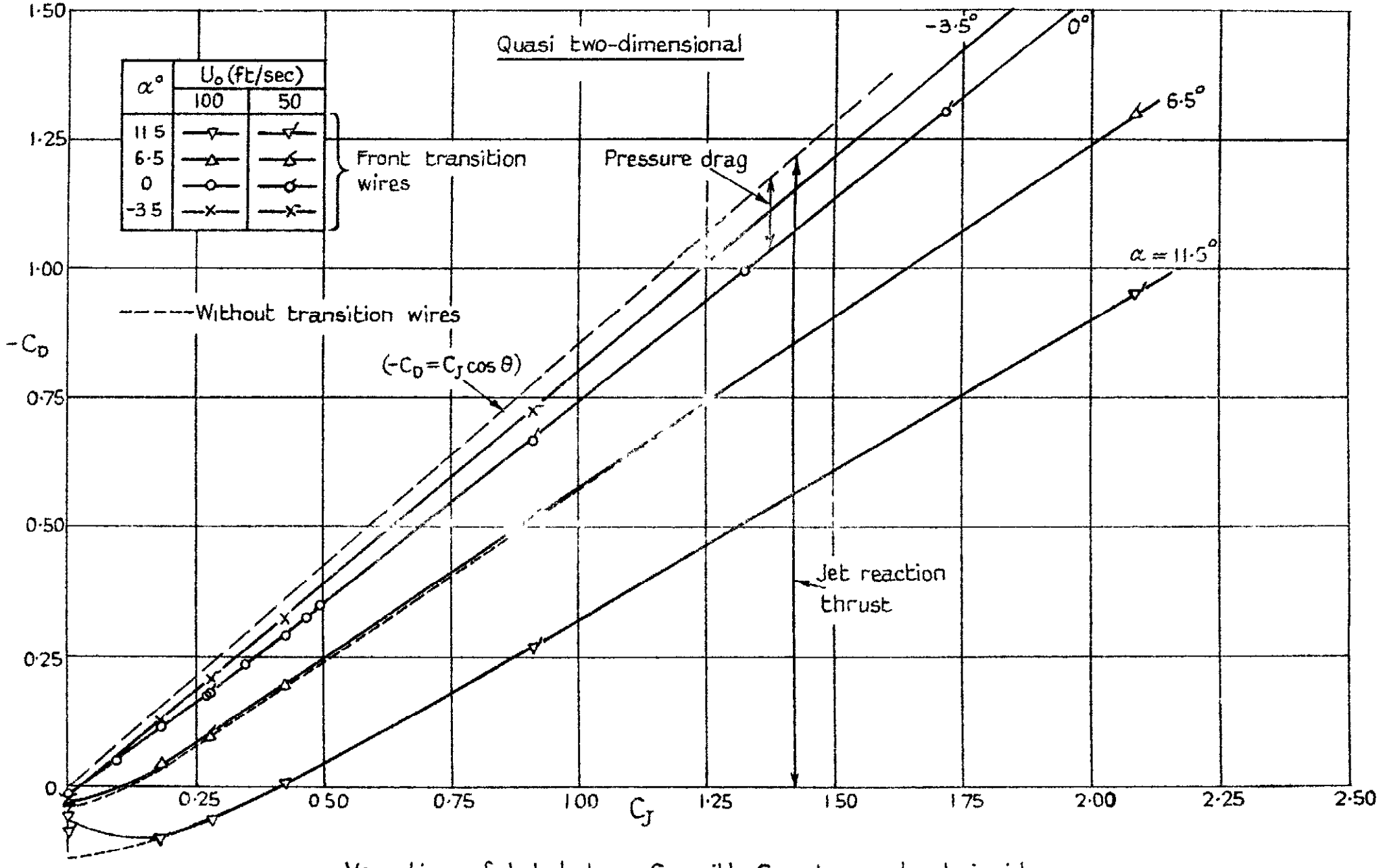

Variation of total drag C_D with C_J at constant incidence

Fig. 15 a.

Fig. 16 b

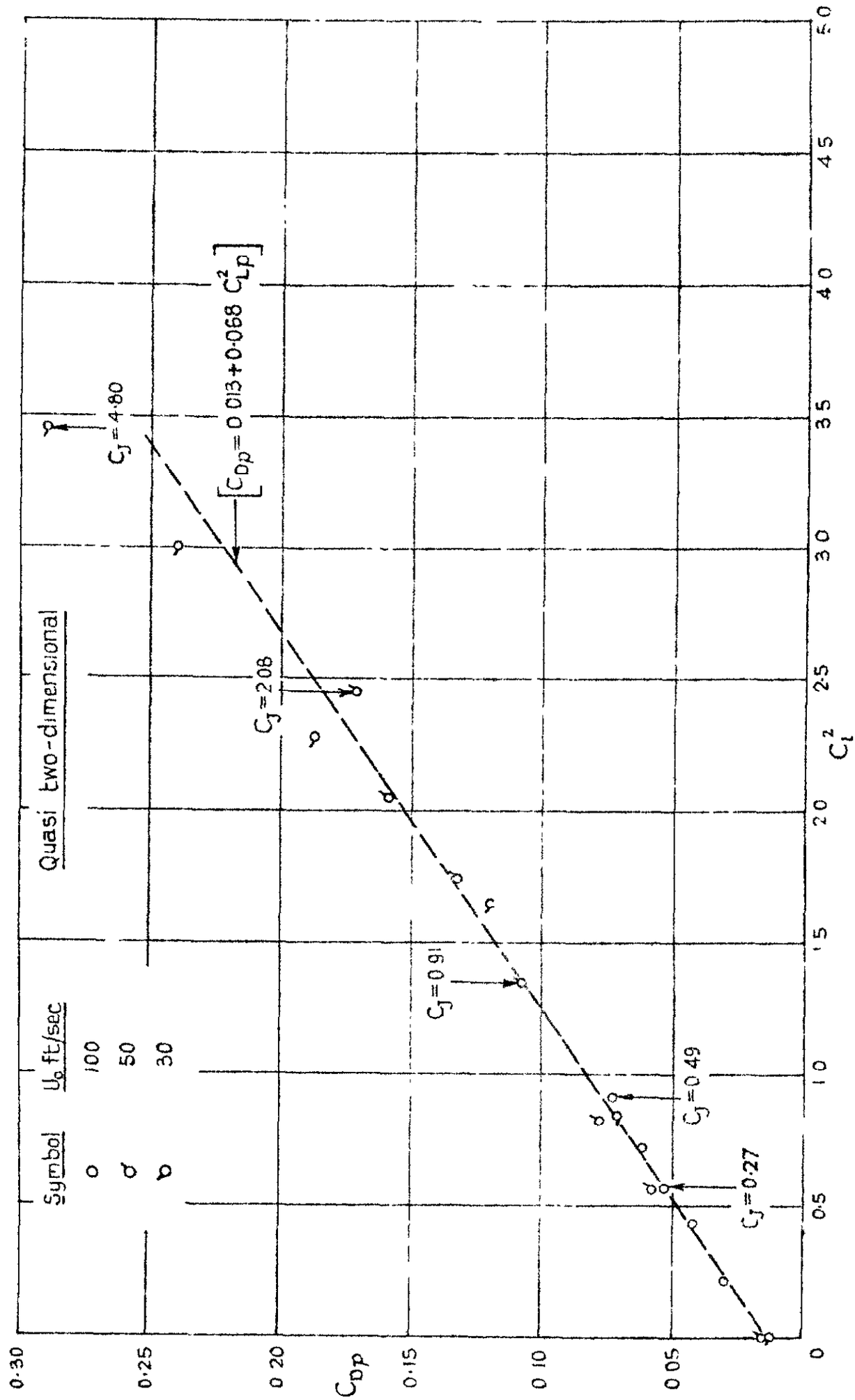

Variation of pressure drag C_D with C_L^2 at zero incidence.

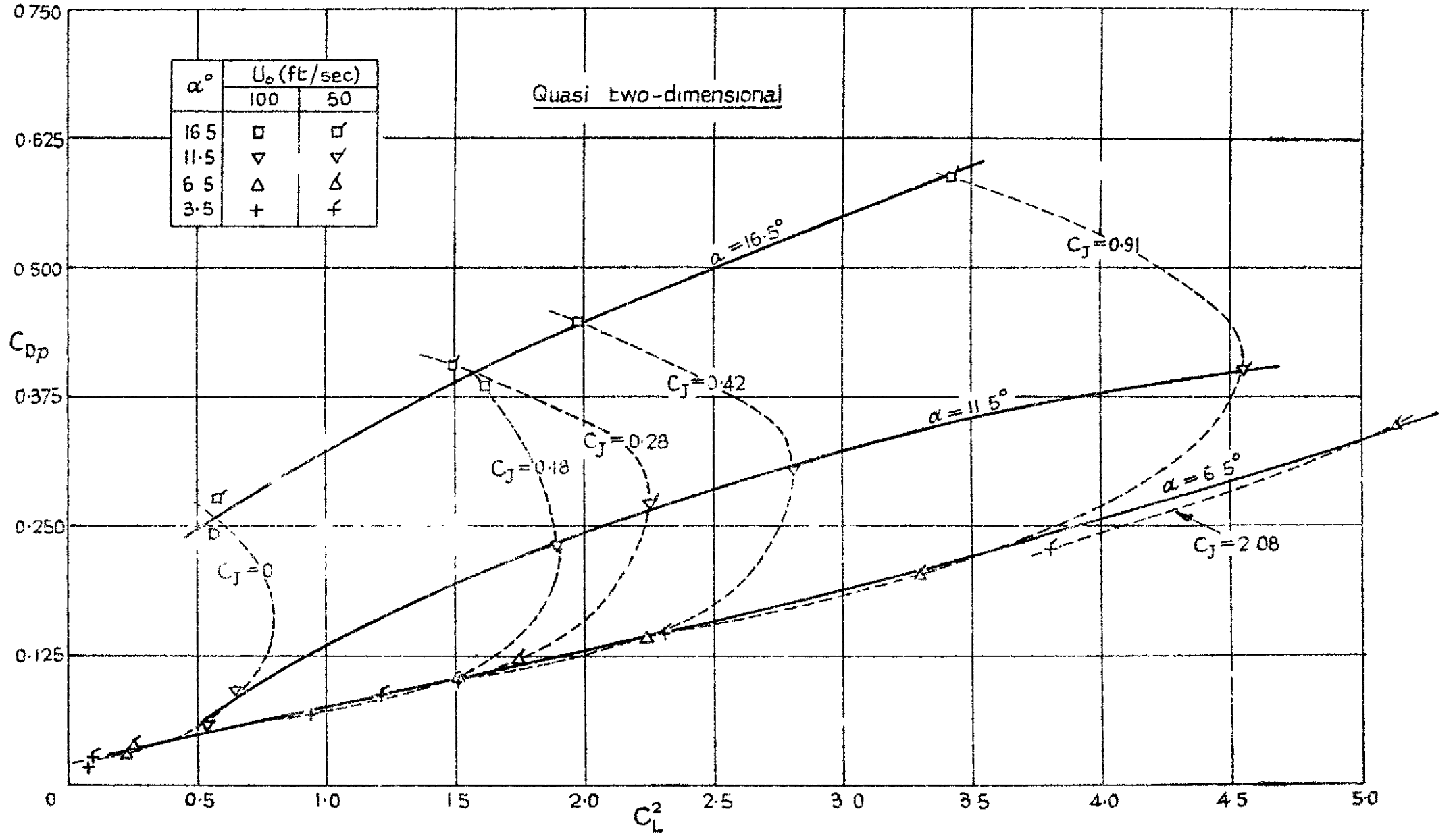

Fig. 16c

Variation of pressure drag C_{Dp} with C_{Lp}^2

FIG. 16 d

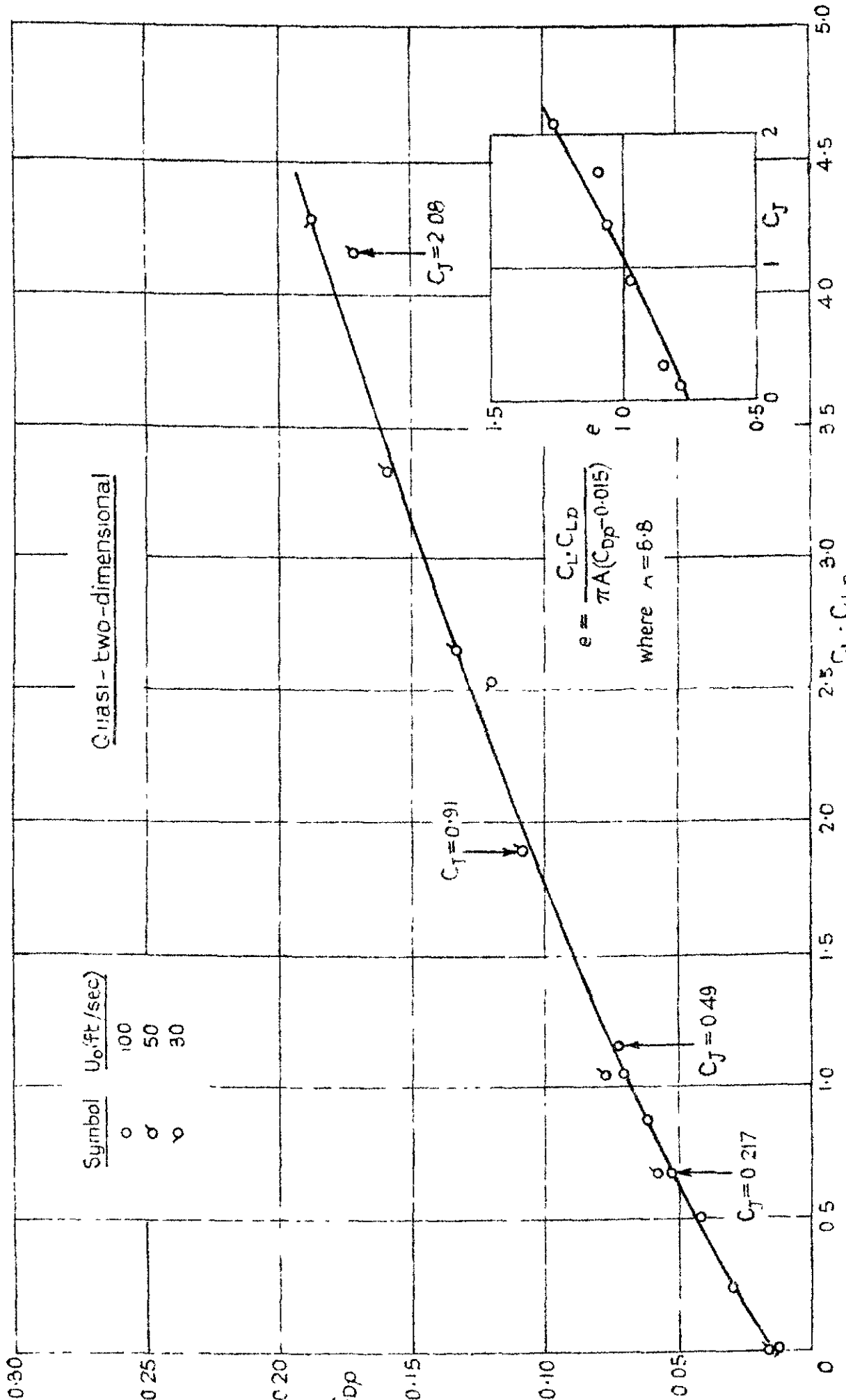

Variation of pressure drag C_{Dp} with $C_L \cdot C_{Lp}$ at zero incidence

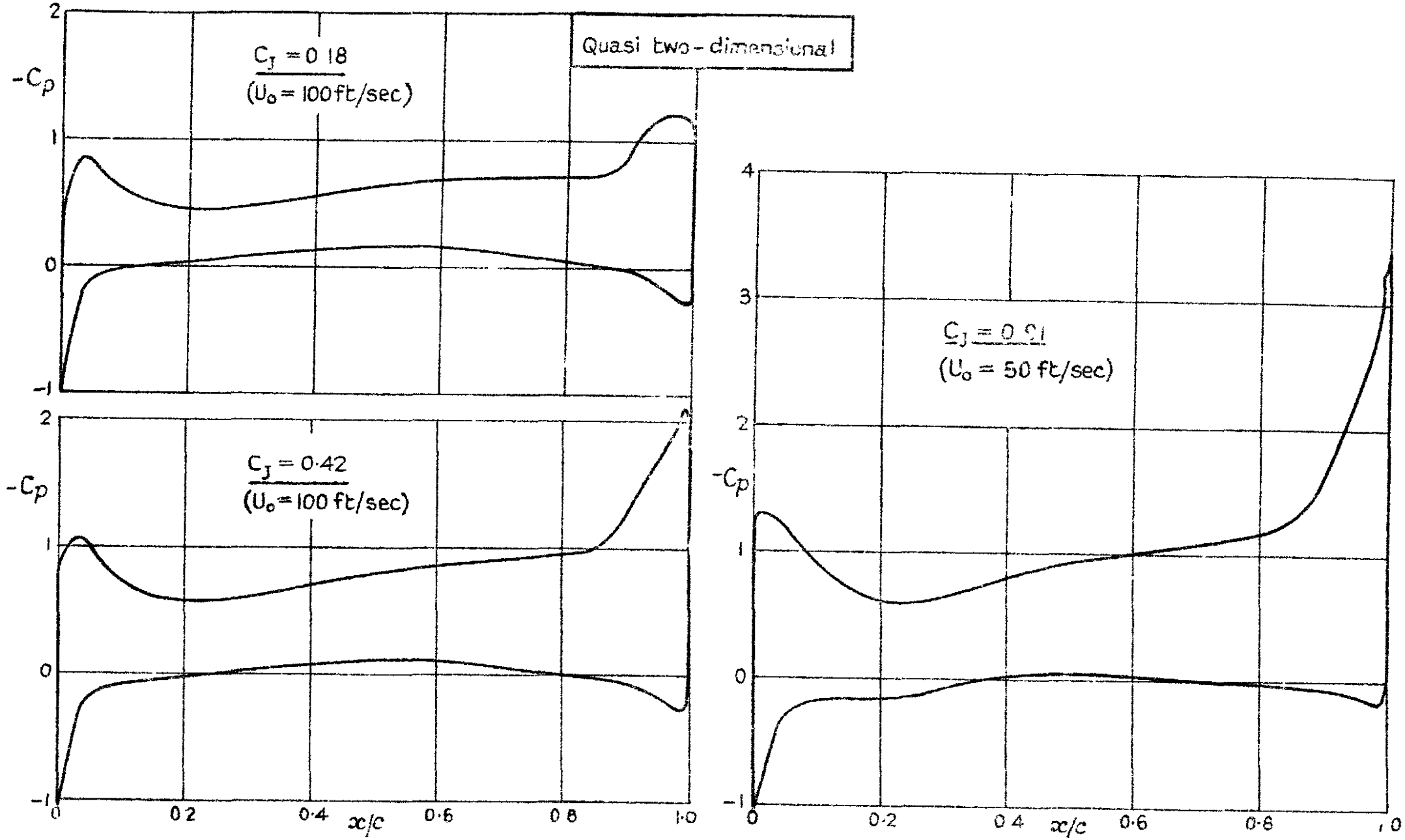

Fig. 17 a.

Chordwise pressure distributions at zero incidence – Variation with C_J.

Fig. 17 a.

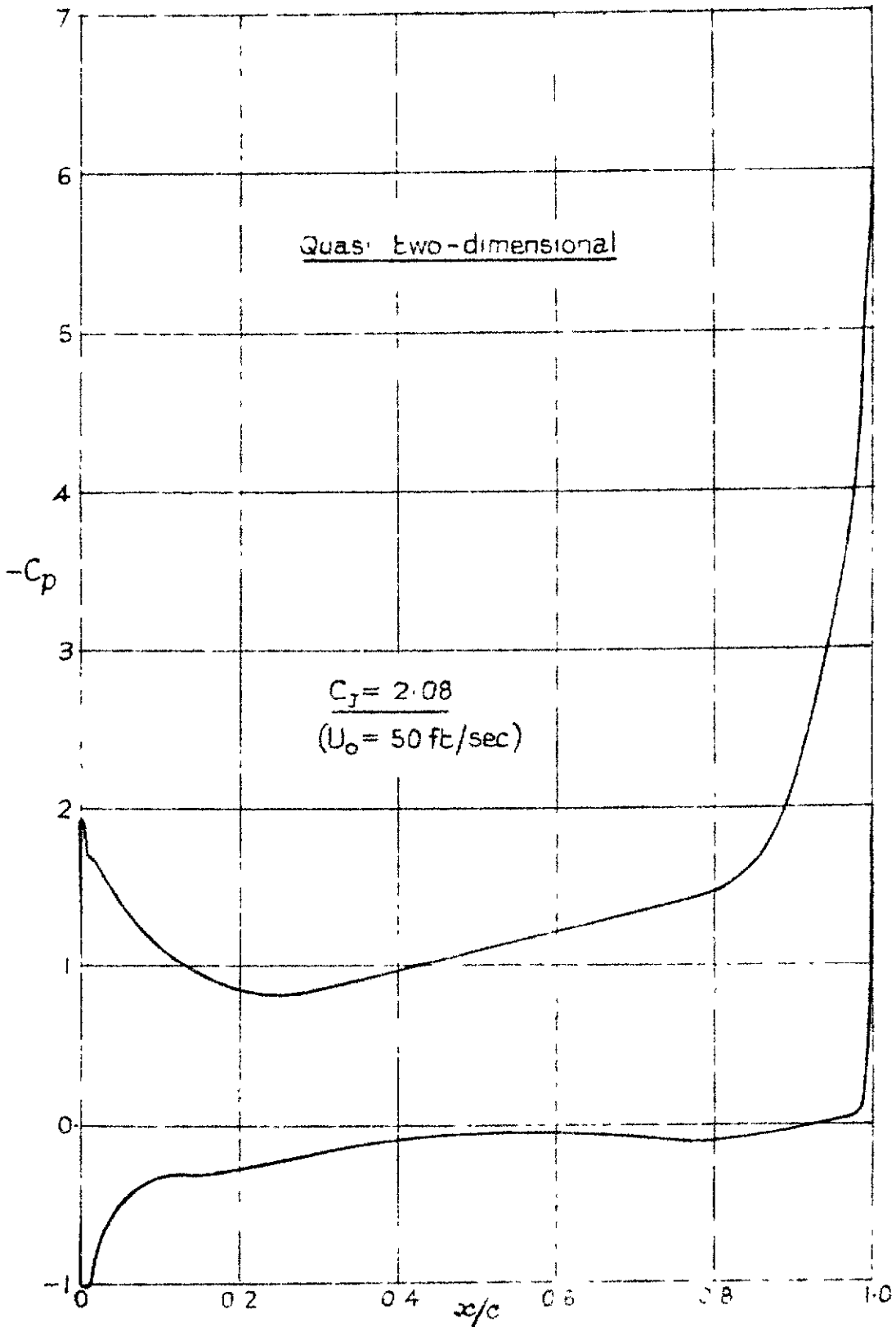

Chordwise pressure distribution at zero incidence – Variation with C_J

FIG. 18 a.

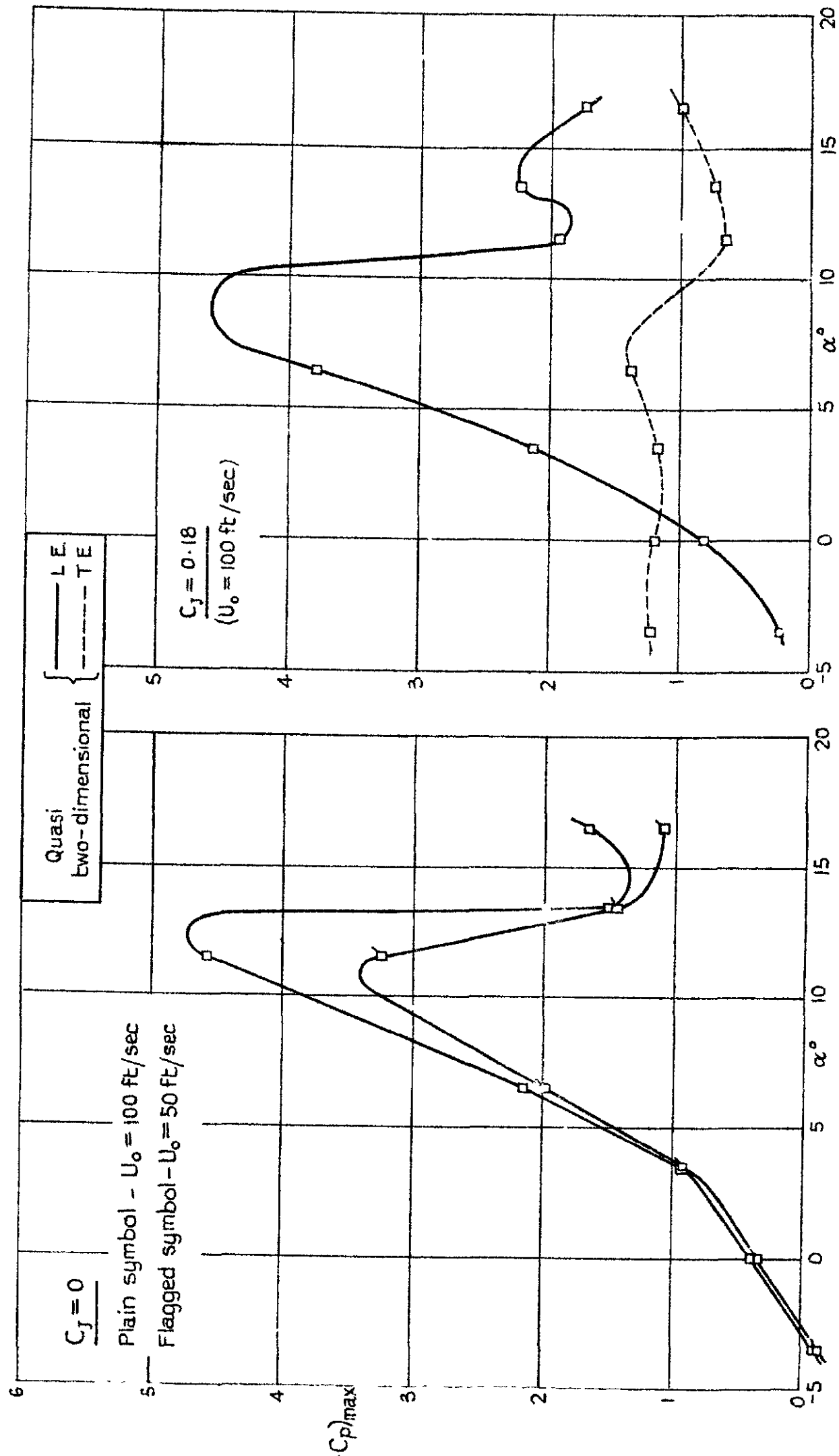

Variation of peak suctions near L.E and T.E.

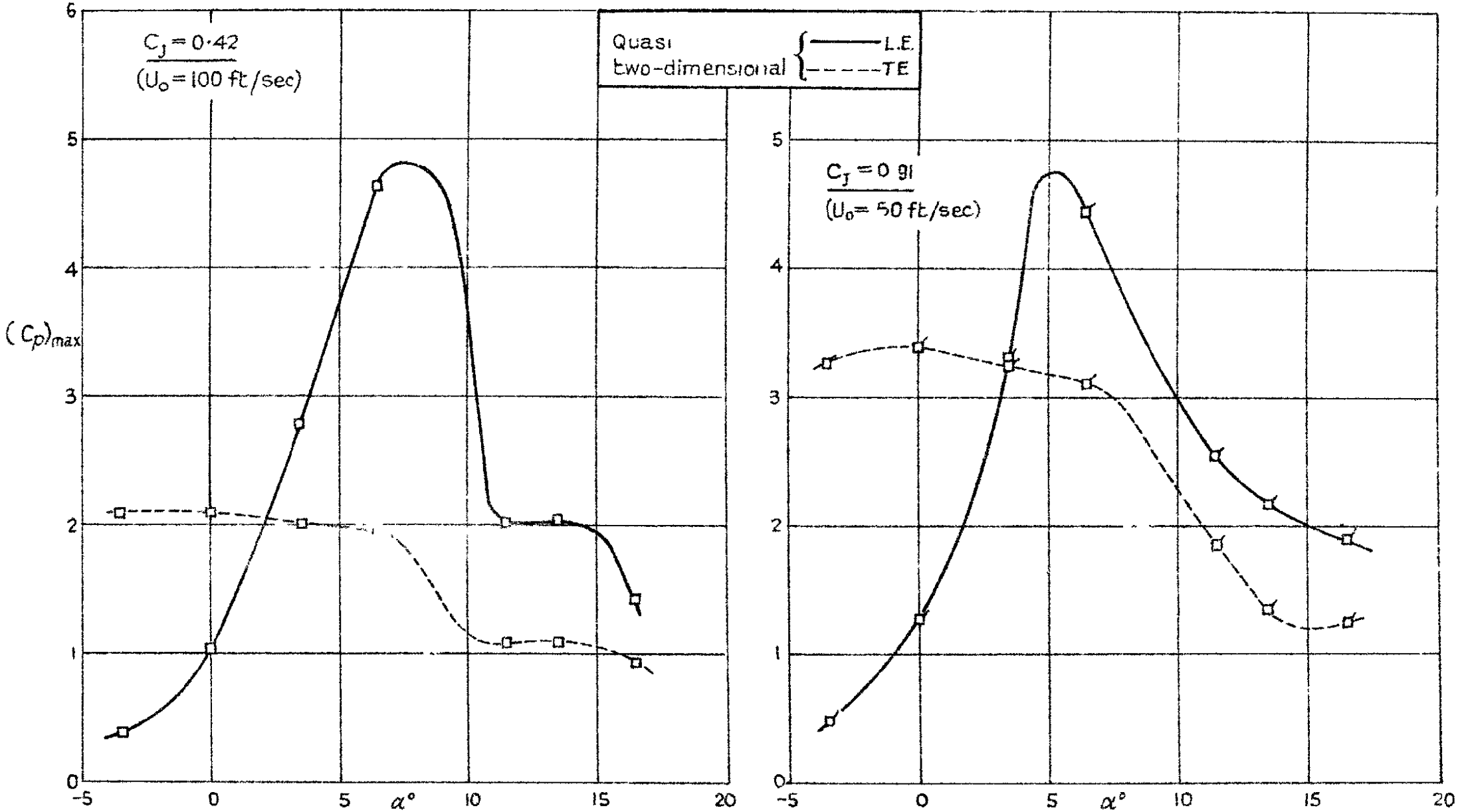

Fig. 18b

Variation of peak suction near L.E. and T.E.

FIG. 18c.

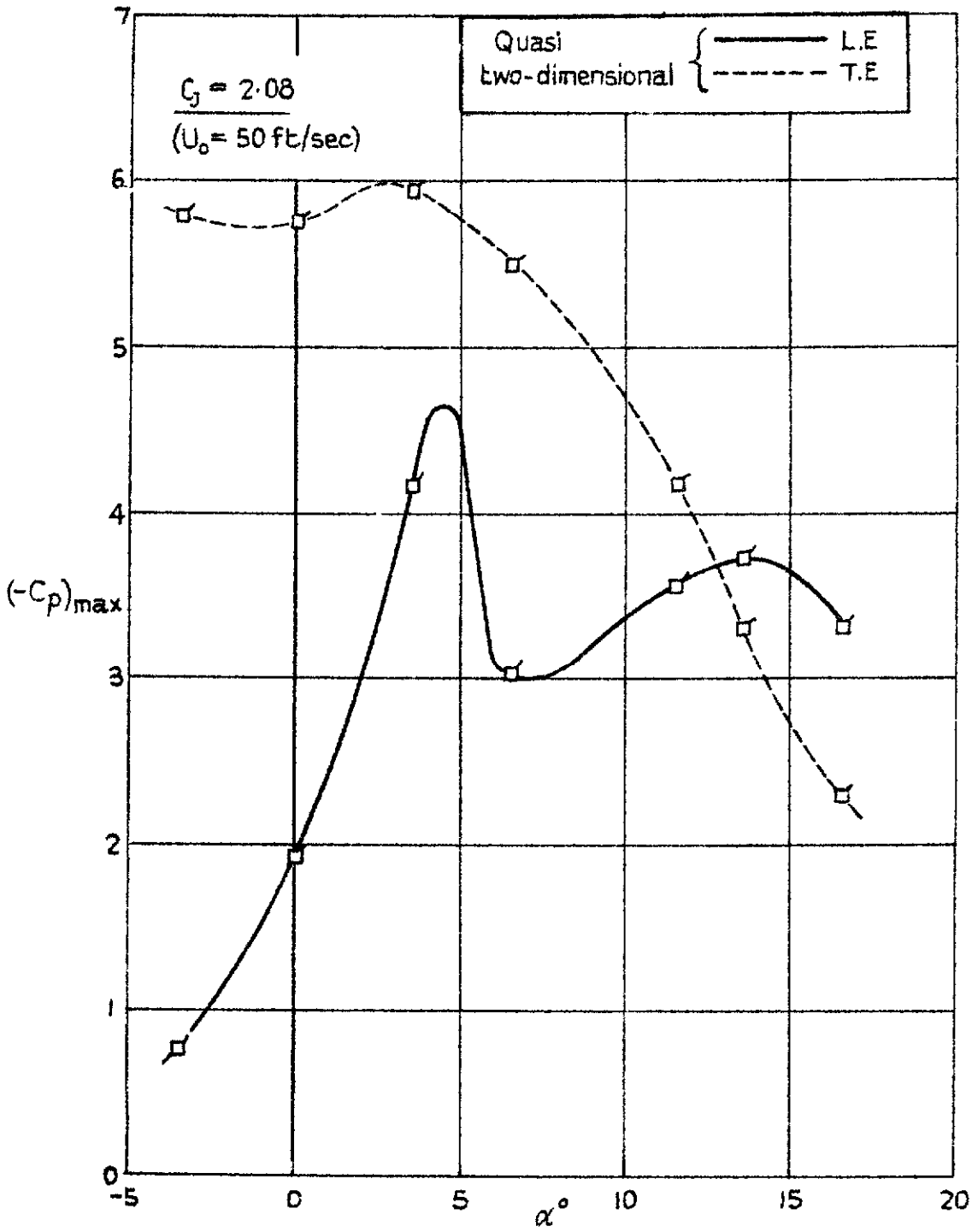

Variation of peak suction near L.E. and T.E.

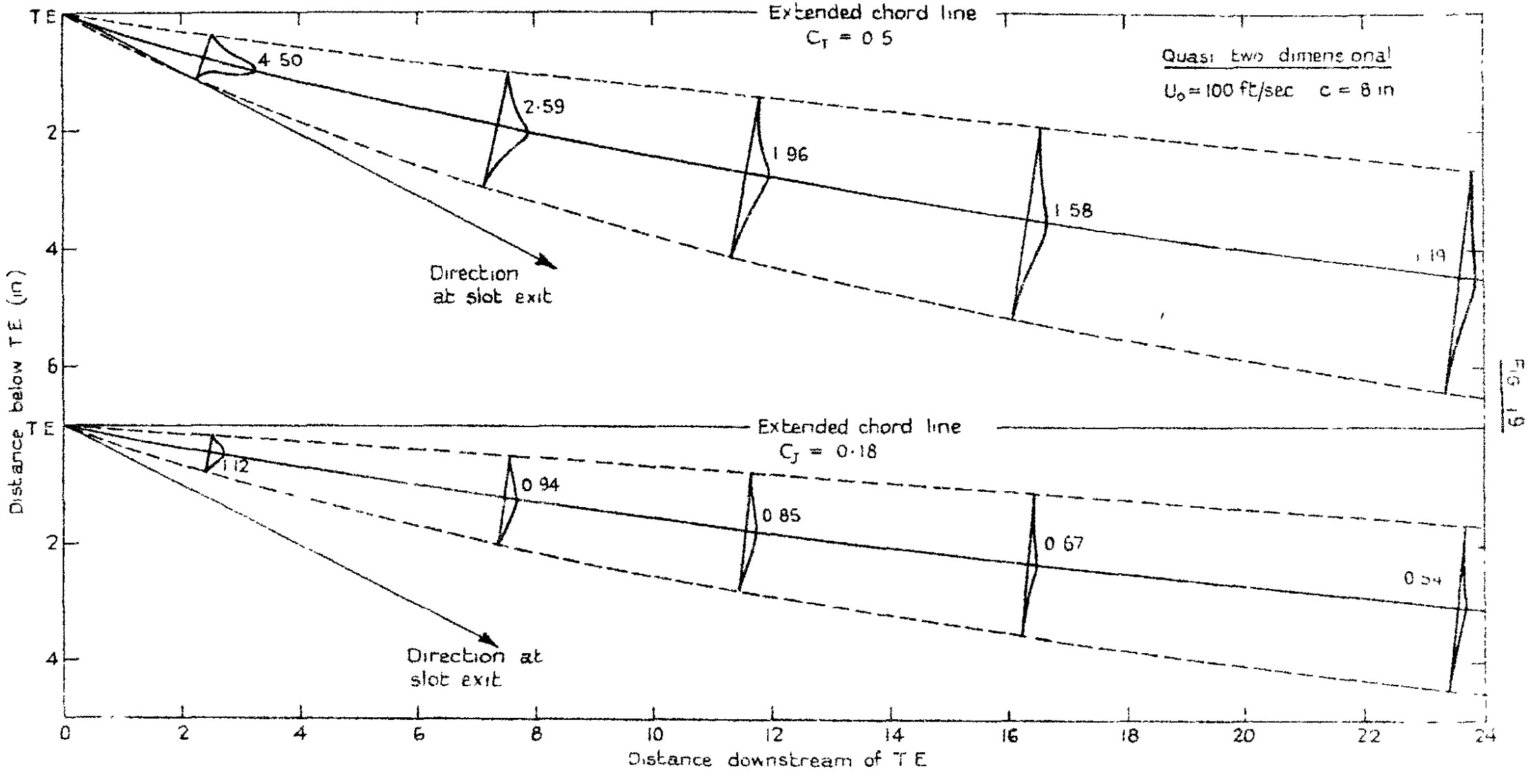

Fig 19

Mean line and total head profiles of jet

Printed and published by
HER MAJESTY'S STATIONERY OFFICE

To be purchased from
York House, Kingsway, London W C 2
423 Oxford Street, London W.1
P O Box 569, London S.E.1
13A Castle Street, Edinburgh 2
109 St. Mary Street, Cardiff
39 King Street, Manchester 2
Tower Lane, Bristol 1
2 Edmund Street, Birmingham 3
80 Chichester Street, Belfast
or through any bookseller

Printed in Great Britain

S.O Code No. 23-9010-4

C.P. No. 311
(18,836)
A.R.C. Technical Report

C.P. No. 311
(18,836)
A.R.C. Technical Report

MINISTRY OF SUPPLY

AERONAUTICAL RESEARCH COUNCIL

CURRENT PAPERS

Turbulence Encountered by Viking Aircraft over Europe

By

J. R. Heath-Smith, B.Sc.(Eng.)

LONDON: HER MAJESTY'S STATIONERY OFFICE

1957

THREE SHILLINGS NET

C.P. No. 311

U.D.C. No. 551.551(4) Viking

Technical Note No. Structures 204

July, 1956

ROYAL AIRCRAFT ESTABLISHMENT

Turbulence encountered by Viking aircraft over Europe

by

J. R. Heath-Smith, B.Sc.(Eng)

SUMMARY

Accelerations in turbulence were recorded on B.E.A. Viking aircraft for 117,000 miles of flying over European routes during three years.

The records show that the number of gusts decreases from sea level to 8000 feet. There is some evidence below 5000 feet that turbulence is greatest in Spring and least in Autumn.

Average gust frequencies during climb and descent were twice those during cruise below 8000 feet and this is attributed to the pilot's discretion in the choice of cruising altitude.

LIST OF CONTENTS

LIST OF APPENDICES

LIST OF TABLES

LIST OF ILLUSTRATIONS

1 Introduction

From November 1951 to November 1954 a Counting Accelerometer was carried in a Viking aircraft of British European Airways, which was operated on normal passenger service over Europe. The records obtained represent 117,000 miles of flight below 10,000 feet.

The data are examined to determine the variation in turbulence with altitude and with season.

2 Description of Equipment and Flying

2.1 Instrument and Installation

The Counting Accelerometer[1] responds to the accelerations imposed on it along one axis and records the number of times each of a series of acceleration levels has been exceeded. Successive counters represent levels at intervals of 0.1g and readings are given for a range of 1.2g to 2.9g for upward accelerations and from 0.8g to -0.9g for downward accelerations. The above values are nominal and have been corrected in this report except where it is stated otherwise. An altimeter, airspeed indicator and spring-driven clock are grouped around the counter dial and the whole assembly is photographed at regular intervals of approximately 10 minutes.

The Counting Accelerometer was rigidly attached to the airframe in the forward luggage compartment about three feet ahead of the centre of gravity of the aircraft and in such an attitude that vertical accelerations were measured when the aircraft was in cruising flight.

2.2 The flying covered by the records

The records were obtained between November 1951 and November 1954 on 350 flights covering 117,000 miles of operational flying on European routes based on London. The distribution of recording time between months of the year is shown in Fig 1. The instrument was carried at different times in Viking aircraft G-AIVH and G-AMGJ.

3 Variation in turbulence with altitude

The recording intervals are of average duration 10.5 minutes and contain the total counts of acceleration during this interval and the speed and height of the aircraft at the end of this interval. Appendix I describes various corrections which are made to these readings and the method of translating the accelerations into gust speeds.

Table I is a summary of the time spent at each speed and altitude during climb, cruise and descent. Table II is a summary of the counts of acceleration grouped according to speed, weight and altitude. Table III is an estimate of the gust speeds encountered in each altitude band during climb, cruise and descent. As the climb and descent gust frequencies are similar they are shown separately and combined.

Fig 2 shows the gust frequencies in each altitude band for cruise and for climb and descent. Fig 3 shows directly the variation with altitude of the frequency of gusts greater than 10, 15 and 20 ft/sec for cruise and for climb and descent. The form of these curves and the difference between cruise and combined climb and descent suggests that the operating conditions and flight plan of the Viking influenced the recorded gust frequencies.

There is evidence in the records from Comet aircraft[4] that gust frequency decreases exponentially with altitude up to about 25,000 ft. This result is practically free from selective recording as the aircraft climbed and descended through this range to a strictly observed flight plan. It is assumed therefore that yearly average turbulence over Europe decreases exponentially with altitude within the altitude range of the Viking and this turbulence is referred to hereafter as atmospheric turbulence to distinguish it from recorded turbulence. As the Comet spectrum refers to world-wide routes it is not used directly for comparison with the Viking recorded turbulence.

There are two ways in which recorded turbulence is influenced by the pilot of the aircraft. Under nearly all conditions of flight the pilot takes sideways avoiding action to some extent when faced with bad weather and for this reason recorded turbulence will be less than atmospheric turbulence at all altitudes. In addition the average flight plan in Table I suggests that the pilot was allowed considerable discretion in the choice of cruising altitude, as the aircraft cruised over a wide range of altitude being limited to 10,000 feet as the cabin was unpressurized. The pilot's choice would be influenced to a great extent by weather conditions; the general result would be the selection of low altitudes during calm weather and of high altitudes during rough weather.

It follows that the gust frequencies recorded during cruise would be less than the atmospheric average at the lowest altitudes and greater than the atmospheric average at the highest altitudes, because flight at the highest altitudes would be made only when the weather was rough and flight at the lowest altitudes would be made only during calm weather. Similarly gust frequencies recorded during climb and descent would be the atmospheric average near sea level and progressively greater than atmospheric average with increasing altitude because the climb to the highest altitudes would be made only in rough weather.

In fact, these effects can be seen in Fig 3 in the curvature and relative position of the cruise curve and climb and descent curve. In the lowest altitude band the same degree of turbulence was recorded in descent and cruise from which it is deduced that altitudes below about 2000 feet were maintained only for landing approaches and circuits.

It has been assumed that atmospheric gust frequency can be represented by a straight line in Fig 3, and its position can be estimated by continuing the low altitude portion of the climb and descent curve as a straight line, shown as a broken line in Fig.3 for gusts greater than 10 ft/sec. This line intercepts the cruise curve in the region of minimum recorded gust frequency which also corresponds approximately with the most usual cruising altitude.

4 Seasonal variation of turbulence

The records best suited to a study of seasonal variation of turbulence are those made at low altitude during climb and descent as they are representative of all weather conditions.

A summary of the 10 ft/sec gust counts and mileages in each month for the altitude range 1500 to 5500 feet are given in Table IV. The turbulence for each month is expressed as the ratio of the average number of gusts per mile in that month to the average number of gusts per mile during the year. The yearly average is the weighted mean of the monthly averages. Turbulence ratio is plotted against month in Fig 4 and

confidence limits are shown for each point within which there is 95% probability that the true average lies. In the estimation of these limits allowance is made for the tendency for gusts to be concentrated in regions[5]. The degree of concentration is estimated by comparing the average number of gusts in a recording interval with the proportion of intervals containing gusts greater than 10 ft/sec. This information is included in Table IV.

The confidence limits in Fig 4, suggest that the monthly sample size is too small for accurate assessment of the variation of turbulence between months but there is some indication that turbulence is greatest in Spring and least in Autumn. To assess the variation quantitatively two hypotheses are now examined using the χ^2 test for goodness of fit.

The first hypothesis is that all the observed variation is sampling error and that average monthly turbulence is constant. The result of this test is a probability of 10% ($\chi^2 = 17$, 11 degrees of freedom).

For the second hypothesis, visual inspection suggests a sinusoidal variation of goodness with a period of one year. If a sine curve is based on the mean annual turbulence with amplitude and phase adjusted to make χ^2 a minimum, the result is a probability of 15% ($\chi^2 = 13$, 9 degrees of freedom).

It appears that neither fit is good but the sine variation is nevertheless more probable than no variation on the present evidence. On the basis of the fitted sine curve the extreme variation in monthly turbulence is about 3 to 1.

5 Conclusions

There is a continuous decrease in gust frequency with increasing altitude from sea level to 8000 feet.

As a result of the pilot's choice of flight path with regard to weather conditions the average gust frequencies during climb and descent were twice as great as average gust frequencies during cruise, at altitudes below 8000 feet.

There is some evidence that turbulence below 5000 feet is greatest in Spring and least in Autumn and that the extreme monthly variation during the year is of the order of 3 to 1.

Acknowledgements

Thanks are due to the British European Airways Corporation for their co-operation in the installation and servicing of the instruments.

REFERENCES

No.	Author	Title, etc
1	J. Taylor	Accelerometer for determining flight loads. Engineering 11th and 18th April, 1952
2	-	Air Publication 970, Chapter 203.
3	J. K. Zbrozek	Gust Alleviation Factors. R & M.2970 - May, 1951.
4	J. R. Heath-Smith	Turbulence encountered by Comet I aircraft. A.R.C. Current Paper No.248
5	N. I. Bullen	The sampling errors of Turbulence Measurements. R.A.E. Report No.Structures 208 May 1956. A.R.C. 18,764

APPENDIX I

Description of acceleration data and gust analysis

The data consist of a series of consecutive records of average duration 10.5 minutes, containing the number of times each acceleration level was exceeded and the speed and altitude of the aircraft at the end of the interval. The speed is expressed to the nearest 10 knots I.A.S. and the altitude to the nearest 1000 feet above sea level.

Those records which may contain the effects of ground loads are discarded with the result that, on average, the first and last 5.25 minutes of each flight are not included in the analysis.

Those records in which the altitude change is greater than 1 unit (nominally 1000 feet) are classified as "climb" or "descent" and the altitude reading is corrected with due regard to the probable variation of gust frequency with altitude. The remaining records are classified as "Cruise". When the speed change during an interval is greater than 1 unit (nominally 10 knots) the mean speed is taken.

The records are sorted into the following altitude bands: 0-1500 feet, 1500-3500 feet, 3500-5500 feet, 5500-7500 feet, 7500-9500 feet and 9500-11500 feet.

The counts of acceleration are grouped and summarized according to the flight condition, altitude and speed of the aircraft.

Mean aircraft weights of 32,400 lb, 31,750 lb and 31,100 lb are calculated for the climb, cruise and descent from the take-off and landing weights known for each flight.

Accelerations are translated into gust speeds by the formula:

$$U = \frac{\Delta n \, w}{F \tfrac{1}{2} \rho_o a V}$$

U	equivalent vertical gust speed
Δn	normal acceleration increment in g units
w	wing loading
F	gust alleviation factor*
ρ_o	air density at sea level (I.C.A.O.)
a	slope of the lift curve (low speed)
V	indicated airspeed

By graphical interpolation the counts are referred to gust speeds of 10, 15, 20, ... ft/sec and a gust speed distribution is obtained for each altitude band and flight condition. The mileage flown in each band is estimated and the gust distributions are obtained in terms of the average distance between gusts exceeding given magnitudes.

---

* The gust is assumed to increase linearly to its maximum value in a horizontal distance of 100 feet. The alleviating factor is calculated as a function of the mass parameter $\mu g = 2w/g \rho \bar{c} a$ where ρ is air density and $\bar{c}$ is the mean aerodynamic chord. Allowance is made for the effect of aspect ratio on the rate of growth of lift. Compressibility effects are neglected.

TABLE I

Estimated time in minutes spent at each speed and altitude

Indicated airspeed in knots	Altitude above sea level (I.C.A.N.) in 1000's of feet																															
	Climb										Cruise												Descent									
	00	01	02	03	04	05	06	07	08	09	00	01	02	03	04	05	06	07	08	09	10	11	00	01	02	03	04	05	06	07	08	09	
100																							105	25	10	10							100
110	5				5							10	10										215	135	20	20	10	10					110
120	30	25	25	10		10					20	20	55	10		10			10	10	10		145	290	210	110	5	30	10	10	10		120
130	160	245	235	120	80	65	40	20	20	40	20	65	115	230	135	95	65	105	190	200	170	20	120	295	355	115	65	65	30	20	10		130
140	130	390	270	230	200	145	190	55	30	40	10	115	315	250	315	335	715	945	1145	1280	600	135	5	150	195	280	170	160	65	65	30	40	140
150		40	120	115	230	265	220	200	30	40		135	355	420	380	1250	2165	2720	2835	2480	1105	170			145	135	190	220	210	200	65	40	150
160			20	75	105	125	85	20	10		20	180	370	390	495	1105	1910	1665	870	305	135	20		10	105	85	145	220	190	180	95	40	160
170				10	10	20	10					20	95	85	85	180	190	65	105	10	10			20		65	160	200	105	75	20		170
180													10		10	10											20	20	20	10			180
Total	325	700	670	560	630	630	545	295	90	120	70	545	1325	1385	1420	2985	5045	5500	5155	4285	2030	315	590	925	1040	800	765	925	630	560	230	120	

Climb: 4,565 mins.

Cruise: 30,090 mins.

Descent: 6,585 mins.

TABLE II

Summary of Acceleration Data from Viking Aircraft

Flight Condition	Altitude above sea level feet	Indicated airspeed knots	Recording Time (10.5 min units)	Number of times each level of acceleration was exceeded Nominal Acceleration-Level (see footnote)													
				0.2g	0.3g	0.4g	0.5g	0.6g	0.7g	0.8g	1.2g	1.3g	1.4g	1.5g	1.6g	1.7g	1.8g	1.9g
Climb	1,500-3,500	120	2								4	1						
		130	10				1	3	19	41	51	16	2	1				
		140	16		1	1	2	3	7	52	100	22	8	1				
		150	20				2	3	13	64	99	13	3	1	1			
		160	9						9	37	60	22	4	2				
		170	1								6							
			58		1	1	5	9	48	194	320	74	17	5	1			
	3,500-5,500	120	1							2	7	1						
		130	10						3	8	16	1						
		140	30		1	1	3	4	11	47	71	10	4	1				
		150	47				1	2	19	75	125	21	4					
		160	22				1	1	2	37	64	11	1					
		170	3						5	5	6	2	1					
			113		1	1	5	7	40	174	289	46	10	1				
	5,500-7,500	130	6					2	7	14	16	9	2	1	1			
		140	23						2	12	29	12	2	1	1	1		
		150	40						3	24	44	9	1					
		160	10						1	14	12							
		170	1							0	0							
			80					2	13	64	101	30	5	2	2	1		
	7,500-9,500	130	6						1	12	15	2	1					
		140	7						1	1	10							
		150	7							0	0							
		160	1							0	0							
			21						2	13	25	2	1					
	Climb total		272		2	2	10	18	103	445	735	152	33	8	3	1		
Cruise	0-1,500	110	1							0	0							
		120	4					2	8	33	85	20	3	1				
		130	8						8	37	44	8						
		140	12		1	1	1	6	31	81	150	47	4	2	1	1		
		150	13						17	38	77	29						
		160	19				3	10	69	180	343	116	15	6				
		170	2				1	2	11	24	57	24	2					
			59		1	1	5	20	144	393	756	244	24	9	1	1		
	1,500-3,500	110	1							0	0							
		120	6						3	15	58	19	6	3				
		130	33						1	2	7							
		140	54				1	1	10	45	114	22	3					
		150	74	1	1	1	3	15	77	285	422	107	14	4				
		160	72		1	2	9	24	78	309	408	92	20	2				
		170	17				2	4	34	110	107	38	8	5	1	1	1	1
		180	1							0	0							
			258	1	2	3	15	44	203	766	1116	278	51	14	1	1	1	1
	3,500-5,500	120	1							0	7	3						
		130	22						1	4	1							
		140	62		1	2	3	7	30	89	127	32	5	2				
		150	155				1	5	44	151	211	45	13	4				
		160	152		1	1	1	5	28	122	178	34	7	2				
		170	25						13	33	23	3						
		180	2							0	1							
			419		2	3	5	17	116	399	548	117	25	8				

TABLE II (Contd)

Flight Condition	Altitude above sea level feet	Indicated airspeed knots	Recording Time (10.5 min units)	Number of times each level of acceleration was exceeded — Nominal Acceleration Level (see footnote)													
				0.2g	0.3g	0.4g	0.5g	0.6g	0.7g	0.8g	1.2g	1.3g	1.4g	1.5g	1.6g	1.7g	1.8g	1.9g
Cruise (Contd)	5,500-7,500	130	16				1	3	7	22	26	6	2	1				
		140	158			1	3	11	37	93	101	32	12	8	2	1		
		150	465		1	2	4	18	73	222	270	60	12	6	2	1		
		160	293				2	8	32	64	118	22	8	3				
		170	24						6	13	28	5						
			956		1	3	10	40	155	414	543	125	34	18	4	2		
	7,500-9,500	120	2							0	3	1						
		130	37					1	5	41	55	5	1					
		140	231				3	6	30	147	243	36	7	1				
		150	506		1	3	7	14	40	134	167	37	7	1				
		160	112					2	21	62	59	9	2					
		170	11						1	4	12	5						
			899		1	3	10	23	97	388	539	93	17	2				
	9,500-11,500	120	1							0	0							
		130	18					1	6	17	24	8						
		140	70				1	3	20	72	95	17	2	1				
		150	121						8	42	55	16	5	2				
		160	15				1	2	5	14	11	4						
		170	1							0	0							
			226				2	6	39	145	185	45	7	3				
	Cruise total		2817	1	7	13	47	150	754	2505	3687	902	158	54	6	4	1	1
Descent	0-1,500	100	1							3	9	4						
		110	1							3	18	2						
		120	7						1	11	19	3						
		130	2					1	2	22	43	12						
		140	5						25	49	57	20	5					
		160	1				1	1	8	16	14	6						
		170	2							0	0							
			19				1	2	36	104	160	47	5					
	1,500-3,500	100	2							3	11	10	5	2	1			
		110	2							5	21	1						
		120	22				1	1	9	51	141	25	1					
		130	28					3	21	83	159	38	7	3				
		140	33				1	8	27	96	157	39	5	2	1			
		150	27					1	17	66	151	27	6	1	1			
		160	18				1	3	9	44	70	12	4	1	1			
		170	6				1	4	40	78	84	27	7	2				
			138				4	20	123	426	794	179	35	11	4			
	3,500-5,500	110	2							1	3							
		120	3							3	11	5	2	1				
		130	12						2	15	45	6	1					
		140	31		1	2	3	6	36	104	147	50	10	6	1			
		150	39				1	5	27	77	143	24	5	2				
		160	35		1	2	8	14	46	133	180	55	9	6				
		170	34						6	41	67	18	1	1	1	1		
		180	4				1	1	1	2	2							
			160		2	4	13	26	118	376	598	158	28	16	2	1		

TABLE II (Contd)

Flight Condition	Altitude above sea level feet	Indicated airspeed knots	Recording Time (10.5 min units)	Number of times each level of acceleration was exceeded Nominal Acceleration Level (see footnote)													
				0.2g	0.3g	0.4g	0.5g	0.6g	0.7g	0.8g	1.2g	1.3g	1.4g	1.5g	1.6g	1.7g	1.8g	1.9g
Descent (Contd)	5,500-7,500	120	2							0	0							
		130	5							0	9							
		140	12					1	7	25	38	9	2					
		150	39					3	18	56	64	16	1	1				
		160	35				1	1	9	35	35	4	1					
		170	17							13	21	3						
		180	3				1	4	13	27	28	11	3	2	1			
			113				2	9	47	156	195	43	7	3	1			
	7,500-9,500	120	1						2	10	21	4						
		130	1							0	0							
		140	7							5	5	1						
		150	10							0	1	1						
		160	13							1	10							
		170	2						1	4	3	1						
			34						3	20	40	7						
	Descent total		464		2	4	20	57	327	1082	1787	434	75	30	7	1		

The necessary corrections for instrument error to the nominal acceleration levels are:

1.2g, 1.3g, 1.4g	+0.03g
1.5g and greater	+0.02g
0.8g, 0.7g, 0.6g	-0.03g
0.5g and smaller	-0.02g

TABLE III

Summary of Gust Speeds Encountered

Flight Condition	Altitude above sea level I.C.A.N.	Mean Altitude in band	Flying distance recorded	Estimated number of times a gust speed was exceeded in the recorded distance flown									
				Vertical gust speed ft/sec E.A.S. (+ up - down)									
	feet	feet	Statute miles	-30	-25	-20	-15	-10	10	15	20	25	30
Climb	1500-3500		1750		1	5	19	107	172	27	4		
	3500-5500		3600		1	3	11	81	122	12	1		
	5500-7500		2620				6	28	59	11	2	1	
	7500-9500		680					7	12	2			
Descent	0-1500		506				5	82	126	26	2		
	1500-3500		3890			2	32	260	470	66	14	3	1
	3500-5500		5260		1	4	29	178	270	34	10		
	5500-7500		3880				6	62	68	7			
	7500-9500		1180					11	23	3			
Climb & Descent	0-1500	600	506				5	82	126	26	2		
	1500-3500	2400	5640		1	7	51	367	642	93	18	3	1
	3500-5500	4500	8860		2	7	40	259	392	46	11		
	5500-7500	6400	6500				12	90	127	18	2	1	
	7500-9500	8400	1960					18	35	5			
Cruise	0-1500	900	1740		1	2	37	250	450	57	5	1	
	1500-3500	2500	8020	1	2	5	45	360	520	55	9	2	1
	3500-5500	4700	13700		1	4	22	198	235	29	6		
	5500-7500	6500	32300		1	5	43	256	220	38	12	2	
	7500-9500	8500	30500		1	9	27	192	188	21	2		
	9500-11500	10100	7790			1	8	72	88	9	2		

TABLE IV

Relative turbulence each month recorded during climb and descent (1,500-5,500 feet)

Month	No. of recording intervals	No. of intervals with gust > 10 ft/sec	Recording Distance in Statute miles	No. of gusts exceeding 10 ft/sec (up + down)	Miles per gust	Turbulence Ratio Yearly miles/gust / Monthly miles/gust
1	14	4	437	66	6.57	1.2
2	33	13	1023	208	4.92	1.7
3	28	13	867	81	10.7	0.76
4	54	33	1678	240	7.00	1.2
5	79	41	2450	402	6.10	1.3
6	19	9	603	121	4.98	1.7
7	75	34	2322	236	9.84	0.82
8	30	11	931	97	9.60	0.85
9	33	22	1023	188	5.44	1.5
10	38	9	1180	32	36.9	0.22
11	36	11	1117	73	15.3	0.53
12	29	6	899	31	29.0	0.28
Totals	468	206	14,530	1775	Average 8.13	

A.R.2078.CP.311.K3 - Printed in Great Britain.

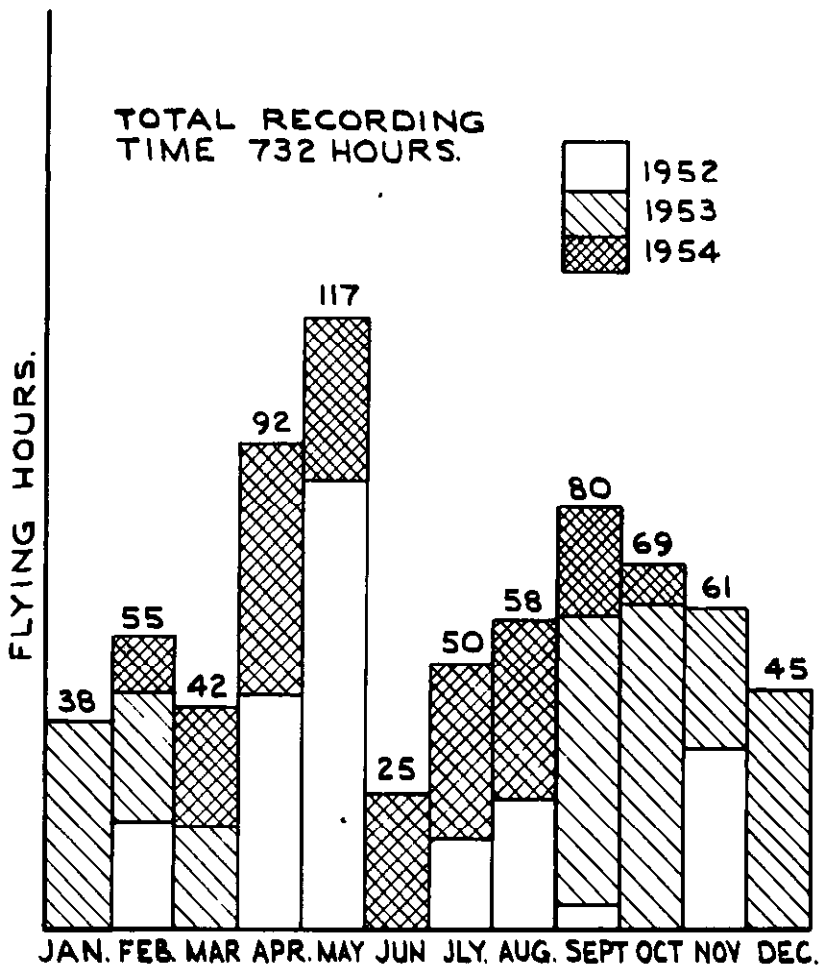

FIG I. MONTHLY DISTRIBUTION OF RECORDED FLYING TIME

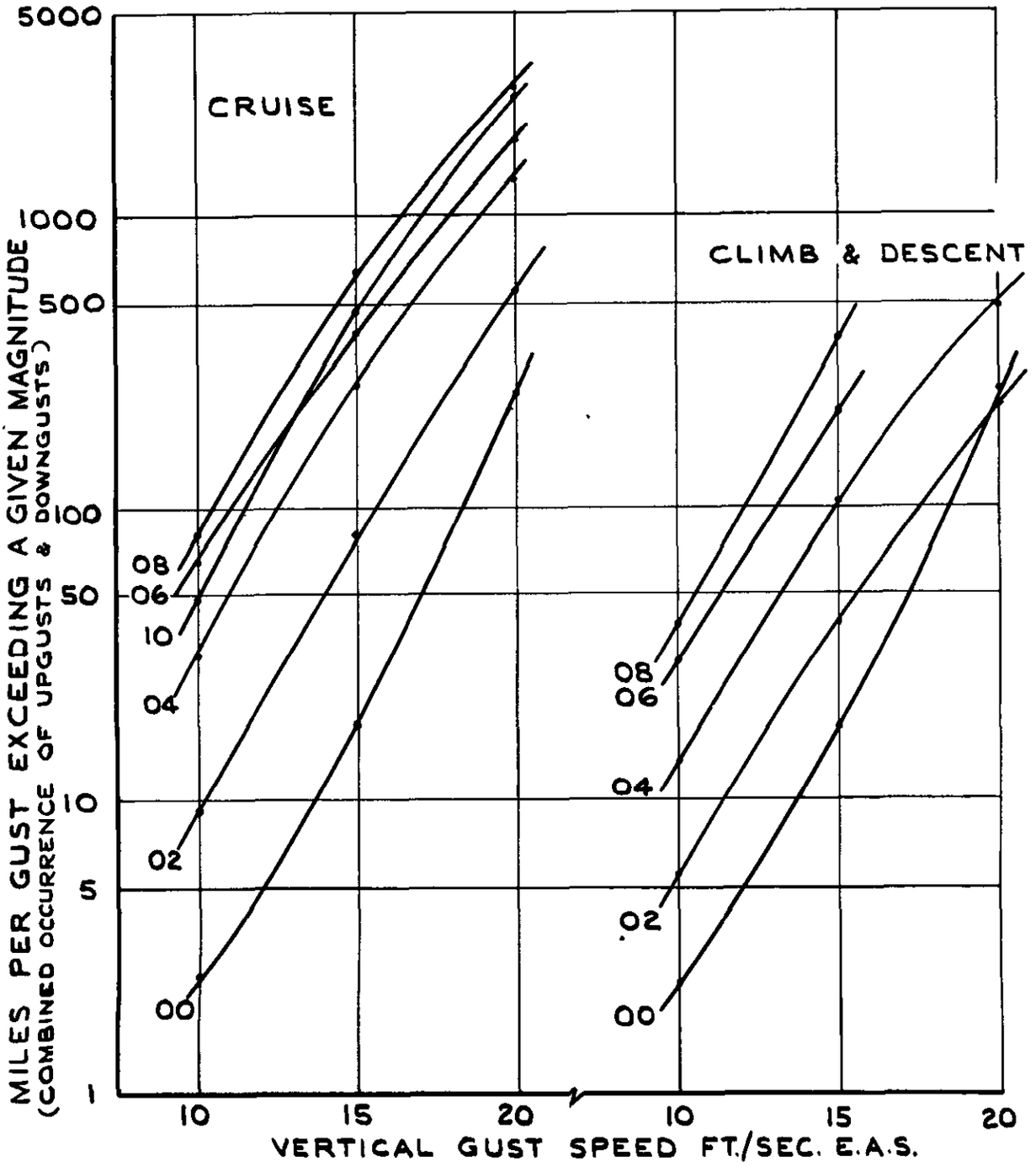

ALTITUDE BAND	ALTITUDE RANGE FEET	MEAN ALTITUDE FEET		DISTANCE. ST. MILES	
		CRUISE	CL' & D	CRUISE	CL' & D.
00	0-1500	900	600	1740	506
02	1500-3500	2500	2400	8020	5640
04	3500-5500	4700	4500	13700	8860
06	5500-7500	6500	6400	32300	6500
08	7500-9500	8500	8400	30500	1960
10	9500-11500	10100	—	7790	—

FIG 2. GUST SPECTRA AT DIFFERENT ALTITUDES.

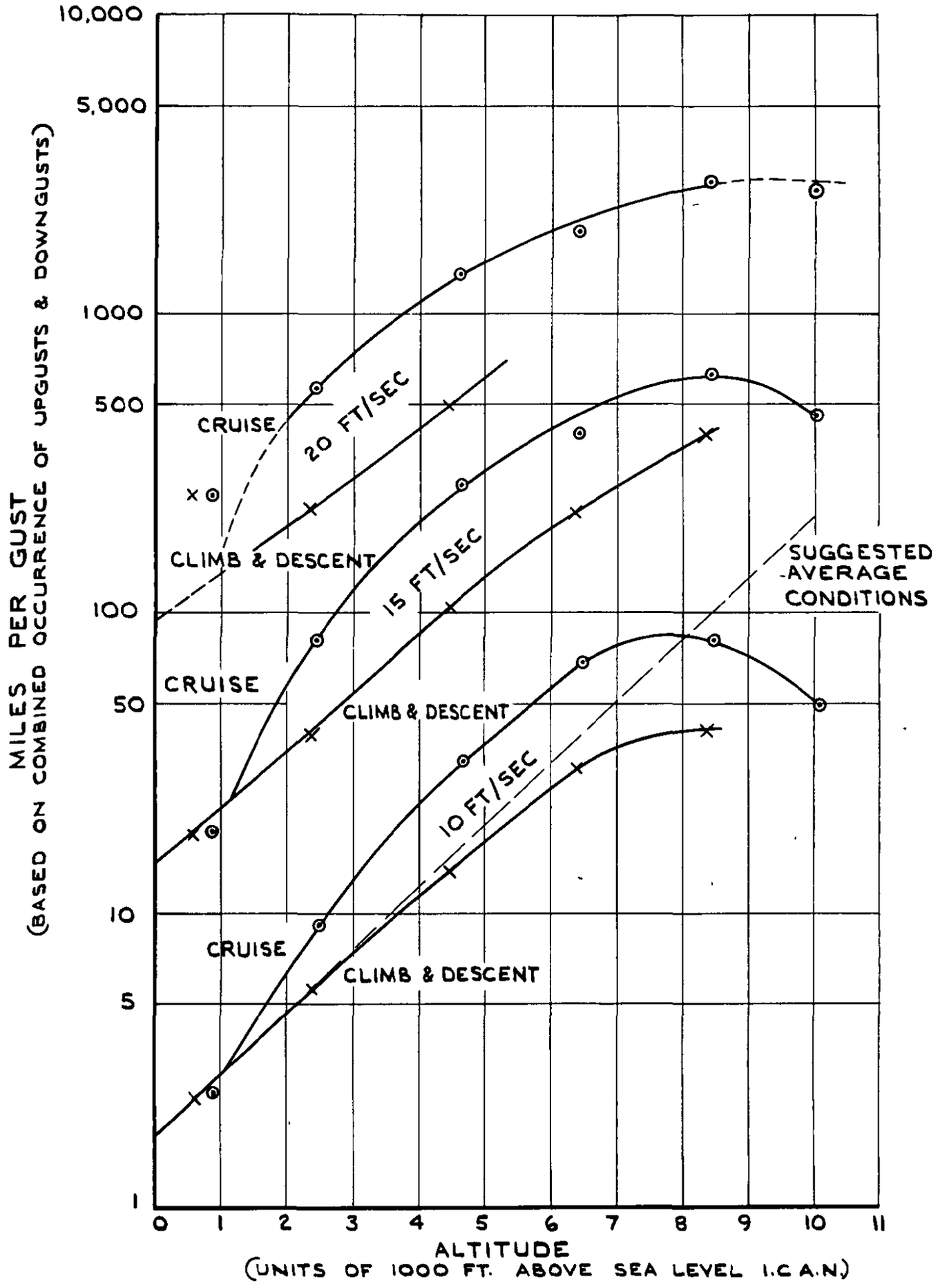

FIG 3. VARIATION OF TURBULENCE WITH ALTITUDE IN TERMS OF GUSTS EXCEEDING 10 FT/SEC 15 FT/SEC AND 20 FT/SEC.

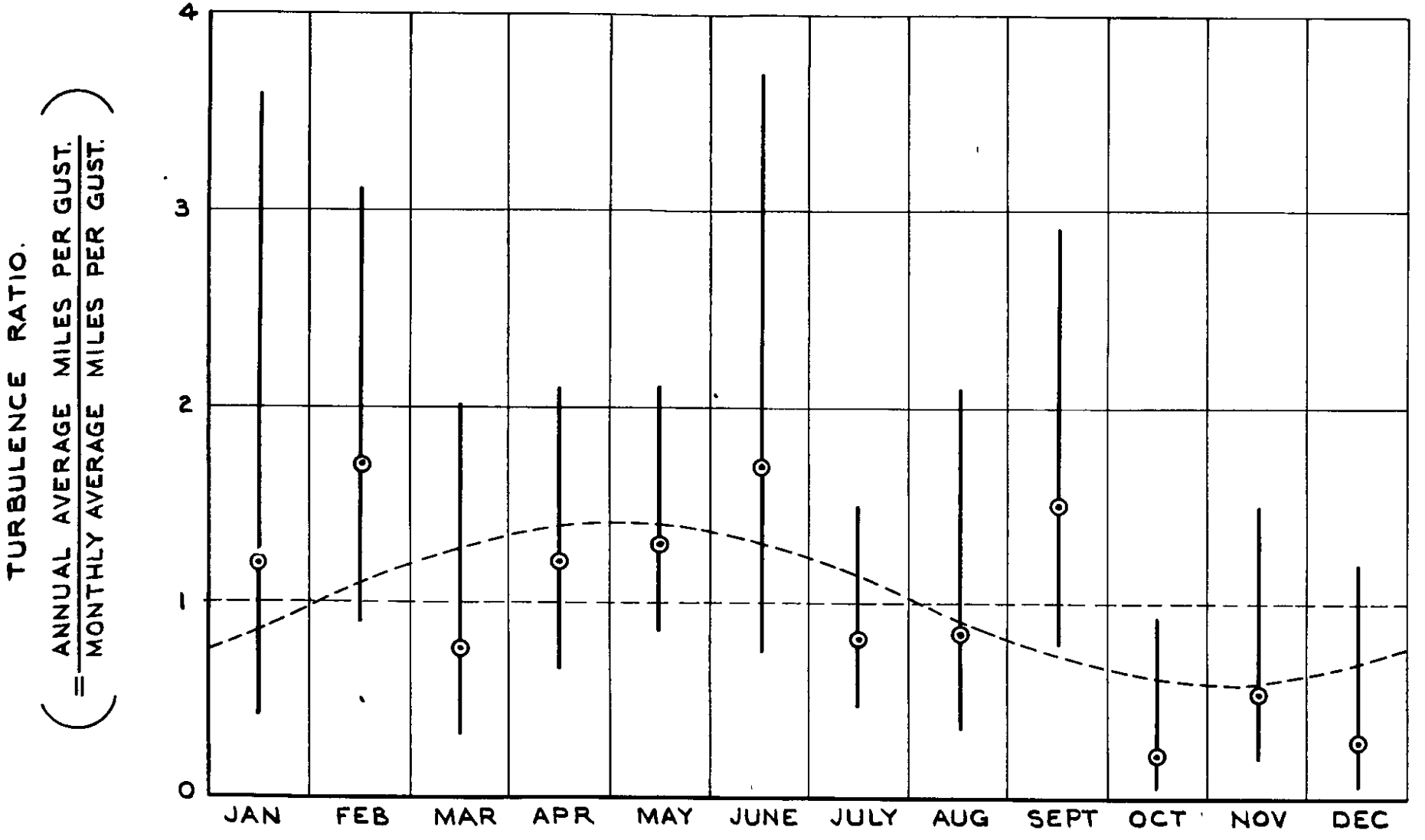

FIG 4. MONTHLY AVERAGE RECORDED TURBULENCE IN TERMS OF 10 FT/SEC GUST FREQUENCY.

C.P. No. 311
(18,836)
A.R.C. Technical Report

Published by
HER MAJESTY'S STATIONERY OFFICE

To be purchased from
York House, Kingsway, London W C 2
423 Oxford Street, London W 1
P O Box 569, London S E 1
13A Castle Street, Edinburgh 2
109 St Mary Street, Cardiff
39 King Street, Manchester 2
Tower Lane, Bristol 1
2 Edmund Street, Birmingham 3
80 Chichester Street, Belfast
or through any bookseller

PRINTED IN GREAT BRITAIN

S.O. Code No. 23-9010-11

C.P. No. 311

C.P. No. 322
(19,022)
A.R.C. Technical Report

C.P. No. 322
(19,022)
A.R.C. Technical Report

MINISTRY OF SUPPLY

AERONAUTICAL RESEARCH COUNCIL

CURRENT PAPERS

Supports for Vibration Isolation

By

W. G. Molyneux

LONDON: HER MAJESTY'S STATIONERY OFFICE

1957

THREE SHILLINGS NET

C.P. No.322

U.D.C. No. 621-752.2

Technical Note No. Structures 211
November, 1956

ROYAL AIRCRAFT ESTABLISHMENT

Supports for Vibration Isolation

by

W. G. Molyneux

SUMMARY

Spring arrangements are described that provide flexible supports of very low stiffness for a limited range of movement. They are suitable as supports for vibration isolation provided the levels of vibration are not too large.

Some particular applications of the arrangements for vibration isolation and in other fields are discussed.

LIST OF CONTENTS

LIST OF ILLUSTRATIONS

1 Introduction

The problem of vibration isolation arises in all fields of engineering where rotating or vibrating machinery is used. Unbalanced forces in the machinery produce unwanted vibrations in the surrounding structure and the problem is either to isolate the machinery from the structure or, if this is impracticable, to isolate components mounted on the structure from the structural vibrations.

The usual practice in vibration isolation is to mount the component to be isolated on flexible supports so that the rigid body frequencies of the component on the supports are very low by comparison with the frequency of the troublesome vibrations[1,2]. In this circumstance the level of vibration transmitted through the supports is a function of the ratio of the rigid body frequencies to the vibration frequency[3]. Obviously the ideal requirement for such supports is that they should provide zero rigid body frequencies, i.e. their stiffness should be zero.

One support satisfying this ideal requirement is the sine spring[4], which provides a pure zero stiffness for a considerable range of movement. However, the latter feature can be an embarrassment since it implies that any slight change in the effective mass of the supported component leads to large excursions of the component on its supports, with no restoring force to return it to the datum position. Further, the sine spring is not well suited for supporting very large loads.

In principle it is adequate for vibration isolation if the support provides zero stiffness over a greater range of movement than the amplitude level of the troublesome vibration. Such levels are generally of the order of hundredths of an inch.

In what follows a spring arrangement with a non-linear stiffness characteristic is described* that provides zero, or very small stiffness for a limited range of movement. Though the stiffness characteristics of the arrangement are non-linear the components used are conventional linear springs. Some applications of the arrangement to vibration isolation and in other fields are discussed.

2 Spring arrangements

2.1 Inclined springs

Consider first the spring arrangement shown in Fig.1. Here there are two inclined compression springs AB and AC each of stiffness k freely hinged at A, B and C to form a triangle of base BC = a and vertex A. Let the unstressed spring lengths AB, AC equal ℓ, where

$$\frac{2\ell}{a} = \sec \alpha \, . \qquad (1)$$

Now suppose a load W is applied at A so that A moves to A', the springs AB, AC being compressed, taking up an inclination θ. The location of A' on the line AA' is defined by

$$x = \frac{a}{2} \tan \theta \, . \qquad (2)$$

Then the expressions for the load W and the stiffness $\frac{dW}{dx}$ along the axis AA' are:

---

* Patent applications 10722/56 and 24268/56.

$$\frac{W}{ka} = (\sec \alpha - \sec \theta) \sin \theta \qquad (3)$$

$$-\frac{1}{k} \cdot \frac{dW}{dx} = 2(1 - \sec \alpha \cos^3 \theta) . \qquad (4)$$

A negative value for $\frac{dW}{dx}$ corresponds to positive stiffness, for x decreases as W increases.

It is apparent from equation (4) that the stiffness along AA' is zero when

$$\cos \theta = \cos^{\frac{1}{3}} \alpha \qquad (5)$$

and there is a maximum in the load-displacement curve for this condition.

Cos α defines the ratio of the ultimate compressed length of the springs to the unstressed length. In Fig.2 the load and stiffness functions (equations (3) and (4)) are plotted for various values of α.

It is apparent that this spring arrangement can provide zero stiffness, but it has little practical value as a support for vibration isolation, since the conditions for zero stiffness result in unstable equilibrium of the system. Any slight increase in load beyond the optimum value leads to a negative stiffness condition, and A then moves rapidly to the opposite side of the datum BC, ultimately coming to rest when the extension in AB and AC balances the applied load.

It is apparent that it is not sufficient merely to satisfy the condition that the support stiffness must be zero; a stability requirement must also be satisfied. The stability requirement is satisfied if the support provides zero stiffness for some optimum load, and positive stiffness if the load is increased or decreased from this optimum value, i.e. the zero stiffness point must be a minimum for the stiffness-displacement curve. This requirement also has the effect of limiting excursions of the load on the support since in any such excursion there will be a restoring force to return the load to the zero stiffness condition.

From a further differentiation of equation (4) we have

$$\frac{a}{k} \cdot \frac{d^2W}{dx^2} = -12 \sec \alpha \cos^4 \theta \sin \theta \qquad (6)$$

which indicates that the stiffness is a minimum when θ is zero (as can be seen from Fig.2b).

This minimum provides zero (rather than negative) stiffness only when α is also zero (equation (5)), i.e. when the unstressed spring length ℓ equals $\frac{a}{2}$, the springs then lying along the datum BC. From equation (3) this requires that there is zero applied load, so that the arrangement is useless as a load carrying flexible support.

2.2 Inclined springs and axial spring

Now consider the effect of adding a further spring DE of stiffness qk along the axis AA' (Fig.1). Prior to coupling E to A let E be at a distance s from the datum BC.

With E coupled to A the expressions for load and stiffness along the axis AA' are

$$\frac{W}{ka} = (\sec \alpha - \sec \theta) \sin \theta + \frac{q}{a}\left(s - \frac{a}{2} \tan \theta\right) \qquad (7)$$

$$-\frac{1}{k} \cdot \frac{dW}{dx} = 2 (1 - \sec \alpha \cos^3\theta) + q \qquad (8)$$

and from a further differentiation of equation (8) we have

$$\frac{a}{k} \cdot \frac{d^2W}{dx^2} = -12 \sec \alpha \cos^4\theta \sin \theta . \qquad (9)$$

From equations (8) and (9) the stiffness has a minimum value of zero when θ is zero and when

$$\sec \alpha = 1 + \frac{q}{2} \qquad (10)$$

and for these conditions there is a point of inflexion in the load displacement curve, the optimum load being given from equation (7) as

$$W = q k s . \qquad (11)$$

It is apparent from equations (1) and (10) that the ratio q of the axial spring stiffness to that of an inclined spring is determined solely by the ratio of the unstressed length to the ultimate compressed length of the inclined springs. Further, from equation (11), the optimum load is simply the load required to extend the axial spring to the datum BC, and the optimum load for the support can therefore be varied simply by moving the anchorage D of the axial spring so as to vary s.

In Fig.3 the load function of equation (7) is plotted against θ and $\tan \theta$ for two different initial conditions for the inclined springs ($\alpha = 30^\circ$ and $\alpha = 60^\circ$). In both cases the value of s for the axial spring is $\frac{a}{2}$. The point of inflexion when θ is zero can be seen. Also plotted against $\tan \theta$ is the corresponding load function for the axial springs alone, and it can be seen that for values of θ between α and zero the combined system carries more load than the axial spring alone, and between zero and $-\alpha$ it carries less load.

The stiffness function for the two conditions is plotted in Fig.4, together with the curve for the axial springs alone. The stiffness of the combined system is less than that of the appropriate axial spring for an appreciable range of $\tan \theta$, and in particular has a minimum zero stiffness when θ is zero.

The significant parameter for vibration isolation is the support frequency, and accordingly the frequency function for the support is plotted in Fig.5. This function is the square root of the ratio of stiffness function to load function, i.e. $\left(\frac{a}{W} \cdot \frac{dW}{dx}\right)^{\frac{1}{2}}$.

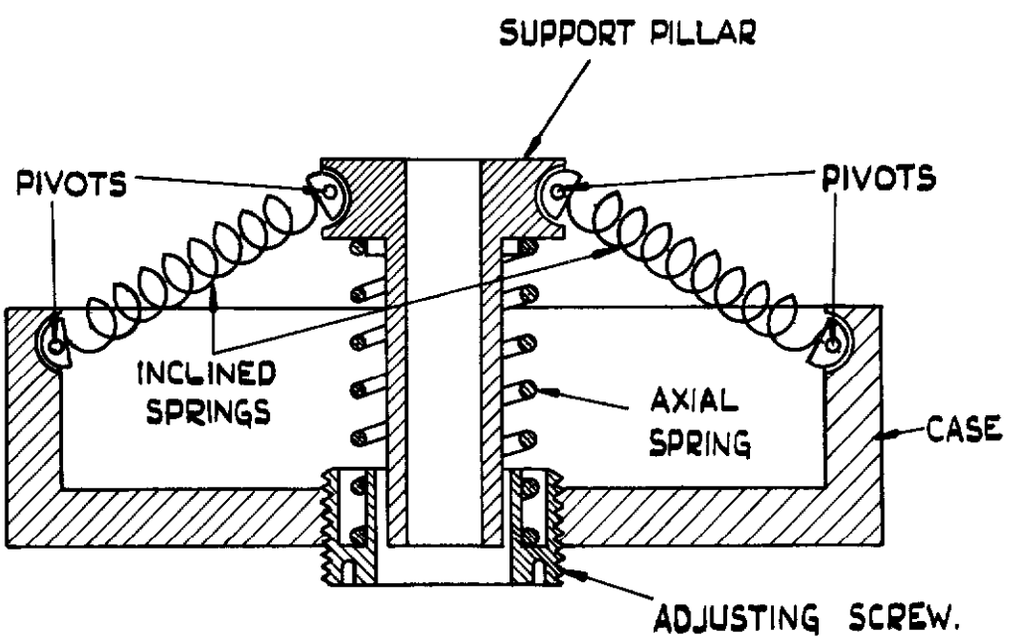

FIG. 6. GENERAL PURPOSE SUPPORT FOR VIBRATION ISOLATION.

in Fig.8. A linkage arm AB is clamped to the torsion member and has compression springs AC, BD of stiffness k and unstressed length ℓ at its ends. Following a similar procedure to that for the axial load system it can be shown that the torsional stiffness of the loaded shaft is a minimum when the shaft is twisted so that DBAC are in line. The springs are then under maximum compression with a compressed length of $\frac{a}{2}$. The stiffness minimum is zero (rather than negative or positive) when

$$\frac{2\ell}{a} = 1 + \frac{q}{2} \qquad (13)$$

where the torsional stiffness of the shaft is defined as qkb^2.

This equation is identical in form with equation (10) since

$$\sec \alpha = \frac{2\ell}{a} .$$

Further the torsion load T in the shaft when the stiffness is zero is given by

$$T = q\,k\,b^2\psi \qquad (14)$$

which, for a given spring system depends only on the initial angle ψ of the shaft when unstressed. This equation may be compared with equation (11) of the axial load system.

3 Some applications to vibration isolation

A few special applications of the linear and torsional systems to vibration isolation are considered. Fig.9 shows their application to road vehicle suspension systems. Coil spring, cantilever spring and torsion bar suspensions are all in current use, but by the addition of an inclined spring the stiffness of the suspension can be markedly reduced, without increasing the deflection. By reducing suspension stiffness a greater degree of isolation of the body from road shocks is obtained.

Fig.10a shows how the stiffness of a cantilever bucket seat can be reduced, isolating the occupant from vibration and shocks and providing greater comfort. Such seats are in common use on agricultural machinery. Applications for other types of sprung seat can be visualised.

Fig.10b shows the suspension for a siesmic type of vibration transducer. This provides very small stiffness for a limited range of movement, which is a necessary requirement for instruments of this type.

4 Other applications

Applications of these spring arrangements in fields other than vibration isolation can be visualised. Three such applications are shown in Fig.11.

Fig.11a shows a mechanical tension meter, that provides a sensitive indication of small variations in tension about some predetermined level. It could be used, for example, as a weighing device to detect small variations in weight of nominally identical objects.

Fig.11b shows a non-linear torque meter, that could be used as the indicator in a variety of instruments. This provides a sensitive indication of torque variations about some predetermined level.

Fig.11c shows a torque regulator, providing a sensitive means of detecting variations in the torque transmitted by a rotating shaft. It could be used in conjunction with an automatic gear changing device.

5 Conclusions

The inclined spring arrangements which have been described are capable of providing low stiffness for a limited range of movement. They can, with advantage, be used as support springs in vibration isolation mechanisms provided the levels of vibration are not too great and for moderate levels of applied acceleration. In aircraft applications the applied acceleration aspect is an important one, because of the accelerations encountered during manoeuvres. The inclined spring arrangement is, however, no worse off in catering for this case than the conventional type of spring mounting and has the advantage of providing improved isolation under normal conditions.

There are many other possible applications for spring arrangements based on this principle. Some of these are described in the paper.

REFERENCES

No.	Author	Title, etc
1	Shapiro, J.S.	Design of vibrating isolating mountings. ARC 16,154. July 1953.
2	Fish, R.W.	Anti-vibration mountings for aircraft cameras. RAE Tech. Note Air. Ph.491. June 1955.
3	Myklestad, N.O.	Vibration Analysis Chap. 4, Section 3. McGraw Hill Book Co. Inc. 1944.
4	Wigan, E.R.	The sine spring. S.R.D.E. Report 1029. ARC. 12,509. Feb. 1949.
5	Molyneux, W.G.	Flexible supports for the ground resonance testing of aircraft. RAE Report Structures 32. ARC 11,964. Sept. 1948.

WT.2078.CP.322.K3. Printed in Great Britain.

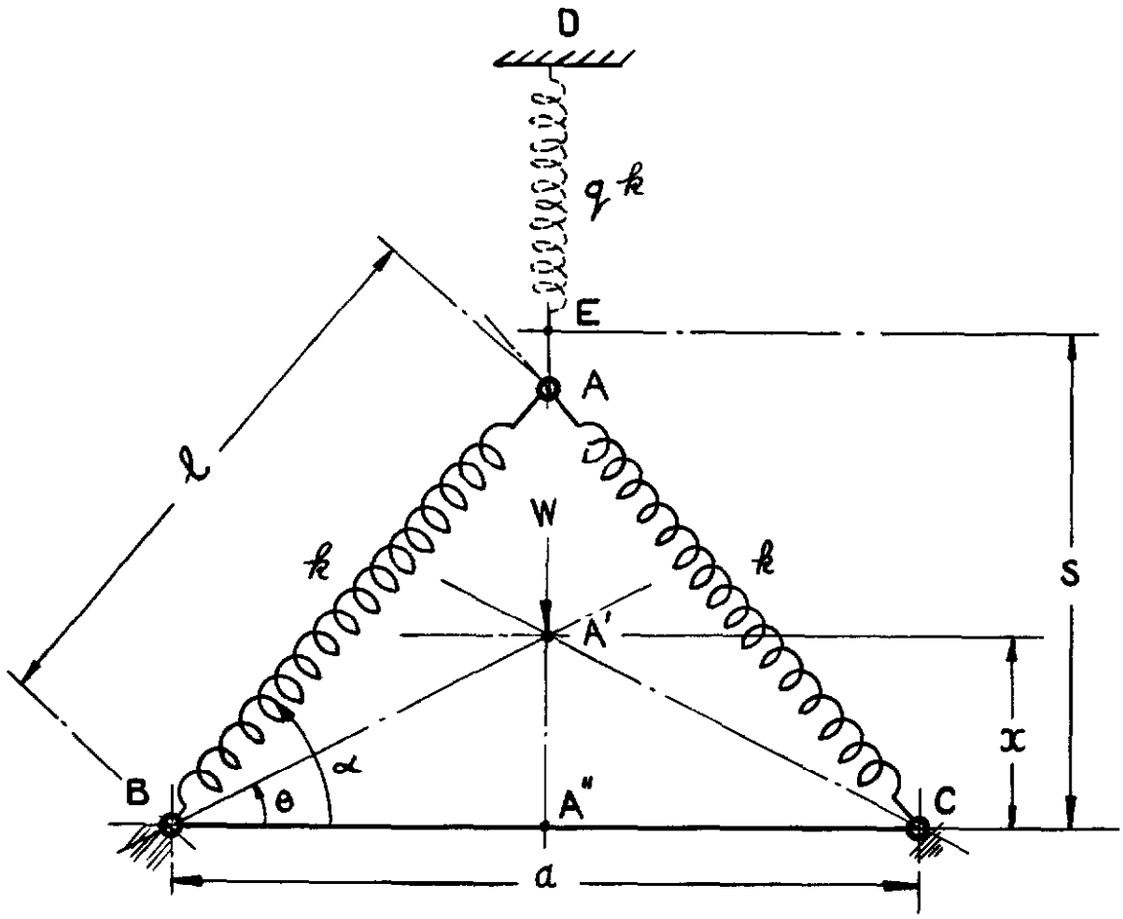

FIG.1. SPRING ARRANGEMENT.

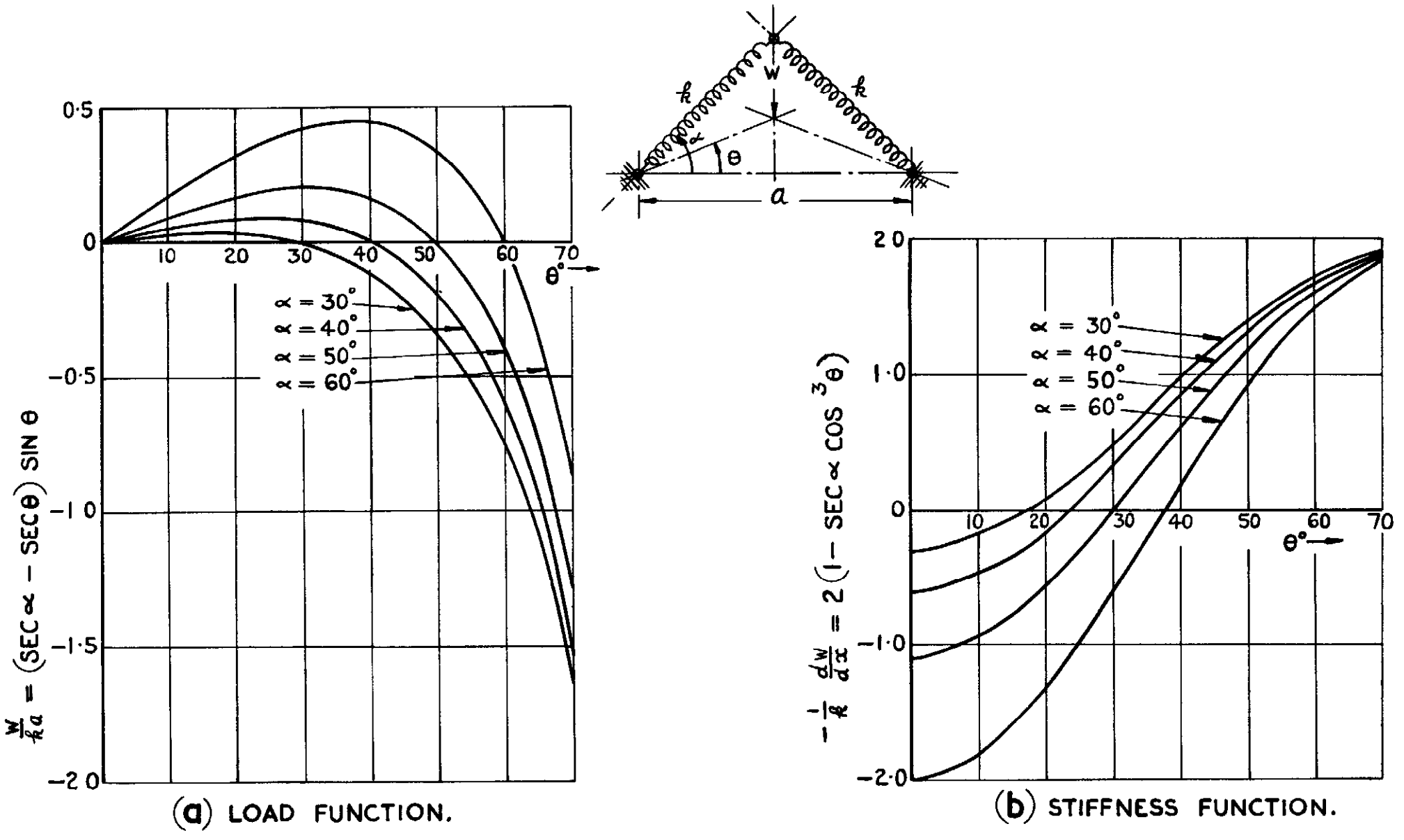

FIG. 2(a&b) LOAD & STIFFNESS FUNCTIONS FOR INCLINED SPRING ARRANGEMENT.

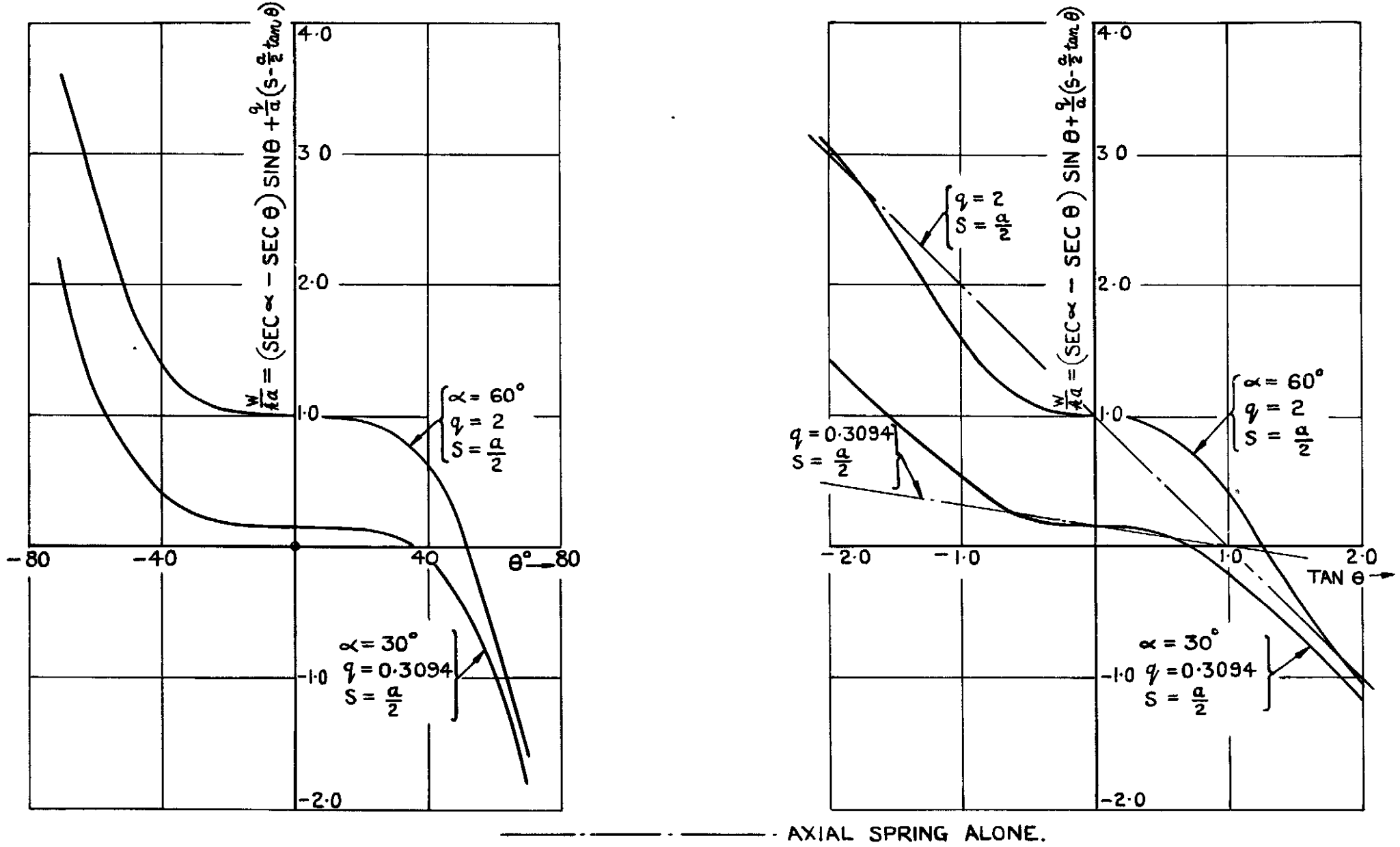

FIG. 3. LOAD FUNCTION—INCLINED SPRINGS WITH OPTIMUM AXIAL SPRING.

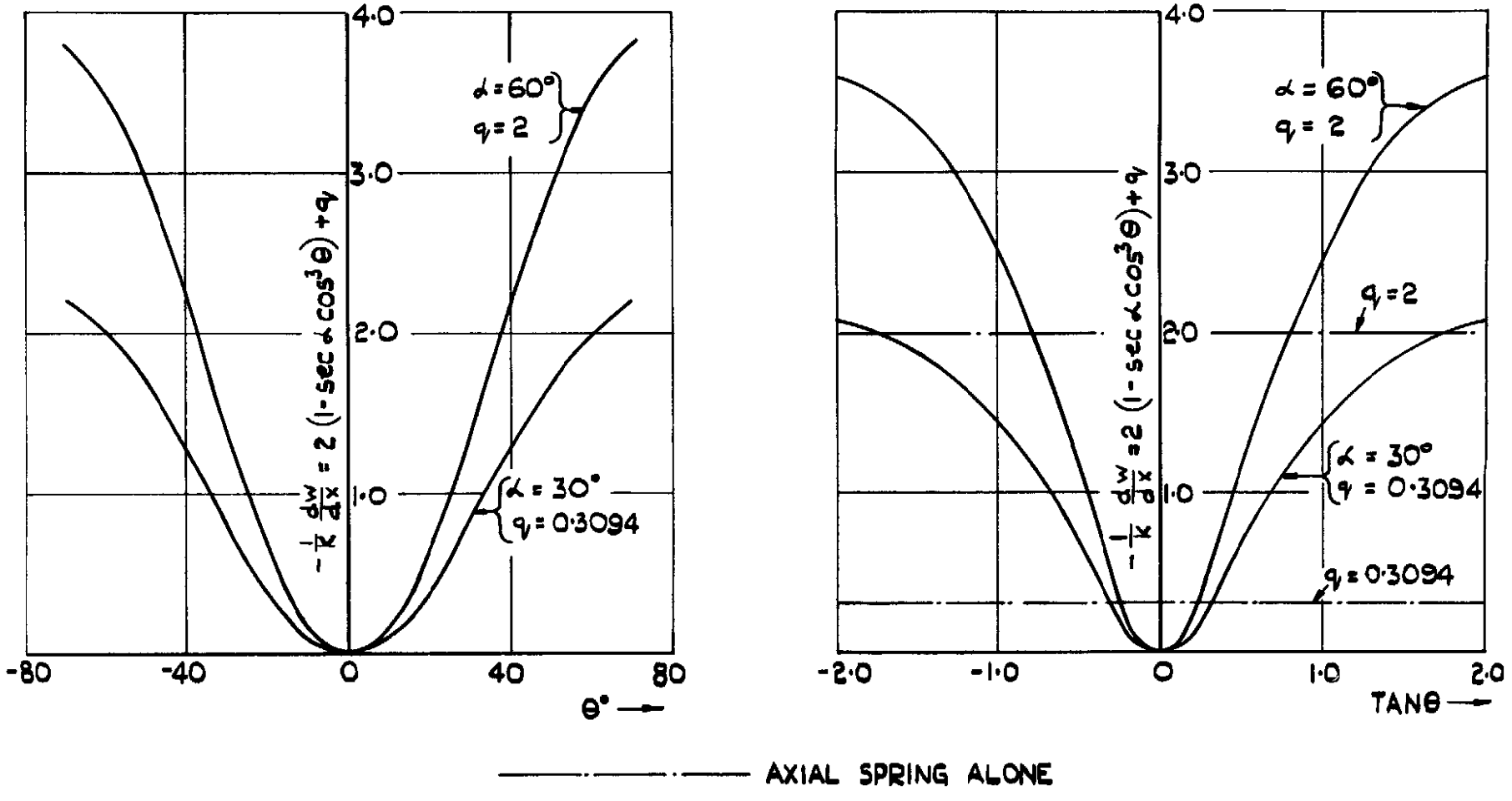

FIG. 4. STIFFNESS FUNCTION – INCLINED SPRINGS WITH OPTIMUM AXIAL SPRING

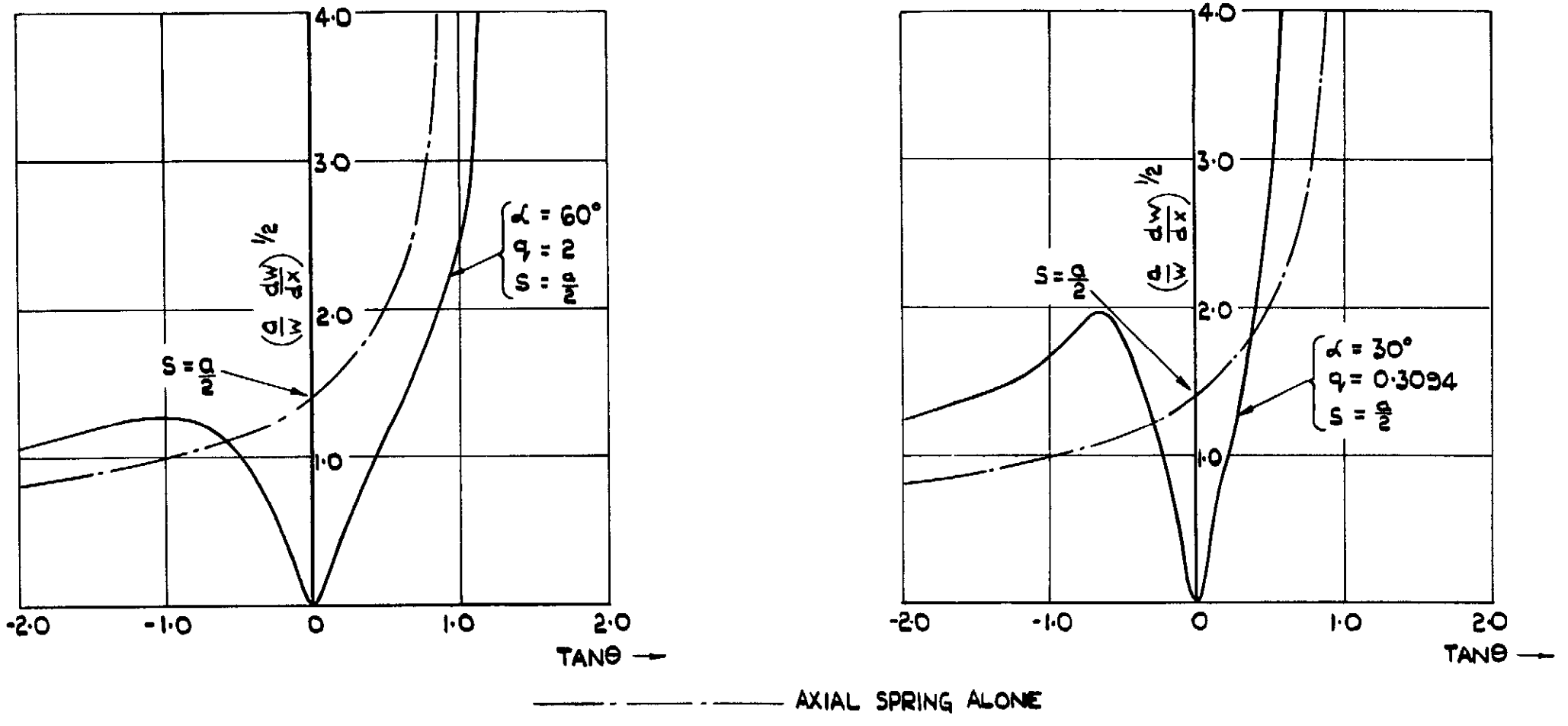

FIG. 5. FREQUENCY FUNCTION - INCLINED SPRINGS WITH OPTIMUM AXIAL SPRING.

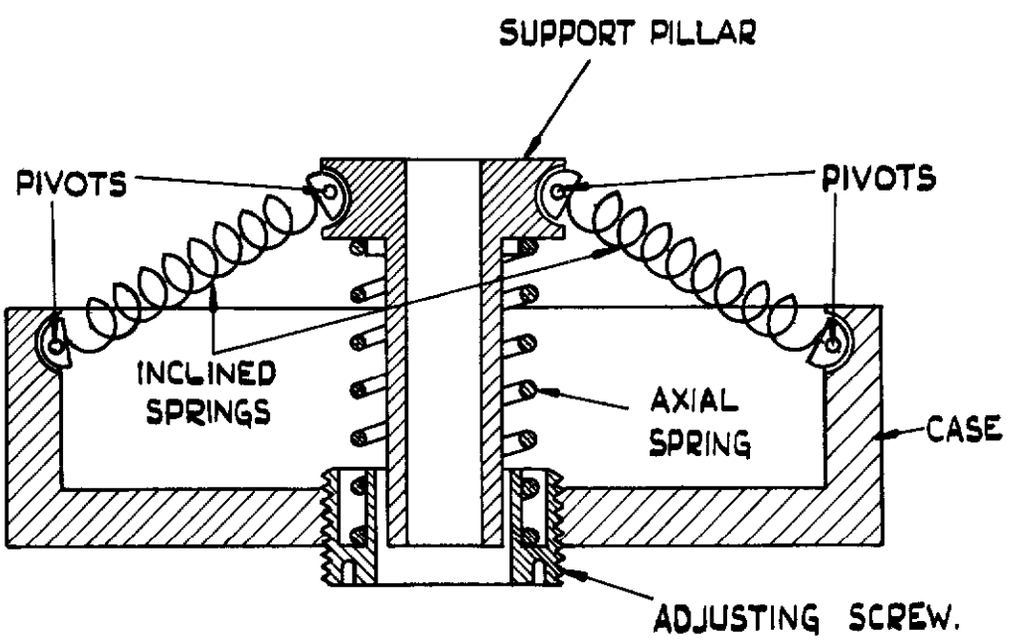

FIG. 6. GENERAL PURPOSE SUPPORT FOR VIBRATION ISOLATION.

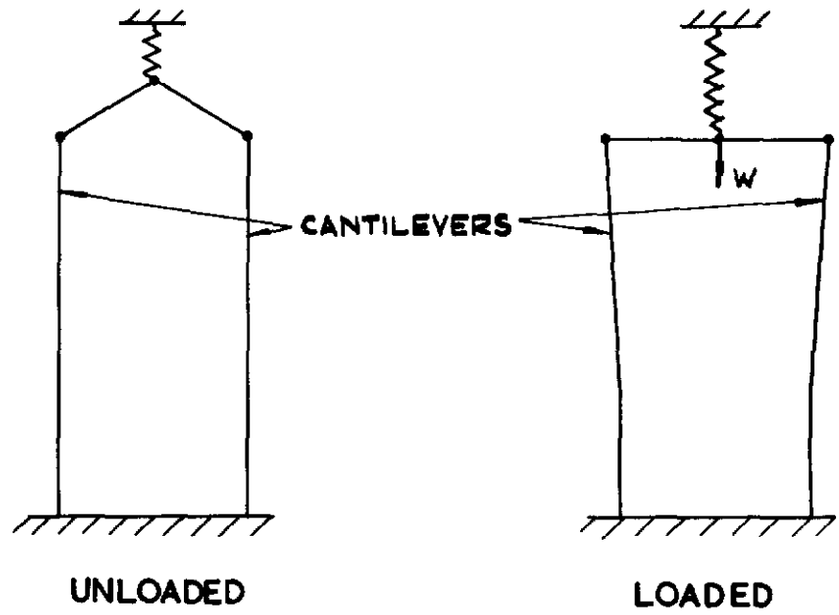

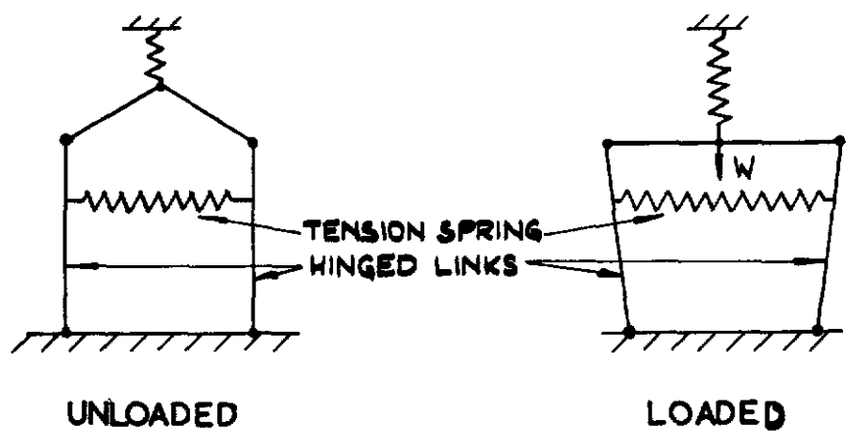

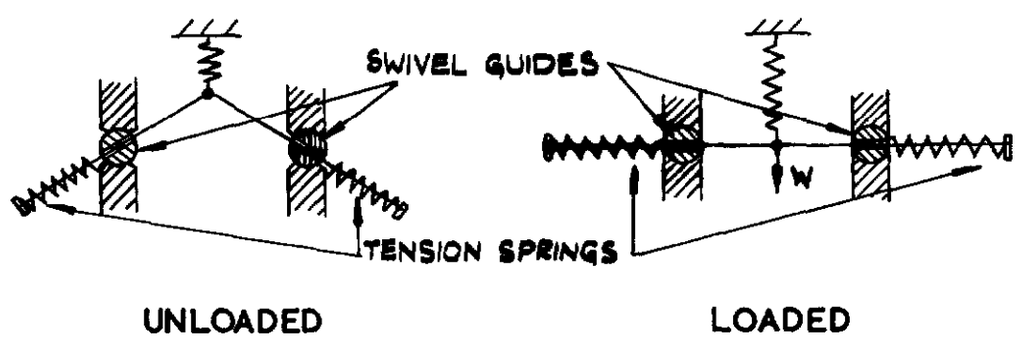

FIG.7. ALTERNATIVE ARRANGEMENTS.

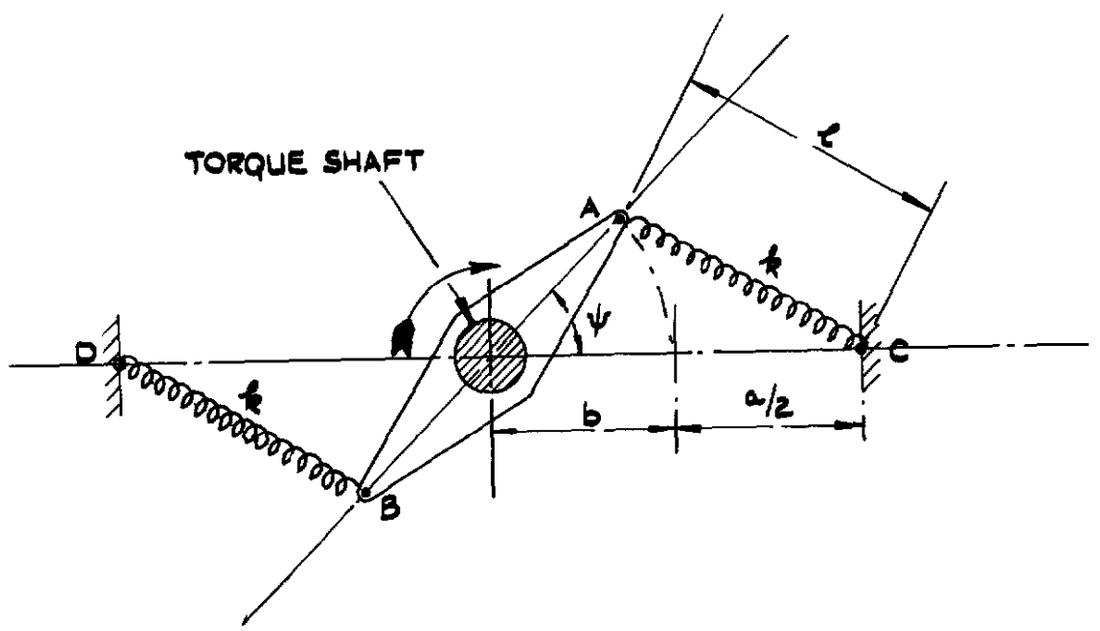

FIG. 8. SPRING ARRANGEMENT - ANGULAR DISPLACEMENT.

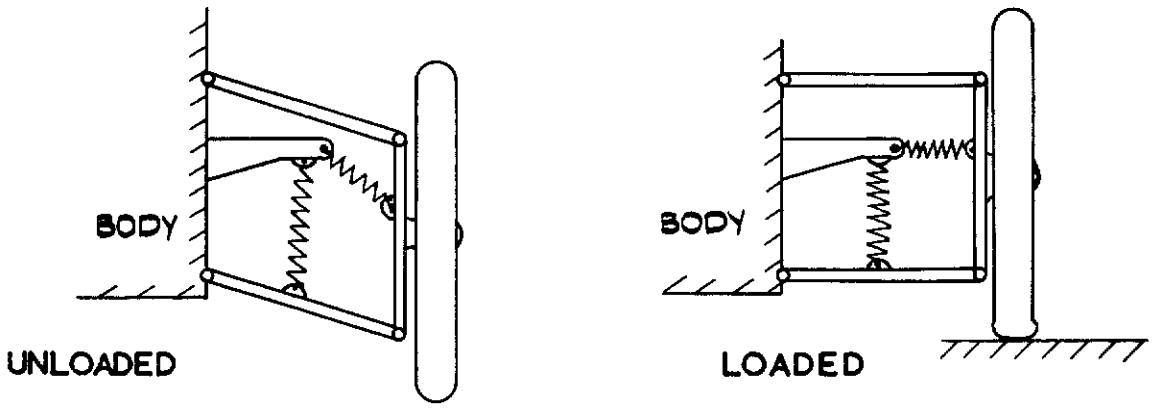

COIL SPRING SUSPENSION.

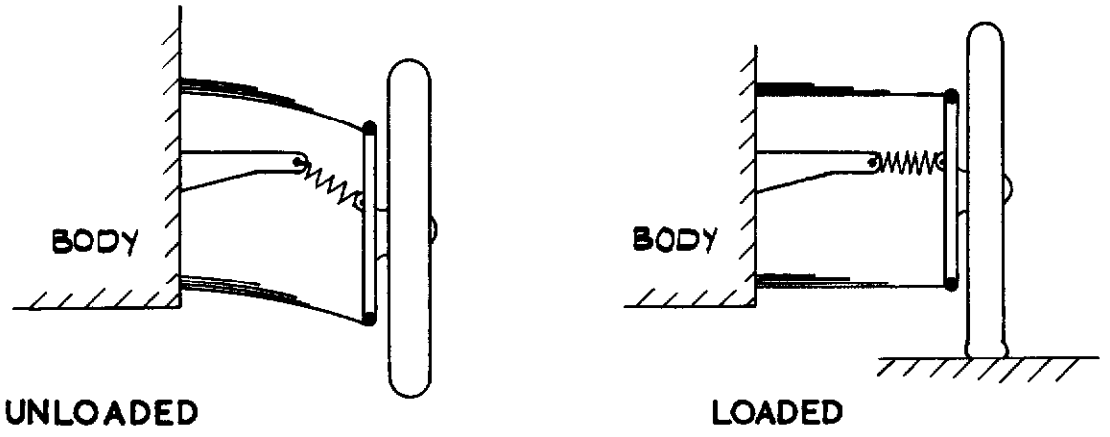

CANTILEVER SPRING SUSPENSION

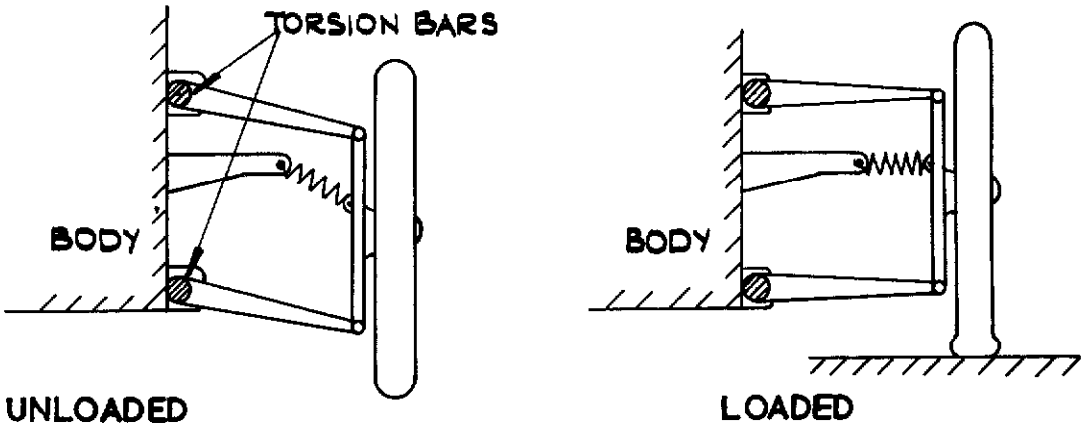

TORSION BAR SUSPENSION.

FIG. 9. APPLICATION TO ROAD VEHICLE SUSPENSION SYSTEMS.

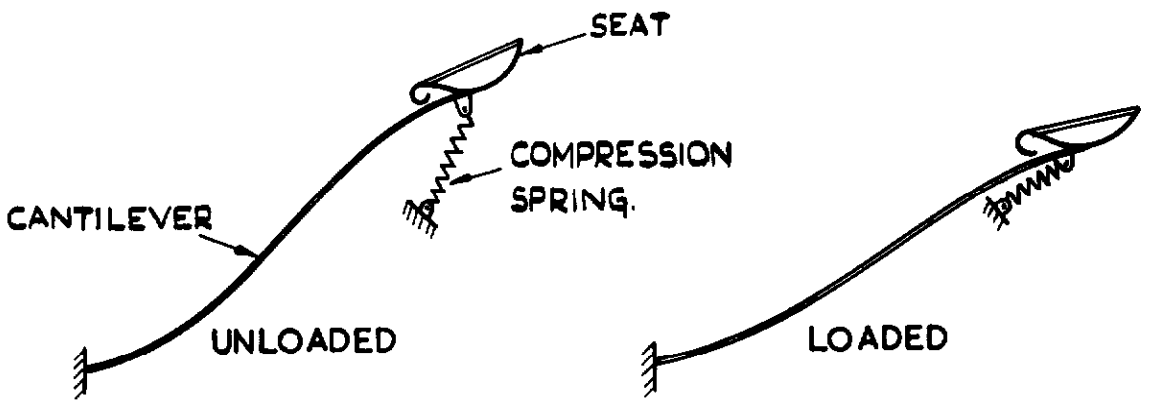

FIG. 10(a) CANTILEVER SUPPORTED BUCKET SEAT.

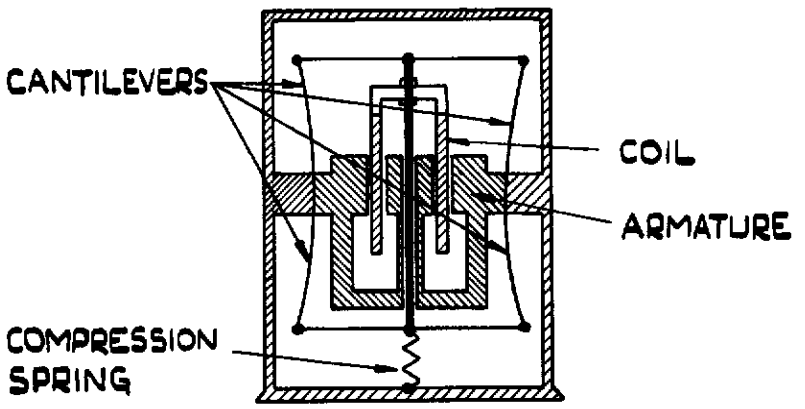

FIG. 10(b) SUSPENSION FOR SIESMIC VIBRATION TRANSDUCER

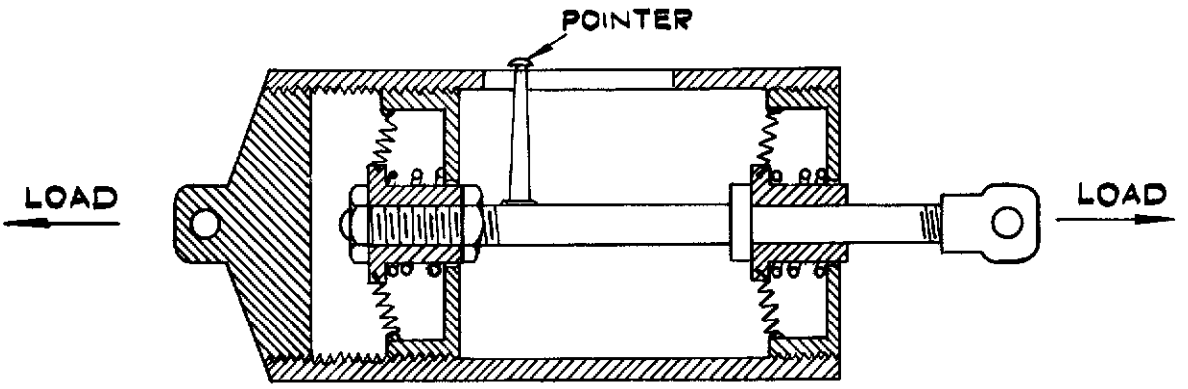

FIG. 11 (a) TENSION METER

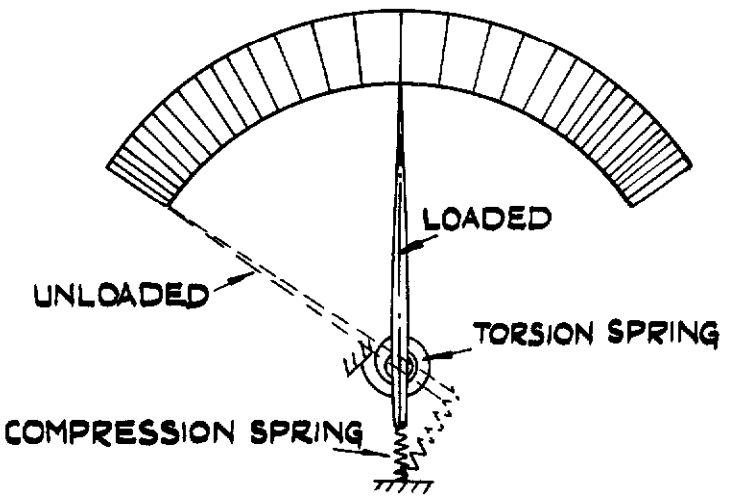

FIG. 11(b) NON-LINEAR TORQUE METER.

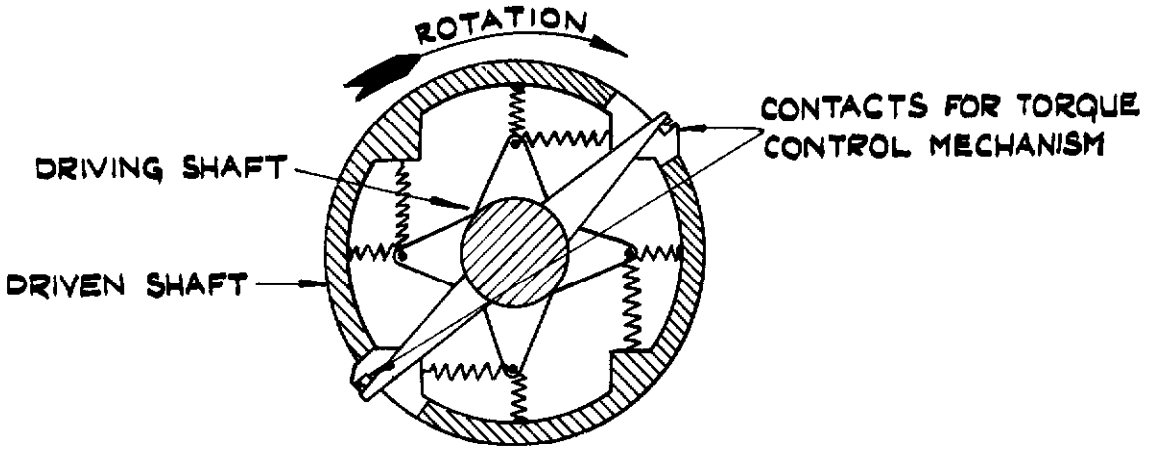

FIG. 11. (c) TORQUE REGULATOR COUPLING.

C.P. No. 322
(19,022)
A.R.C. Technical Report

Published by
HER MAJESTY'S STATIONERY OFFICE
To be purchased from
York House, Kingsway, London W C.2
423 Oxford Street, London W.1
P O Box 569, London S.E.1
13A Castle Street, Edinburgh 2
109 St Mary Street, Cardiff
39 King Street, Manchester 2
Tower Lane, Bristol 1
2 Edmund Street, Birmingham 3
80 Chichester Street, Belfast
or through any bookseller

PRINTED IN GREAT BRITAIN

S.O. Code No. 23-9010-22

C.P. No. 322

C.P. No. 323
(19,031)
A.R.C. Technical Report

C.P. No. 323
(19,031)
A.R.C. Technical Report

MINISTRY OF SUPPLY

AERONAUTICAL RESEARCH COUNCIL

CURRENT PAPERS

Low Speed Wind Tunnel Tests on Perforated Square flat plates normal to the airstream:

Drag and Velocity Fluctuation Measurements

By

B. G. de Bray, M.Sc.

LONDON: HER MAJESTY'S STATIONERY OFFICE

1957

PRICE 2s. 6d. NET

C.P. No.323

U.D.C. No. 621.45-59

Technical Note No. Aero 2475

October, 1956

ROYAL AIRCRAFT ESTABLISHMENT

Low Speed Wind Tunnel Tests on Perforated Square Flat Plates Normal to the Airstream: Drag and Velocity Fluctuation Measurements

by

B. G. de Bray, M.Sc.

SUMMARY

The effects of perforations upon the drag, and velocity fluctuations downstream, of square plates normal to the airstream are described.

It is shown that perforations can have a powerful effect upon the level of velocity fluctuations, particularly the low-frequency components, with only a comparatively small reduction in drag coefficient.

It is also shown that perforating the central region only of a square plate is as effective in reducing velocity fluctuations as perforating the whole plate while giving a slightly higher drag coefficient than the latter. On the other hand, perforations near the periphery only are less effective.

LIST OF CONTENTS

LIST OF ILLUSTRATIONS

1 Introduction

The work described in the present note is a continuation of the investigations into the behaviour of flat plates at high incidences, with particular reference to their use as air brakes.

Previous work[1,2] dealt with the effect of incidence and the shape and aspect ratio of solid (i.e. unperforated) plates.

At incidences of the order of 50° and above, the flow round a solid plate separates at the whole of the periphery of the plate and a bubble is formed behind the plate. This type of flow is usually associated with velocity fluctuations having large low-frequency components, which may cause vibration troubles in any installation of such a plate as an air brake.

The present work is an investigation into the effect of perforations on the drag and velocity fluctuations with this type of flow. Perforations admit air into the bubble and tend to reduce the general level of velocity fluctuations.

The work is limited to isolated square plates normal to the airstream. The presence of a body adjacent to one edge of the plate, as in an air brake installation, is not considered likely to have a major effect upon the findings[3].

2 Description of Tests

The experiments were made in the 4 ft x 3 ft tunnel at a speed of 140 ft/sec. The apparatus and technique used have been fully described in reference 2.

Details of the 5" x 5" square plates tested are given in Table I and Fig.1. The main series of plates (Nos.1 to 5) have 80 holes based on a square mesh of 0.5" pitch. In order to obtain the large perforation area of plate 6 it was necessary to use a roughly hexagonal mesh with 92 holes. Plate 4a was made in order to test the effect of individual hole area as against total hole area.

The numbering of the plates corresponds approximately to their free area ratio, e.g. plate No.1 has approximately 10%, plate No.2 20%, etc.

The perforations were sharp-edged in all cases.

Tests were made with plate No.4 to find the effect of perforating only part of the surface. For this purpose, successive rows of holes were blocked up, working from the centre outwards and then from the edge inwards.

The experiments consisted of:-

(i) Drag measurements, using a capacity-type drag balance.

(ii) Measurements of longitudinal velocity fluctuations in a plane 18" behind the plate, using a hot-wire placed normal to the airstream and radial to the axis of the plate. The distance of 18" was chosen to be clear of the bubble.

R.M.S. velocity fluctuations were measured at points along a radial line parallel to one pair of edges of the plates and to the 4 ft dimension of the tunnel.

In addition, frequency spectra were obtained at 4" radius, this position being approximately that at which the maximum total fluctuations occurred.

3 Presentation of Results

3.1 Drag measurements

Drag coefficients for the uniformly perforated plates are plotted in Fig.2 against free area ratio S_F/S. Fig.3 shows the drag coefficients for plate No.4 partly perforated. Starting with the solid plate, opening successive rows from the centre outward gave the upper curve, and opening the outer row (i.e. nearest the edges) first and working inward towards the centre gave the lower curve.

The drag coefficients are expressed in terms of the gross area of the plates, and are corrected for blockage by the semi-empirical method of Maskell[4].

3.2 Measurements of velocity fluctuations

The r.m.s. velocity fluctuations are presented as the ratios $\frac{u}{U_o}$, plotted against radial distances from the centre of the plates.

The spectra are presented in the form $nF(n)$ plotted against $\log n$. n is the non-dimensional frequency $\left(\frac{f\ell}{U_o}\right)$ and $F(n)$ the spectrum function, defined so that $F(n)\,dn$ is the contribution to $\frac{u^2}{U_o^2}$ of frequencies between n and $(n + dn)$.

It follows that:-

$$\frac{u^2}{U_o^2} = \int_o^\infty F(n)\,dn$$

$$= \int_o^\infty nF(n)\,d(\log n).$$

In the case of spectra, the mean square of the analyser output Δu^2 is measured over a bandwidth Δn ($\frac{\Delta n}{n}$ being small), so that:-

$$F(n) = \frac{\Delta u^2}{(U_o^2 \Delta n)}$$

and $$nF(n) = \frac{\Delta u^2}{(U_o^2 \varepsilon_A)}$$ approximately,

where $\varepsilon_A = \frac{\Delta n}{n}$, the analyser bandwidth ratio.

Figs. 4(a&b) give the r.m.s. velocity fluctuations $\frac{u}{U_o}$ in a plane 18" downstream of the plate. The maximum fluctuations occur at about 4" radius $\left(\frac{y}{\sqrt{S}} = 0.8\right)$ in all cases, so this radius was selected for the spectra, which

are plotted in Figs. 5(a&b). In addition, spectra (not shown) were obtained at 8" radius to determine the main shedding frequency, which can be done more accurately where the general turbulence level is low.

In order to assess the relative merits of the plates tested from the point of view of the low-frequency component of the velocity fluctuations, which is the most important component in causing buffeting when such plates are used as air brakes, the $nF(n)$ curves were integrated between limits $n = 0.01$ and $n = 0.05$, the results converted to units of $\frac{u}{U_o}$, and plotted in Fig.6.

$$\left[\frac{u}{U_o}\right]_{n=0.01}^{n=0.05} = \sqrt{\int_{0.01}^{0.05} nF(n) \log n \, .}$$

The range of frequencies covered by the chosen limits of n, taking representative values of U_o and $\sqrt{S}$ are as follows:-

U_o	$\sqrt{S}$	f	
		$n = 0.01$	$n = 0.05$
800	2	4.0	20.0
	3	2.7	13.3
500	2	2.5	12.5
	3	1.7	8.3

4 Discussion of Results

Considering first the uniformly perforated plates, increase in the free area ratio $\frac{S_F}{S}$ gives progressive reductions in C_D (Fig.2), r.m.s. velocity fluctuations (Fig.4a), and $nF(n)$ (Fig.5a). Up to $\frac{S_F}{S} = 0.35$, the main shedding frequency (shown by the position of the peaks of the spectra) remains constant at $n = 0.115$, but the peak amplitudes decrease progressively. Beyond $\frac{S_F}{S} = 0.35$ the shedding peak does not appear. The curves of Fig.5a can therefore be divided into two distinct groups.

The reduction in $nF(n)$ with increase in free area ratio is more marked in the frequency range below $n = 0.115$ than at higher frequencies. This reduction is shown in Fig.6, which also shows a break in the curve at the point at which shedding is suppressed.

Of the two arrangements of partially perforated plates tested, that with central perforations, $\frac{S_F}{S} = 0.25$, gave as low $\frac{u}{U_o}$ values as a uniformly perforated plate with $\frac{S_F}{S} = 0.40$, and a drag coefficient 6% higher. On the other hand, perforations near the edges only gave higher $\frac{u}{U_o}$ values than a uniformly perforated plate of equal $\frac{S_F}{S}$ value (0.29), and a drag coefficient 16% lower.

These results for partial perforations are associated with the values of the main shedding frequencies (Fig.5b), which are largely determined by the size and shape of the unperforated portions. These consist, respectively, of a hollow square rim about 1" wide and 20" peripheral length, and a solid square with about 3" sides. The latter, as expected, gave a shedding frequency somewhat higher than for the solid 5" square plate. The shedding frequency for a square rim is unknown, but if it be considered as a strip of high aspect ratio, closed end to end, previous experiments[2] indicate a value of n much higher than for a square, together with a higher C_D.

A shedding frequency associated with the spacing between individual holes (0.5" for the 80 hole plates) was not detected, probably due to the relatively large distance downstream to the measuring plane.

The single test with very small holes (plate 4a) did not show any scale effect for the size of individual holes, either upon C_D or velocity fluctuations. (Compare plates 4 and 4a in Figs. 2, 4a and 5a). This result will not necessarily apply to a case where shedding occurs.

5 Conclusions

For the isolated square plates tested, uniform perforations give substantial reductions in the level of velocity fluctuations, at the expense of comparatively small reductions in drag coefficient.

The reductions in fluctuations are more marked at the low-frequency end of the spectrum, this being the more important range of frequencies from the point of view of buffeting in the wake when using these plates as air brakes.

A free area ratio of 0.40 (with uniform perforations) gives a reduction in the low-frequency component of velocity fluctuations to about one-third of that for an unperforated plate, with a loss in drag coefficient of less than 20%. It is suggested that this value of 0.40 should be a minimum for design purposes.

With free area ratios larger than 0.40, the gain in fluctuation level becomes less but the loss in drag greater.

A somewhat better arrangement is to perforate only the central portion, leaving an unperforated rim. In the arrangement tested, such a plate with a free area ratio of 0.25 gave as low velocity fluctuations as a uniformly perforated plate with a ratio 0.40, with 6% higher drag coefficient.

Perforating near the edges only is less effective than uniform perforating from the point of view of both drag and velocity fluctuations.

A single test to determine the effect of size of individual holes gave negligible scale effect.

List of Symbols

C_D = Drag coefficient, corrected for blockage

S = Gross area of plate (sq ft)

S_F = Free area of plate (total area of perforations) (sq ft)

U_o = Tunnel speed, corrected for blockage

f = frequency (cycles/sec)

$n = \frac{f\sqrt{S}}{U_o}$

u = root mean square value of longitudinal velocity fluctuations

y = transverse distance from axis of plate

$F(n)$ = Spectrum function (see para. 3.2)

Δu^2 = mean square value of velocity fluctuations passed by analyser

Δn = analyser bandwidth

$\varepsilon_A = \frac{\Delta n}{n}$ = analyser bandwidth ratio

$\left[\frac{u}{U_o}\right]_{n=0.01}^{n=0.05}$ = mean value of $\frac{u}{U_o}$ between n values of 0.01 and 0.05

REFERENCES

No.	Author	Title, etc
1	R. Fail, T.B. Owen, R.C.W. Eyre	Preliminary low speed wind tunnel tests on flat plates and air brakes: flow, vibration and balance measurements. C.P.251. January 1955.
2	R. Fail, J.A. Lawford, R.C.W. Eyre	Low speed experiments on the wake characteristics of flat plates normal to an airstream. To be published
3	T.B. Owen	Low speed static and fluctuating pressure distributions on a cylindrical body with a square flat plate air brake. C.P.288. January 1956.
4	E.C. Maskell	A theory of wind tunnel blockage effects on stalled flows. To be published.

TABLE I

Particulars of Perforated Plates

Plate Ref.No.	No. of Holes	Hole Dia. (ins)	Free Area Ratio ($\frac{S_F}{S}$)
1	80	0.214	0.114
2	"	0.280	0.197
3	"	0.341	0.292
3.5	"	0.372	0.347
4	"	0.406	0.414
4a	2600	0.069	0.395
5	80	0.454	0.517
6	92	0.472	0.643

WT.2078.C.P.323.K3 - Printed in Great Britain.

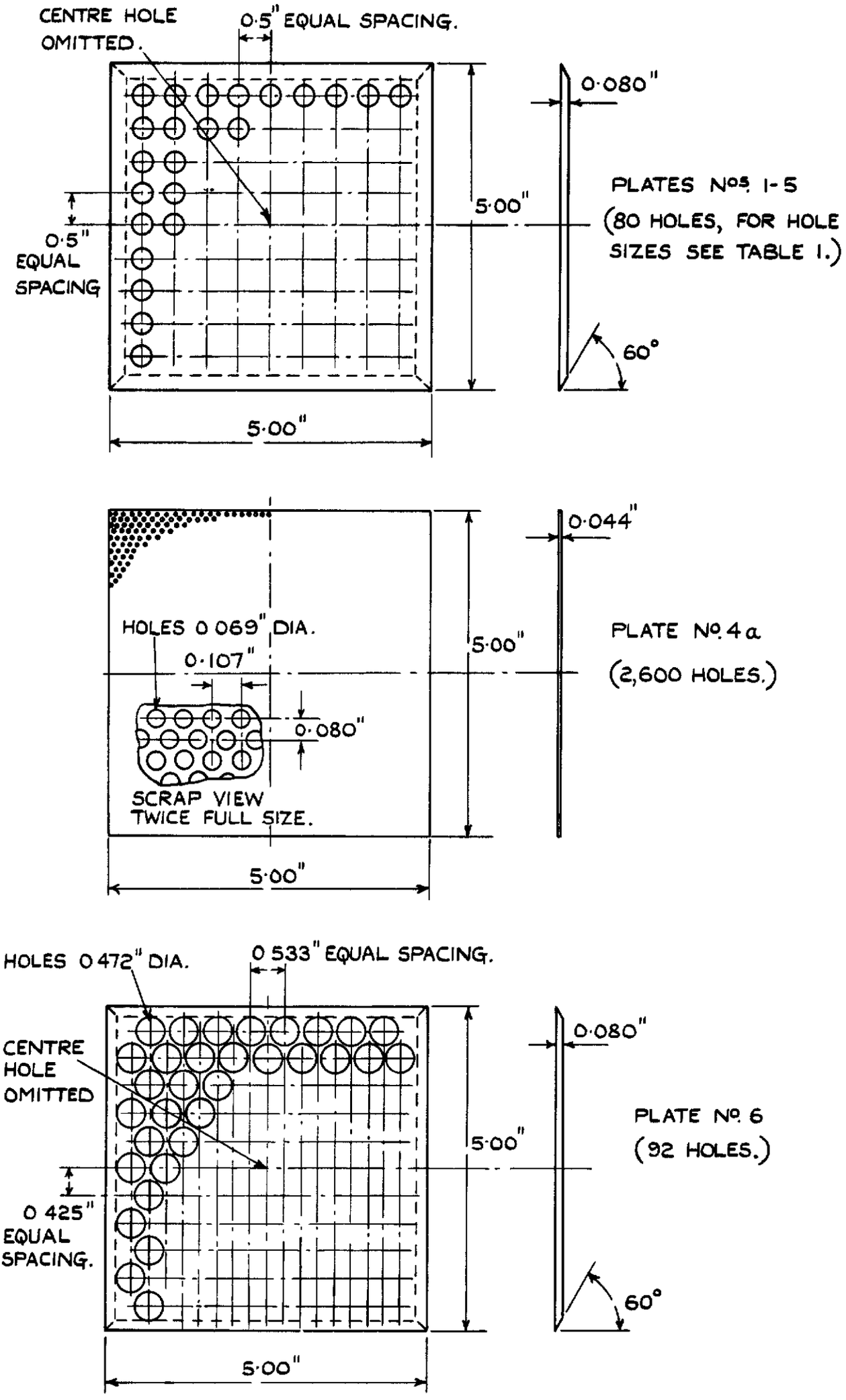

FIG. 1. DETAILS OF PERFORATED PLATES.

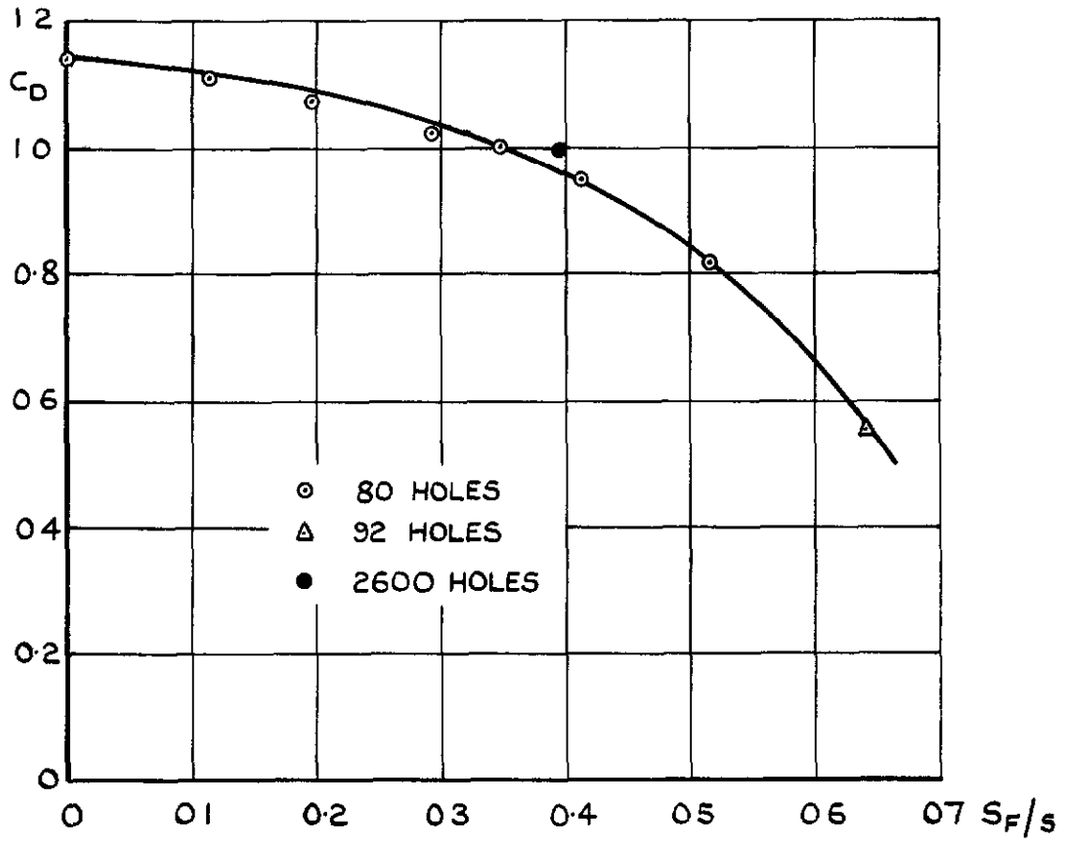

FIG. 2. DRAG OF UNIFORMLY PERFORATED PLATES.

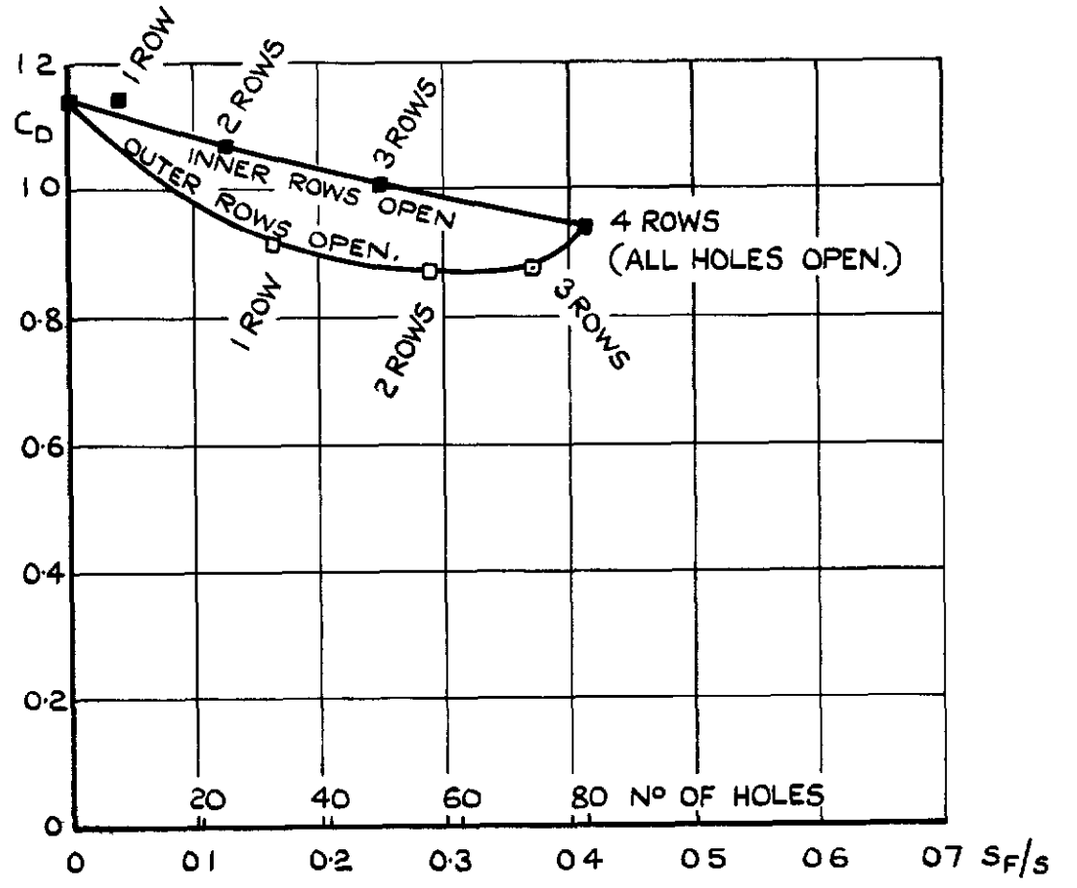

FIG. 3. DRAG OF PLATE No. 4. PARTLY PERFORATED.
(SIZE & SPACING OF HOLES AS FIG. 1.)

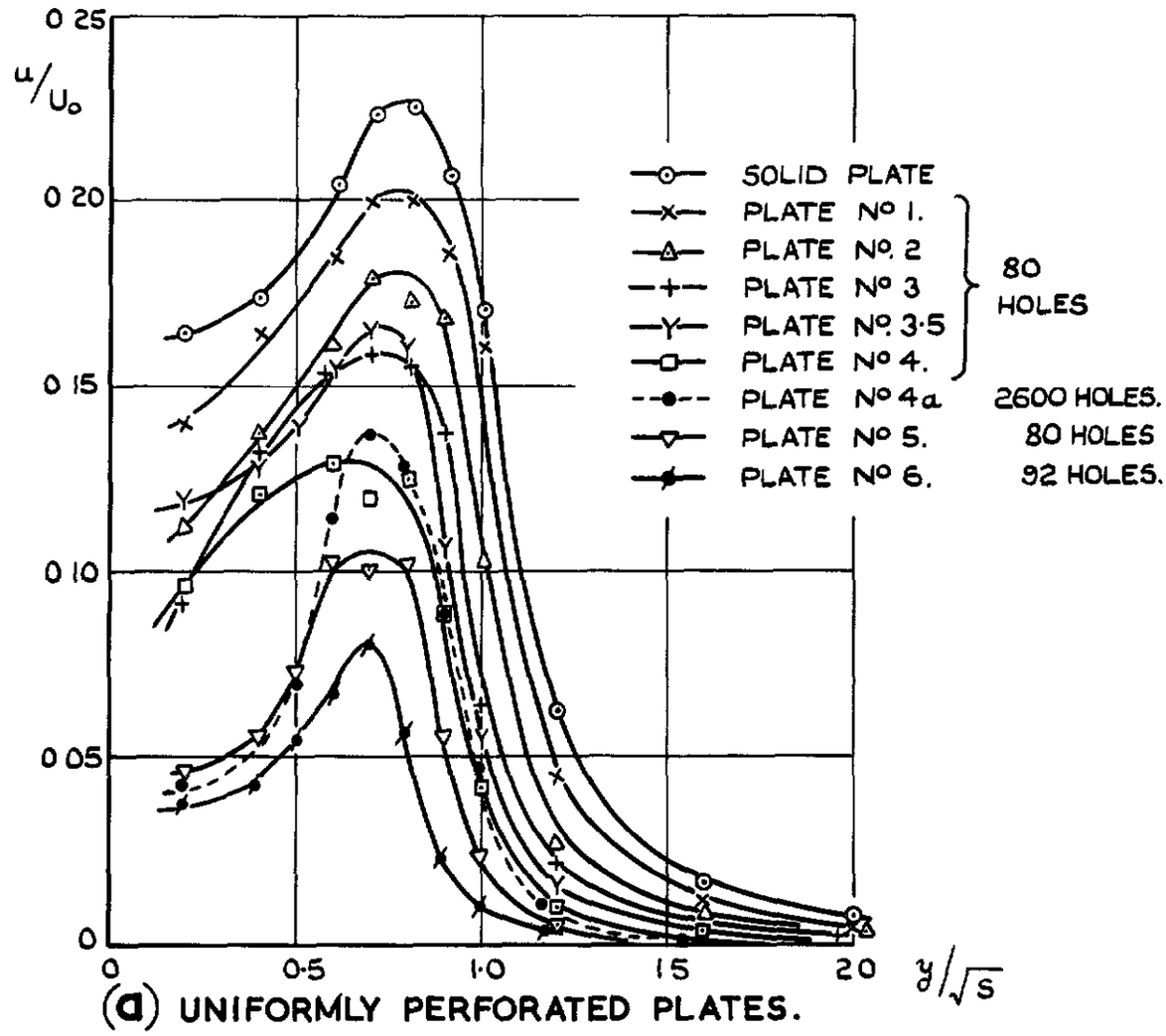

(a) UNIFORMLY PERFORATED PLATES.

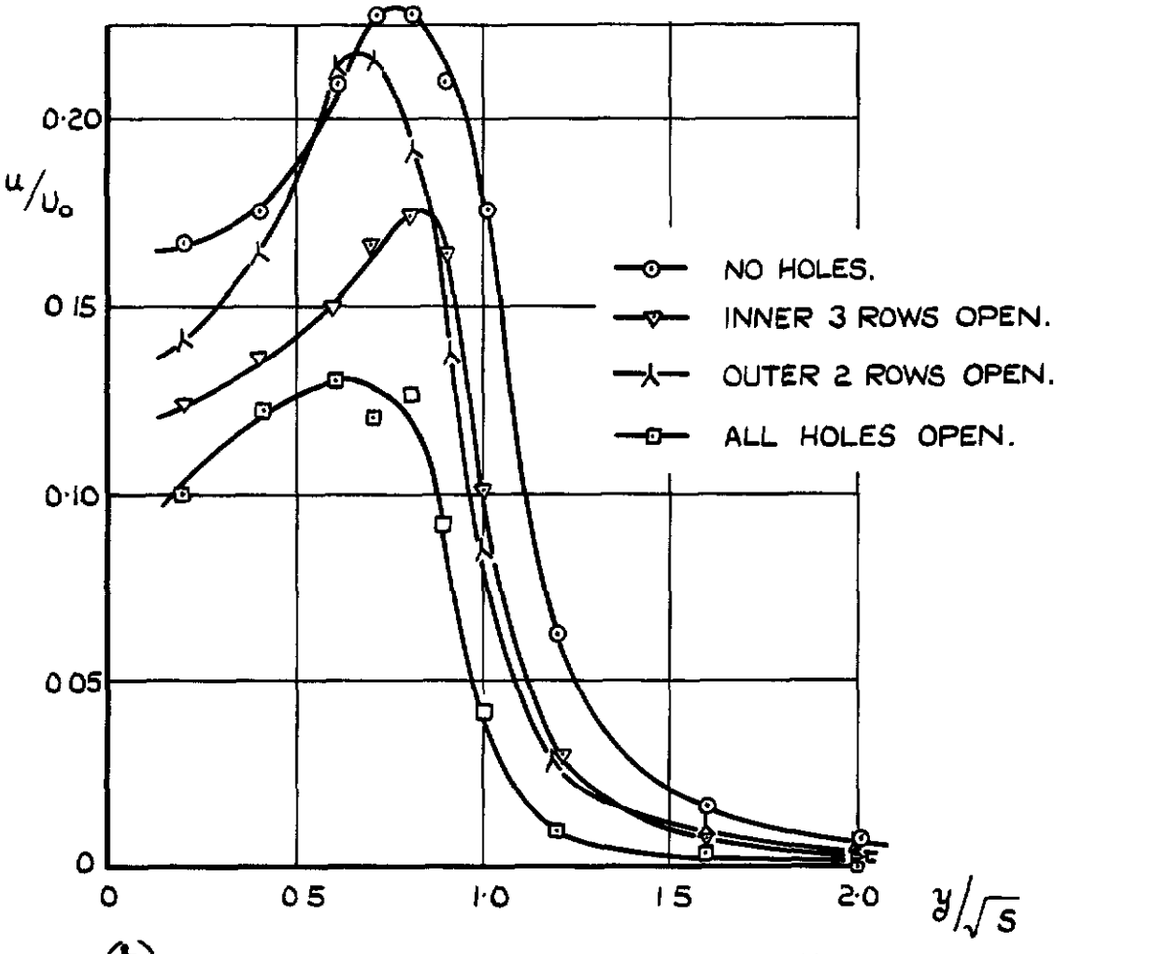

(b) PLATE No. 4. PARTLY PERFORATED.

FIG. 4. (a & b) R.M.S. VELOCITY FLUCTUATIONS. 18" BEHIND PLATES.

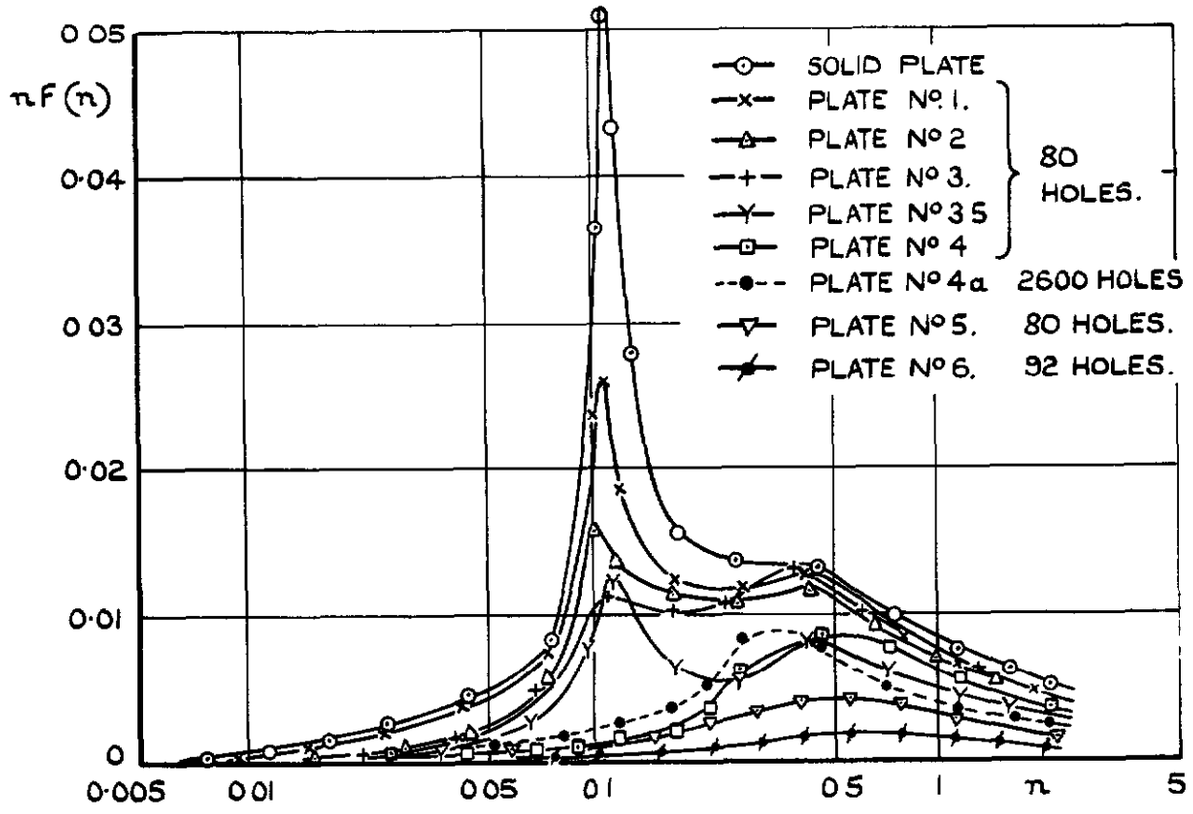

(a) UNIFORMLY PERFORATED PLATES.

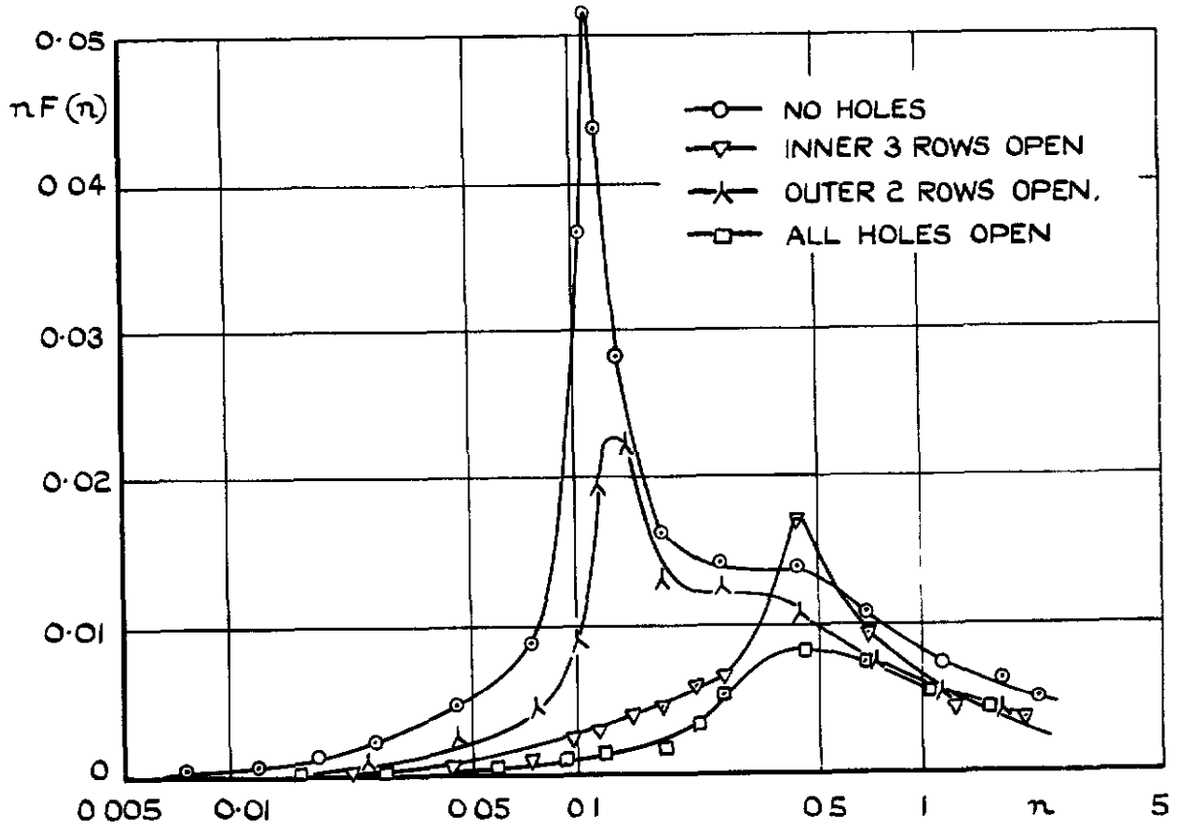

(b) PLATE No. 4. PARTLY PERFORATED.

FIG.5 (a & b) VELOCITY FLUCTUATION SPECTRA. 18" BEHIND PLATES $y/\sqrt{s} = 0.8$.

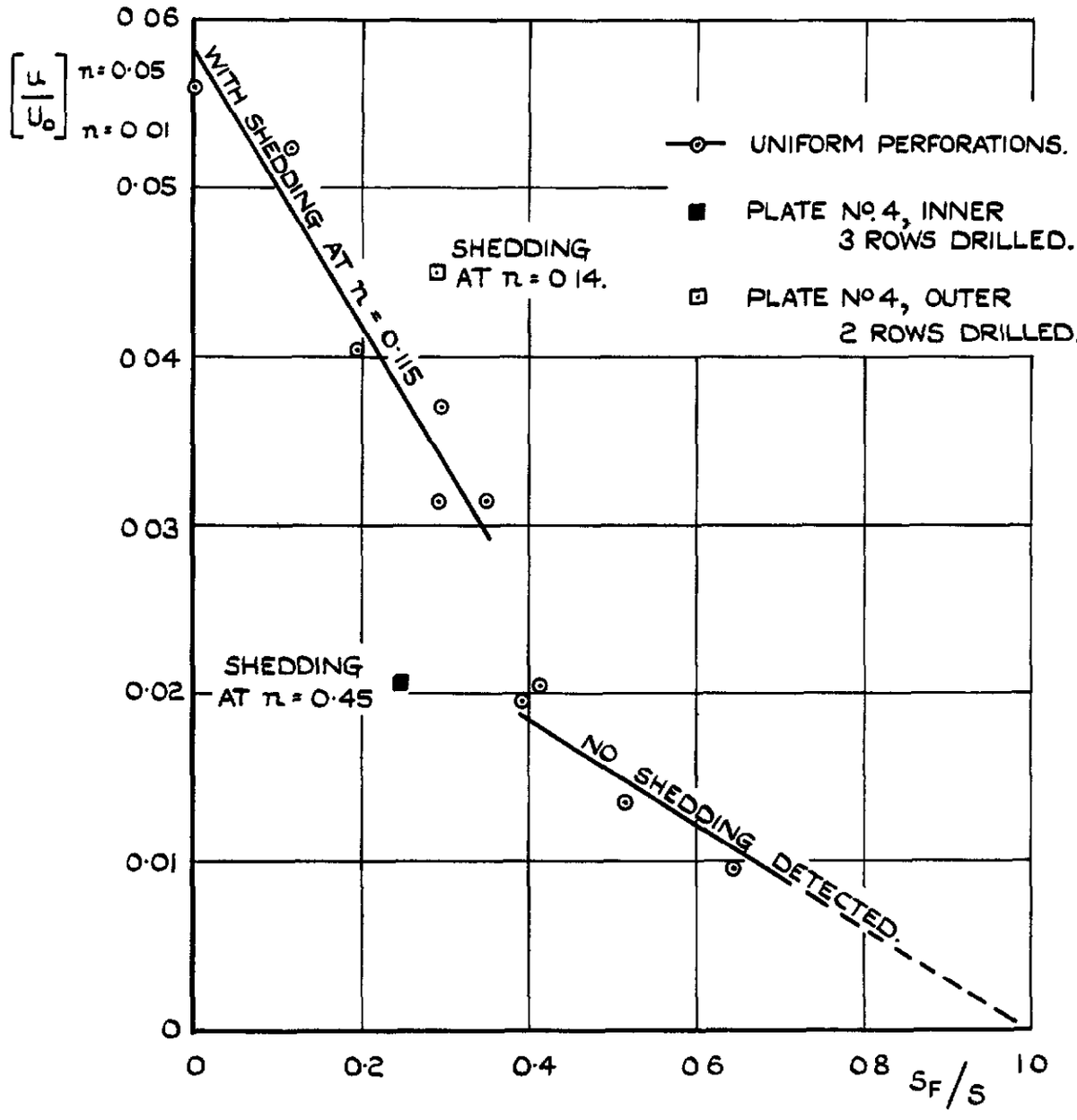

FIG. 6. LOW-FREQUENCY BAND OF VELOCITY FLUCTUATIONS 18" BEHIND PLATES.

Published by
HER MAJESTY'S STATIONERY OFFICE

To be purchased from
York House, Kingsway, London W C 2
423 Oxford Street, London W 1
P O Box 569, London S E 1
13A Castle Street, Edinburgh 2
109 St. Mary Street, Cardiff
39 King Street, Manchester 2
Tower Lane, Bristol 1
2 Edmund Street, Birmingham 3
80 Chichester Street, Belfast
or through any bookseller

PRINTED IN GREAT BRITAIN

C.P. No. 324
(18,870)
A.R.C. Technical Report

C.P. No. 324
(18,870)
A.R.C. Technical Report

MINISTRY OF SUPPLY

AERONAUTICAL RESEARCH COUNCIL

CURRENT PAPERS

The Variation of Gust Frequency with Gust Velocity and Altitude

By

N. I. Bullen, B.Sc.

LONDON: HER MAJESTY'S STATIONERY OFFICE

1957

THREE SHILLINGS NET

C.P. No.324

U.D.C. No. 551.551 : 533.6.013.8

Report No. Structures 216

October, 1956

ROYAL AIRCRAFT ESTABLISHMENT

The variation of Gust Frequency with Gust Velocity and Altitude

by

N. I. Bullen, B.Sc.

SUMMARY

Information on atmospheric turbulence obtained from counting accelerometer records is examined and relations giving the variation of gust frequency with gust velocity and altitude are obtained. The results are summarized in a form convenient for use in estimating the fatigue life of an aircraft.

LIST OF CONTENTS

LIST OF ILLUSTRATIONS

1 Introduction

The gust loads on an aircraft are important from the standpoint of both static strength and fatigue. Records of aircraft acceleration in flight are obtained from counting accelerometers which record the number of times various acceleration levels are reached[1,2]. The objective is to record accelerations of the centre of gravity and it is important to be certain how faithfully this is done in reality. The accelerometer is mounted in the fuselage and records the response to a gust with undefined space and time gradients. The record, moreover, relates to the local structure on which the accelerometer is mounted so that even when the position coincides with the centre of gravity of the undistorted aircraft, the records may be influenced by structural deflections under load.

The accelerometer counts are directly applicable only to the particular aircraft and operating conditions under which they are recorded. In order to give the results more general application, it is necessary to estimate the appropriate atmospheric conditions. For this purpose the height and speed of the aircraft are required and these are recorded photographically, together with the counts, at intervals of ten minutes. In the subsequent analysis, the effect of the flexibility of the aircraft is ignored and the recorded acceleration is assumed to be that of the centre of gravity of the aircraft*.

In order to convert the recorded acceleration to gust velocity the method given by Zbrozek[3, 4], is used. To simplify the aerodynamic analysis he assumes a rigid aircraft and ignores the pitching response induced by the gust. The gust velocity is assumed to increase linearly to its maximum value. After conversion of the recorded accelerations to gust velocities by this method, the number of gusts exceeding each magnitude in the required series is calculated.

2 The variation of gust frequency with gust velocity

A typical set of records is given in Ref 5 relating to Hermes aircraft. The original data from which this report has been prepared were obtained from about 2000 hours flying on B.O.A.C. routes. The flying is grouped in altitude bands of 5000 ft and Fig 1 shows miles per gust plotted on a logarithmic scale against gust velocity. The ordinate corresponding to a given gust velocity is the logarithm of the total number of miles flown in the altitude band, divided by the number of times the given gust velocity is equalled or exceeded. It will be seen that the variation of frequency with gust velocity is substantially the same at all altitudes, with perhaps the exception of the highest band which consists of only a small sample. This band is more turbulent than would be expected and shows a slight increase in frequency of the higher velocity gusts. However, in order to estimate the relative gust frequencies it seems reasonable to total the gusts recorded at all altitudes. This has been done for each of the four aircraft for which records are at present available[5, 6, 7, 8]. Data from test flying on the Comet are also included[9]. The graphs of log (number of occurrences) against gust velocity are of approximately the same slope for all the aircraft. The small variation may be attributed to the differences in flexibility of the aircraft, for which no allowance is made.

---

* If allowance is made for flexibility in stressing, its effect on both acceleration and stress should be included.

The result of totalling the data from all the four aircraft is given below and shown plotted on Fig 2

Cust Vel. ft/sec	-45	-40	-35	-30	-25	-20	-15	-10	10	15	20	25	30	35
No. of gusts	2	2	8	15	64	259	1192	6665	9878	2022	462	103	26	5

Up to a gust velocity of 30 ft/sec up gusts are more frequent than down gusts in the ratio of about 3 to 2. This may be partly due to manoeuvring accelerations which are superimposed on those produced by gusts, although it is doubtful whether the effect of this can account for all the disparity. At higher gust velocities the down gusts appear to predominate although the numbers are too small for this to be very significant. A possible explanation is that no allowance is made for any changes which might occur in the slope of the lift curve at the high positive incidences involved; when the aircraft is in level flight at a positive incidence, a stalling up-gust is of a lower velocity than a stalling down-gust, and thus errors introduced by assuming a constant slope to the lift curve near the stall have a greater influence on the estimates of the up-gusts.

In the estimation of fatigue damage from gust data it is usual to assume that an up gust is associated with a down gust of equal magnitude, and to take the mean of the numbers of up and down gusts as the number of fatigue loading cycles. For this purpose the numbers of up and down gusts given above are added and an empirical curve fitted. Standardized to give 1000 gusts of 10 ft/sec or greater the formula is:-

$$F = 27{,}800\ e^{-0.34411v} + 878.2\ e^{-0.20816v}$$

where v is the gust velocity in feet per second and F is the number of gusts equal to or exceeding v ft/sec. The above form of the expression is of use when calculating damage[10]. For calculating frequencies a more convenient form is:-

$$F = 10^{4.4441-0.14945v} + 10^{2.9436-0.09040v}$$

The relation is shown graphically in Fig 3. In most cases, the lowest measured acceleration corresponds to a gust velocity well below 10 ft/sec and usually approaches 5 ft/sec. In this range the frequency distribution shows no abrupt change and accordingly it is thought justifiable to extrapolate the curve to 5 ft/sec. For any given velocity a confidence range can be estimated and that for 95% confidence is shown in the figure. The estimated range makes allowance for the tendency of the gusts to occur near together in regions of turbulence[11]. The frequencies given by the formula for velocities above 35 ft/sec., should be used with caution as the total number of gusts recorded above this value is only 13 and the sampling errors are large. The ringed points on the figure correspond to experimental values. It is misleading, however, to compare their deviations from the fitted curve with the given confidence band as the experimental points are not independent. Apart from the fact that cumulative frequencies are plotted, high or low numbers of gusts tend to occur together for all gust velocities and the experimental points are highly correlated.

A numerical comparison between the observed and calculated frequencies is made in the following table, the empirical formula being factored to fit the observed frequency at 10 ft/sec.

v ft/sec	F Observed	F Calculated
10 or more	16,543	16,543 (fitted)
15 " "	3,214	3,276
20 " "	721	698
25 " "	167	164.3
30 " "	41	43.3
35 " "	13	12.7
40 " "	2	4.0
45 " "	2	1.3

3 Variation of Gust Frequency with Altitude

Having examined the variation of gust frequency with gust velocity it is necessary to examine the variation with altitude. This is done for a gust velocity of 10 ft/sec; the frequency of gusts of any other velocity may then be deduced from the relation given above. When considering the data from this point of view it is important to remember that they do not represent a random sample of atmospheric conditions, but are influenced by any action which the pilot may take to avoid turbulence. This has little effect on the relative frequencies observed at differing gust velocities discussed in para 2, but has a marked effect on the observed variation with altitude. While cruising, the pilot endeavours to avoid turbulence by small changes of both direction and height. On the other hand an aircraft with a high cruising altitude normally climbs to, and descends from, this altitude through any turbulence it may encounter, without any avoiding action being taken.

(i) Fig 4 shows data for 10 ft/sec gusts for Comet aircraft[6]. The normal cruising height is about 34,000 ft and it may be assumed that the records up to at least 25,000 ft are representative of average atmospheric conditions. Up to this altitude the relation between log (miles per gust) and altitude shows no significant departure from linearity[11].

(ii) A comparison is now made with data from an aircraft cruising at a much lower altitude. Fig 5 shows observations for Comet plotted with observations for Viking aircraft[7]. The Viking observations have been classified as climb, cruise or descent depending on the difference in the recorded heights at the beginning and end of each ten-minute interval. The curves for the Viking lie almost wholly above that for the Comet, the exception being in the lowest altitude band, and show that during cruise, by selecting a favourable altitude and course, an average improvement corresponding to a factor of about 3 can be achieved. The pronounced maximum in the cruise curve at the normal cruising altitude is a result of selecting a favourable altitude. The aircraft climbs to its normal cruising altitude and stays there unless turbulence is encountered, in which case it climbs in an attempt to find smoother conditions. Consequently flying above the normal cruising altitude only occurs in conditions which are worse than average. The curve for the Viking climb and descent shows similar tendencies, indicating that even under these conditions the pilot's avoiding action has a considerable effect, and confirming that climbing above the normal cruising altitude only takes place in adverse conditions.

(iii) The data for the Hermes[5] have not been classified into climb, cruise and descent, but it can be assumed that the majority of flying above 8,000 ft is under cruising conditions. Fig 6 shows a comparison between the Comet and Hermes. A similar trend to that observed in the case of the Viking is found, although to a lesser extent. The indications are that the pilot's avoiding

action becomes less effective as the altitude increases. If this is the case the change in slope shown by the Comet curve at about 25,000 ft may not in fact be due to the pilot's avoiding action but may represent a real change in atmospheric trend. Further light on this question will be obtained as records from aircraft cruising at greater altitudes become available.

Estimates of the average gust frequency at various heights based on all the relevant data are given in Fig 7, where a confidence range of 95% is shown about each experimental point, allowance being made for the tendency of the gusts to occur in groups. The value shown for the lowest altitude of 1050 ft is the mean of the Comet, Hermes and Viking, climb, cruise and descent. With the exception of the Comet these show little significant difference. The value for the Comet is somewhat high but is, however, based on a very small sample, (only 860 miles). Apart from this altitude band, the remainder of the main curve follows values obtained from the Comet data.

The value for the cruise of each aircraft has been obtained by taking the average of the highest three or four altitude bands. This is thought to give a more representative figure than that for the normal cruising altitude only, which is obtained under selectively good conditions. The improvement achieved under cruising conditions by the pilot's avoiding action is indicated by the dashed line in Fig 7.

4 Conclusions

The present information on the variation of gust frequency with gust velocity and altitude is conveniently summarized in Figs 3 and 7. These figures give a representation of atmospheric turbulence which may be used for the estimation of aircraft fatigue damage resulting from gust loads.

REFERENCES

No.	Author	Title
1	J. Taylor	Design and use of counting accelerometers R & M 2812. June 1950
2	J. R. Sturgeon	Unpublished work on acceleration measurements.
3	J. Zbrozek	Gust alleviation factor Part of R & M 2970. August, 1953
4	J. Zbrozek	Compressibility effect on gust loads Part of R & M 2970. August, 1953
5	J. R. Heath-Smith	Turbulence encountered by Hermes IV aircraft To be published
6	J. R. Heath-Smith	Turbulence encountered by Comet I aircraft C.P. No.248. May, 1955
7	J. R. Heath-Smith	Turbulence encountered by Viking aircraft over Europe. C.P.311. July, 1956
8	J. E. Aplin	Unpublished work
9	J. R. Heath-Smith	Unpublished work
10	J. Taylor	The estimation of fatigue lives To be published
11	N.I. Bullen	The sampling errors of turbulence measurements. R.A.E. Report Structures 208, May 1956. A.R.C. 18,764

WT.2078.CP.324.K3. Printed in Great Britain.

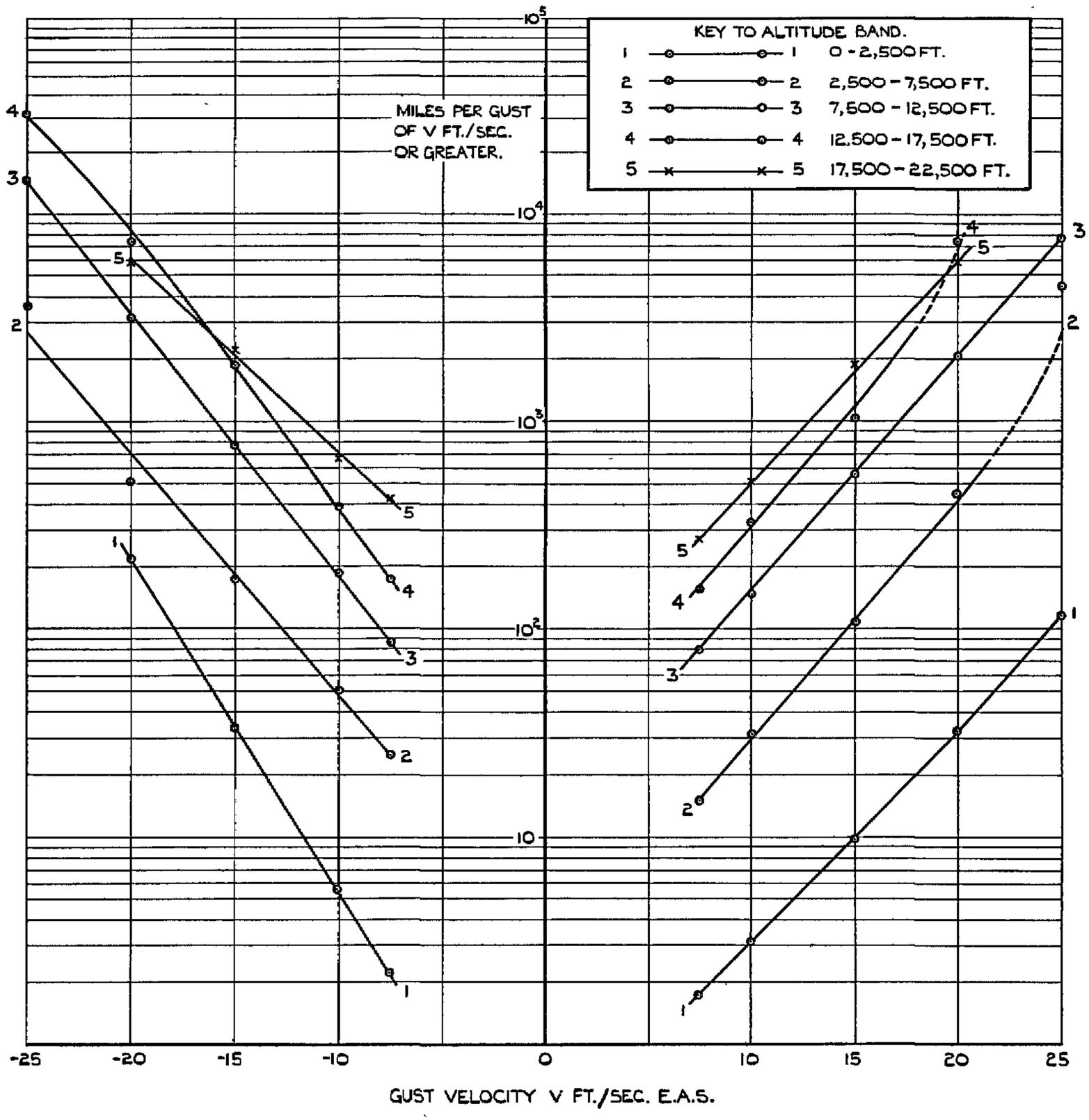

FIG. 1. TURBULENCE ENCOUNTERED BY HERMES AIRCRAFT.

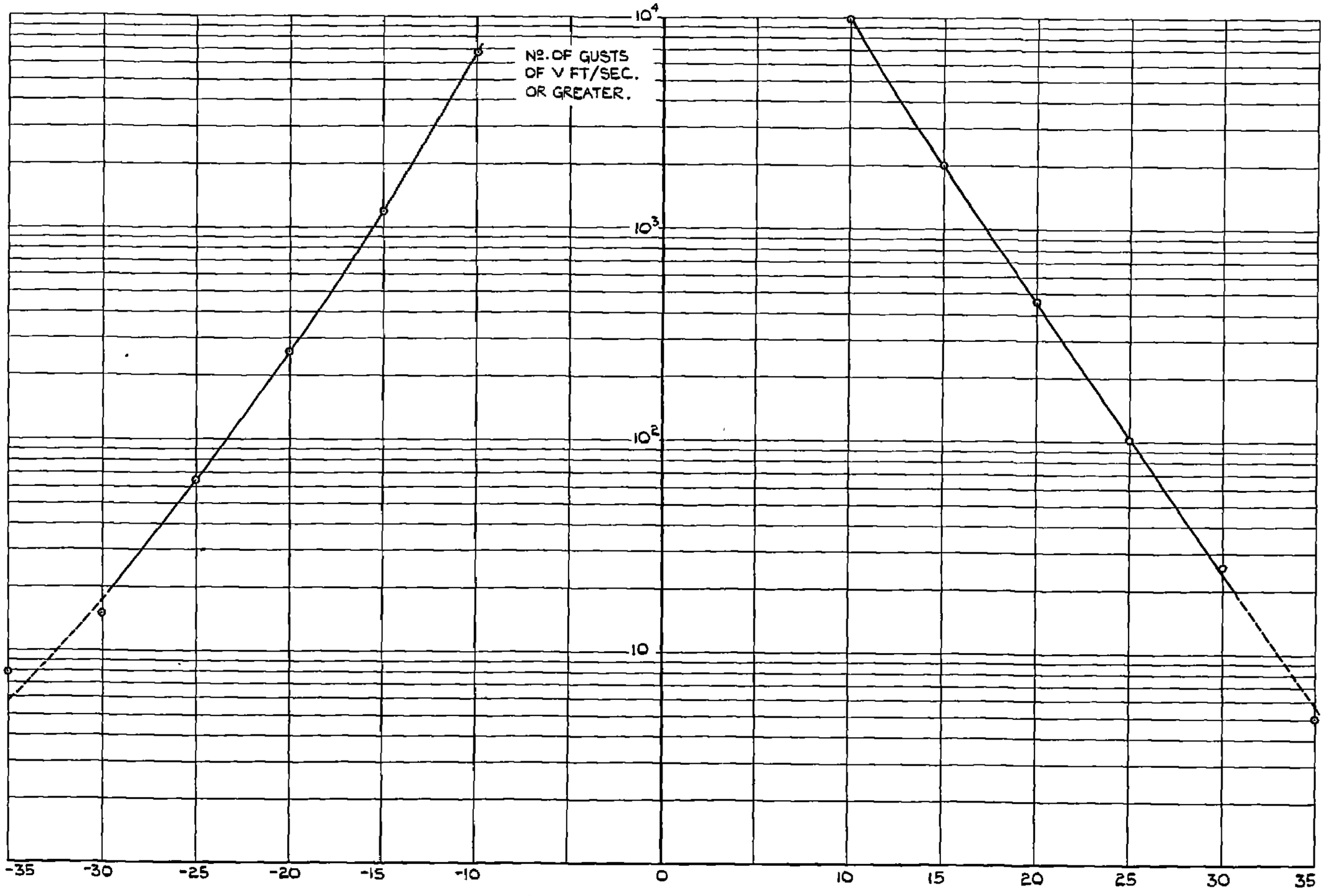

FIG. 2. TOTAL NUMBERS OF GUSTS RECORDED ON HERMES, COMET, VIKING AND BRISTOL FREIGHTER.

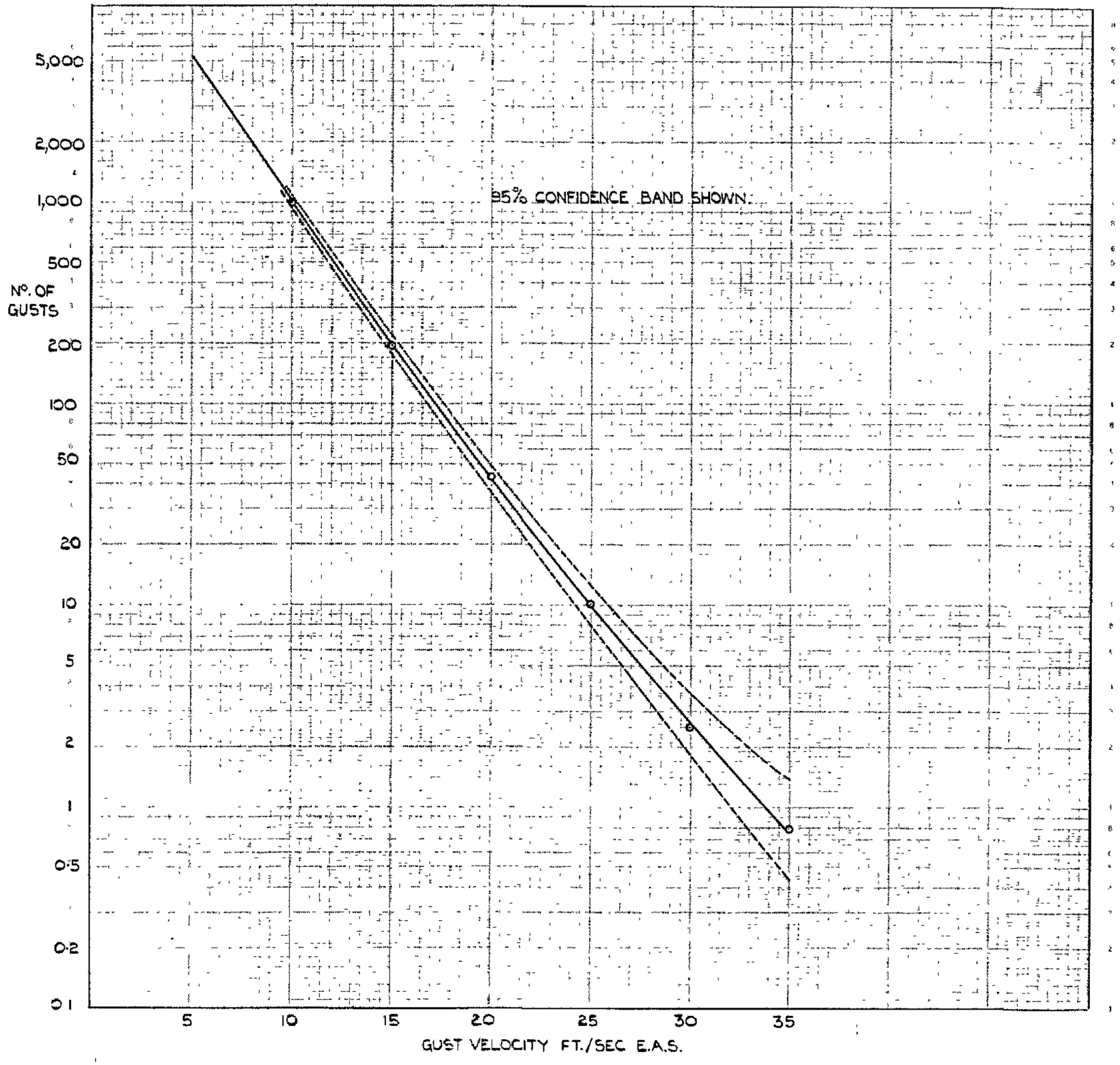

FIG. 3. NUMBER OF GUSTS EXCEEDING DIFFERENT MAGNITUDES PER THOUSAND EXCEEDING 10 FT./SEC. E.A.S.

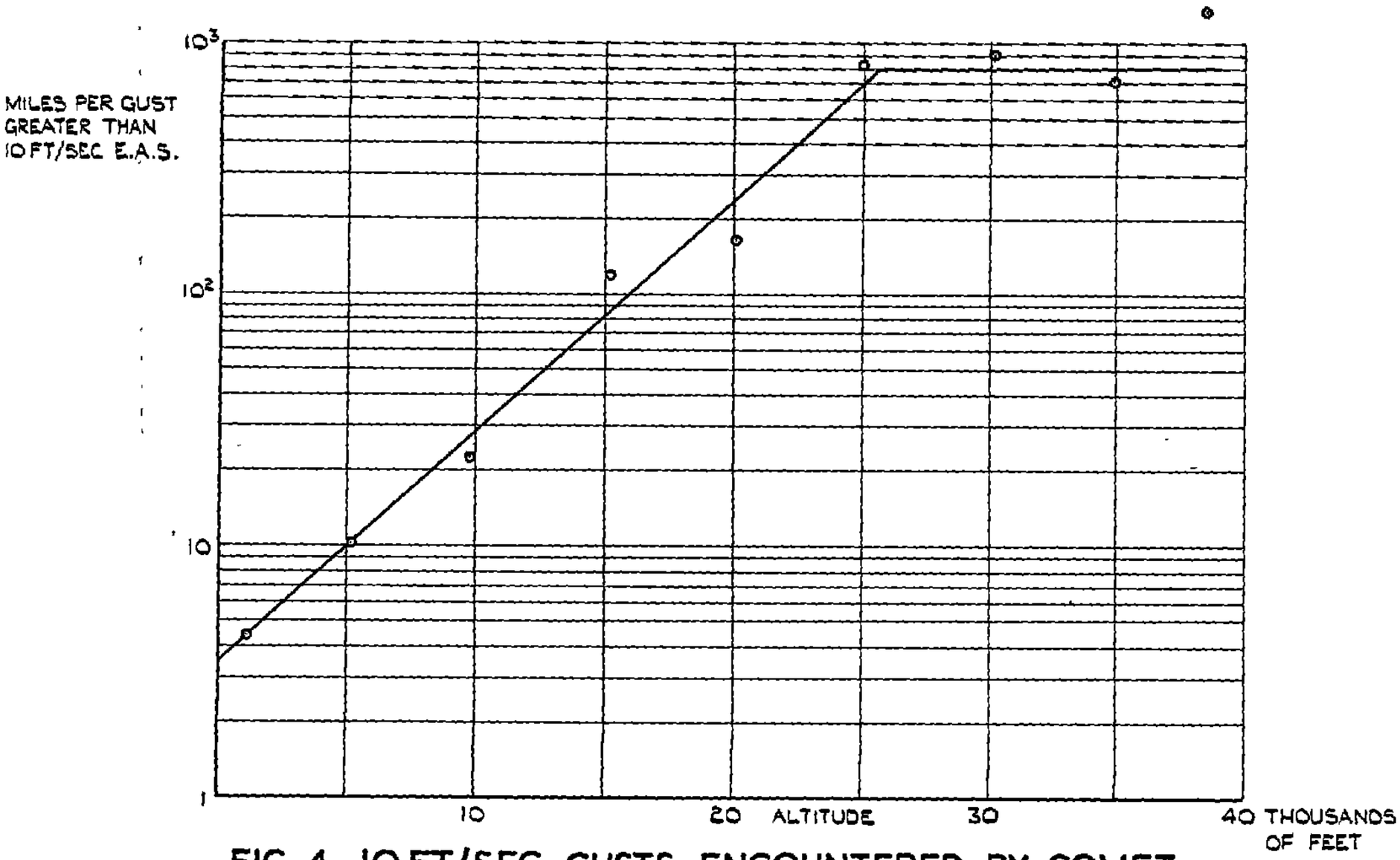

FIG. 4 . 10 FT/SEC. GUSTS ENCOUNTERED BY COMET.

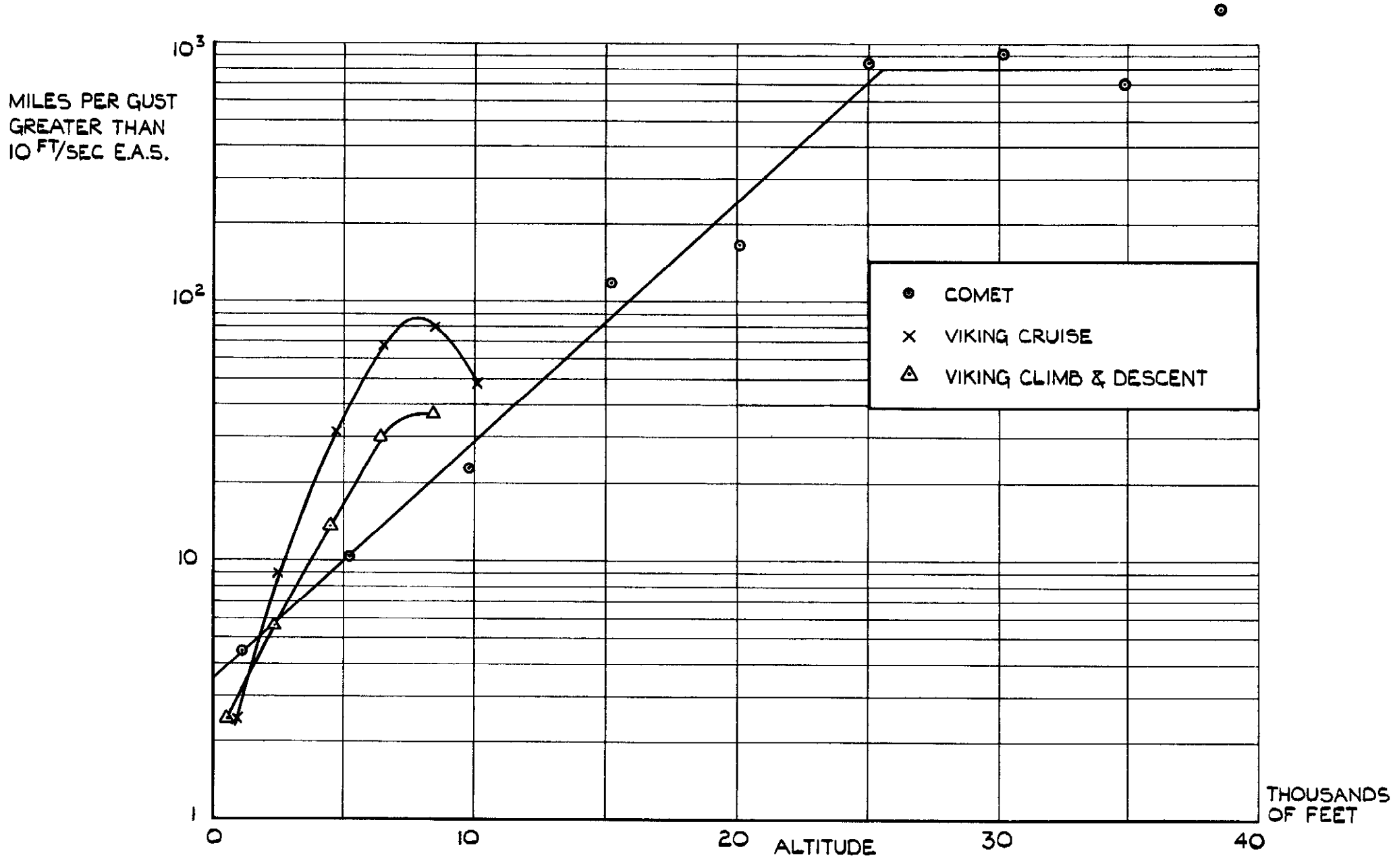

FIG.5. 10 FT/SEC. GUSTS ENCOUNTERED BY COMET & VIKING.

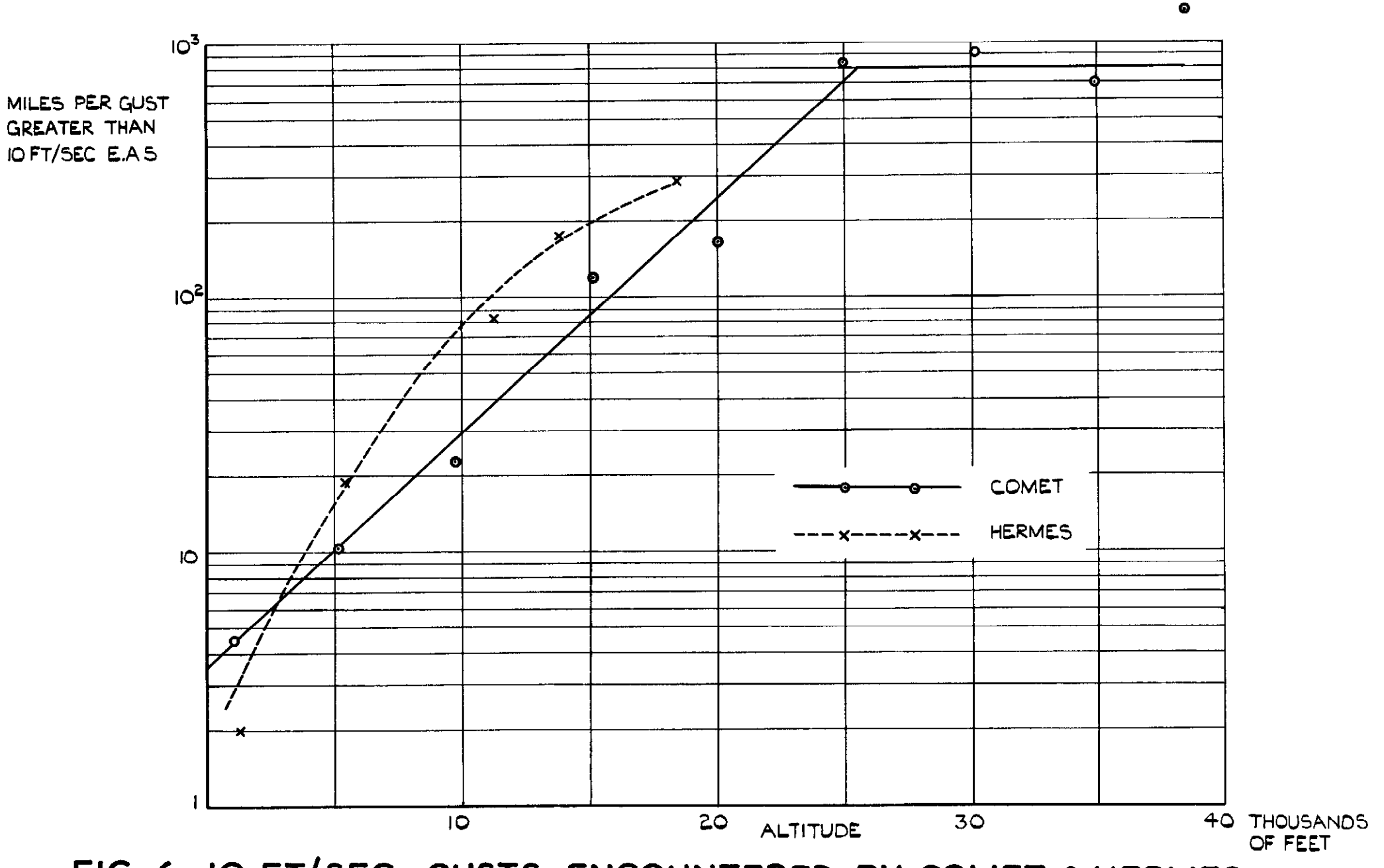

FIG. 6. 10 FT/SEC. GUSTS ENCOUNTERED BY COMET & HERMES.

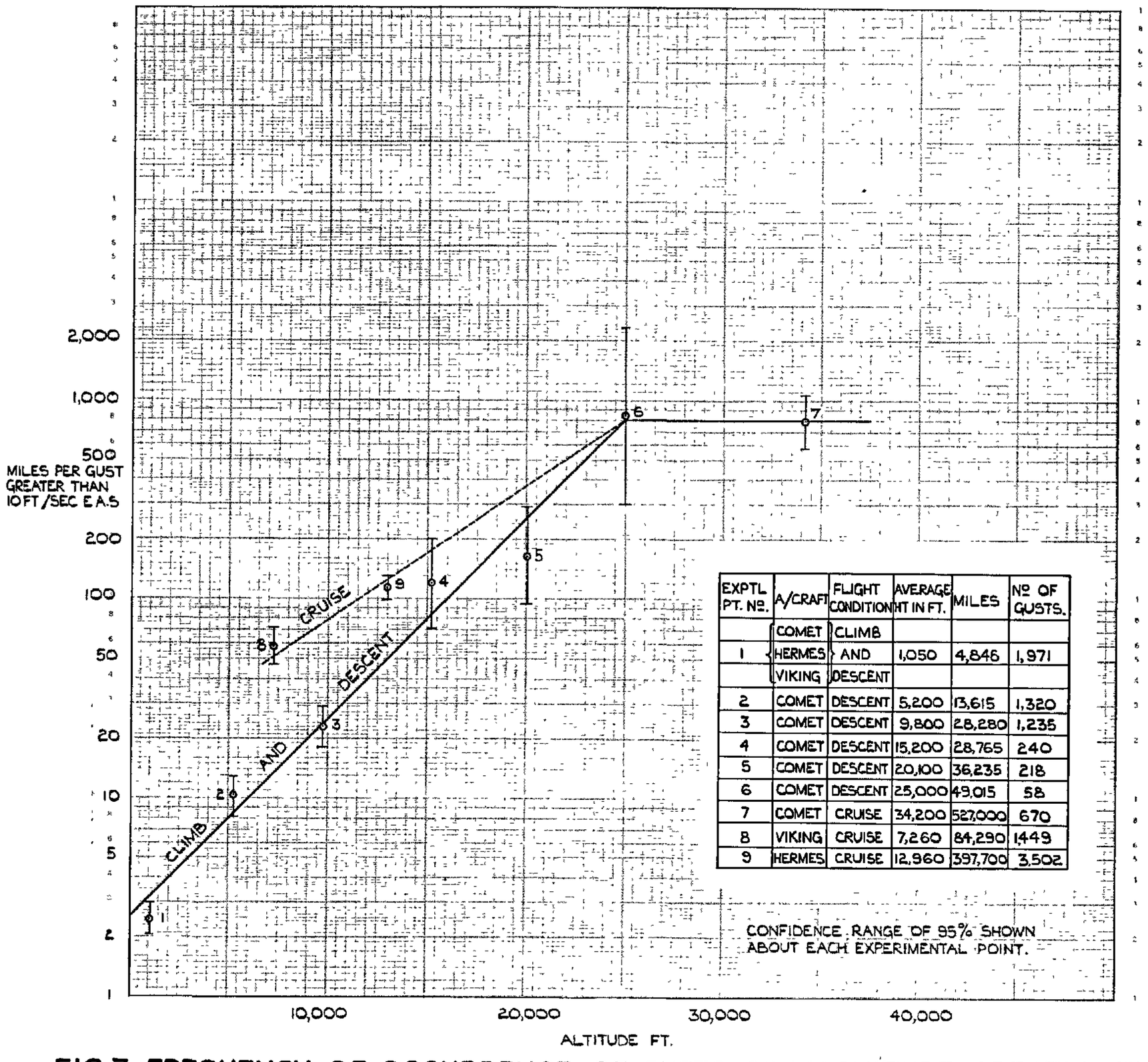

EXPTL PT. Nº.	A/CRAFT	FLIGHT CONDITION	AVERAGE HT IN FT.	MILES	Nº OF GUSTS.
	COMET	CLIMB			
1	HERMES	AND	1,050	4,846	1,971
	VIKING	DESCENT			
2	COMET	DESCENT	5,200	13,615	1,320
3	COMET	DESCENT	9,800	28,280	1,235
4	COMET	DESCENT	15,200	28,765	240
5	COMET	DESCENT	20,100	36,235	218
6	COMET	DESCENT	25,000	49,015	58
7	COMET	CRUISE	34,200	527,000	670
8	VIKING	CRUISE	7,260	84,290	1449
9	HERMES	CRUISE	12,960	397,700	3,502

FIG.7. FREQUENCY OF OCCURRENCE OF GUSTS OF MAGNITUDE GREATER THAN 10 FT./SEC. E.A.S. AT DIFFERENT HEIGHTS.

C.P. No. 324
(18 870)
A.R.C. Technical Report

Published by
HER MAJESTY'S STATIONERY OFFICE

To be purchased from
York House, Kingsway, London W.C 2
423 Oxford Street, London W 1
P O Box 569, London S E 1
13A Castle Street, Edinburgh 2
109 St Mary Street, Cardiff
39 King Street, Manchester 2
Tower Lane, Bristol 1
2 Edmund Street, Birmingham 3
80 Chichester Street, Belfast
or through any bookseller

PRINTED IN GREAT BRITAIN

S.O. Code No. 23-9010-24

C.P. No. 324